Design and Synthesis of New Organic Semiconductors for Organic Solar Cells

Xiaomei Ding

A dissertation

submitted in partial fulfillment of the

requirements for the degree of

Doctor of Philosophy

University of Washington

2021

Reading Committee:

Samson A. Jenekhe, Chair

Forrest E. Michael

Robert E. Synovec

Program Authorized to Offer Degree:

Chemistry

University of Washington

Abstract

Design and Synthesis of New Organic Semiconductors for Organic Solar Cells

Xiaomei Ding

Chair of the Supervisory Committee:
Professor Samson A. Jenekhe
Department of Chemistry

Molecular design and synthesis play critical roles in the development of organic semiconductors for organic photovoltaics (OPVs). This dissertation describes the design, synthesis, and characterization of three classes of organic semiconductors for OPVs: p-type semiconducting polymers, n-type semiconducting polymers, and non-fullerene small molecule acceptors. The relative merits of alternative building blocks and design strategies for organic semiconductors are investigated. Complex factors governing the underlying structure-property-processing-performance relationships are discussed in detail. The fundamentals of organic semiconductors and organic solar cells, state-of-the-art materials and devices, and challenges in the design and synthesis of materials are reviewed in Chapter 1.

Chapter 2 discusses the strategy of selenophene substitution as a potential method to improve photovoltaic performance of the regular thiophene-based p-type semiconducting

polymers. New selenophene-containing polymers were synthesized based on a widely used polymer, PBDB-T, where the original thiophene units at various side chain and backbone positions were substituted with selenophene. This study revealed the intramolecular and intermolecular interactions related with selenophene substitution, thus provided important guidelines in designing selenophene-containing polymers.

Chapter 3 presents a comparative study of the alternating naphthalene diimide-*thiophene* copolymer, PNDIT-hd, and naphthalene diimide-*selenophene* copolymer, PNDIS-hd. The effects of selenophene substitution on the intrinsic and photovoltaic blend properties of n-type semiconducting naphthalene diimide-arylene copolymers with simple donor−acceptor architecture were investigated. This study demonstrated multiple advantages of selenophene substitution including enhancing light harvesting, formation of favorable morphology, and reducing charge recombination losses in all-polymer solar cell devices.

Towards enhancing the intrinsic stability of small molecule acceptors, novel *tridecacyclic* ladder structure was designed and realized via Friedlander condensation reactions. The tridecacyclic ladder molecule acceptors (LMAs) described in Chapter 4 combined good solubility with enhanced stabilities and high photovoltaic performance. One of the new LMAs, LTX-4Cl, demonstrated a high PCE of 11.5% with high fill factor of 0.75. This study also unraveled the significant impact of side chains and halogenations on the molecular packing characteristics of the LMAs and the resulted photovoltaic performance.

Finally, the results of the above studies are summarized in Chapter 5 and an outlook is given for future development of organic semiconductors and the organic photovoltaic technology.

TABLE OF CONTENTS

LIST OF FIGURES

LIST OF TABLES

LIST OF SCHEMES

ACKNOWLEDGEMENTS

First, I would like to thank my advisor, Prof. Samson A. Jenekhe, for his continuous support and guidance. His insightful comments and valuable suggestions have been indispensable to the successful completion of this work. I would also like to thank Prof. Forrest E. Michael, Prof. Robert E. Synovec and Prof. Bruce J. Hinds for their service as my committee members and their kind support.

During my graduate studies in Jenekhe lab, I have encountered many people from diverse cultural background. My interactions with the past and current group members not only helped me grow as a scientist, but also enriched my education as a person. I would like to thank Dr. Haiyan Li, Dr. Taeshik Earmme, Dr. Selvam Subramaniyan, Dr. Ye-Jin Hwang, Brett A. E. Courtright, Frank E. Eberle, Dr. Daiki Kuzuhara, Dr. Nagesh N. Kolhe, Hyunjong Lee, Duyen K. Tran, Sarah West, and Mary Nguyen, for they have been the significant figures throughout my graduate school experience. I give my special thanks to Dr. Daiki Kuzuhara. During his one-year stay as a visiting scholar, he taught me various skills in organic synthesis. In the following years, he has become an important collaborator in conducting 2D GIXD measurements, for which I would also like to acknowledge Dr. Tomoyuki Koganezawa at the Japan Synchrotron Radiation Facility SPring-8. My special thanks also go to Duyen K. Tran, who joined the group later and has been a great help in conducting device-related experiments. Without her simultaneous efforts in characterizing the materials I synthesized and providing quick feedback, I would have to spend much longer time to complete this work. I would also like to thank Sarah West for her help in synthesizing important precursors. Her contribution is essential to drive my projects forward. Additionally, I would like to acknowledge Dr. Werner Kaminsky for solving all my single crystal samples.

I would like to acknowledge Department of Chemistry at University of Washington, National Science Foundation, and the Office of Naval Research for their financial support in different parts of this work.

Finally, I would like to take this opportunity to thank my elder sister Xiaoying Ding, for she has been the daughter staying around my parents while I have been away for so many years. I would also like to take this opportunity to thank Dr. Sumeng Liu, who has been a kind and supportive companion during my difficult times. The conversations with him have been the source of inspirations for some of my most important work. In addition, I would like to thank my former roommates, Carolyn Eller, Kylee Blatchford, Dr. Derya Itir Dilmen, and Hope Greenlee. The years living together in the beautiful house by Lake Washington shaped my unique experience and unforgettable memories in Seattle.

Chapter 1. INTRODUCTION

1.1 ORGANIC SEMICONDUCTORS

Organic semiconductors are a class of materials that are electronically semiconducting and synthetically accessible. Organic semiconductors combine the abilities to absorb/emit light and conduct charge carriers, with synthetically tunable chemical structures that could afford tailored electronic structures and optical absorption/emission, solution-processability, light weight and mechanical flexibility. Using low-cost solution-processing techniques or vacuum deposition methods, various semiconductor applications such as displays, lighting fixtures, transistors, solar cells, and thermoelectrics can be produced with organic materials instead of conventional inorganic semiconductors. Currently, the well-established commercialization of organic semiconductors includes photocopier machines (electrophotography), organic light-emitting diode (OLED) displays, OLED lighting panels and more. Today, OLEDs are widely used in cellphones, tablets, digital cameras, and TV sets. New ideas and prototype products have also been under rapid development. (**Figure 1.1**) It is evident that organic semiconductors are involved with a huge industry in present and would continue to grow in future.

Organic semiconductors are π-conjugated molecules or polymers consisted of carbon and hydrogen atoms and heteroatoms such as sulfur, nitrogen, and oxygen. The overlapping p_z orbitals perpendicular to the conjugation backbone form the occupied and unoccupied molecular orbitals. (**Figure 1.2**) The difference between the highest occupied molecular orbital (HOMO) and the lowest unoccupied molecular orbital (LUMO) is known as the energy band gap (E_g), which is associated with the absorption and emission of light, as well as conductivity. The field of organic semiconductors and organic electronics was significantly boosted by the discovery of the first

highly conducting polymer (chemically doped polyacetylene) in 1970s,[1-2] which demonstrated that high conductivity could be obtained in π-conjugated hydrocarbon materials. For the discovery and development of conductive polymers, three scientists were rewarded with the Novel Prize in Chemistry in 2000: Heeger, MacDiarmid, and Shirakawa.

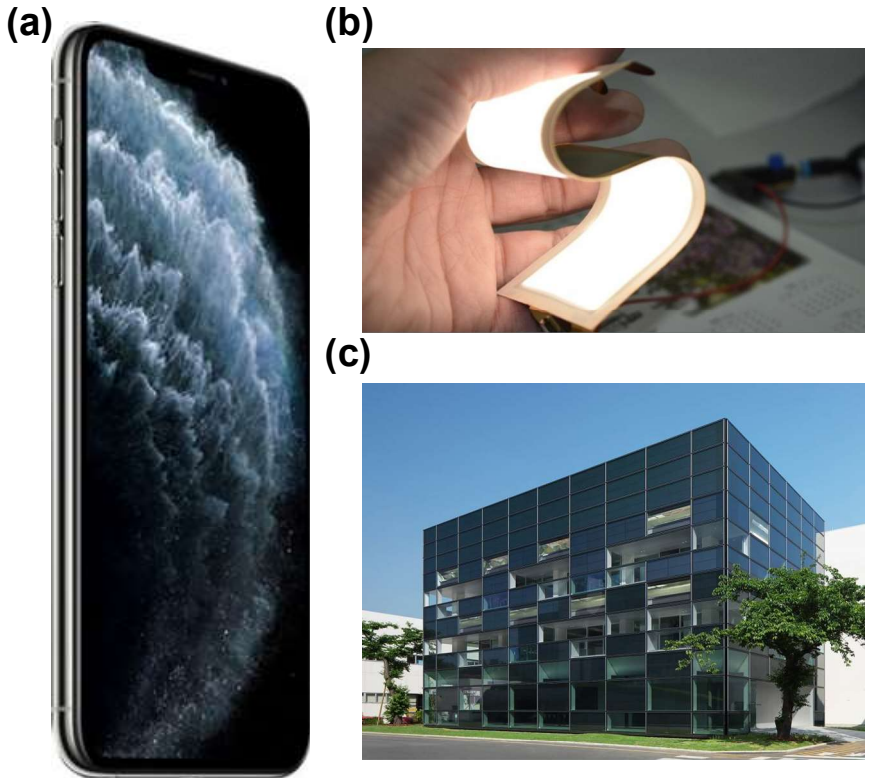

Figure 1.1. Examples of present and futuristic products based on organic semiconductors: (a) iPhone 11 pro max used *state-of-the-art* OLED display that provides high on-screen absolute picture quality and high absolute color accuracy; (b) A flexible lighting panel made by LG Chem; and (c) Taisei Corp.'s Zero Energy Building in Yokohama as an example of how buildings' walls can be covered with organic solar cells. The solar cells used on the building were provided by Mitsubishi Chemical Corp.

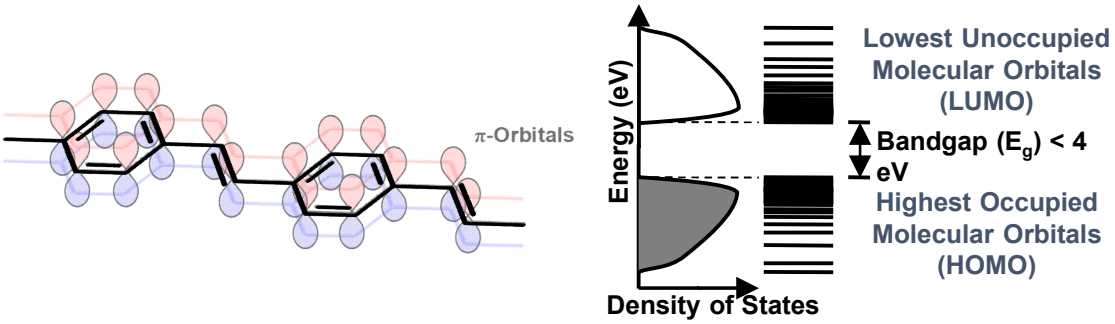

Figure 1.2. Schematic of π-conjugation and resulted band structure in a representative polymer semiconductor, poly (p-phenylene vinylene) (PPV).

It is important to understand that the "*semiconducting*" nature of organic semiconductors differs from that of inorganic semiconductors. Conventional inorganic semiconductors are silicon (Si), germanium (Ge), and gallium arsenide (GaAs), where the arrangement of elements in the lattice gives rise to delocalized electronic states and band structures. Free charge carriers (electrons and holes) can be generated by thermal or photo excitation from valence band to conduction band. Coulomb effects between electrons and holes are not important due to high dielectric constant ($\varepsilon_{GaAs} \sim 13$). In contrast, organic semiconductors are insulators with rather low dielectric constant ($\varepsilon_r \sim 3.5$) but become semiconducting under various circumstances such as doping, the injection of charges, or the dissociation of photogenerated electron-hole pairs (also known as *excitons*). Knowing the differences between organic semiconductors and their inorganic counterparts is crucial to understand their photophysical properties and electronic processes, to design and synthetically modify their chemical structures, and to improve their device performance.

1.2 ORGANIC PHOTOVOLTAICS

Photovoltaics (PV) refers to the process of converting light to electricity using semiconducting materials. Photovoltaic devices are also called solar cells. Needless to say, organic photovoltaics (OPV), or organic solar cells (OSC), are light-to-electricity conversion devices based on organic semiconductors. Today's industrialized solar panels, which are based on inorganic semiconductors, are recognized not only as an effective method to provide power supply for the remote area without grid access, but also as a way to reduce the environmental damage caused by conventional fossil fuel electricity generation. Compared with inorganics-based solar cells, OSCs are lightweight, flexible, inexpensive to manufacture (for example, *via* roll-to-roll printing), customizable at molecular level and have great potential to exhibit transparency, which is appealing for applications in self-powered windows, building walls, *etc*. Currently, the efficiency of OSCs is still lagging significantly behind their inorganic counterparts, according to the chart maintained by national renewable energy laboratory (NREL), which tracks the highest confirmed conversion efficiencies for research cells for various photovoltaic technologies from 1979 to the present. (**Figure 1.3**) Thus, developing new organic semiconducting materials (small molecules and polymers) to boost the efficiency of OSCs has been the top priority for researchers.

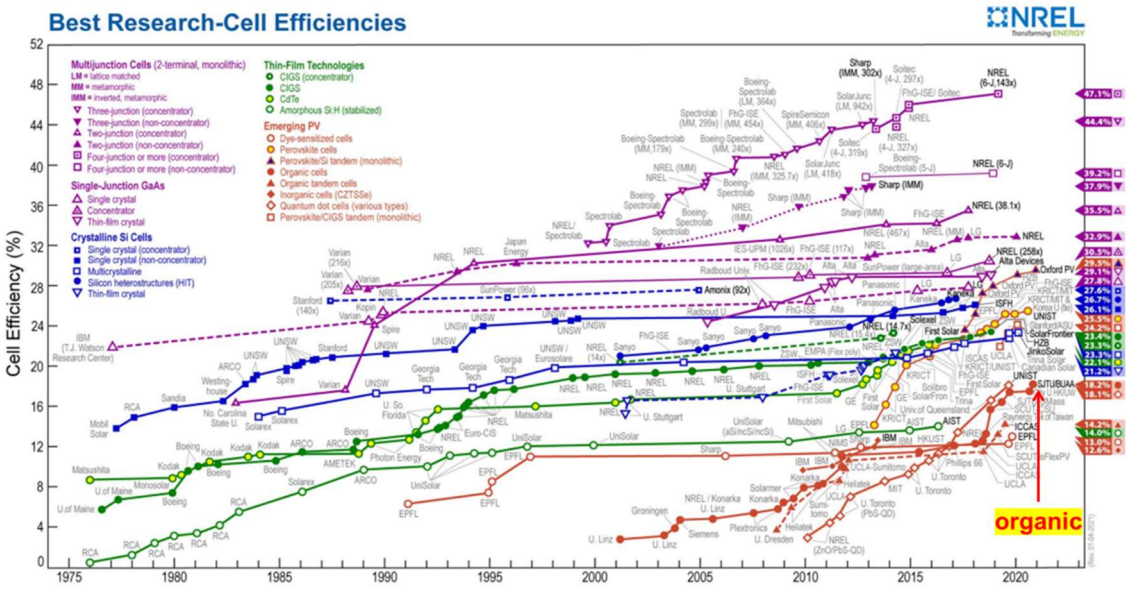

Figure 1.3. NREL's best research-cell efficiencies chart, highlighting the records for emerging photovoltaic technologies. (https://www.nrel.gov/pv/cell-efficiency.html)

1.2.1 *Brief History of Development*

The first OPV devices were investigated in 1950s, using a number of organic dye molecules, such as anthracene, porphyrins, chlorophyll, *etc*.[3] In the 1980s the first polymers (including poly (sulfur nitride) and polyacetylene) were investigated in OPV devices. Research efforts that lasted nearly four decades led to the realization that the PCE of simple single-component dye or polymer PV devices will probably remain below 0.1%.[3] (**Figure 1.4**a) The major breakthrough came in 1986 when Tang[4-5] discovered that a bilayer heterojunction device consisted of two materials that have different HOMO and LUMO energy levels (namely, a *donor* and an *acceptor*) could yield PCE of 1%, ten times greater than the efficiency of single-component devices. (**Figure 1.4**b) This concept of *heterojunction* has since been widely exploited in donor:acceptor bilayer PV devices, including small molecule:small molecule, polymer:small molecule, and polymer: polymer material systems. In a heterojunction PV device, organic

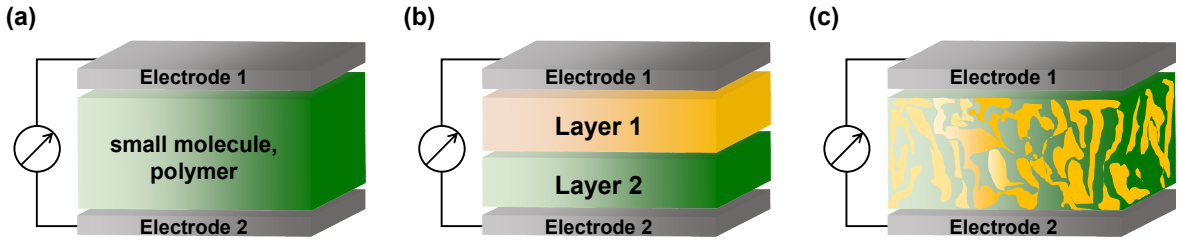

Figure 1.4. Illustration of organic photovoltaic devices with different photoactive layers: (a) single layer, (b) bilayer, and (c) bulk heterojunction.

semiconductors form excitons upon absorption of light, which dissociate into free electrons and holes after migrating to the donor: acceptor interface. The typical diffusion length of excitons is less than 20 nm, at which point excitons are deactivated into ground state. The usual film thickness of organic semiconductors, however, needs to be around 100 nm to absorb light efficiently. It follows that thicker layer of donor or acceptor would enhance light absorption, but only a fraction of the generated excitons would be able to reach the interface and dissociate into free charges. Therefore, the concept of *bulk heterojunction* (BHJ) was introduced, (**Figure 1.4**c) where donor and acceptor are mixed and form nanoscale phase separation to ensure efficient exciton diffusion and dissociation. This concept was first demonstrated by Hiramoto *et al.* with co-evaporation of donor and acceptor small molecules *via* vacuum deposition method.[6] In 1995, the first efficient BHJ OPV devices were independently realized by Heeger *et al.* and Friend *et al.* with polymer:fullerene[7] and polymer:polymer[8] blends, respectively. Today, organic solar cells mostly adopt such BHJ photoactive layers, which could be readily processed from a mixed solution of donor and acceptor materials. The various solar cells to be discussed in the following chapters belong to this category of BHJ devices only.

1.2.2 *Fundamentals on Organic Solar Cell Device Operation*

A typical BHJ OPV device consists of a multi-layer structure, where the photoactive blend is sandwiched between a transparent indium tin oxide (ITO) electrode and a metal electrode. Interfacial layers, the electron transporting layer (ETL) and the hole transporting layer (HTL), were added between the photoactive layer and the electrodes to enhance alignment of energy levels and selectively transport charge carriers (electron-only and hole-only). In a *conventional* device architecture, (**Figure 1.5**) HTL such as PEDOT:PSS was first deposit onto ITO glass substrate, followed with the active layer, ETL and finally a low work function (WF) metal electrode such as calcium (Ca) and aluminum (Al). The low WF metals could be easily oxidized in the presence of oxygen and/or moisture. Thus, the *inverted* device architecture was developed, (**Figure 1.5**b) where ETL such as zinc oxide (ZnO) and titanium oxide (TiO_x) were deposit onto ITO, and HTL was on top of the photoactive layer, followed with a high WF metal electrode such as gold or silver. The inverted device architecture offered many advantages including improved stability in ambient environment.

The operation of an OPV device can be described as four fundamental steps: (1) photon absorption and exciton generation, (2) exciton diffusion and dissociation at interface, (3) charge transport (free electrons and holes), and (4) charge collection by electrodes. Donor (D) and acceptor (A) materials, as well as HTL and ETL, with a cascade-like energy levels were selected to facilitate these processes. (**Figure 1.5**c) Specifically, upon absorption of photons, either donor or acceptor could generate excitons. The excitons diffuse to the D/A interface where the offset between HOMOs and LUMOs serve as driving force for excitons to dissociate into free electrons and holes. Electrons and holes are transported by acceptor and donor, respectively, through the interpenetrating pathways and eventually collected by electrodes. Recombination and trapping of

charges could occur during these processes, which is one of the important factors affecting device efficiency.

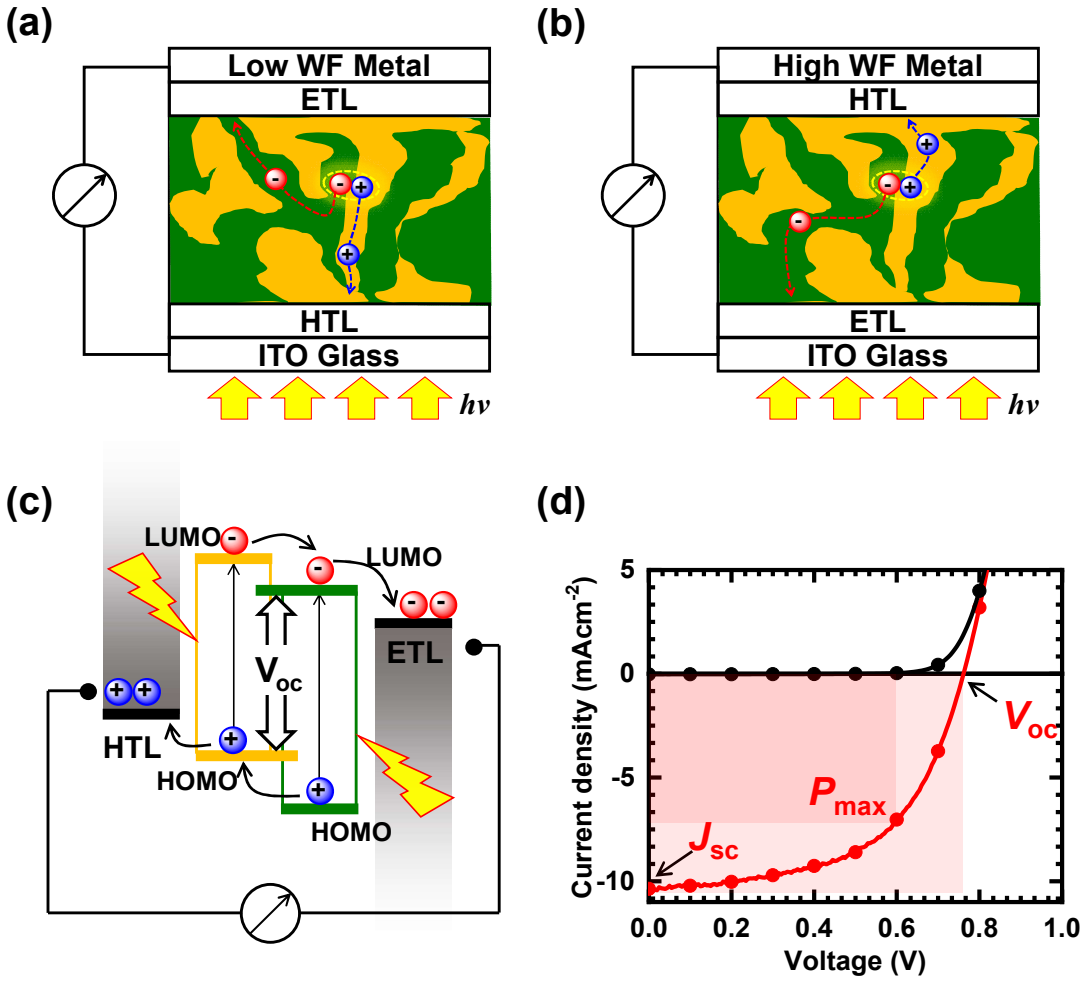

Figure 1.5. (a) BHJ OPV device with conventional architecture, e.g. ITO/PEDOT:PSS/active layer/LiF/Al; (b) BHJ OPV device with inverted architecture, e.g. ITO/ZnO/active layer/MoO3/Ag; (c) Schematic of general working mechanism within OPV devices and the energy diagram, including photon absorption, exciton formation, charge transfer/transport, and charge collection; (d) A typical current density (J) -voltage (V) profile, characterizing dark current, photo current and other important parameters of an OPV device.

Three important parameters determine the power conversion efficiency (PCE) of an OPV device: open circuit voltage (V_{oc}), short circuit current density (J_{sc}) and fill factor (FF). (**Figure 1.5**d) V_{oc} is the maximum voltage generated. J_{sc} is the photo generated current that reached the electrodes under zero applied field. The product of voltage (V) multiplied by current density (J) is the power (P) generated by the device. Along the J-V curve of an OPV device, a maximum power point (P_{max}) could be identified. The ratio of P_{max} to theoretical maximum power ($V_{oc} \times J_{sc}$) is defined as fill factor (FF), essentially represents a measure of the device quality. Mathematically, $\mathrm{FF} = \frac{P_{max}}{V_{oc} \times J_{sc}}$, $\mathrm{PCE} = \frac{P_{max}}{P_{in}} = V_{oc} \times J_{sc} \times \mathrm{FF}$, where P_{in} represent input power from sunlight. Under standard AM1.5G condition, 1 sun is equal to 100 mW/cm^2 of irradiance. (**Figure 1.6**)

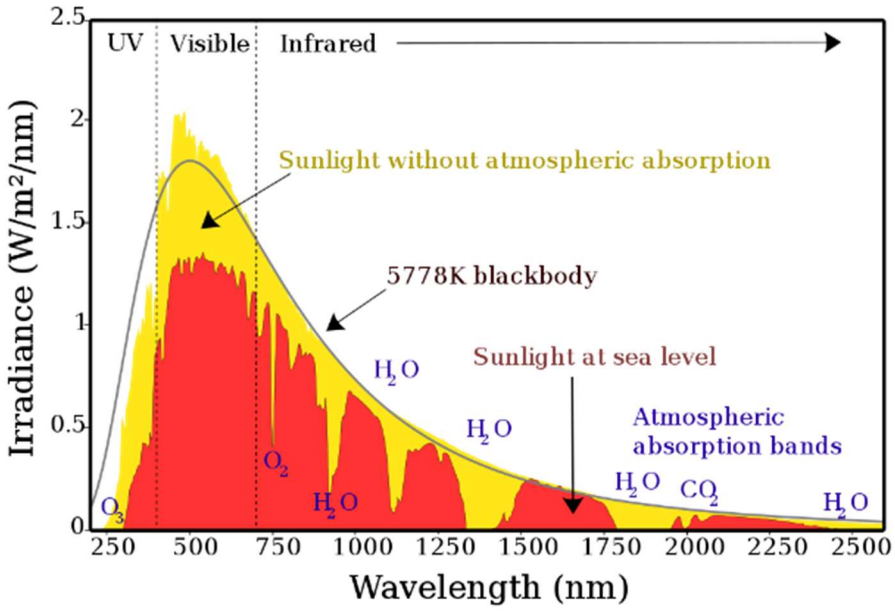

Figure 1.6. Solar radiation spectrum on earth at sea level (red) and out of the atmosphere (yellow). (Credit: By Nick84 - File:Solar_spectrum_ita.svg, CC BY-SA 3.0, https://commons.wikimedia.org/w/index.php?curid=24648395)

To achieve better photovoltaic performance, efforts should be directed toward improving efficiencies of each of the photo electronic processes occurred within the device. For instance, donor and acceptor materials that have broad, intense, and complementary absorption bands should be selected to ensure maximized coverage of the solar spectrum. (**Figure 1.6**) The broadness and absorption intensity of light by the photoactive blend is directly related to J_{sc}. Besides, the energy levels of donor and acceptor should provide sufficient driving force ($LUMO_D$-$LUMO_A$) for effective exciton dissociation and maximum output voltage (V_{oc}). V_{oc} is empirically related to the magnitude of ($LUMO_A$-$HOMO_D$) (**Figure 1.5**c). Furthermore, selecting donor and acceptor materials that are highly miscible with each other and form nanoscale phase separation is also crucial, since high charge carrier mobilities of the blend and well-connected interpenetrating network benefit balanced and trap-free charge transport, which is related to FF. In addition, suitable interfacial layers and metal electrodes are needed to provide ohmic contact for efficient charge collection.

1.3 Materials in the Photoactive Layer

Despite the highly interdisciplinary nature of OPV research, the donor and acceptor materials used for the photoactive layer remain to be the cornerstones for the development of high performing OPV devices. From a broad historical perspective, major progresses toward higher PCE of OPV devices have been tied most closely to the discovery of new materials with novel structural design. Establishing the interconnecting *structure-property-processing-performance* relationships of organic semiconductors in the context of OPV application is of vital importance. (**Figure 1.7**)

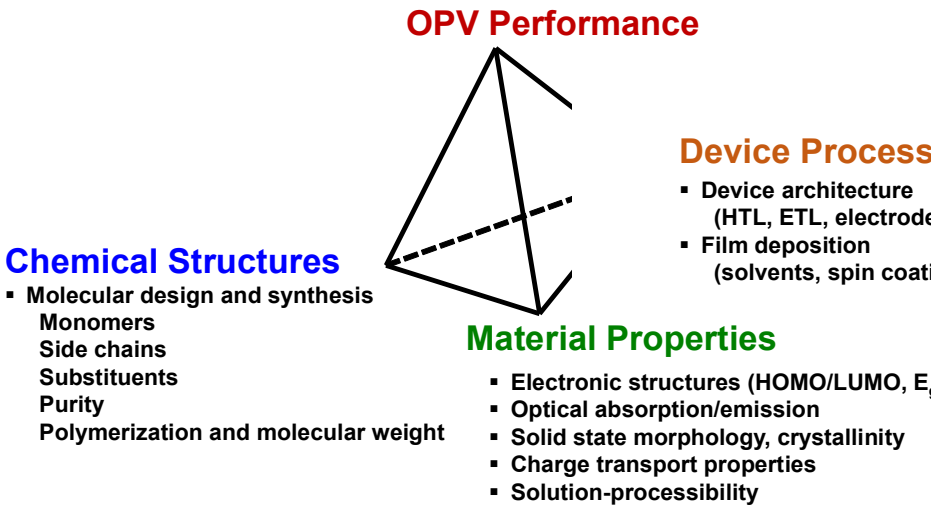

Figure 1.7. The MSE tetrahedron that describes the organic semiconductors in OPV devices.

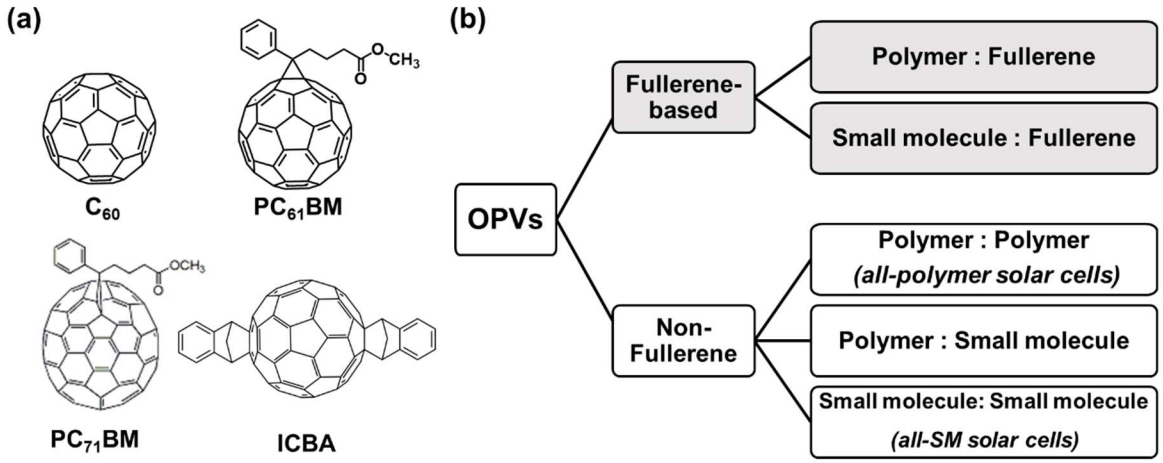

Figure 1.8. (a) Chemical structures of fullerene and its derivatives; (b) general categorization of BHJ OPVs based on the materials within the photoactive layer.

In the photoactive layer of BHJ OPV devices, the donor materials have relatively higher-lying HOMO and LUMO energy levels and are electron rich and hole-transporting (p-type), whereas the acceptor materials have relatively lower-lying energy levels and are electron deficient and electron-transporting (n-type). Before 2010s,[9-10] polymer:fullerene blend systems had dominated the field of high-efficiency OPVs, with the C_{60} fullerene and its various derivatives (**Figure 1.8**a) playing the essential role of acceptor in the photoactive layer, due to their strong electron negativity and high electron mobility. At the time, major efforts were devoted to developing donor materials, generating a rich library of p-type conjugated polymers and small molecules with a variety of chemical and electronic structures. The search for alternative acceptor materials has never stopped though, as fullerenes are also known to have their limitations, such as narrow optical absorption, difficult chemical modification, poor photostability and high manufacture cost. Non-fullerene OPVs (**Figure 1.8**b) with comparable or better efficiencies than the fullerene-based systems have just emerged in the past a few years. The non-fullerene acceptor materials are generally recognized as two categories: *n-type semiconducting polymers* and *small molecule acceptors*. OSCs that use the blends of p-type polymer and n-type polymer are also referred to as *all-polymer solar cells*. (**Figure 1.8**b)

Below, the three most important classes of organic semiconductors used for OPV devices will be further introduced: (1) p-type semiconducting polymers; (2) n-type semiconducting polymers ; (3) small molecule acceptors.

1.3.1 *P-Type Semiconducting Polymers*

One of the earliest p-type semiconducting polymers is poly[2-methoxy-5-(2'-ethylhexyloxy)-p-phenylene vinylene] (MEH-PPV).[7, 11] (**Figure 1.9**a) Although PCE of 2.5-3%[12-

[13] was achieved for PPV-based OPVs with extensive optimization, further improvement was hindered due to low hole mobility and narrow optical absorption. Soluble polythiophenes, especially P3HT, (**Figure 1.9**a) with their high hole mobility and broader absorption coverage, was the next milestone in OPV research in the 2000s. Higher PCE of 4-5% for P3HT:fullerene blend system was obtained in 2005 with morphology optimization,[14-15] attracting worldwide attention at the time.

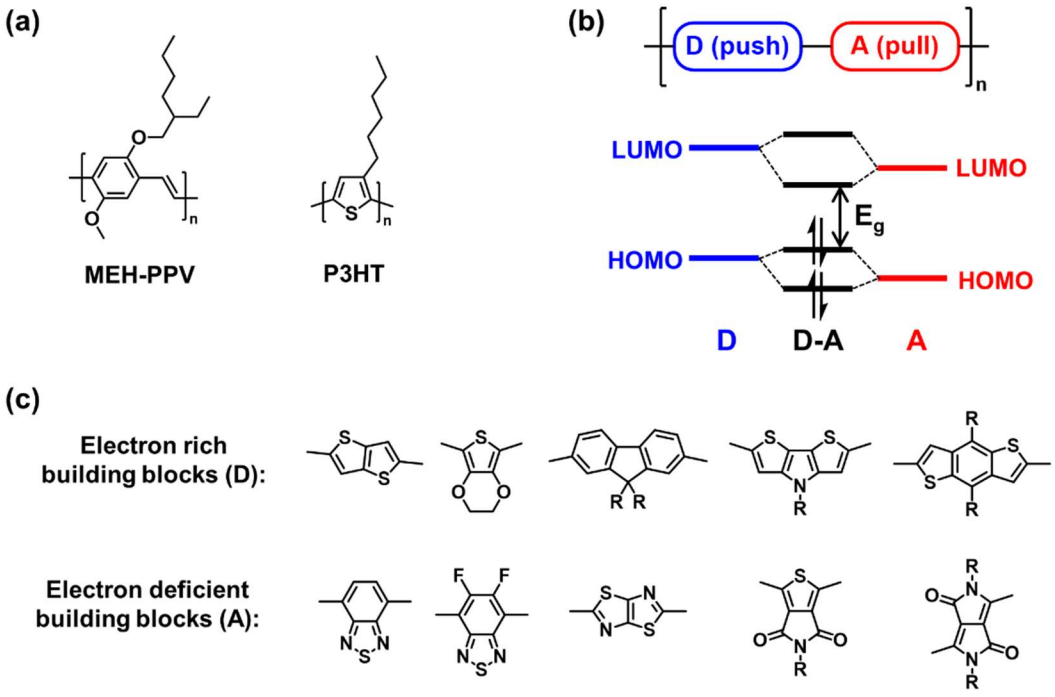

Figure 1.9. (a) Chemical structures of MEH-PPV and P3HT; (b) illustration of molecular orbital hybridization of an electron-rich moiety (D) and an electron-deficient moiety (A) leading to narrower band gap; (c) representative examples of electron-rich and electron-deficient building blocks.

Given the fixed electronic structure and optical absorption of fullerenes, a rational approach to improve the photovoltaic performance of polymer:fullerene blend system was to develop p-type polymers with narrow band gaps to broaden the overall optical absorption. Thus, the strategy of constructing alternating electron-rich (donor, D) and electron-deficient (acceptor, A) moieties in the backbone of conjugated polymers was adopted. Narrower bandgaps were achieved due to orbital hybridization of the donor and acceptor moieties.(**Figure 1.9**b) By selecting various donor and acceptor building blocks,(**Figure 1.9**c) the "donor-acceptor" (D-A) polymers or "push-pull" polymers allowed for endless tunability in the frontier molecular orbital energy levels and the optical absorption ranges, therefore directly impact V_{oc} and J_{sc} in solar cell devices. Using the versatile D-A approach, numerous p-type polymers were synthesized, gradually driving the PCE of the polymer:fullerene systems to nearly a plateau at around 10% in 2010s, enabled by a p-type polymer, poly(4,8-bis(5-(2-ethylhexyl)thiophen-2-yl)-benzo[1,2-b;4,5-b′]dithiophene-2,6-diyl-alt-(4-(2-ethylhexyl)-3-fluorothieno[3,4-b]thiophene-)-2-carboxylate-2-6-diyl)) (PTB7-Th).[16-17] (**Figure 1.10**a)

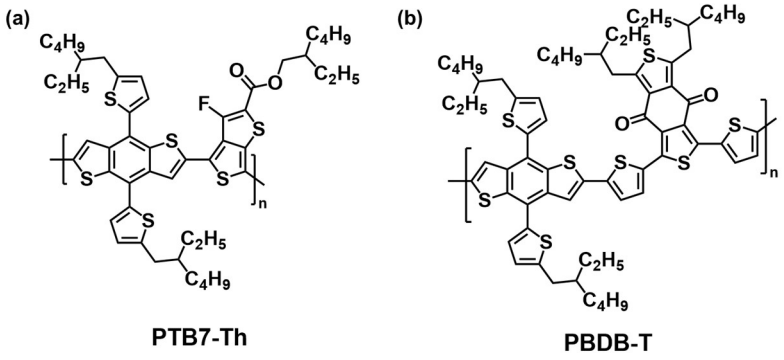

Figure 1.10. Chemical structures of representative p-type semiconducting polymers: (a) PTB7-Th and (b) PBDB-T.

Recently, in the emerging non-fullerene OPVs such as all-polymer solar cells and polymer:SMA solar cells, p-type polymers continue to play the role of donor in the photoactive blends. Since non-fullerene acceptors (n-type semiconducting polymers and small molecule acceptors) got rid of the limitations of fullerenes (fixed energy levels and optical absorption, limited optical absorption, *etc.*), those p-type polymers that were perhaps not effective for polymer:fullerene systems may find their superiority in the post-fullerene era. P-type polymers with medium (1.6 eV < E_g < 1.8 eV) to wide (E_g > 1.8 eV) band gaps were not preferred in the polymer:fullerene systems, but their perfectly complementary absorption band is precisely what is needed to pair with the low-bandgap non-fullerene acceptors. For example, all-polymer solar cells most often used an n-type polymer called N2200 (PNDI2OD-T2), which has broad optical absorption covering up to 800 nm. Similarly, in the polymer:SMA systems, a widely used small molecule acceptor, ITIC, and its various derivatives have their major optical absorption in the near-infrared (NIR) region. In both cases, the acceptors absorb in the long-wavelength region, thus medium- or wide- band gap p-type polymers are desired to avoid spectral overlap. A representative polymer named as PBDB-T (**Figure 1.10**b) has been found to have high outstanding absorption coefficient, medium band gap, deep-lying highest occupied molecular orbital (HOMO) level, and high carrier mobility. A recent review[18] has given a thorough introduction on this polymer and its numerous derivatives since they have contributed significantly to the rapid progress of OPVs. In the foreseeable future, the pool of p-type semiconducting polymers will continue to expand as the search continues to find suitable matches with the emerging non-fullerene acceptors.

1.3.2 *N-type Semiconducting Polymers*

N-type semiconducting polymers (electron-transporting) have their unique merits in the OPV applications, especially in all-polymer solar cells. In addition to the tunability in molecular structures, energy levels and optical absorption, the polymer:polymer blends are exceptionally promising for large-area solution processing, morphological stability and mechanical flexibility.[19] In the past decades, many n-type polymers have been developed as acceptor materials for OPVs based on various electron-deficient building blocks, adopting an alternating donor-acceptor strategy similar to the p-type semiconducting polymers.[20] Arylene diimides,[21] including naphthalene diimide (NDI),[22-25] perylene diimide (PDI),[23] tetraazabenzodifluoranthene diimide (BFI),[26-28] naphthodithiophenediimide (NDTI),[29-31] and bithiophene diimide (BTI),[32-34] are the most widely investigated electron-deficient building blocks in the design of *n-type* semiconducting copolymers with D-A architectures for applications in all-PSCs.[19, 23-25, 35-50] Since 2017, polymerization of the emerging small molecule acceptors has also become a popular strategy to construct n-type semiconducting polymers, enabling all-PSCs with high PCEs over 15%.[51-52] These n-type polymers not only inherited the advantages of small molecule acceptor building blocks such as narrow bandgap, strong absorption and tunable energy levels, but also possessed good film-forming capability as polymers.

1.3.3 *Non-fullerene Small Molecule Acceptors*

Non-fullerene small molecule acceptors (SMAs) have experienced the most rapid progress in the past a few years.[20, 53] Owing to the rigorous molecular modification and device engineering, SMA-based OSCs have made breakthrough in achieving high power conversion efficiency (PCE) currently exceeding 18% in single junction solar cell devices,[54] significantly surpassing those based on fullerene acceptors. The most important classes of SMAs are the ITIC,[9] IDTBR[55-56] and Y6[57] families,[53] (**Figure 1.11**) which in nature share similar acceptor-donor-aceptor (A-D-A) backbone architecture and were synthesized in similar fashion via Knoevenagel condensation reactions of aromatic dialdehyde building blocks and active methylene end groups.

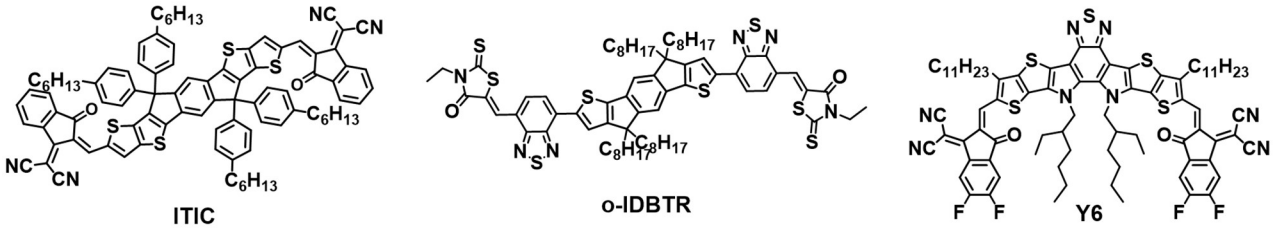

Figure 1.11. Chemical structures of representative non-fullerene small molecule acceptors: ITIC, o-IDBTR and Y6.

1.4 CHALLENGES AND OBJECTIVES

Recent development of non-fullerene acceptors (NFAs) has presented brand new opportunities that are otherwise impossible in fullerene-based OPVs. In the meantime, new challenges are waiting to be tackled for future application of this promising technology. The primary objective of this work is to design, synthesize, and characterize new conjugated polymers and small molecules, and to deepen the understanding of the structure-property-processing-performance relationships for the application of organic solar cells. The specific scope of this research includes:

(1) **Design and synthesis of new medium-bandgap p-type semiconducting polymers for non-fullerene organic solar cells.** As the significant partner of the NFAs, the p-type semiconducting polymers has been progressing at a relatively slower pace.[58] The match-up of donor and acceptor materials is crucial to achieve the best photovoltaic performance, requiring complementary absorption bands, closely aligned energy levels, suitable phase separation within blend films, balanced bulk charge transport, *etc*. Today, the most widely used and the best performing donor polymers paired with NFAs are PBDB-T[59-60] and its halogenated derivatives such as PBDB-T-2F (PM6)[61] and PBDB-T-2Cl (PM7).[62-63] Thus, in Chapter 2, I explored the strategy of selenophene substitution on the known polymer, PBDB-T, and synthesized three new polymers with selenophene at various backbone and side chain positions to finely tune their optical absorption, electronic properties and intermolecular interactions.

(2) **Investigate the effects of the donor moiety substitution on the intrinsic and photovoltaic blend properties of n-type semiconducting polymers** with the simplest possible D−A macromolecular structure based on the NDI acceptor moiety, i.e. (-D-NDI-), where the donor moiety “D” is a simple unicyclic ring such as thiophene or selenophene. In Chapter 3, a detailed

comparative study of the alternating naphthalene diimide-*thiophene* copolymer, PNDIT-hd, and naphthalene diimide-*selenophene* copolymer, PNDIS-hd, is presented.

(3) **Design and synthesis of novel ladder molecule acceptors to enhance the intrinsic stability.** Extensive research efforts have dramatically increased the power-conversion efficiencies of OPVs to such levels that are sufficient for many of their intended applications. Towards the ultimate goal of commercialization, researchers must start to prioritize reliability research, which includes integrating stability assessments into materials development and device engineering, improving packaging and expanding accelerated lifetime testing.[64] In Chapter 4, I designed and synthesized novel tridecacyclic ladder structures as an effective method to enhance the intrinsic photochemical stabilities of small molecule acceptors. Investigation of a series of ladder molecules also revealed the significant impact of the side chains and halogenations in governing the solubility, optical and electronic properties, crystallinity, morphology, as well as the resulted photovoltaic performance.

Chapter 2. SYNTHESIS AND CHARACTERIZATION OF NEW SELENOPHENE-CONTAINING P-TYPE SEMICONDUCTING POLYMERS FOR ORGANIC SOLAR CELLS

2.1 INTRODUCTION

Bulk-heterojunction (BHJ) polymer solar cells (PSCs), where the photoactive layer is comprised of a blend of p-type and n-type organic semiconductors, have undergone rapid development in recent years.[7, 65] The most notable progress has come from the n-type component that functions as electron acceptor within the photoactive blend, especially the non-fullerene acceptors (NFAs).[66-67] In 2015, the report of ITIC by Zhan *et al* with a power conversion efficiency (PCE) of 6.8%[9] started the booming of FREAs. The photovoltaic performance of ITIC derivatives was further improved to over 14%.[62, 68] Later in 2019, a new FREA named as Y6 was developed, reporting encouraging PCE of 15.7%.[69] Subsequent studies of PSCs based on Y6 and its derivatives have demonstrated growing PCE up to 16-17%.[70-72] As the significant partner of the FREAs, the p-type component in the blend, however, has been progressing at a slower pace.[58] Today, the most widely used and the best performing donor polymers paired with FREAs are PBDB-T[59-60] and its derivatives such as PBDB-T-2F (PM6)[61], PBDB-T-2Cl (PM7),[62-63] and terpolymers.[73-74] The match-up of donor and acceptor materials is crucial to achieve the best photovoltaic performance, contributed by complementary absorption bands, closely aligned energy levels, suitable phase separation within blend films, balanced bulk charge transport, *etc*. Therefore, continuous development of new p-type polymers to fulfill requirements of the emerging FREAs is still in critical demand.

Incorporation of selenophene has long been documented as a unique and effective strategy to tune the optical and electronic properties of alternating donor-acceptor (D-A) polymers and improve their photovoltaic performance.[75] The advantages of the selenophene-based conjugated polymers are anticipated based on following rationales: (1) selenium (Se) atom is less electronegative than sulfur (S) atom, hence, with lower aromaticity, selenophene-based polymers has more quinoidal character than their thiophene analogues, leading to improved planarity, longer effective conjugation length, and red-shifted absorption; (2) Se is larger in size and more polarizable than S. Due to the interchain Se···Se interaction, selenophene-based polymers often demonstrate higher charge carrier mobilities.

In addition, the location of selenophene substitution in the widely used two-dimensional (2D) donor polymers, whether in the main chain or in the side chain, also plays an important role in fine-tuning energy levels, absorption and even morphology in the blend films. It has been generally observed that substitution of thiophene units in the polymer main chain leads to reduced band gap and raised HOMO level. With slight sacrifice in the open-circuit voltage (V_{oc}) in the resulted solar cells, the overall photovoltaic performance is often complemented with superior short-circuit current (J_{sc}), as a result of greatly improved light-harvesting ability and charge carrier mobilities.[75-77] On the other hand, Yang et al.[78] reported that replacing alkylthienyl side-chain in PTB7-Th with alkylselenophenyl group resulted in stronger intermolecular interaction with minimal influence in absorption and energy levels, which allowed for optimal device performance of 8.8% PCE with no requirement of any solvent additive. Nevertheless, the reported selenophene-containing donor polymers so far have been mostly targeted at polymer:fullerene systems. Studies of such polymers in combination of NF acceptor materials are very limited.

In this part, PBDB-T was used as the host polymer to be substituted with selenophene at various positions in the polymer backbone or side chain. Three new polymers were synthesized, named as PBDB-S, PBDBS-T and PBDBS-S (**Scheme 2.1**) which allow for modulation of the molecular properties and investigation of the structure-property-performance relationship in NF PSCs.

2.2 Experimental Methods

Materials. Selenophene (97%) (2) was purchased from Sigma-Aldrich (367141 Aldrich). 2,6-Bis(trimethylstannyl-4,8-bis(5-(2-ethylhexyl)thiophen-2-yl)benzo[1,2-b:4,5-b']dithiophene (5) was purchased from Solarmer and was used as received. Thiophene-3,4-dicarboxylic acid (7) was purchased from Ark Pharm (AK-44618) and used as received. All other reagents and catalysts were from Sigma-Aldrich and used as received. Bulk solvents were supplied by Fisher Chemical.

4,8-Bis(5-ethylhexylselenophen-2-yl)benzo[1,2-b:4,5-b']dithiophene (BDT-S). In a 250mL argon purged round-bottom flask, compound 4 (4.3g, 17.6 mmol) was dissolved in 45 mL anhydrous THF and the solution was cooled down to 0 ºC. 2.5M n-butyllithium solution in hexane (7.76 mL, 19.4 mmol) was added into the solution dropwise. The reaction was slowly warmed up to 50 ºC and kept stirring for 1 h. Subsequently, 4,8-dihydrobenzo[1,2-b:4,5-b']dithiophene-4,8-dione (1.94 g, 8.8 mmol) was added into the reaction mixture at 50 ºC. The reaction mixture was kept stirring at 50 ºC for additional 1h. After cooling down to room temperature, tin (II) chloride dehydrate (20 g, 88 mmol) in 10% HCl (20 mL) was added and the mixture was stirred for another 2 h. After reaction, the mixture was poured into ice water, extracted with ether. Combined organic layer was washed with brine, dried over anhydrous $MgSO_4$, and concentrated under vacuum. ^1H NMR (300 MHz, $CDCl_3$), δ(ppm): 7.65 (d, J = 5.6 Hz, 2H), 7.44 (d, J = 5.6 Hz, 2H), 7.40 (d, J =

3.3 Hz, 2H), 7.04 (d, *J* = 3.0 Hz, 2H), 2.92 (d, *J* = 6.5 Hz, 4H), 1.71-1.59 (m, 2H), 1.50-1.23 (m, 16H), 0.95 (m, 12H). ^{13}C NMR (125 MHz, $CDCl_3$), δ (ppm): 153.8, 142.7, 138.8, 136.2, 130.0, 127.5, 126.2, 123.5, 42.2, 37.0, 32.5, 28.9, 25.7, 23.0, 14.2, 10.9.

2,6-Bis(trimethyltin)-4,8-bis(5-ethylhexylselenophen-2-yl)benzo[1,2-b;4,5-b']dithiophene (6). In a 100mL argon purged round-bottom flask, BDTS (1.7 g, 2.5 mmol) was dissolved in 26 mL anhydrous THF and the solution was cooled to -78 ºC. 2.5M n-butyllithium solution in hexane (2.3 mL, 5.8 mmol) was added into the solution dropwise. Reaction mixture turned into dark greenish slurry. Cooling bath was removed, and reaction was kept stirring at room temperature for another 2 h. The mixture was then cooled to -78 ºC again and 1.0M trimethyltin chloride solution in THF (6.6 mL, 6.6 mmol) was added in one portion, turning the reaction mixture into clear yellow solution. The mixture was kept stirring for additional 3 h at room temperature. After reaction, 10 mL DI water was injected to quench the reaction. The mixture was extracted with ether and washed with brine. Combined organic layer was dried over $MgSO_4$ and concentrated under reduced pressure. Crude product was recrystallized with ether/ethanol mixed solvent. Pale yellow crystals was obtained as purified product (2.1 g, 83%) and was used for polymerization . ^{1}H NMR (300 MHz, $CDCl_3$), δ (ppm): .^{13}C NMR (125 MHz, $CDCl_3$), δ (ppm): 153.5, 143.6, 143.0, 142.2, 137.0, 131.3, 129.8, 127.5, 124.6, 42.2, 37.1, 32.5, 29.0, 25.8, 23.0, 14.2, 11.0, -8.3.

2-Trimethylstannylselenophene (12). In a 100mL argon purged flask, selenophene (2) (2g, 15.3 mmol) was dissolved in 100 mL anhydrous THF. The solution was cooled down to -78 ºC. 2.5M n-butyllithium solution in hexane (6.12 mL, 15.3 mmol) was added into the solution dropwise. The solution was kept stirring at -78 ºC for 30min, after which 1.0M trimethyltin chloride solution in hexane (18.3 mL, 18.3 mmol) was slowly added. The reaction was then

brought to room temperature and kept stirring for overnight. After reaction, the mixture was poured into water and extracted with dichloromethane. Organic layer was washed with brine and dried over anhydrous Na_2SO_4. Product was first concentrated on rotary evaporator and then solvent residue was completely removed under high vacuum. Light brown oil was obtained as crude product (3.6 g, 80%), which was used subsequently for next step without further purification. ^{1}H NMR (300 MHz, $CDCl_3$), δ (ppm): 8.49-8.26 (m, 1H), 7.57-7.45 (m, 2H), 0.43 (m, 9H).

1,3-Bis(2-ethylhexyl)-5,7-di(selenophene-2-yl)-benzo[1,2-c:4,5-c′]-dithiophene-4,8-dione (DSBDD). In an argon purged flask, BDD (2.7 mmmol, 1.64 g) and 2-trimethylstannylselenophene (12) (6.8 mmol, 2g) were dissolved in 18 mL anhydrous toluene. $Pd(PPh_3)_4$ (62.4 mg, 0.054 mmol) was added into the solution. The mixture was refluxed in inert atmosphere for 12 h. After reaction, solvent was removed at reduced pressure and residue was purified by column chromatography with hexane/dichloromethane as eluting solvent. Recrystallization with ethanol afforded product as yellow-orange solid (1.8 g, 94%). ^{1}H NMR (300 MHz, $CDCl_3$), δ (ppm): 8.29 (dd, J = 5.8, 1.08 Hz, 2H), 7.97 (dd, J = 4.0, 1.1 Hz, 2H), 7.39 (dd, J = 5.8, 4.0 Hz, 2H), 3.32 (m, 4H), 1.78 (br, 2H), 1.59-1.20 (m, 16H), 0.92 (m, 9H). ^{13}C NMR (125 MHz, $CDCl_3$), δ (ppm): 177.9, 153.0, 144.9, 137.2, 137.1, 132.8, 132.5, 131.0, 129.4, 41.1, 33.6, 32.8, 28.8, 26.0, 23.0, 14.2, 10.9.

1,3-Bis(5-bromoselenophene-2-yl)-5,7-bis(2-ethylhexyl)-benzo[1,2-c:4,5-c′]-dithiophene-4,8-dione (14). In a 100mL round-bottom flask equipped with a condenser, DSBDD (300 mg, 0.43 mmol) was dissolved in 15 mL chloroform/acetic acid mixture (2:1 by volume). The flask was fully covered with aluminum foil. N-bromosuccinimide (168 mg, 0.94 mmol) was added in one portion. The reaction mixture was heated to 70 ºC and kept stirring for 2 h. After completion of bromination, the mixture was poured into water and extracted with

dichloromethane. Organic layer was washed with water and brine, dried over anhydrous Na_2SO_4, and concentrated at reduced pressure. The residue was then purified with column chromatography eluting with hexane/dichloromethane (10:1 by volume). Recrystallization with dichloromethane/methanol afforded product as orange colored solid (280 mg, 76%). ^{1}H NMR (300 MHz, $CDCl_3$), δ (ppm): 7.59 (d, J = 4.4 Hz, 2H), 7.30 (d, J = 4.4 Hz, 2H), 3.33-3.20 (m, 4H), 1.76 (m, 2H), 1.48-1.23 (m, 16H), 0.92 (m, 12H). ^{13}C NMR (125 MHz, $CDCl_3$), δ (ppm): 177.3, 153.6, 144.2, 137.8, 132.6, 132.1, 131.3, 129.9, 125.7, 40.9, 33.7, 33.0, 29.0, 26.1, 23.1, 14.3, 10.9.

PBDB-T. In a 250mL argon-purged Schlenck tube, DTBDD-Br_2 (13) (520 mg, 0.68 mmol) and BDTT distannane (5) (613.5 mg, 0.68 mmol) were dissolved into 26 mL anhydrous chlorobenzene. $Pd(dba)_3$ (12.42 mg, 0.014 mmol) and P(o-Toly)$_3$ (16.51 mg, 0.054 mmol) were premixed in a vial with 6 mL anhydrous chlorobenzene, degassed and added into the solution. Reaction mixture was vigorously stirred, slowly heated up to 120-130 ºC and kept refluxing for 72 h. Dark viscous reaction mixture was dropped into methanol containing 2 vol% hydrochloric acid. The mixture was kept stirring for overnight and filtered. Obtained dark solid was then further purified with Soxhlet extraction in following sequence: acetone, hexane, chloroform. The chloroform fraction was reprecipitated into methanol, filtered and completely dried in vacuum oven. Dark solid was obtained as final product 778g, 98%.

PBDB-S. In a 250mL argon purged Schlenck tube, DTBDD-Br_2 (13) (520 mg, 0.68 mmol) and BDTS distannane (6) (677.1 mg, 0.68 mmol) were dissolved into 26 mL anhydrous chlorobenzene. $Pd(dba)_3$ (12.42 mg, 0.014 mmol) and P(o-Toly)$_3$ (16.51 mg, 0.054 mmol) were premixed in a vial with 6 mL anhydrous chlorobenzene, degassed and added into the solution. Reaction mixture was vigorously stirred, slowly heated up to 120-130 ºC and kept refluxing for 72 h. Dark viscous reaction mixture was dropped into methanol containing 2 vol% hydrochloric acid.

The mixture was kept stirring for overnight and filtered. Obtained dark solid was then further purified with Soxhlet extraction in following sequence: acetone, hexane, chloroform and chlorobenzene. The chloroform and chlorobenzene fractions were reprecipitated into methanol, filtered and completely dried in vacuum oven. Chloroform fraction: 220 mg, 25%. Chlorobenzene fraction: 595 mg, 69%. The chlorozenzene fraction was used for further characterization and device application.

PBDBS-T. In a 250mL argon purged Schlenck tube, DSBDD-Br_2 (14) (490 mg, 0.57 mmol) and BDTT distannane (5) (515 mg, 0.57 mmol) were dissolved into 26 mL anhydrous chlorobenzene. $Pd(dba)_3$ (10.43 mg, 0.011 mmol) and P(*o*-Toly)$_3$ (13.87 mg, 0.045 mmol) were premixed in a vial with 6 mL anhydrous chlorobenzene, degassed and added into the solution. Reaction mixture was vigorously stirred, slowly heated up to 110 ºC. The reaction mixture turned dark and highly viscous shortly after heating. Reaction mixture became immobile within three hours. The reaction vessel was kept at 110 ºC for overnight and cooled back to room temperature. Resulted gel-like mixture was dissolved into hot 1,2-dichlorobenzene and dropped into methanol containing 2 vol% hydrochloric acid. The mixture was kept stirring for overnight, filtered and completely dried in vacuum over. Obtained dark solid was then further purified with Soxhlet extraction in following sequence: acetone, hexane, and chloroform. The chloroform fraction was reprecipitated into methanol. Residue within the thimble was scraped out, redissolved in hot 1,2-dichlorobenzene, then reprecipitate into methanol, filtered and completely dried in vacuum oven. Chloroform fraction: 135 mg, 19%. *O*-DCB fraction: 522 mg, 72%. The *o*-DCB fraction was used for further characterization and device application.

PBDBS-S. In a 250mL argon purged Schlenck tube, DSBDD-Br_2 (14) (511 mg, 0.59 mmol) and BDTS distannane (6) (592.9 mg, 0.59 mmol) were dissolved into 16 mL anhydrous

chlorobenzene. $Pd(dba)_3$ (11.24 mg, 0.014 mmol) and P(*o*-Toly)$_3$ (14.32 mg, 0.054 mmol) were premixed in a vial with 5 mL anhydrous chlorobenzene, degassed and added into the solution. Reaction mixture was vigorously stirred, slowly heated up to 110 ºC. The reaction mixture turned dark and highly viscous shortly after heating. Reaction mixture became immobile within three hours. The reaction vessel was kept at 110 ºC for overnight and cooled back to room temperature. Resulted gel-like mixture was dissolved into hot 1,2-dichlorobenzene and dropped into methanol containing 2 vol% hydrochloric acid. The mixture was kept stirring for overnight, filtered and completely dried in vacuum oven. Obtained dark solid was then further purified with Soxhlet extraction in following sequence: acetone, hexane, and chloroform. The chloroform fraction was reprecipitated into methanol. Residue within the thimble was scraped out, redissolved in hot 1,2-dichlorobenzene, then reprecipitated into methanol, filtered and completely dried in vacuum oven. Chloroform fraction: 128 mg, 16%. *O*-DCB fraction: 655 mg, 80%. The *o*-DCB fraction was used for further characterization and device application.

Cyclic voltammetry measurements. Cyclic voltammetry (CV) measurements were performed on an EG&G Princeton Applied Research potentiostat/galvanostat (model 273A). A three-electrode cell was used, using platinum (Pt) wires as both counter and working electrodes. Silver/silver ion (Ag in 0.01 M $AgNO_3$ solution) was used as the reference electrode. For thin films, the working electrode was a Pt wire coated with the synthesized polymers, dip-coated from concentrated solution in chlorobenzene or dichlorobenzene and air dried for overnight. CV measurements of thin films were carried out in 0.1 M tetrabutylammonium hexafluorophosphate (Bu_4NPF_6) solution in acetonitrile at a scan rate of 50 mV/s. The scan rate was 100 mV/s. Solutions were purged with inert gas for 20 min before measurements. All recorded reduction and oxidation potentials were calibrated with the ferrocene/ferrocenium (Fc/Fc^+) couple.

Solar cell fabrication and characterization. The inverted device structure fabricated and evaluated was: ITO/ZnO/PEI/blend active layer/ MoO_3(0.5 nm)/Ag(100 nm), where PEI or polyethylenimine is a cathode buffer layer.[79] The ITO glass substrates were sequentially sonicated in acetone, deionized (DI) water and isopropanol for 20 min each and then plasma cleaned for 10 min. The ZnO layer (~30 nm) was spin-coated from the precursor solution (0.5 g of zinc acetate dihydrate, 0.14 g of ethanolamine and 5 mL of 2-methoxyethanol) and baked at 250 ºC for 30 min in open air. Solution of PEI (M_w = 25k, Aldrich 408727) in 2-methoxyethanol (0.05 wt%) was then spin-coated onto the ZnO layer and dried at 120 ºC for additional 10 min. The resulting substrates were then stored in an argon-filled glovebox for deposition of active layers. The blend solutions were stirred overnight with low heating to achieve a homogeneous mixture. Each blend solution was then spin-coated onto the cleaned substrate and annealed on a hot plate for 10 min to afford dried thin films with a thickness of 95 ± 5 nm. Finally, the MoO_3 layer and Ag electrode were deposited within a thermal evaporator. Defined active area of 0.0314 cm^2 was achieved for individual devices through a shadow mask. The photovoltaic cells were tested under AM 1.5G solar illumination at 100 mW/cm^2 in ambient air using a Solar Simulator (model 16S, Solar Light Co., Philadelphia, PA) with a 200W Xenon Lamp Power Supply (Model XPS 200, Solar Light Co., Philadelphia, PA) calibrated by NREL certified Si photodiode (Model 1787–04, Hamamatsu Photonics K.K., Japan) and a HP4155A semiconductor parameter analyzer (Yokogawa Hewlett-Packard, Japan). After the *J–V* measurement, the EQE was measured by using a solar cell quantum efficiency measurement system (Model QEX10, PV Measurements, Inc., Boulder, CO) with a 2 mm^2 (2 × 1 mm) size masked incident light source and TF Mini Super measurement apparatus for multiple devices in a single substrate.

SCLC. The space charge limited current (SCLC)[80] devices fabricated and evaluated had the structures: ITO/PEDOT:PSS/blend/MoO_3/Ag (hole-only), where poly(3,4-ethylenedioxythiophene):poly(styrenesulfonate) (PEDOT:PSS) is a hole injection layer; and ITO/ZnO/PEI/active layer/PFN-Br/Al (electron-only). The blend active layers in these SCLC devices had the same composition as the corresponding photovoltaic devices. Current-voltage (*J-V*) characteristics of the SCLC devices were plotted as $J^{0.5}$ versus V and fitted by using the following formula: $J = 9\ \varepsilon_0\ \varepsilon_r\ \mu V^2/8d^3$, where J is the current density, ε_0 is the permittivity of free space, ε_r is the relative dielectric constant of the transport medium, μ is the carrier mobility, V is the applied voltage, d is the thickness of blend active layer.

2D GIWAXS. Two-dimensional (2D) Grazing incidence wide-angle X-ray scattering (GIWAXS) experiments were conducted at the Japan Synchrotron Radiation Facility SPring-8 by using the beamline BL46XU. The thin-film samples investigated were prepared in the same manner as the corresponding photovoltaic devices on ZnO-coated ITO substrates, without the thermal deposition of top MO_3/Ag electrodes. The X-ray beam was monochromatized by a double-crystal Si(111) monochromator, and the X-ray energy in this experiment was 12.40 keV (λ = 0.1 nm). The angle of incident X-ray to sample surface was 0.12° with a Huber diffractometer. The scattered profile from the film sample was detected using an area detector (PILATUS 300K) for 5 s at room temperature, and the distance between the sample and detector was 174.4 mm. The crystal coherence length (L_c) of samples was determined by using the Scherrer equation: $L_c = 2\pi K/\Delta q$, where K is a shape factor (typically 0.89) and Δq is the full width at half-maximum (FWHM) of the diffraction peak.

2.3 RESULTS AND DISCUSSION

Scheme 2.1. Selenophene Substitution at Various Positions in Monomers and the Corresponding Conjugated Polymers

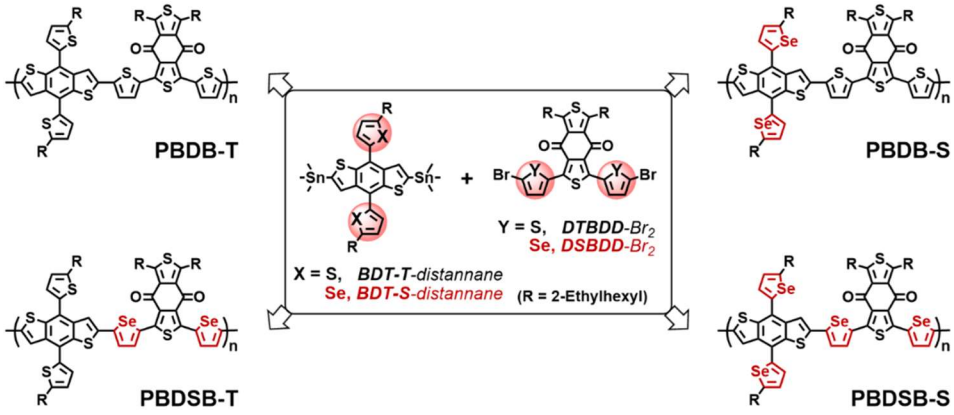

Scheme 2.2. Synthetic Routes Toward Distannane and Dibromide Monomers

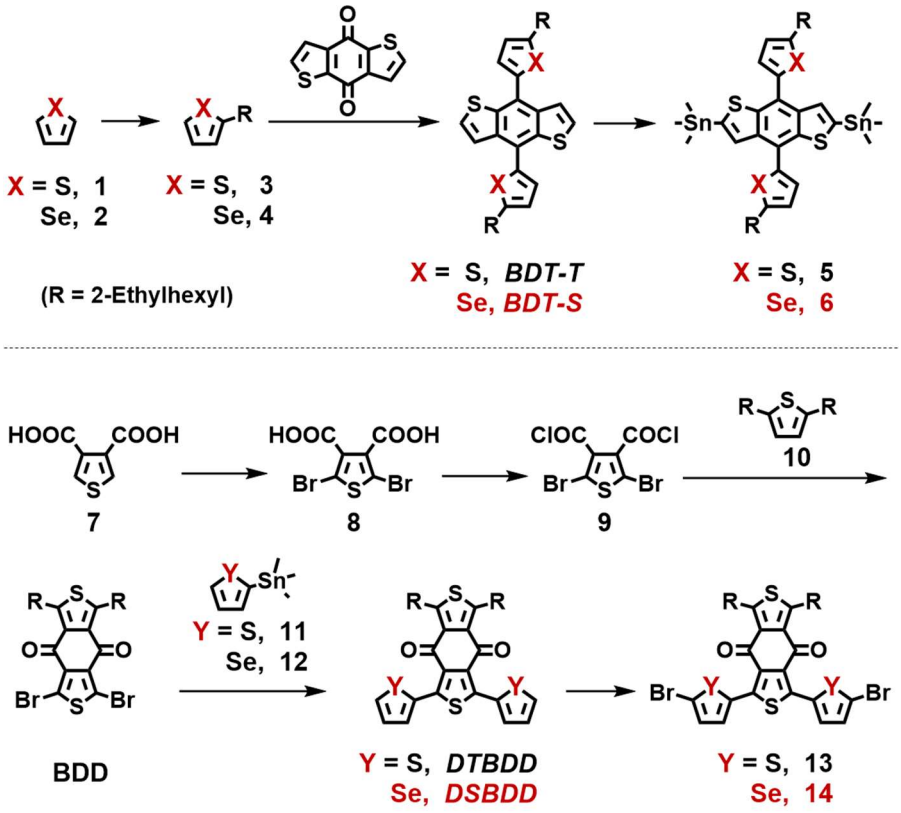

Table 2.1. Thermal, Optical and Electrochemical Properties of Synthesized Polymers

Polymers	T_d	λ_{max}[a] [nm]	λ_{onset}[a] [nm]	[b]E_g^{opt} [eV]	[c]E_{HOMO} [eV]	[d]E_{LUMO} [eV]
PBDB-T	414	578, 616	670	1.85	-5.35	-3.50
PBDB-S	408	579, 617	678	1.83	-5.35	-3.52
PBDBS-T	427	605, 659	712	1.74	-5.22	-3.48
PBDBS-S	390	610, 659	720	1.72	-5.24	-3.52

[a]Thin-film. [b]$E_g^{opt} = 1240/\lambda_{onset}$. [c]$E_{HOMO} = -(E_{ox}^{onset} + 4.8)$ eV. [d] $E_{LUMO} = -E_{HOMO} + E_g^{opt}$.

2.3.1 *Synthesis and Characterization of Donor Polymers.*

The four donor polymers were synthesized by Stille coupling of the corresponding distannane and dibromide monomers. (**Scheme 2.1**) Detailed synthetic routes toward the respective monomers are presented in **Scheme 2.2**. Some important intermediates such as 2-(2-ethylhexyl)-selenophene (4)[81], 2,5-dibromothiophene-3,4-dicarboxylic acid (8)[82], 2,5-dibromo-3,4-thiophenedicarbonyl dichloride (9)[82], 2,5-Bis(2-ethylhexyl)-thiophene (10)[83], and 1,3-Dibromo-5,7-bis(2-ethylhexyl)benzo[1,2-c:4,5-c′]-dithiophene-4,8-dione (BDD)[59] were synthesized according to literature procedures. Details on synthetic procedures are described in Experimental Section and the characterization data such as ^{1}H NMR and ^{13}C NMR spectra are included in Supporting Information. For Stille coupling reactions, chlorobenzene was used as solvent and $Pd(dba)_3$/P(*o*-Toly)$_3$ were used as catalyst/ligand. All polymerization reactions were carried out under the same conditions with identical monomer and catalyst concentrations and reaction temperature. While polymerizations of PBDB-T and PBDB-S went smoothly yielding dark and viscous solutions after 72 hours, during the polymerizations of PBDBS-T and PBDBS-S, reaction mixtures turned viscous shortly after initiation and became immobile gel in the reaction vessel within 3 hours. (**Figure Sx)** The gel formation of PBDBS-T and PBDBS-S was probably related to strong intermolecular interactions induced by selenophene in the polymer backbone. More details on post-polymerization processing are described in experimental section. All four polymers demonstrated excellent thermal stability with high decomposition temperatures (T_d) ranging from 390º to 427º, (**Table 2.1**) determined with temperatures at 95% weight loss from thermogravimetric analysis (TGA). (**Figure S2.6**) No significant endo- and exothermal peaks were observed in the differential scanning calorimetry (DSC) scans. (**Figure S2.7**)

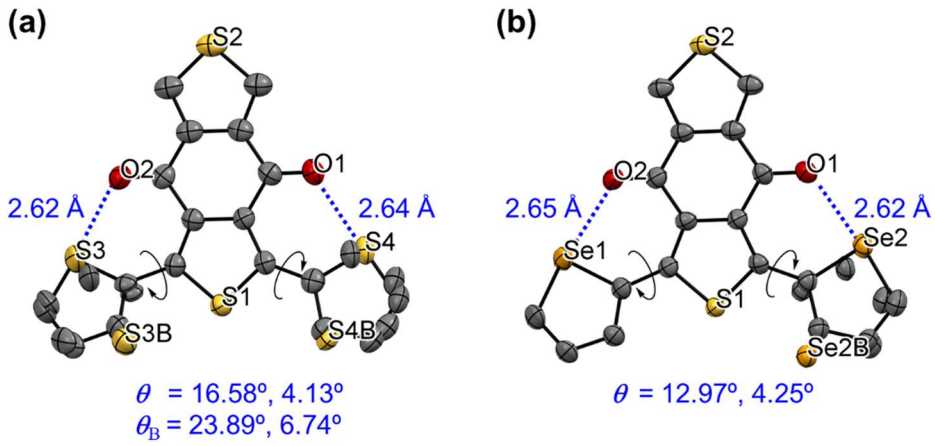

Figure 2.1. ORTEP of the crystal structures with thermal ellipsoids at the 50% probability level: (a) DTBDD and (b) DSBDD. Disordered alkyl chains are omitted for clarity. S3B, S4B, and Se2B represent sites occupied in minor conformations. Torsion angles (θ) were measured from the calculated mean planes of adjacent aromatic rings.

2.3.2 *Crystal Analysis of Monomers and DFT Simulations.*

Single crystals of DTBDD and DSBDD were obtained from vapor diffusion method with chloroform/methanol. DTBDD and DSBDD share high similarities in unit cell parameters (**Table S2.3, Table S2.4**) and packing characteristics (**Figure S2.8**) The distances of sulfur to carbonyl oxygen within DTBDD are measured to be 2.62 Å (S3-O2) and 2.64 Å (S3-O1). The distances of selenium to carbonyl oxygen within DSBDD are 2.65 Å (Se1-O2) and 2.62 Å (Se2-O1). These values are larger than the sums of the covalent radii of 1.71 Å (S 1.05 Å, O 0.66 Å) and 1.86 Å (Se 1.20 Å, O 0.66 Å),[84] respectively, but are smaller than the sums of the van der waals radii, 3.32 Å (S 1.80 Å, O 1.52 Å) and 3.42 Å (Se 1.90 Å, O 1.52 Å),[85] suggesting that there are intramolecular nonbonding interactions between sulfur/seleninum and carbonyl oxygen. Such S···O and Se···O interactions are likely originated from chalcogen bonding or Coulombic attraction,[86-87] thus could enable "conformation lock".[88] The greatest contrast in the crystal structures of DTBDD and

DSBDD lies in the backbone disorder. In DTBDD, one thiophene (S3/C1-C4) is disordered at site occupancies of 0.670(6) and 0.330(6) (S3B/C1B-C4B), while the other thiophene (S4/C7-C10) is disordered at site occupancies of 0.890(5) and 0.110(5) (S4B/C7B-C10B). (**Figure 2.1**a) In DSBDD, however, there is only a small disorder of selenophene (Se2B/C7B-C10B) at site occupancy of 0.004(1). (**Figure 2.1**b) It concludes that in DSBDD, the flanking selenophenes possess much lower conformational disorder, which likely originated from dual effects of higher quinoid characteristics of selenophene than thiophene, and stronger Se···O interaction than S···O interaction.

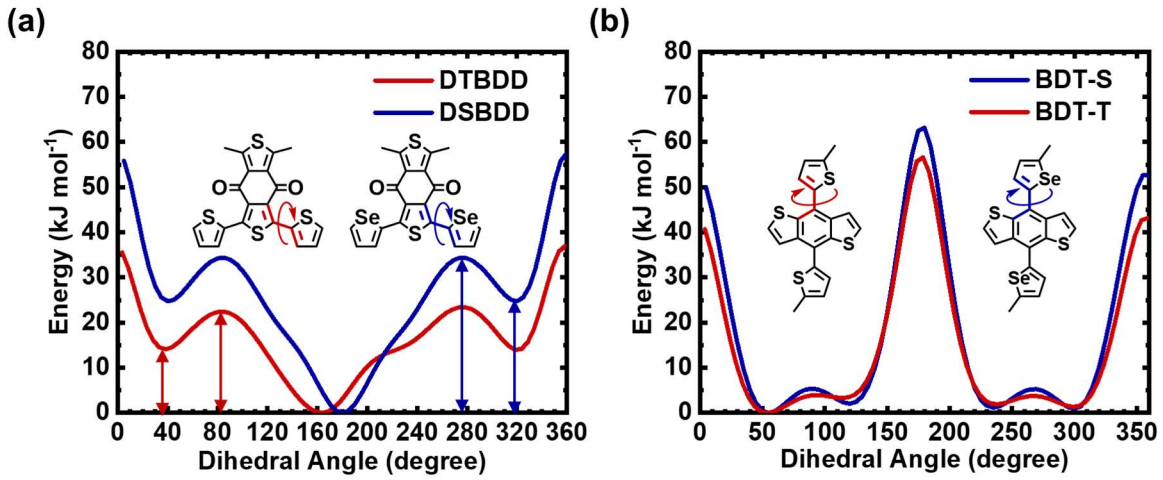

Figure 2.2. Potential energy surface scan of the acceptor moieties (a) DTBDD and DSBDD, and the donor moieties (b) BDTT and BDTS, with B3LYP/6-31G(d,p) basis set.

DFT calculations with B3LYP/6-31G(d,p) basis set were performed to first optimize the geometries of DTBDD and DSBDD, (**Figure S2.9**ab) followed with rotational rigid scan of thiophene/selenophene on one side to obtain the respective potential energy surface (PES). (**Figure 2.2**a) Alkyl chains were replaced with methyl groups for simplification. Geometry optimizations

suggest that DTBDD is slightly twisted with a torsion angle of 17.98º, while DSBDD is highly planar with negligible torsion angle of 0.08º, which are consistent with the aforementioned crystal data. In DTBDD, two optimal conformations exist with an energy difference of 13.97 kJ/mol. (**Figure 2.2**a) The first optimal conformation of DTBDD has the C=C-C=C dihedral angle of 163º, where the S atom of the side thiophene is close to carbonyl oxygen. The second optimal conformation has the dihedral angle of 38º with the S atom rotated away from carbonyl oxygen. The rotation barrier for DTBDD to overcome from first to second optimal conformation is 22.45 kJ/mol. Similarly, in DSBDD, the energy difference between the two optimal conformations is 24.73 kJ/mol and the rotation barrier is 34.37 kJ/mol. The larger energy gap between first and second optimal conformations in DSBDD and the larger rotation barrier suggest that DSBDD, compared to DTBDD, is more likely to adopt the first optimal conformation with the S atom close to carbonyl oxygen. Results from DFT simulations are in good agreement with the analysis of crystal structures in that DSBDD provides higher rigidity and more unified backbone conformations than DTBDD. Such rigidity and conformational uniformity should be expected to retain in the corresponding polymers and contribute to strong intermolecular packing. For the donor moieties, BDTT and BDTS, however, the geometry optimization (**Figure S2.9**cd) and similarly obtained PES from rotational rigid scan (**Figure 2.2**b) suggest that the optimal conformations have torsion angles of 55.33º for BDTT and 56.15º for BDTS, and the side-chain conformations of these quasi-2D building blocks are rather random if without external intermolecular forces.

2.3.3 *Optical absorption and electronic structrues.*

The UV-vis absorption spectra of the four polymers in thin films are presented in **Figure 2.3**a, and the detailed data are listed in **Table 2.1**. Selenophene substitution at the side chain

positions did not significantly impact the optical absorption range of the polymer (PBDB-T v.s. PBDB-S, PBDBS-T v.s. PBDBS-S), but appeared to slightly enhance the distinction coefficient. Selenophene substitution at the backbone positions, however, resulted in red-shifted absorption band by ~40 nm (PBDB-T *vs* PBDBS-T, PBDB-S *vs* PBDBS-S) leading to reduced optical bandgaps. Cyclic voltammetry (CV) measurements were taken and the oxidative cyclic voltammogram were used to calculate the HOMO energy levels of the four polymers based on the formula: E_{HOMO} = - (E_{ox}^{onset} + 4.8) eV. The estimated HOMO energy levels are as following: PBDB-T (-5.35 eV), PBDB-S (-5.35 eV), PBDBS-T (-5.22 eV) and PBDBS-S (-5.24 eV). The LUMO energy levels could not be accurately obtained from the reductive cyclic voltammogram due to the electron-rich nature of the polymers, thus were estimated using the thin film optical bandgaps according to the formula: E_{LUMO} = - E_{HOMO} + E_g^{opt}. The energy diagrams of the four polymers are plotted in **Figure 2.3**b. The results suggest that selenophene substitution in the side chain positions had minimal impact on the energy levels, whereas selenophene substation in the backbone positions raised the HOMO energy levels by ~0.1 eV.

2.3.4 *Photovoltaic performance and charge transport*

Inverted device architecture was used to evaluate the photovoltaic performance of these polymers paired with the commercially available small molecule acceptor, Y6: ITO/ZnO/PEI/polymer:Y6/MoO_3/Ag, where PEI was cathode interlayer.[79] For each polymer:Y6 combination, devices were individually optimized by varying the donor:acceptor (D:A) weight ratios, the annealing temperature, and addition of processing additives. The thin film absorption spectra and the HOMO/LUMO energy levels of Y6 are plotted aside the donor polymers in **Figure 2.3**a,b. The current density-voltage (*J-V*) curves and the EQE spectra of the best performing devices are presented in **Figure 2.3**c,d. The detailed photovoltaic parameters including open-

circuit voltage (V_{oc}), short-circuit current density (J_{sc}), fill factor (FF) and power conversion efficiency (PCE) are summarized in **Table 2.2**. The optimized devices based on PBDB-T:Y6 blend showed PCE of 8.59% with a J_{sc} of 25.70 mA/cm^2, a V_{oc} of 0.76 V and a low FF of 0.44. Under similar conditions, the devices based on PBDB-S:Y6 demonstrated improved PCE of 10.41% with a further improved J_{sc} of 26.76 ± 0.91 mA/cm^2, a reduced V_{oc} of 0.67 V and an enhanced FF of 0.58. The enhancement of J_{sc} is also reflected on the EQE spectrum shown in **Figure 2.3**d, where PBDB-S:Y6 showed higher quantum efficiency than PBDB-T:Y6 in the broad range of 450 – 800 nm. The simultaneous enhancement in both J_{sc} and FF indicated that the blend of PBDB-S:Y6 probably formed more favorable bulk morphology than the blend of PBDB-T:Y6. In addition, we also fabricated hole-only and electron-only devices to evaluate the bulk charge carrier mobilities of the blends using the space-charge limited current (SCLC) model. The PBDB-T:Y6 blend demonstrated hole mobility (μ_h) of 2.39×10^{-4} cm^2/(Vs) and electron mobility (μ_e) of 1.03×10^{-4} cm^2/(Vs), whereas the PBDBS:Y6 blend had μ_h of 1.65×10^{-3} cm^2/(Vs) and μ_e of 1.68×10^{-4} cm^2/(Vs). Especially, the PBDB-S:Y6 blend showed exceptional μ_h that is one order of magnitude higher than that of PBDB-T:Y6, suggesting that selenophene substitution at the sidechain positions significantly enhanced the charge transport properties of the donor polymer.

For PBDBS-T and PBDBS-S that incorporated selenophene in the backbone positions, we found it rather difficult in solution processing. Dichlorobenzene had to be used instead of the commonly used chlorobenzene. Consequently, devices based on PBDBS-T:Y6 and PBDBS-S:Y6 blends yielded relatively lower photovoltaic performance with PCE of 6.28 ± 0.45% and 5.32 ± 0.58%, respectively.

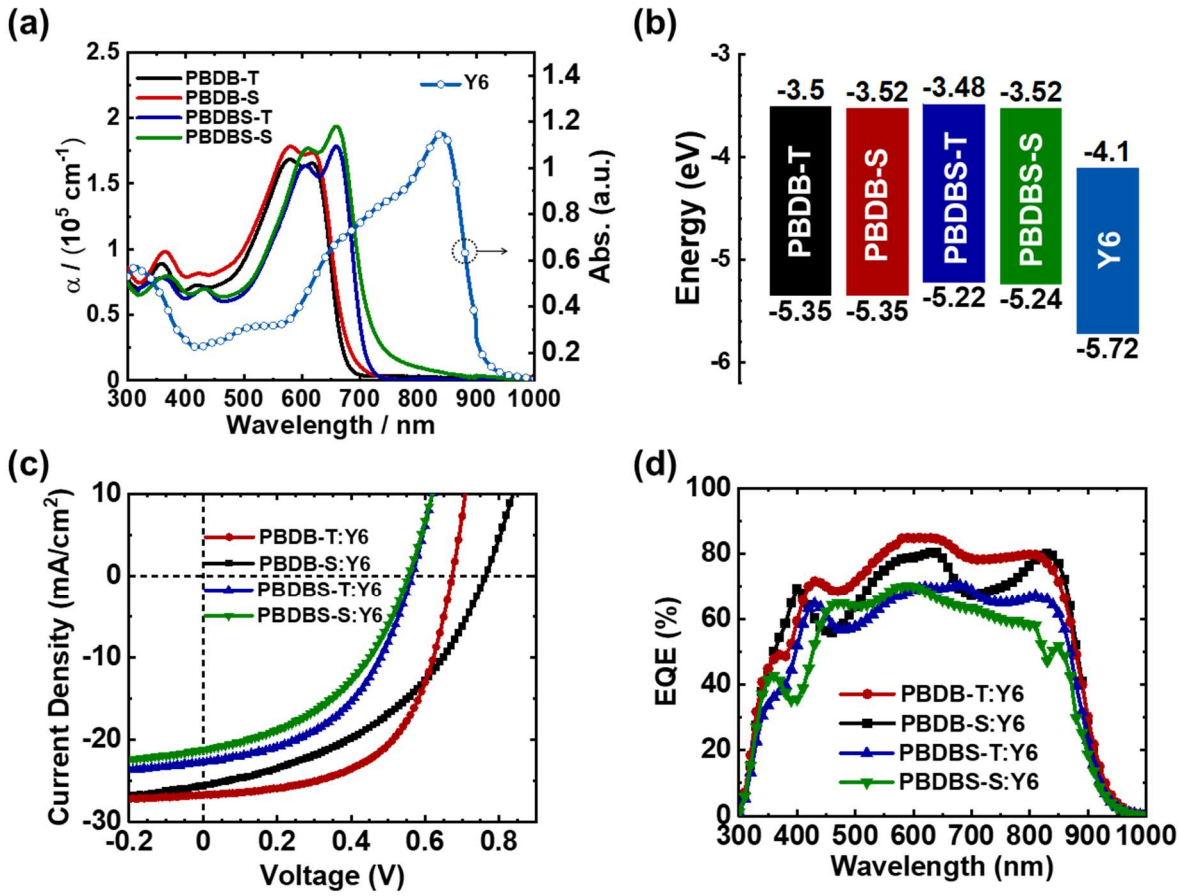

Figure 2.3. (a) UV-vis absorption spectra and (b) HOMO/LUMO energy levels of the donor polymers and the small molecule acceptor Y6 in thin films; (c) *J-V* curves and (d) the corresponding EQE spectrum for the blend films of PBDB-T:Y6, PBDB-S:Y6, PBDBS-T:Y6 and PBDBS-S:Y6 at optimal conditions.

Table 2.2. Summarized Photovoltaic Parameters for Polymer:Y6 Blends at Optimal Conditions

Blends	J_{sc} (mA/cm^2)	V_{oc} (V)	FF	PCE (%)	μ_h (10^{-4} cm2/(Vs))	μ_e (10^{-4} cm^2/(Vs))	μ_h/μ_e
PBDB-T:Y6	25.70 ± 0.60	0.76 ± 0.01	0.44 ± 0.02	8.59 ± 0.47	2.39	1.03	2.32
PBDB-S:Y6	26.76 ± 0.91	0.67 ± 0.01	0.58 ± 0.02	10.41 ± 0.45	16.5	1.68	9.83
PBDBS-T:Y6	22.77 ± 0.88	0.56 ± 0.01	0.49 ± 0.02	6.28 ± 0.45	-	-	-
PBDBS-S:Y6	21.27 ± 1.12	0.55 ± 0.01	0.45 ± 0.03	5.32 ± 0.58	-	-	-

2.3.5 *2D GIWAXS analysis*

We used two dimensional grazing incidence wide-angle X-ray scattering (2D GIWAXS) measurements to investigate the structural ordering and crystallinity of the neat polymer films and the related blend films. For the neat films, the 2D diffraction patterns and the corresponding 1D line-cut profiles in the in-plane (IP) and out-of-plane (OOP) directions are presented in **Figure 2.4**. All the four polymers showed dominant "*face-on*" orientation evidenced with strong π-π diffractions in the OOP direction at the large q_z region. The π-π diffraction peak positions were determined at 1.683 Å^{-1}, 1.672 Å^{-1}, 1.682 Å^{-1}, and 1.671 Å^{-1} for PBDB-T, PBDB-S, PBDBS-T and PBDBS-S, respectively, corresponding to the π-π stacking distances (d_{010}) of 3.73 Å, 3.76 Å, 3.74 Å, and 3.76 Å. The results showed that, PBDB-S and PBDBS-S, with selenophene substitution in the side chain positions, demonstrated slightly larger π-π stacking distance relative to PBDB-T and PBDBS-T. Meanwhile, selenophene substitution in the backbone position had little impact on the π-π stacking distances. In the IP direction, PBDB-T, PBDB-S, PBDBS-T and PBDBS-S showed intense lamellar peaks at q_{xy} of 0.286 Å^{-1}, 0.277 Å^{-1}, 0.285 Å^{-1}, 0.274 Å^{-1}, corresponding to *d*-spacing distances (d_{100}) of 21.97 Å, 22.70 Å, 22.05 Å, 22.93 Å, respectively. Based on the full width at half maximum (fwhm) values of the (100) peaks, average crystallite

sizes of 5.90 – 6.15 nm were estimated for all four films.(**Table S2.5**) We observed that selenophene substitution slightly decreased crystallinity of the neat films, regardless of substitution positions. Overall, PBDB-S and PBDBS-S showed larger lamellar packing distances than PBDB-T and PBDBS-T, suggesting that selenophene substitution in the side chain position led to larger lamellar packing distances, whereas selenophene substitution in the backbone position did not significantly affect the lamellar packing distances. Therefore, we conclude that both the π-π stacking distances and the lamellar packing distances of these polymers were governed by the quasi-2D donor moieties, specifically, BDTT and BDTS. In a polymer structure like PBDB-T, substituting thiophene with selenophene in the side chain positions would result in larger π-π stacking distances as well as larger lamellar packing distances. These findings are the opposite from previous reports[75-76] showing that selenophene substitution often resulted in closer lamellar packing and closer π-π distances.

The 2D diffraction pattern and 1D line-cut profiles of Y6 neat film processed from chlorobenzene are included in Supporting Information. (**Figure S2.10**) The multiple ring-shaped diffractions suggested that Y6 adopted random orientations, consistent with literature report.[89] The 2D diffraction pattern and 1D line-cut profiles for the blend films of polymer:Y6 are shown in **Figure 2.5**. All four blends showed significant (010) π-π diffractions in the OOP directions together with intense (100) lamellar peaks in the IP directions, suggesting dominantly *face-on* orientation. Estimated from the (100) lamellar peaks, relatively longer crystalline coherence lengths were observed for PBDB-T:Y6 (L_c = 8.05 nm) and PBDB-S:Y6 (L_c = 8.40 nm), compared to PBDBS-T:Y6 (L_c = 7.10 nm)and PBDBS-S:Y6 (L_c = 7.22 nm), which contribute to the better photovoltaic performance. (**Table S2.5**) The higher crystallinity of PBDB-S:Y6 than PBDB-T:Y6 is consistent with the higher hole and electron mobilities estimated from SCLC measurements.

The cross comparisons among the four blends indicate that selenophene substitution in the side chain positions slightly increased crystallinity in the blend films (PBDB-T:Y6 vs PBDB-S:Y6, PBDBS-T:Y6 vs PBDBS-S:Y6), whereas selenophene substitution in the backbone positions decreased crystallinity (PBDB-T:Y6 vs PBDBS-T:Y6, PBDB-S:Y6 vs PBDBS-S:Y6).

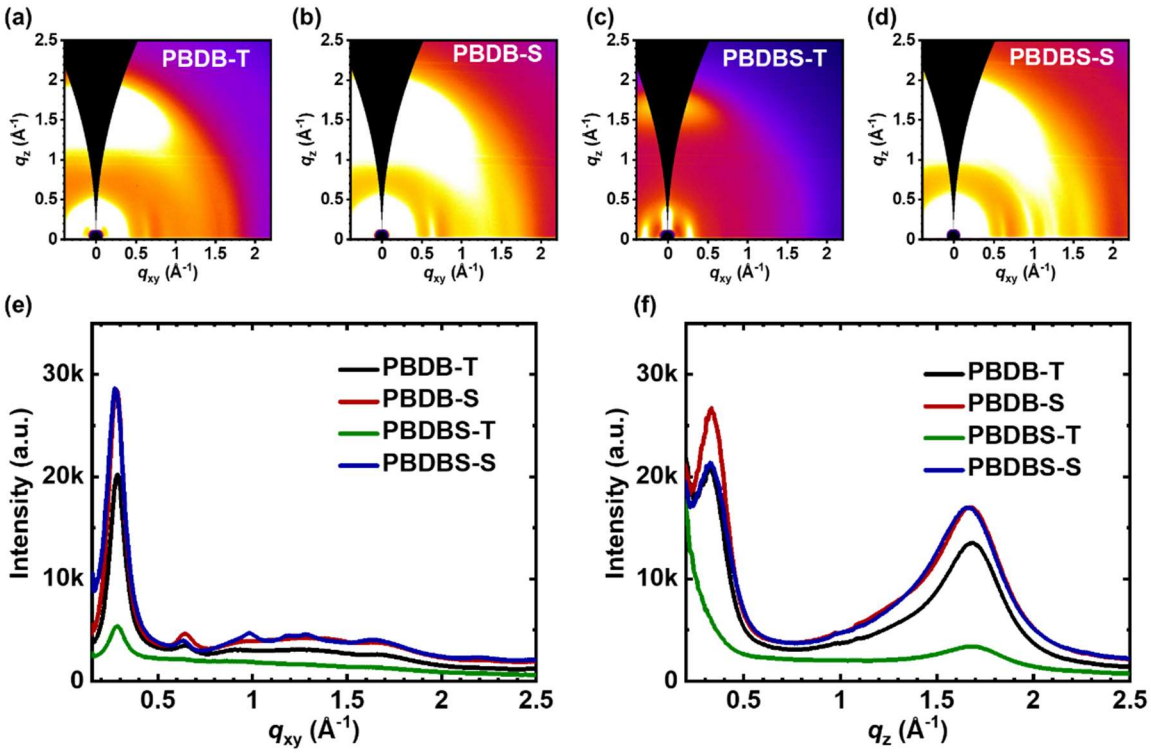

Figure 2.4. 2D GIWAXS diffraction patterns for the neat films of (a) PBDB-T, (b) PBDB-S, (c) PBDBS-T, and (d) PBDBS-S and the corresponding 1D line-cut profiles for (e) in-plane (IP) and (f) out-of-plane (OOP) directions.

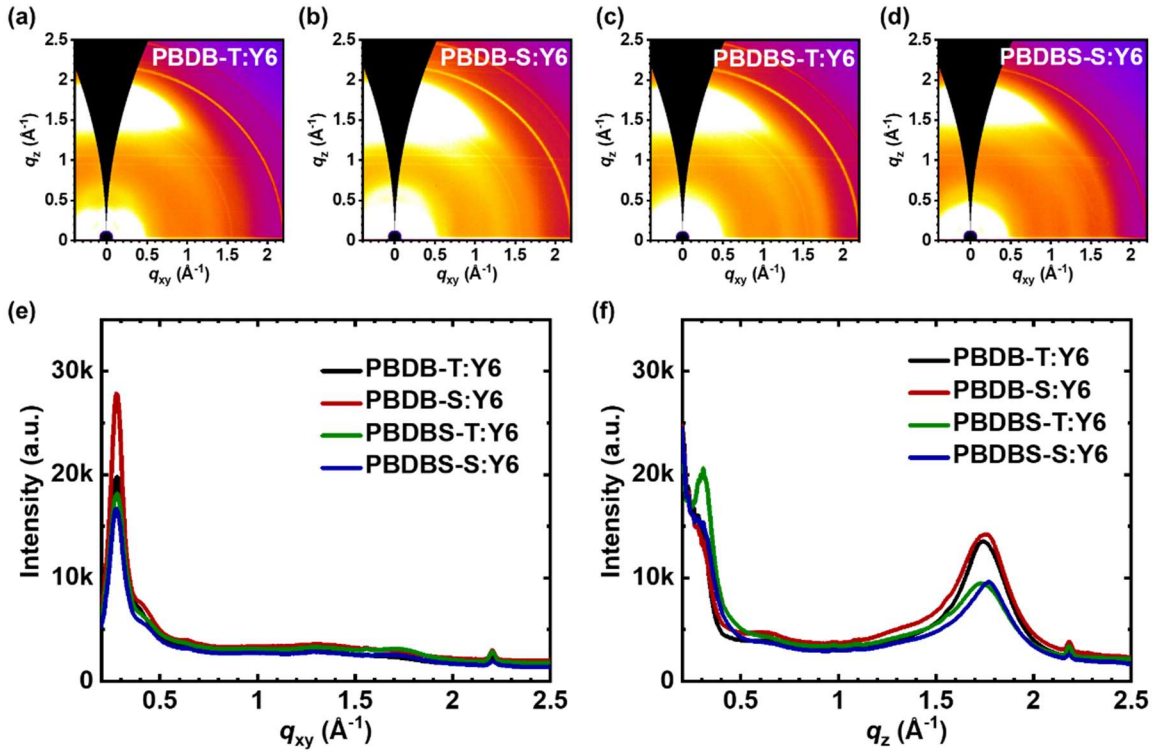

Figure 2.5. 2D GIWAXS diffraction patterns for the blend films of (a) PBDB-T:Y6, (b) PBDB-S:Y6, (c) PBDBS-T:Y6, and (d) PBDBS-S:Y6 and the corresponding 1D line-cut profiles for (e) in-plane (IP) and (f) out-of-plane (OOP) directions.

2.4 CONCLUSIONS

In summary, based on the known donor polymer, PBDB-T, we developed three new selenophene-containing donor polymers, PBDB-S, PBDBS-T and PBDBS-S, where the original thiophene units in various side chain and backbone positions were substituted with selenophene units. We found that selenophene substitution in the side chain positions had minimal impact on the electronic structures of the polymers, but slightly enhanced the optical absorption coefficient. On the other hand, selenophene substitution in the backbone positions led to red-shifted the optical absorption by ~40 nm, reducing the optical bandgaps from 1.83 – 1.85 eV to 1.72 – 1.74 eV. Estimated from the oxidative cyclic voltammograms, selenophene substitution in the backbone positions raised the HOMO energy levels by ~0.1 eV. Photovoltaic devices based on PBDB-T:Y6 and PBDB-S:Y6 blends demonstrated high PCE of 8.59% and 10.41%, respectively. The PBDB-S:Y6 blend showed enhanced J_{sc} and FF, as well as superior hole and electron mobilities compared to PBDB-T:Y6 blend. The improvement in PBDB-S relative to PBDB-T was attributed to the enhanced light-harvesting ability and the higher crystallinity induced by selenophene substitution in the side chain positions. Devices based on PBDBS-T:Y6 and PBDBS-S:Y6 blends, however, showed relatively lower PCE of 6.28% and 5.32%, respectively. This is largely due to the low solubility and poor solution-processibility of PBDBS-T and PBDBS-S. Single crystal analysis of the monomers DTBDD and DSBDD revealed that strong Se···O intramolecular interactions enabled "conformation lock" in addition to enhanced intermolecular π-π interactions, thus explains the poor solubility of PBDBS-T and PBDBS-S. This work demonstrated different intermolecular and intramolecular interactions resulted from selenophene substitution at various positions of a polymer, as well as their impact on optical absorption, electronic structures, and photovoltaic properties. While the strategy of selenophene substitution has demonstrated potential to improve

the regular thiophene-based polymers in light-harvesting ability, charge transport properties and photovoltaic performance, it is important to additionally recognize various intramolecular and intermolecular interactions and the resulted issue of solubility and solution-processibility.

2.5 SUPPORTING INFORMATION

X-ray Crystallography of DTBDD. A yellow needle, measuring 0.60 × 0.04 × 0.03 mm^3 was mounted on a loop with oil. Data was collected at -173°C on a Bruker APEX II single crystal X-ray diffractometer, Mo-radiation.

Crystal-to-detector distance was 40 mm and exposure time was 60 seconds per frame for all sets. The scan width was 0.5º. Data collection was 99.9% complete to 25 in ϑ. A total of 12336 merged reflections were collected covering the indices, -40 <= h <= 39, -10 <= k <=10, -30 <= l <= 30. 6419 reflections were symmetry independent and the R_{int} = 0.0386 indicated that the data was good. Indexing and unit cell refinement indicated a C-centered monoclinic lattice. The space group was found to be C 2/c (No. 15). The data was integrated and scaled using SAINT, SADABS within the APEX2 software package by Bruker.[90]

Solution by direct methods (SHELXS, SIR97[90]) produced a complete heavy atom phasing model consistent with the proposed structure. The structure was completed by difference Fourier synthesis with SHELXL97.[91-93] Scattering factors are from Waasmair and Kirfel.[94] Hydrogen atoms were placed in geometrically idealized positions and constrained to ride on their parent atoms with C---H distances in the range 0.95-1.00 Angstrom. Isotropic thermal parameters U_{eq} were fixed such that they were 1.2U_{eq} of their parent atom U_{eq} for CH's and 1.5U_{eq} of their parent atom U_{eq} in case of methyl groups. All non-hydrogen atoms were refined anisotropically by full-matrix least-squares. Data were summaried in **Table S2.3**.

X-ray Crystallography of DSBDD. An orange needle, measuring 0.60 × 0.04 × 0.03 mm^3 was mounted on a loop with oil. Data was collected at -173°C on a Bruker APEX II single crystal X-ray diffractometer, Mo-radiation.

Crystal-to-detector distance was 40 mm and exposure time was 60 seconds per frame for all sets. The scan width was 0.5º. Data collection was 99.9% complete to 25º in ϑ. A total of 30570 reflections were collected covering the indices, -42 <= h <= 42, -11<= k <= 11, -32 <= l <= 2. 7957 reflections were symmetry independent and the R_{int} = 0.0732 indicated that the data was of average quality. Indexing and unit cell refinement indicated a C-centered monoclinic lattice. The space group was found to be C 2/c (No. 15). The data was integrated and scaled using SAINT, SADABS within the APEX2 software package by Bruker.[90]

Solution by direct methods (SHELXS, SIR97[90]) produced a complete heavy atom phasing model consistent with the proposed structure. The structure was completed by difference Fourier synthesis with SHELXL97.[91-93] Scattering factors are from Waasmair and Kirfel.[94] Hydrogen atoms were placed in geometrically idealised positions and constrained to ride on their parent atoms with C---H distances in the range 0.95-1.00 Angstrom. Isotropic thermal parameters U_{eq} were fixed such that they were 1.2U_{eq} of their parent atom U_{eq} for CH's and 1.5U_{eq} of their parent atom U_{eq} in case of methyl groups. All non-hydrogen atoms were refined anisotropically by full-matrix least-squares. Data were summaried in **Table S2.4**.

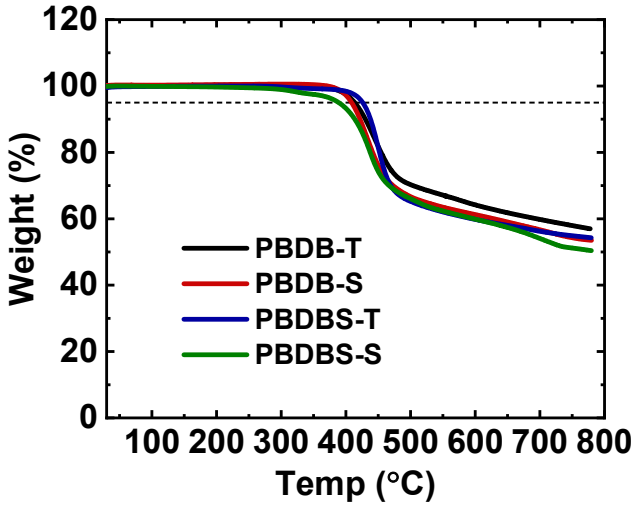

Figure S2.6. TGA traces of PBDB-T, PBDB-S, PBDBS-T, and PBDBS-S.

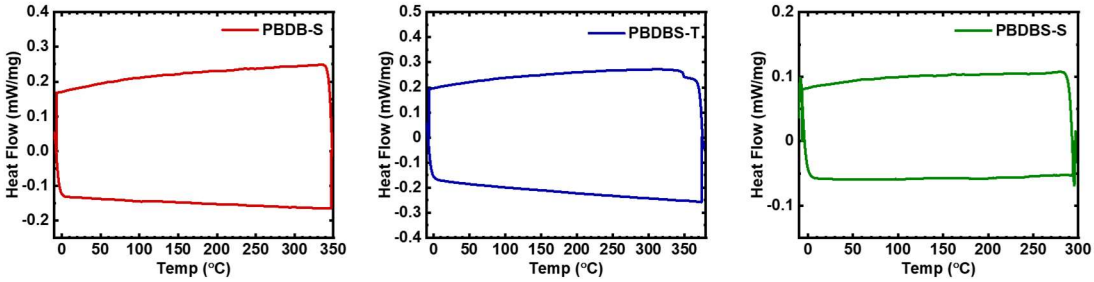

Figure S2.7. DSC traces of PBDB-S, PBDBS-T, and PBDBS-S.

Table S2.3. Crystallographic Data for DTBDD.

Empirical formula	C34 H40 O2 S4	
Formula weight	608.90	
Temperature	100(2) K	
Wavelength	0.71073 Å	
Crystal system	Monoclinic	
Space group	C 2/c	
Unit cell dimensions	a = 32.024(3) Å	α= 90°.
	b = 8.1136(6) Å	β= 100.946(4)°.
	c = 24.3611(19) Å	γ = 90°.
Volume	6214.5(8) $Å^3$	
Z	8	
Density (calculated)	1.302 Mg/m^3	
Absorption coefficient	0.336 mm^{-1}	
F(000)	2592	
Crystal size	0.600 x 0.040 x 0.030 mm^3	
Theta range for data collection	1.703 to 26.521°.	
Index ranges	-40<=h<=39, -10<=k<=10, -30<=l<=30	
Reflections collected	12336	
Independent reflections	6419 [R(int) = 0.0386]	
Completeness to theta = 25.000°	99.9 %	
Refinement method	Full-matrix least-squares on F^2	
Data / restraints / parameters	6419 / 127 / 442	
Goodness-of-fit on F^2	1.002	
Final R indices [I>2sigma(I)]	R1 = 0.0740, wR2 = 0.2037	
R indices (all data)	R1 = 0.1265, wR2 = 0.2472	
Largest diff. peak and hole	0.698 and -0.598 $e.Å^{-3}$	

Table S2.4. Crystallographic Data for DSBDD.

Empirical formula	C34 H40 O2 S2 Se2	
Formula weight	702.70	
Temperature	100(2) K	
Wavelength	0.71073 Å	
Crystal system	Monoclinic	
Space group	C 2/c	
Unit cell dimensions	a = 32.179(5) Å	α= 90°.
	b = 8.2195(13) Å	β= 102.199(9)°.
	c = 24.520(4) Å	γ = 90°.
Volume	6338.9(18) $Å^3$	
Z	8	
Density (calculated)	1.473 Mg/m^3	
Absorption coefficient	2.494 mm^{-1}	
F(000)	2880	
Crystal size	0.600 x 0.040 x 0.030 mm^3	
Theta range for data collection	1.907 to 28.470°.	
Index ranges	-42<=h<=42, -11<=k<=11, -32<=l<=32	
Reflections collected	30570	
Independent reflections	7957 [R(int) = 0.0732]	
Completeness to theta = 25.000°	99.8 %	
Refinement method	Full-matrix least-squares on F^2	
Data / restraints / parameters	7957 / 109 / 426	
Goodness-of-fit on F^2	1.004	
Final R indices [I>2sigma(I)]	R1 = 0.0500, wR2 = 0.1183	
R indices (all data)	R1 = 0.0989, wR2 = 0.1408	
Largest diff. peak and hole	1.035 and -0.661 e.$Å^{-3}$	

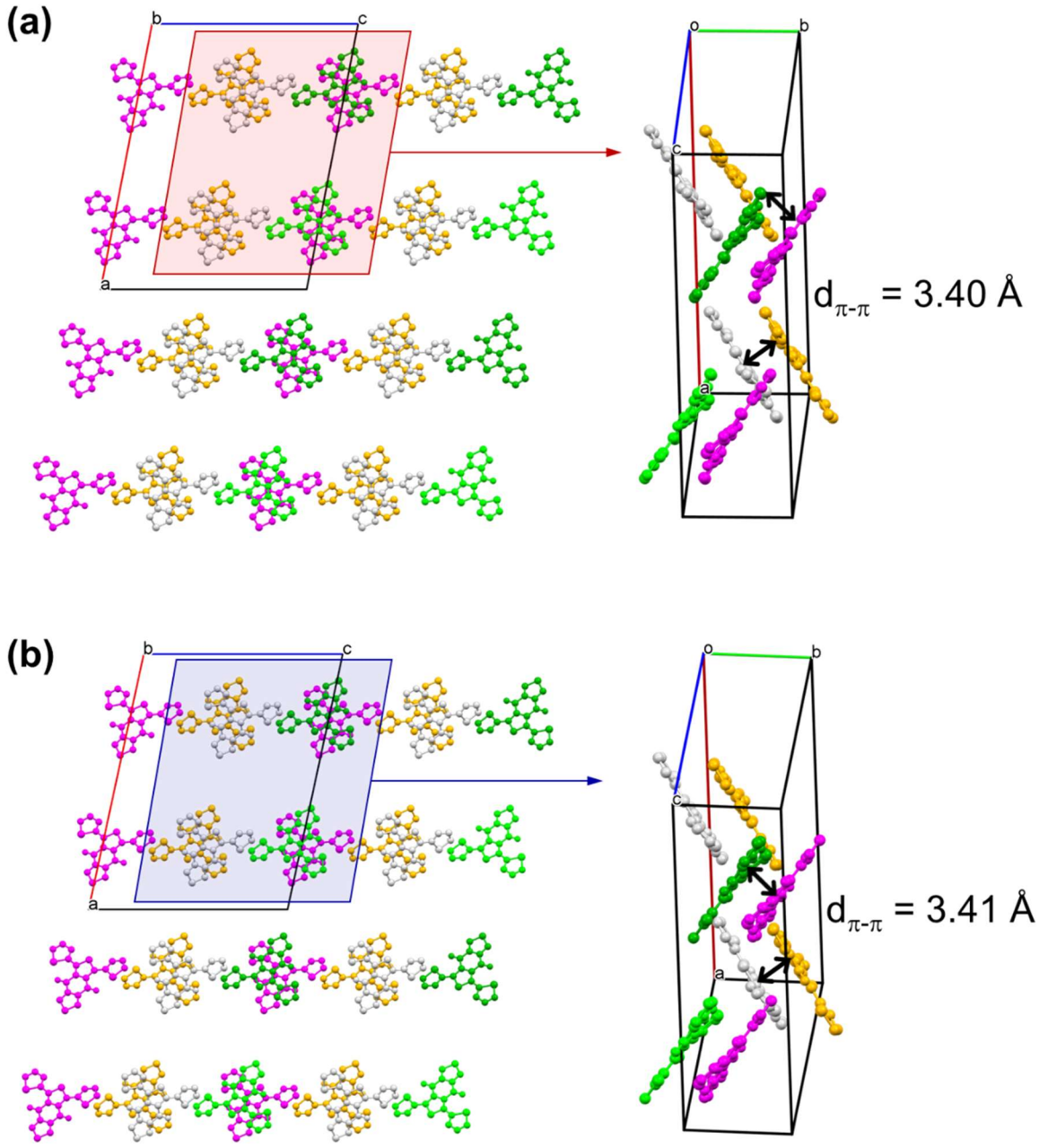

Figure S2.8. Crystal packing of (a) DTBDD and (b) DSBDD.

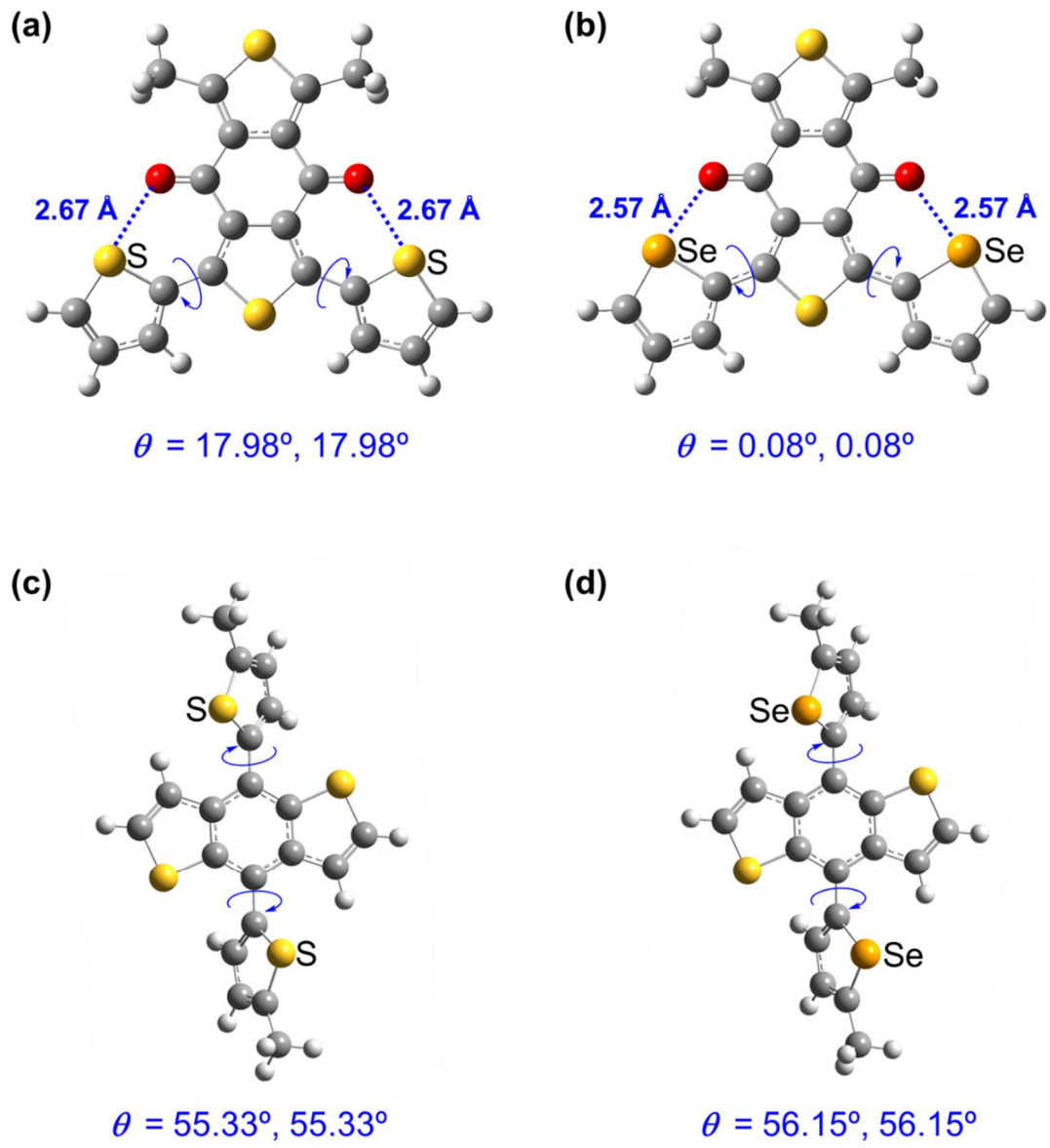

Figure S2.9. Optimized geometries of (a) DTBDD, (b) DSBDD, (c) BDT-T, and (d) BDT-S by DFT calculation with B3LYP/6-31G(d,p) basis set. Alkyl chains were replaced with methyl groups for simplification. Torsional angles (θ) were measured from the calculated mean planes of adjacent ring structures.

Table S2.5. 2D GIWAXS Peak Positions and Estimated Crystalline Coherence Length for the Neat films of Donor Polymers and the Blend Films of Polymer:Y6.

Film Composition	In-Plane (IP)					Out-of-Plane (OOP)				
	q_{xy} (Å^{-1})	*d*-spacing (Å)	L_c **(nm)**	q_{xy} (Å^{-1})	*d*-spacing (Å)	q_z (Å^{-1})	*d*-spacing (Å)	q_z (Å^{-1})	*d*-spacing (Å)	L_c **(nm)**
PBDB-T	0.286	21.97	**6.14**	0.650	9.67	0.332	18.93	1.683	3.73	**1.45**
PBDB-S	0.277	22.70	**6.02**	0.644	9.76	0.332	18.93	1.672	3.76	**1.37**
PBDBS-T	0.285	22.05	**6.30**	0.644	9.76	N/A	N/A	1.682	3.74	**1.50**
PBDBS-S	0.274	22.93	**5.90**	0.632	9.95	0.326	19.28	1.671	3.76	**1.40**
PBDB-T:Y6	0.280	22.44	**8.05**	0.393	16.00	Broad	N/A	1.745	3.60	**2.53**
PBDB-S:Y6	0.277	22.70	**8.40**	Shoulder	N/A	Broad	N/A	1.767	3.56	**2.28**
PBDBS-T:Y6	0.282	22.28	**7.10**	Shoulder	N/A	0.308	20.43	1.728	3.64	**2.13**
PBDBS-S:Y6	0.277	22.70	**7.22**	Shoulder	N/A	broad	N/A	1.773	3.54	**2.16**

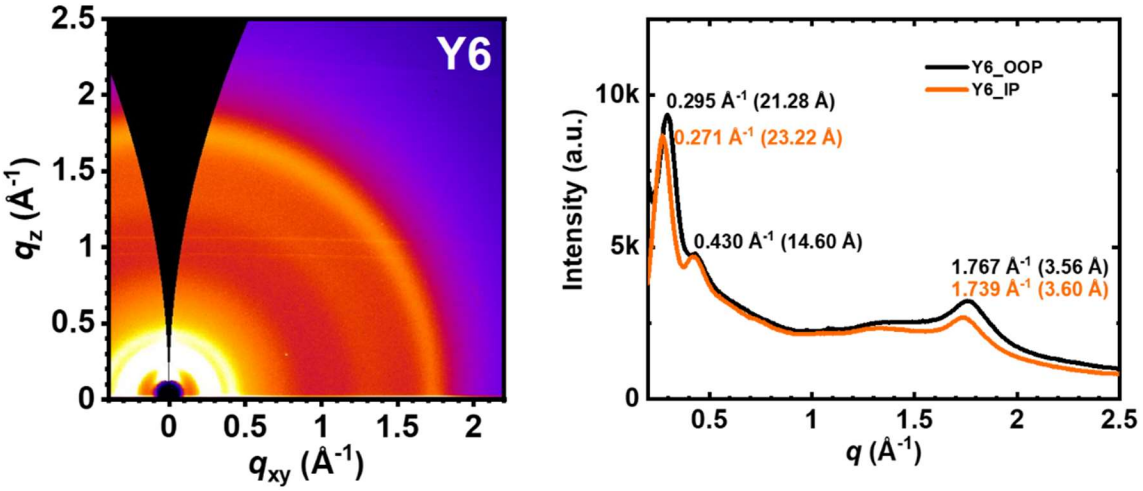

Figure S2.10. 2D GIWAXS diffraction patterns of Y6 neat film and the corresponding 1D line-cut profiles in the in-plane (IP) and out-of-plane (OOP) directions.

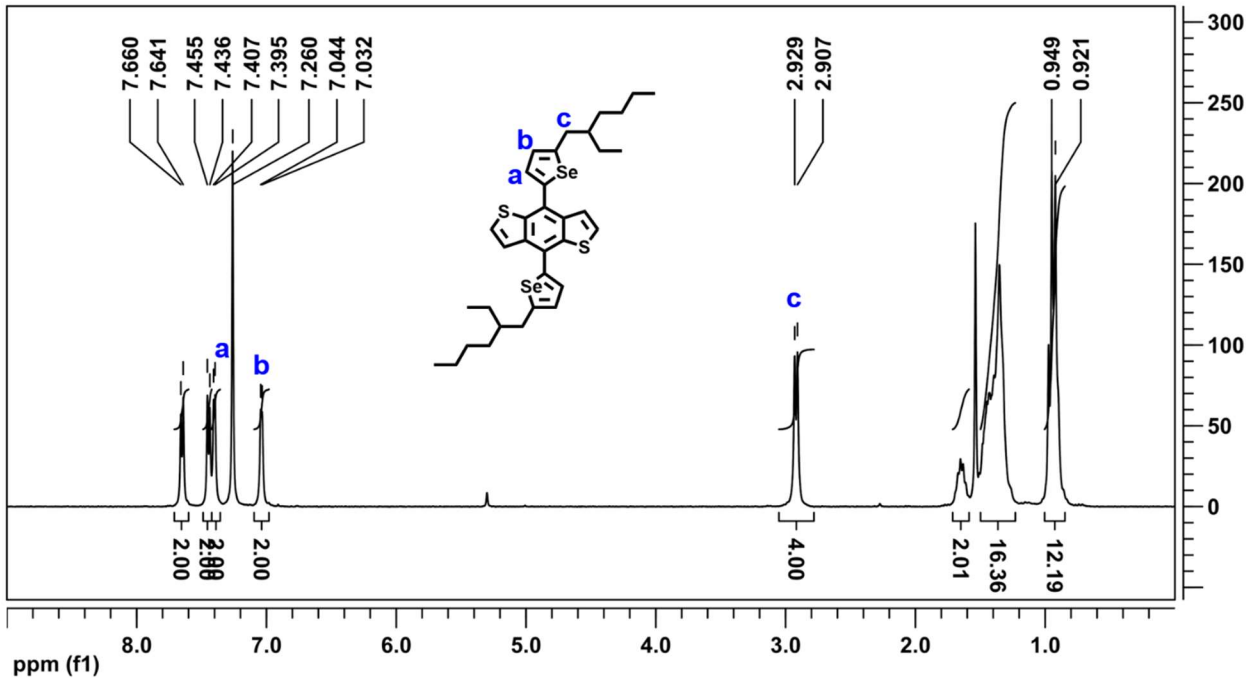

Figure S2.11. ^{1}H NMR (300 MHz, $CDCl_3$) spectrum of BDTS.

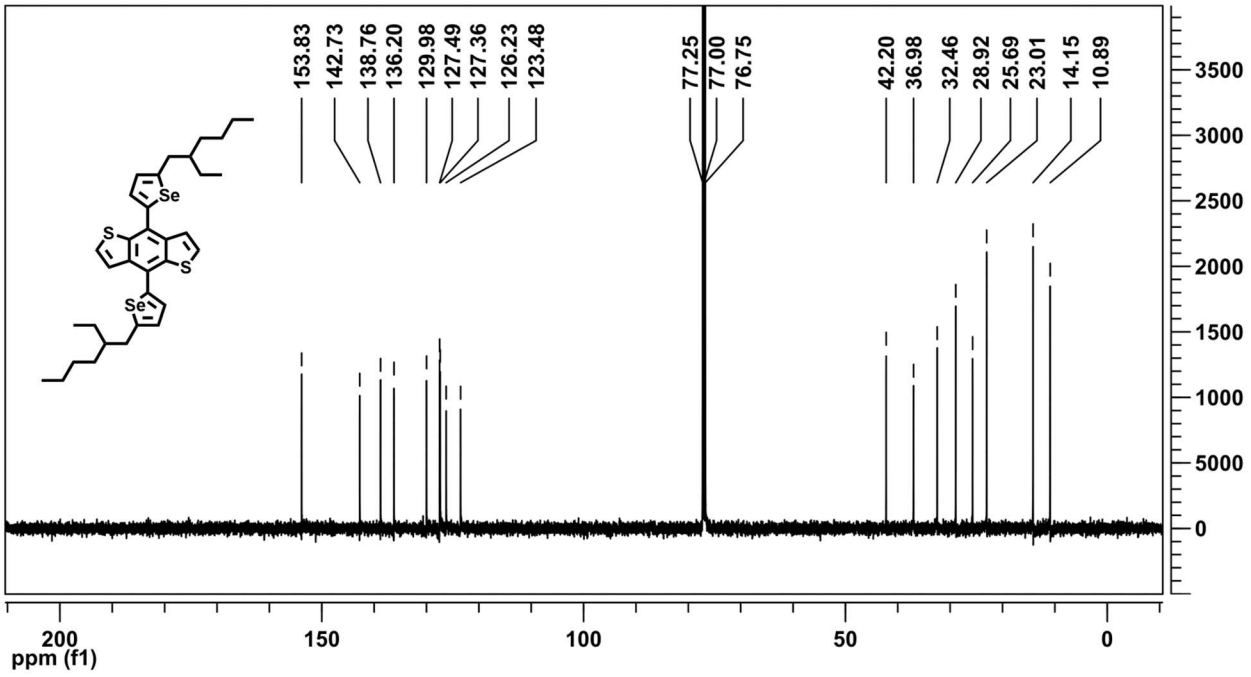

Figure S2.12. ^{13}C NMR (125 MHz, $CDCl_3$) spectrum of BDTS.

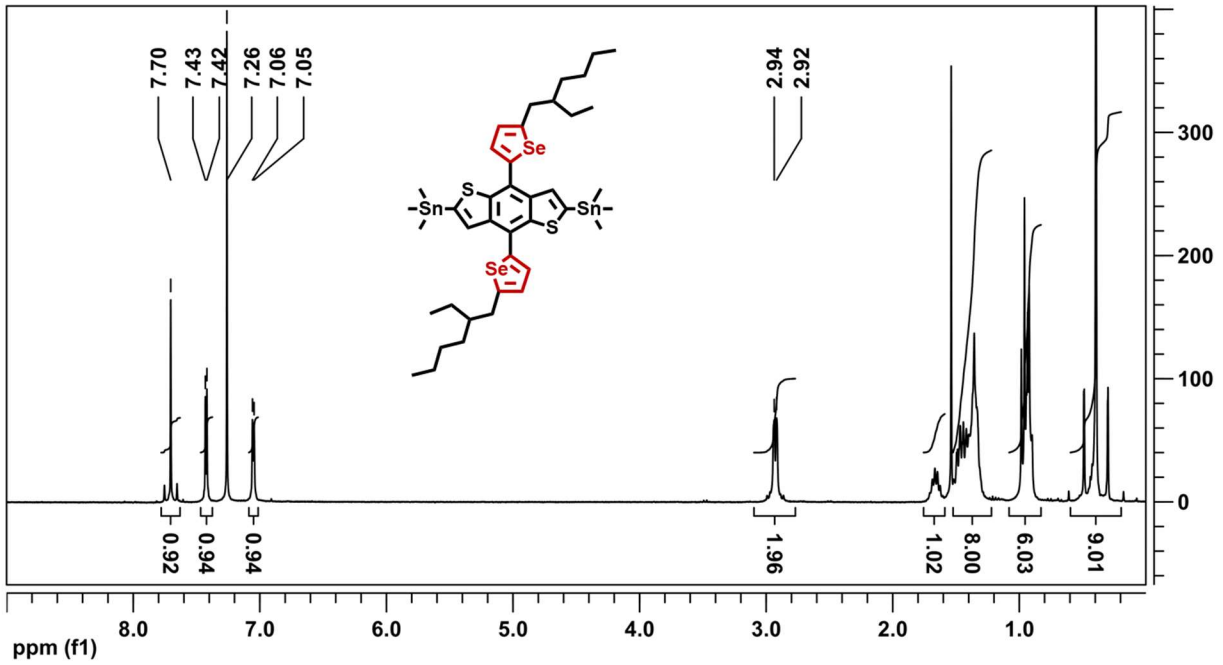

Figure S2.13. ^{1}H NMR (300 MHz, $CDCl_3$) spectrum of compound 6.

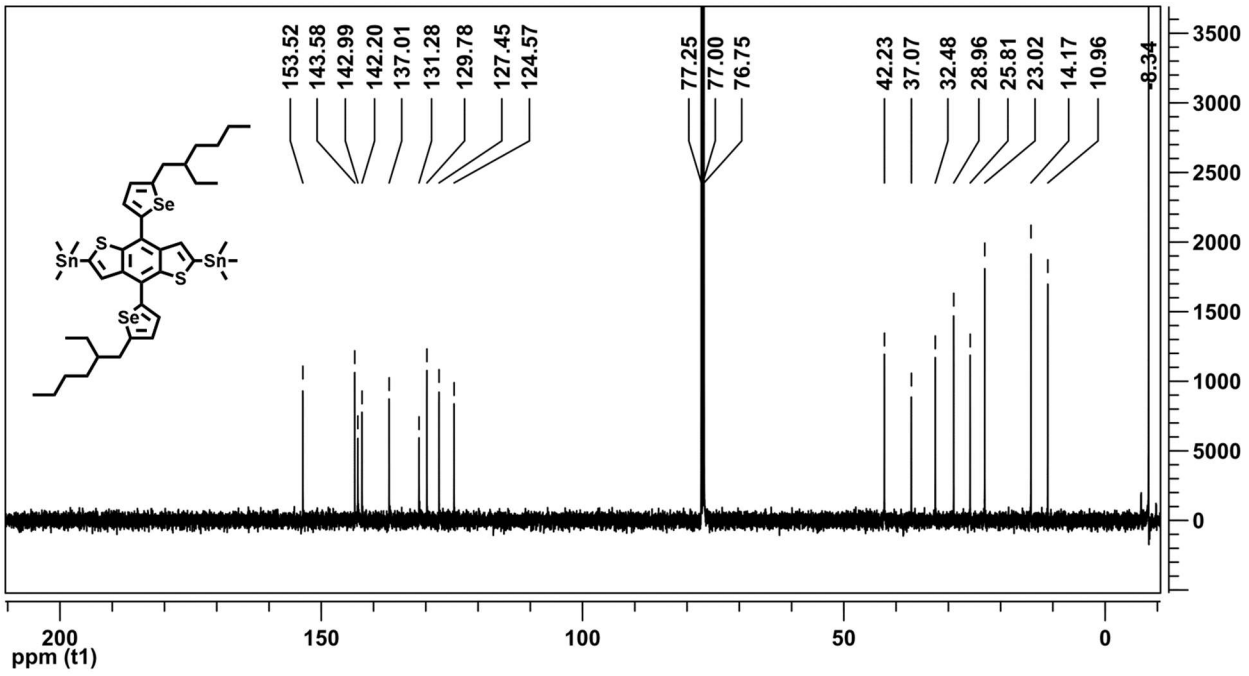

Figure S2.14. ^{13}C NMR (125 MHz, $CDCl_3$) spectrum of compound 6.

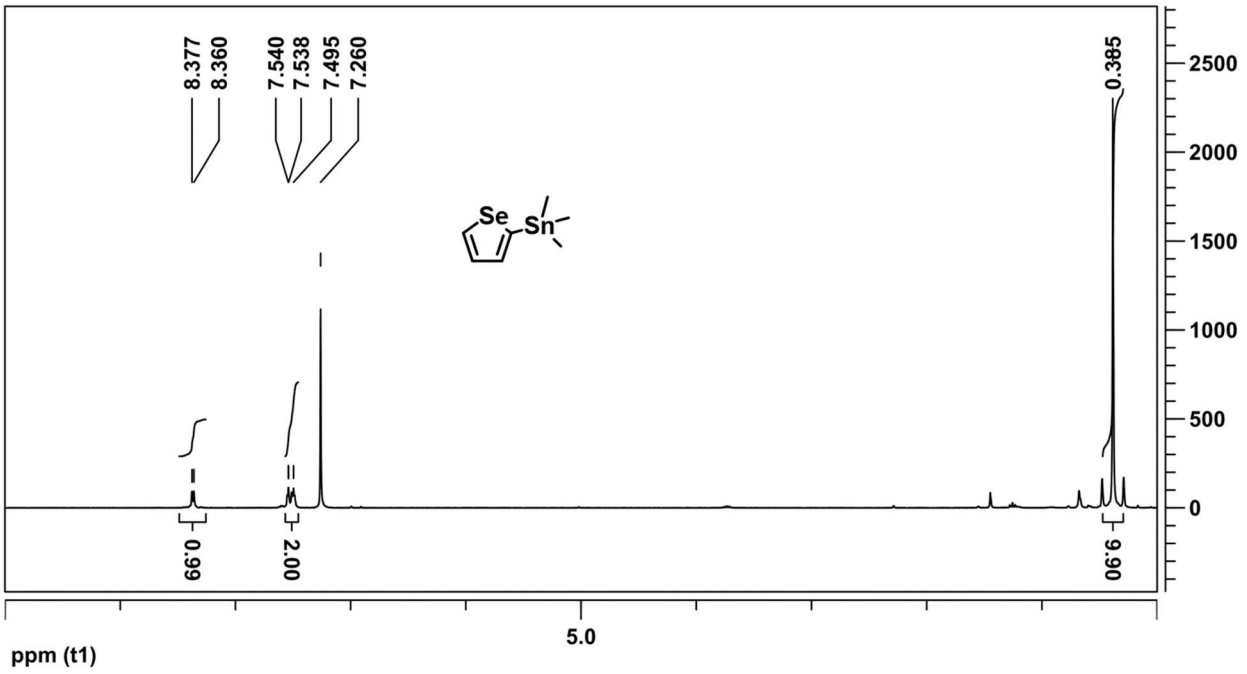

Figure S2.15. ^{1}H NMR (300 MHz, $CDCl_3$) spectrum of compound 12.

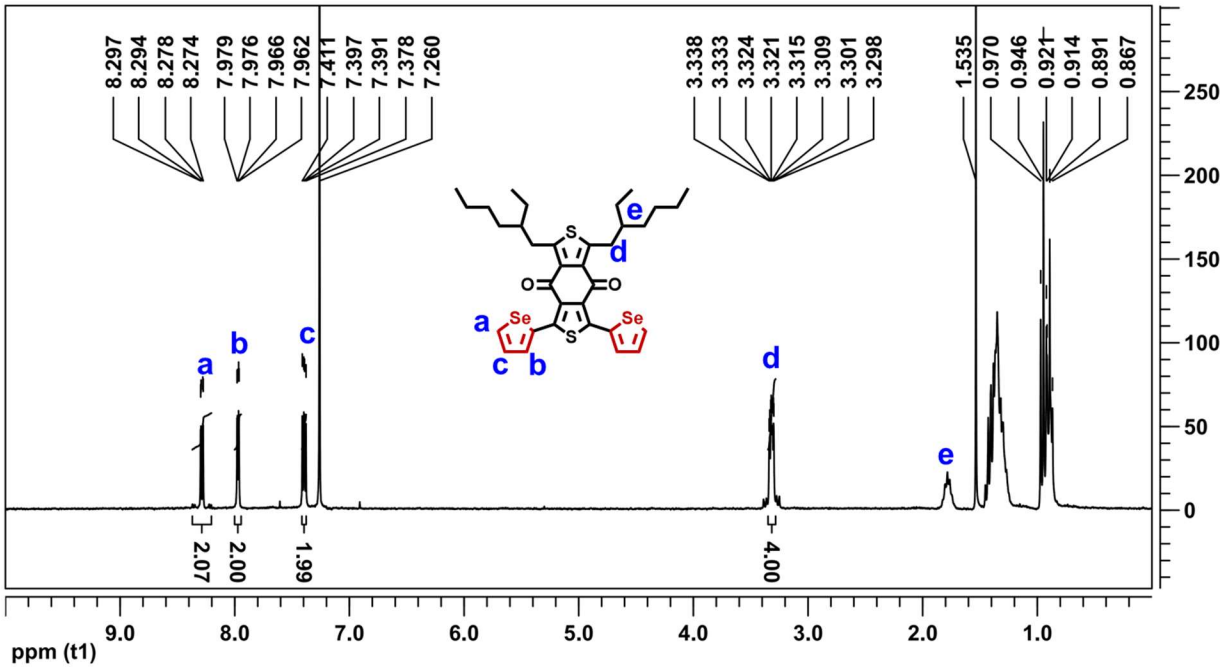

Figure S2.16. ^{1}H NMR (300 MHz, $CDCl_3$) spectrum of DSBDD.

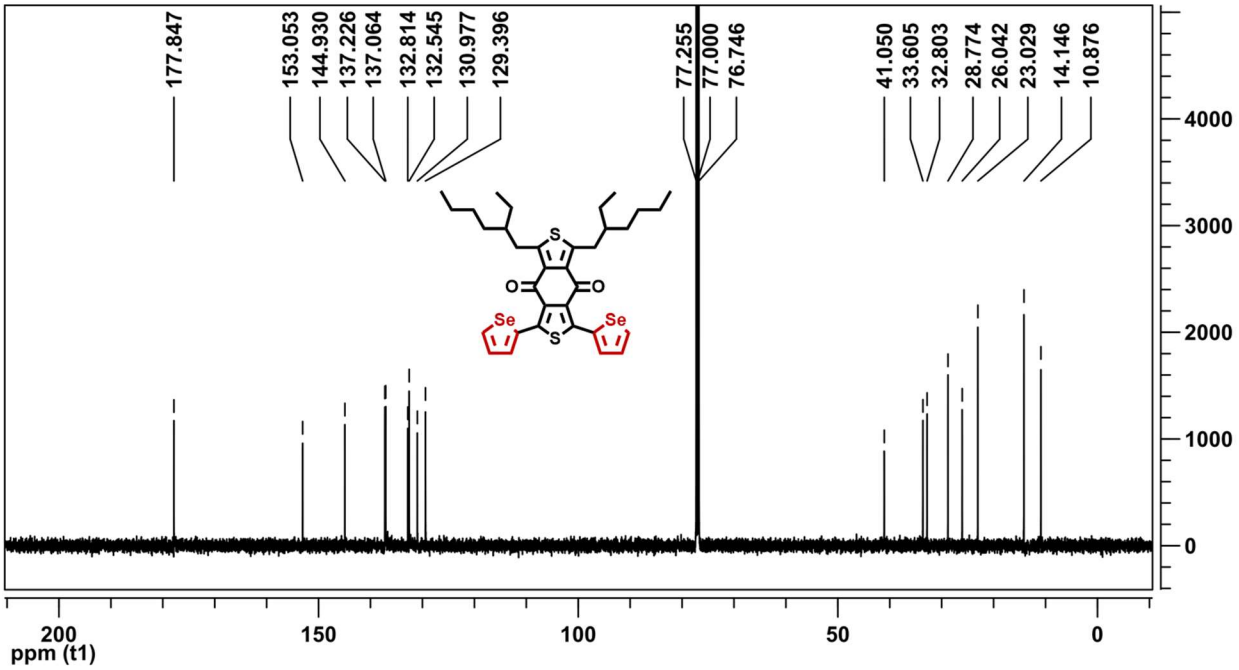

Figure S2.17. ^{13}C NMR (125 MHz, $CDCl_3$) spectrum of DSBDD.

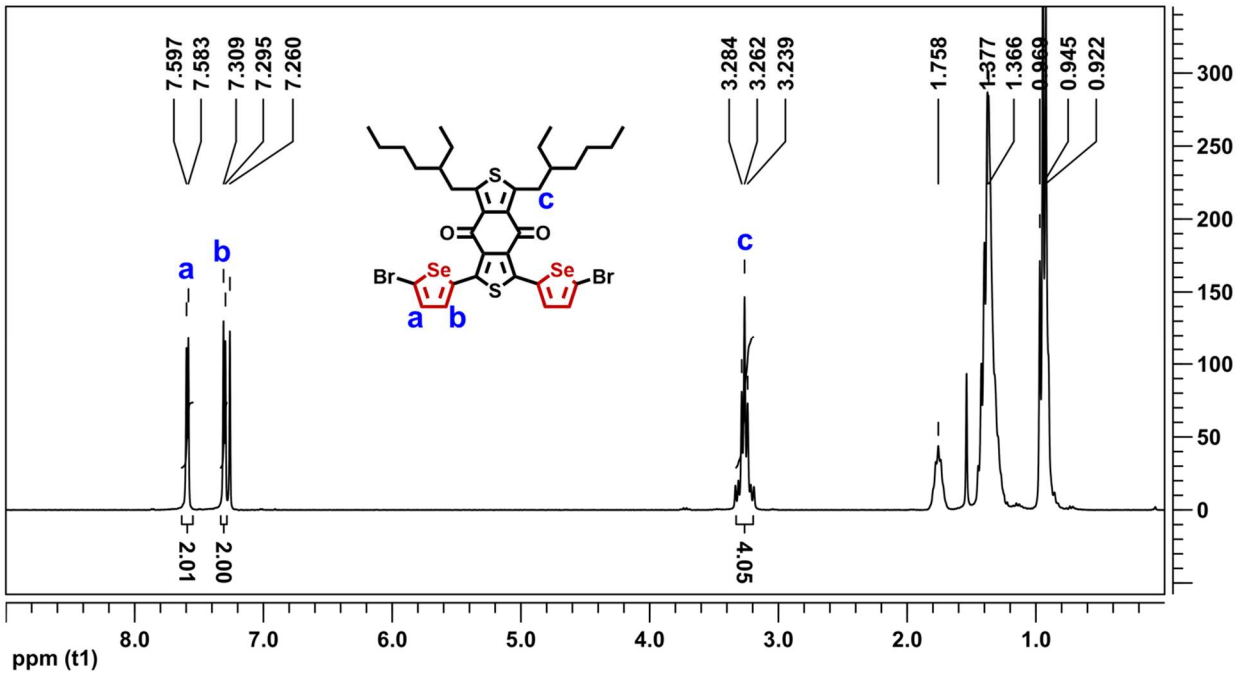

Figure S2.18. ^{1}H NMR (300 MHz, $CDCl_3$) spectrum of compound 14.

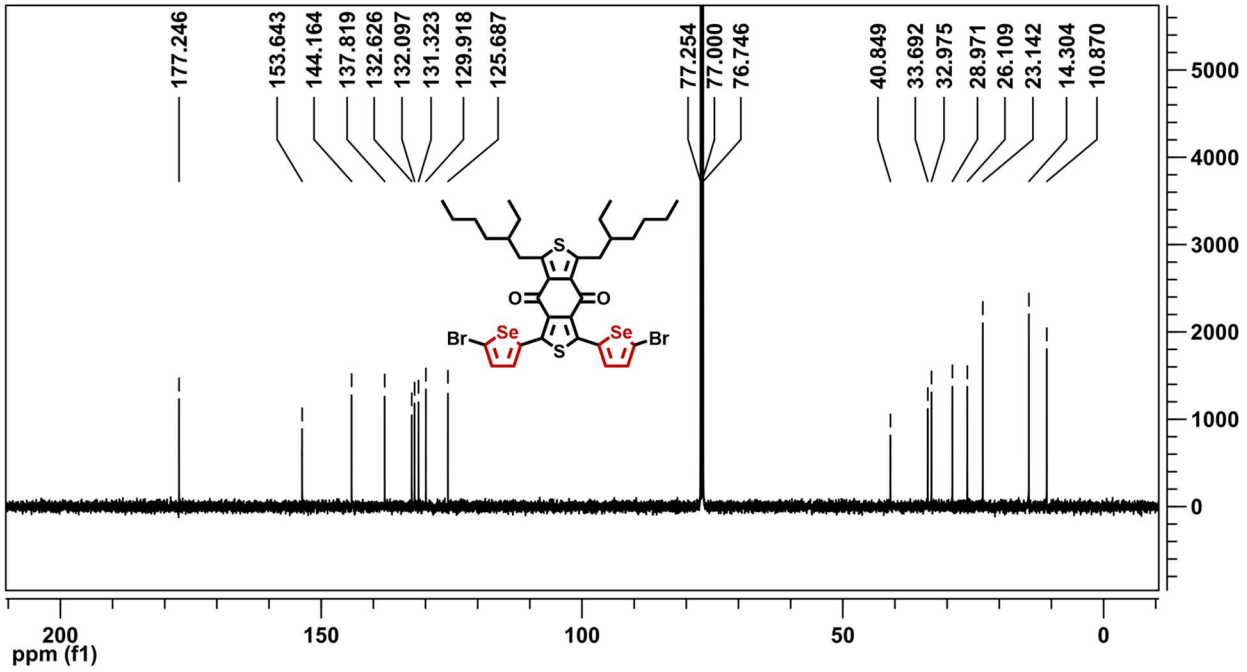

Figure S2.19. ^{13}C NMR (125 MHz, $CDCl_3$) spectrum of compound 14.

Chapter 3. COMPARATIVE STUDY OF SELENOPHENE- AND THIOPHENE-CONTAINING NAPHTHALENE DIIMIDE-BASED N-TYPE POLYMERS FOR HIGH PERFORMANCE ALL-POLYMER SOLAR CELLS

This chapter is reproduced with permission from: Ding, X.; Tran, D. K.; Kuzuhara, D.; Koganezawa, T.; Jenekhe, S. A. "Comparative Study of Selenophene- and Thiophene-Containing n-Type Semiconducting Polymers for High Performance All-Polymer Solar Cells." *ACS Appl. Polym. Mater.* **2020**, *3*, 49-59. Copyright 2020 American Chemical Society. http://pubs.acs.org/articlesonrequest/AOR-JD66EUM49Q6MDFBW7XRA

3.1 INTRODUCTION

All-polymer solar cells (all-PSCs)[19, 23-25, 35-50] are typically composed of a binary blend of two different conjugated polymers, one that functions as a *p-type* semiconductor and the other that functions as an *n-type* semiconductor. As a special class of organic photovoltaics, all-PSCs have many unique advantages including their excellent mechanical properties, their rugged thermo-mechanical stability, the great potential for their integration into buildings, textiles, and other structures, scalable and cost-effective manufacturing of the devices, and the facile tunability of the properties of polymeric materials.[19, 35-38, 95-96] Although progress in increasing the power conversion efficiency (PCE) of all-PSCs was relatively slow for a long time compared to polymer/fullerene devices,[65] the last 7 years has seen rapid advances largely due to the emergence of new generations of n-type semiconducting polymers.[19, 35-38] Indeed, the efficiency of all-PSCs

has climbed from below 2%[38-39] in 2012 to 8%[24, 97] in 2015 and to over 10-14% recently.[40, 44, 47-50, 98]

The new generations of both p-type and n-type semiconducting polymers that have enabled advances in the performance of polymer solar cells, including all-PSCs, in the last two decades have emerged from a powerful macromolecular design strategy – the so-called "donor-acceptor architecture"[99] – whereby the conjugated copolymer repeat unit is composed of alternating electron-donating (D) and electron-accepting (A) moieties of varying complexities and permutations.[100-102] The modular nature of such D-A conjugated copolymers has enabled the facile tuning of the electronic band structure, light-harvesting properties, and charge transport properties of the materials. A general feature of all D-A copolymers is that they exhibit an intramolecular charge transfer (ICT) band, in their optical absorption spectra, whose strength and spectral range depend on the strength of the ICT interaction.[99-100] The relative strengths of the electron-deficient moiety A and electron-donating moiety D incorporated into the D-A conjugated copolymer determine the electronic band structure, including the electron affinity and ionization energy or HOMO/LUMO energy levels, and thus whether the material will be primarily a p-type or n-type semiconductor or even an ambipolar semiconductor.[103-104] Numerous p-type semiconducting polymers with D-A architectures that have high bulk hole mobility and suitable HOMO energy level (< -5.0 eV) have been initially developed for applications in polymer/fullerene solar cells.[65] Although lagging behind their p-type counterparts, many n-type semiconducting polymers with D-A architectures that have high bulk electron mobility and suitable LUMO energy level (< -3.4 eV) have similarly been developed and these have enabled advances in all-PSCs. [19, 23-25, 35-50, 105-106]

Arylene diimides,[21] including naphthalene diimide (NDI),[22-25] perylene diimide (PDI),[23] tetraazabenzodifluoranthene diimide (BFI),[26-28] naphthodithiophenediimide (NDTI),[29-31] and bithiophene diimide (BTI),[32-34] are the most widely investigated electron-deficient building blocks "A" in the design of *n-type* semiconducting copolymers with D-A architectures for applications in all-PSCs.[19, 23-25, 35-50] Currently, NDI-based D-A copolymers have been the most widely studied and successful class of n-type semiconducting (or acceptor) polymers for all-PSCs due to their combination of large electron affinity, high electron mobility, and excellent self-assembly and semi-crystalline properties.[21, 107] Although early studies of NDI-based D-A copolymers focused on understanding the effects of the choice of various donor moieties on the HOMO/LUMO energy levels, the tendency towards unipolar or ambipolar charge transport, and carrier mobility,[103, 108-109] recent applications in all-PSCs have largely focused on *bithiophene*-NDI, *biselenophene*-NDI, and related random copolymers, which have enabled solar cell efficiencies above 9-10%.[25, 46, 98, 110] Here, our primary goal is to explore the effects of the donor moiety substitution on the intrinsic and photovoltaic blend properties of n-type semiconducting polymers with the simplest possible donor-acceptor (D-A) macromolecular structure based on the NDI acceptor moiety, i.e. (-D-NDI-), where the donor moiety "D" is a simple unicyclic ring such as thiophene or selenophene. For example, the nature and strength of the ICT interaction, intermolecular interactions, the molecular packing and electronic properties of (-D-NDI-) type polymers can be expected to be very different compared to those with (-D-D-NDI-) structure.[25, 108] Hence, relative to the more widely studied but more complex (-D-D-NDI-) architectures such as *bithiophene*-NDI and *biselenophene*-NDI,[25, 108] we expect a comparative study of (-D-NDI-) type structures to provide new insights for the design and application of semiconducting polymers with D-A architectures.

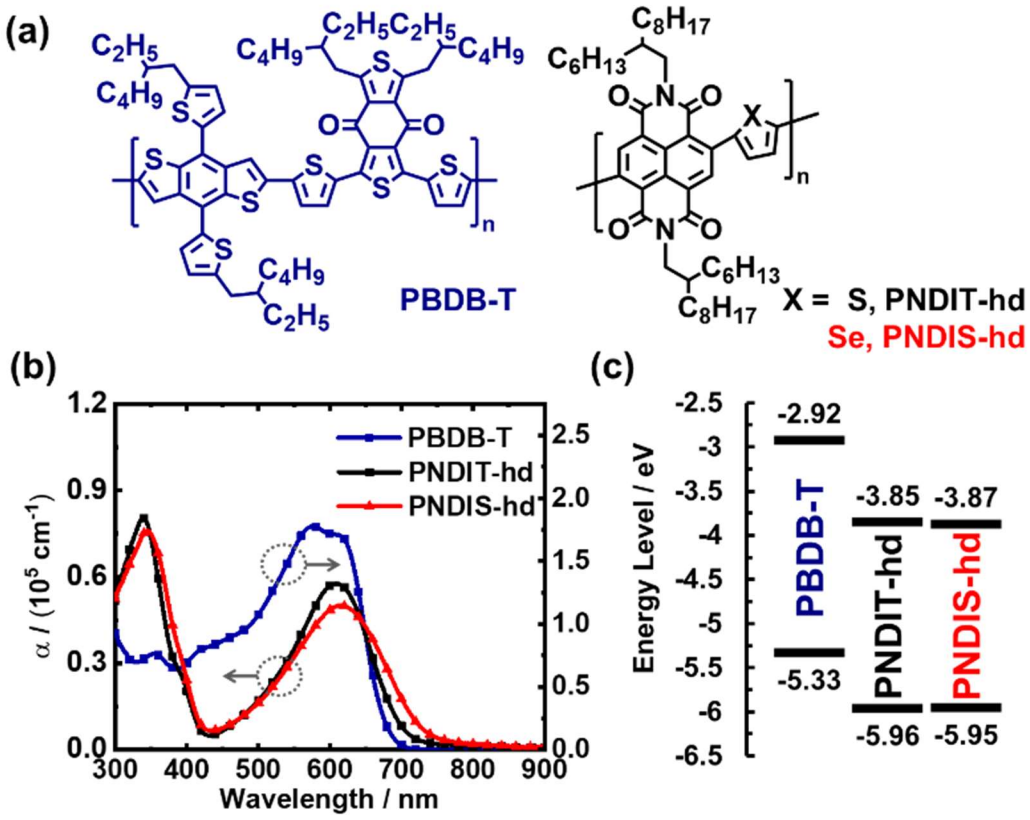

Figure 3.1. (a) Molecular structures, (b) thin-film optical absorption spectra, and (c) HOMO/LUMO energy levels of acceptor polymers PNDIT-hd and PNDIS-hd and donor polymer PBDB-T.

In this chapter, I will present a comparative study of alternating naphthalene diimide-*thiophene* copolymer (PNDIT-hd) and naphthalene diimide-*selenophene* copolymer (PNDIS-hd) as model (-D-NDI-) type D-A copolymer acceptors, whose molecular structures are shown in **Figure 3.1**, in all-PSCs. The backbone substitution of selenophene for thiophene in going from PNDIT-hd to PNDIS-hd was found to have minimal impact on the HOMO/LUMO energy levels of the n-type semiconducting copolymers. However, the thin-film optical absorption spectrum of PNDIS-hd was slightly red-shifted, resulting in a 0.07 eV decrease of optical bandgap relative to

PNDIT-hd. Binary blends of PNDIT-hd and PNDIS-hd respectively with the wide-bandgap donor polymer PBDB-T[59-60] (**Figure 3.1**), produced all-PSCs in which the *selenophene*-containing acceptor polymer has significantly improved photocurrent and overall photovoltaic power conversion efficiency. PNDIT-hd:PBDB-T based all-PSCs could thus achieve a PCE of 6.7% (J_{sc} = 12.18 mA/cm^2, FF = 0.66) whereas the corresponding PNDIS-hd:PBDB-T devices showed a higher PCE of 8.4% (J_{sc} = 14.50 mA/cm^2, FF = 0.71). The observed enhanced photovoltaic properties of the selenophene-containing polymer PNDIS-hd are largely accounted for by the improved light harvesting and formation of optimal blend morphology compared to its thiophene counterpart, PNDIT-hd.

3.2 Experimental Methods

Materials and Characterization. The donor polymer PBDB-T was purchased from Brilliant Matters Inc. (Quebec, Canada): M_n= 60 kDa, $Đ$ = 1.9, metallic impurities content < 0.01%. The acceptor polymers, PNDIT-hd and PNDIS-hd, were synthesized according to our previous report.[24, 39] The molecular structures of PNDIT-hd and PNDIS-hd were confirmed by ^{1}H NMR spectra (**Error! Reference source not found.** and Figure S3.8). The molecular weight of the acceptor polymers was characterized by gel-permeation chromatography (GPC) against polystyrene standards and eluting with chloroform at room temperature: PNDIT-hd (M_n = 10.0 kDa, M_w = 21.0 kDa, $Đ$ = 2.10), PNDIS-hd (M_n = 22.1 kDa, M_w = 64.9 kDa, $Đ$ = 2.94). Thermogravimetric analysis (TGA) of the polymers was conducted on a TA Instruments model Q50 TGA at a heating rate of 10 °C/min under a flow of N_2 with scans from room temperature to 800 °C. Differential scanning calorimetry (DSC) analysis was performed on a TA Instruments model Q100 DSC under N_2 by scanning from 20 to 400 °C at a heating rate of 20 °C/min. Optical

absorption spectra were obtained from a PerkinElmer Lambda 900 UV-vis/near-IR spectrophotometer.

The HOMO/LUMO energy levels of the polymers were determined from cyclic voltammetry (CV) experiments performed on an EG&G Princeton Applied Research potentiostat/galvanostat (model 273A). A three-electrode cell was used, using platinum (Pt) wires as both counter and working electrodes. Silver/silver ion (Ag in 0.01 M $AgNO_3$ solution) was used as the reference electrode. The working electrode was a Pt wire coated with a polymer thin film dip coated from each polymer solution in chlorobenzene (PNDIT-hd, PNDIS-hd, and PBDB-T). All the CV measurements were carried out in 0.1 M tetrabutylammonium hexafluorophosphate (Bu_4NPF_6) solution in acetonitrile at a scan rate of 50 mV/s. The reduction and oxidation potentials were referenced to the ferrocene-ferrocenium (Fc/Fc^+) couple by using ferrocene as an internal standard; to derive the HOMO/LUMO energy levels from the redox potentials, HOMO energy level of ferrocene is taken to be at -4.8 eV relative to the vacuum level. The Fc/Fc^+ couple was found at 0.09 V in our experiments. Thus, the LUMO and HOMO energy levels of the semiconducting polymers investigated were determined by using following relationships: E_{LUMO} = -(E_{red}^{onset} + 4.71) eV and E_{HOMO} = -(E_{ox}^{onset}+4.71) eV, respectively.

Solar Cell Fabrication and Testing. The inverted all-PSC device structure fabricated and evaluated was: ITO/ZnO/PEI/blend active layer/ MoO_3(0.5 nm)/Ag(100 nm), where PEI or polyethylenimine is a cathode buffer layer.[79] The ITO glass substrates were sequentially sonicated in acetone, deionized (DI) water and isopropanol for 20 min each and then plasma cleaned for 10 min. The ZnO layer (~30 nm) was spin-coated from the precursor solution (0.5 g of zinc acetate dihydrate, 0.14 g of ethanolamine and 5 mL of 2-methoxyethanol) and baked at 250 ºC for 30 min in open air. Solution of PEI (M_w = 25k, Aldrich 408727) in 2-methoxyethanol (0.05 wt%) was then

spin-coated onto the ZnO layer and dried at 120 ºC for additional 10 min. The resulting substrates were then stored in an argon-filled glovebox for deposition of active layers.

The active layer blend solution was prepared by mixing a chlorobenzene solution of the donor polymer PBDB-T (10 mg/mL) respectively with a chlorobenzene solution of PNDIT-hd (25 mg/mL) or PNDIS-hd (20 mg/mL); various solution volumes of the component polymers were mixed in the right proportions to afford the desired blend film compositions. In cases where a diphenyl ether (DPE) processing additive was used, the chlorobenzene:DPE (v/v %) mixed solvent was achieved by adding the DPE to a prepared blend solution. The blend solutions were stirred overnight with low heating to achieve a homogeneous mixture. Each blend solution was then spin-coated onto the cleaned substrate and annealed on a hot plate for 10 min to afford dried thin films with a thickness of 95 ± 5 nm. Finally, the MoO_3 layer and Ag electrode were deposited within a thermal evaporator. Defined active area of 0.0314 cm^2 was achieved for individual devices through a shadow mask. The photovoltaic cells were tested under AM 1.5G solar illumination at 100 mW/cm^2 in ambient air using a Solar Simulator (model 16S, Solar Light Co., Philadelphia, PA) with a 200W Xenon Lamp Power Supply (Model XPS 200, Solar Light Co., Philadelphia, PA) calibrated by NREL certified Si photodiode (Model 1787–04, Hamamatsu Photonics K.K., Japan) and a HP4155A semiconductor parameter analyzer (Yokogawa Hewlett-Packard, Japan). After the *J–V* measurement, the EQE was measured by using a solar cell quantum efficiency measurement system (Model QEX10, PV Measurements, Inc., Boulder, CO) with a 2 mm^2 (2 × 1 mm) size masked incident light source and TF Mini Super measurement apparatus for multiple devices in a single substrate.

SCLC Device Fabrication and Testing. The space charge limited current (SCLC)[80] devices fabricated and evaluated had the structures: ITO/PEDOT:PSS/blend/MoO_3 (7.5

nm)/Ag(100 nm) (hole-only), where poly(3,4-ethylenedioxythiophene):poly(styrenesulfonate) (PEDOT:PSS) is a hole injection layer; and ITO/ZnO/PEI/blend/LiF(1 nm)/Al(100 nm) (electron-only). The blend active layers in these SCLC devices had the same composition as the corresponding photovoltaic devices. Current-voltage (*J-V*) characteristics of the SCLC devices were plotted as $J^{0.5}$ versus V and fitted by using the following formula: $J = 9\ \varepsilon_0\ \varepsilon_r\ \mu V^2/8d^3$, where J is the current density, ε_0 is the permittivity of free space, ε_r is the relative dielectric constant of the transport medium, μ is the carrier mobility, V is the applied voltage, d is the thickness of blend active layer.

Atomic Force Microscopy (AFM) Imaging. The surfaces of the actual all-polymer solar cell devices were imaged by using the atomic force microscope (Model: Bruker Dimension ICON).

2D GIXD Measurements. Two-dimensional (2D) grazing incidence X-ray scattering (GIXD) experiments were conducted at the Japan Synchrotron Radiation Facility SPring-8 by using the beamline BL46XU. The thin-film samples investigated were prepared in the same manner as the corresponding photovoltaic devices on ZnO-coated ITO substrates, without the thermal deposition of top MO_3/Ag electrodes. The X-ray beam was monochromatized by a double-crystal Si(111) monochromator, and the X-ray energy in this experiment was 12.40 keV (λ = 0.1 nm). The angle of incident X-ray to sample surface was 0.12° with a Huber diffractometer. The scattered profile from the film sample was detected using an area detector (PILATUS 300K) for 5 s at room temperature, and the distance between the sample and detector was 174.4 mm. The crystal coherence length (L_c) of samples was determined by using the Scherrer equation: $L_c = 2\pi K/\Delta q$, where K is a shape factor (typically 0.89) and Δq is the full width at half-maximum (FWHM) of the diffraction peak. Here, the $L_c(100)$ was obtained from the FWHM of the (100) diffraction peak in the-plane (q_{xy}) line cut.

3.3 Results and Discussion

3.3.1 *Synthesis and Characterization of Acceptor Polymers.*

The acceptor polymers, PNDIT-hd and PNDIS-hd, were synthesized by using Stille copolymerization approach according to the procedures of previous reports.[24, 39] The molecular structures of both polymers were confirmed by ^{1}H NMR spectra. The polymers are readily soluble in common organic solvents such as chloroform (CF) and chlorobenzene (CB). The molecular weight of the polymers was determined by gel-permeation chromatography (GPC) eluting with chloroform at room temperature. The number-average molecular weight (M_n) of PNDIT-hd and PNDIS-hd was 10.0 and 22.1 kDa, with dispersity ($Đ$) of 2.10 and 2.94, respectively. (**Table 3.1**) The M_n values of both PNDIT-hd and PNDIS-hd were within the low range of polymer molecular weight (< 30 kDa), therefore were not considered to be impactful factors on their photovoltaic performance.[111-112] Thermogravimetric analysis (TGA) showed that the decomposition temperature (5% weight loss) is 442 ºC for PNDIT-hd and 401 ºC for PNDIS-hd (Figure S3.9a), indicating excellent thermal stability of both acceptor polymers. Differential scanning calorimetry (DSC) scans showed that PNDIS-hd has broad melting peaks at 315 and 335 ºC and a broad recrystallization peak over the range of 320-290 ºC in the cooling scan (Figure S3.9b). In contrast, PNDIT-hd showed melting transition peak in the 260-270 ºC range and a relatively sharp recrystallization peak at 246 ºC. The significantly higher melt transition temperature of the selenophene-containing PNDIS-hd implies stronger intermolecular interactions due to Se-Se interactions,[107, 113] given that both polymers (PNDIS-hd and PNDIT-hd) are otherwise similar in molecular structure.

Table 3.1. Molecular Weight, Optical Properties, and Energy Levels of the Acceptor Polymers

Polymer	M_n [kDa]	$Đ$	$\lambda_{max}{}^a$ [nm]	$\lambda_{max}{}^b$ [nm]	$\lambda_{onset}{}^b$ [nm]	$E_g{}^{opt}$ [eV]	E_{ox} [eV]	E_{red} [eV]	E_{HOMO} [eV]	E_{LUMO} [eV]
PNDIT-hd	10.0	2.10	325, 543	338, 605	702	1.77	1.25	-0.86	-5.96	-3.85
PNDIS-hd	22.1	2.94	341, 567	347, 608	731	1.70	1.24	-0.84	-5.95	-3.87

[a]Solution. [b]Thin-film. [c]$E_g{}^{opt} = 1240/\lambda_{onset}$.

The thin-film optical absorption spectra of the acceptor polymers, PNDIT-hd and PNDIS-hd, are shown in **Figure 3.1**b while those in dilute (10^{-6} M) chlorobenzene solutions are shown in Figure S3.10. The absorption spectra are similar to previous reports,[39, 114] with both PNDIT-hd and PNDIS-hd showing two characteristic absorption peaks, one centered at 320-350 nm attributed to the π-π* transition and the other at 540-610 nm due to intramolecular charge transfer (ICT).[99-100] In both dilute solution and thin film, PNDIS-hd exhibits a broader absorption band than PNDIT-hd in agreement with previous reports[39, 114] that showed that selenophene substitution for thiophene ring can slightly enhance light-harvesting. The bandgap (E_g) derived from the thin-film optical absorption edge was 1.77 eV for PNDIT-hd and 1.70 eV for PNDIS-hd. (**Table 3.1**)

The HOMO/LUMO energy levels of the acceptor polymers were determined from cyclic voltammetry (CV) experiments (**Figure S3.11**) and relevant data are listed in **Table 3.1**. The HOMO/LUMO values observed, -5.96/-3.85 eV for PNDIT-hd and -5.95/-3.87 eV for PNDIS-hd, are essentially identical, which suggests that selenophene substitution for thiophene in the NDI-arylene copolymer backbone does not significantly modify the electronic structure. We note that this result is very different from comparison between NDI-arylene copolymers containing biselenophene and bithiophene, where large differences in electronic structure, optical bandgap

and electron mobility were observed due to enhanced intramolecular charge transfer effects in favor of the NDI-biselenophene copolymer.[25, 108]

The thin-film absorption spectrum and the HOMO/LUMO energy levels for the donor polymer PBDB-T are also shown in **Figure 3.1**. Although the optical bandgap (E_g^{opt}) of PBDB-T (~1.8 eV)[59-60] is slightly larger than those of the acceptor polymers, there is a large spectral overlap between PBDB-T and both acceptor polymers (**Figure 3.1**b). The lack of complimentary absorption among PBDB-T and PNDIT-hd or PNDIS-hd means that their binary blends are not ideal for the broader coverage of solar light harvesting. Furthermore, the absorption coefficient of PBDB-T (1.78×10^5 cm^{-1}) is much higher than that of either PNDIT-hd (0.58×10^5 cm^{-1}) and PNDIS-hd (0.5×10^5 cm^{-1}). The HOMO/LUMO energy levels for PBDB-T are -5.33/-2.92 eV.[60] Thus, the offset of the HOMO levels (ΔHOMO) in the PBDB-T:PNDIT-hd and PBDB-T:PNDIS-hd binary blends is 0.93-0.95 eV, and the offset of the LUMO levels (ΔLUMO) is 0.62-0.63 eV (**Figure 3.1**c), ensuring sufficiently large driving forces for efficient electron and hole transfer processes and overall charge separation.[115]

Table 3.2. Summary of Photovoltaic Properties of PNDIT-hd:PBDB-T and PNDIS-hd:PBDB-T Blends

Blend	DPE	J_{sc} (mA/cm^2)	V_{oc} (V)	FF	PCE_{max} (PCE_{avg}[c]) (%)	EQE_{max}(%)	Int J_{sc} (mA/cm^2)
PNDIT-hd[a]	-	11.45	0.83	0.68	6.52 (6.35±0.14)	70.0	11.16
PNDIT-hd[a]	1%	12.18	0.83	0.66	6.74 (6.46±0.14)	72.9	11.57
PNDIS-hd[b]	-	14.29	0.82	0.68	8.01 (7.72±0.26)	83.2	13.71
PNDIS-hd[b]	0.5%	14.50	0.82	0.71	8.36 (8.05±0.19)	85.7	14.22

[a] Annealed at 155 °C for 10 min. [b] Annealed at 135 °C for 10 min. [c] Average of over 10 devices.

3.3.2 *Photovoltaic Properties.*

We fabricated and evaluated all-polymer solar cells (all-PSCs) with an inverted device structure: ITO/ZnO(PEI)/blend/MoO_3 (0.5 nm)/Ag (100 nm) as depicted in Figure 1a. The blend composition in terms of the donor:acceptor (D:A) ratio and the active layer processing conditions, including the concentration of any processing additive, film thickness, annealing temperature and duration of annealing, were varied and optimized to achieve the best performance for each blend system (**Table S3.5**, **Table S3.6**, **Table S3.7**)The optimal D:A ratio was found to be 1:1.25 for both PBDB-T:PNDIT-hd and PBDB-T:PNDIS-hd bends. The optimal annealing temperatures were 155 °C for PBDB-T:PNDIT-hd and 135 °C for PBDB-T:PNDIS-hd and the optimal thicknesses were found to be 90-100 nm. The photovoltaic device parameters of the optimized all-PSCs under different processing conditions are summarized in **Table 3.2**. The optimized PNDIT-hd:PBDB-T all-PSCs, fabricated without using any processing additive, achieved a maximum PCE of 6.52% with J_{sc} = 11.45 mA/cm^2, V_{oc} = 0.83 V and a high FF of 0.68. The similarly fabricated PNDIS-hd:PBDB-T blend all-PSCs afforded a much higher efficiency of 8.01% PCE with J_{sc} = 14.29 mA/cm^2, V_{oc} = 0.82 V an equally high FF of 0.68. The similarity of the V_{oc} of both PNDIS-hd and PNDIT-hd all-PSCs is in excellent agreement with their identical electronic structures or HOMO/LUMO energy levels. It is clear that the primary effect of the selenophene substitution on the photovoltaic properties is the substantial enhancement in photocurrent and thus efficiency of PNDIS-hd blends, since both the photovoltage and fill factor are identical in both PNDIT-hd and PNDIS-hd blend devices. The origin of the large difference in photocurrent is not obvious given that both PNDIT-hd and PNDIS-hd have very similar optical absorption bands and thus light-harvesting properties; we will seek to elucidate the origin of this difference through studies of blend photophysics, blend morphology, and charge transport in active layers as discussed below.

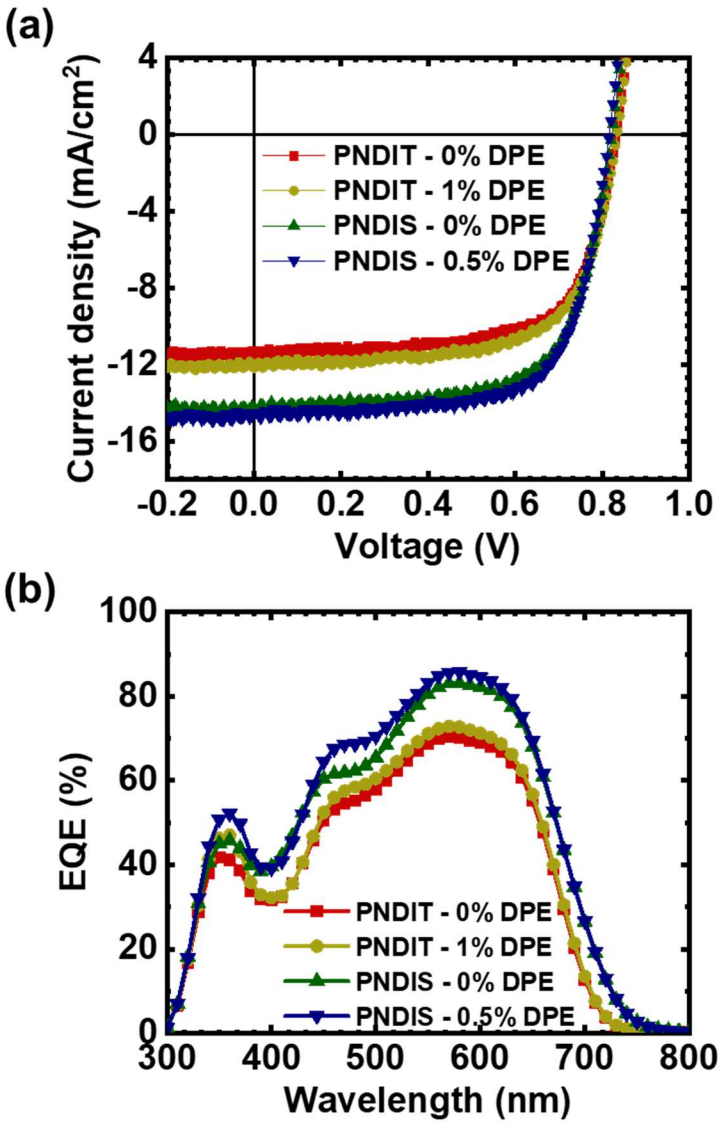

Figure 3.2. Current density-voltage (*J-V*) curves (a) and external quantum efficiency (EQE) profiles (b) for PNDIT-hd:PBDB-T and PNDIS-hd:PBDB-T all-PSCs fabricated without and with DPE processing additive.

The addition of an optimal amount of a processing additive, diphenyl ether (DPE), during the solution processing of the active layers in the all-PSCs was explored as a way to further improve the performance of each binary blend system. The current density -voltage (*J-V*) curves of PBDB-T:PNDIT-hd and PBDB-T:PNDIS-hd all-PSCs fabricated by means of a DPE-processing additive are presented in **Figure 3.2**a and the photovoltaic parameters are summarized in **Table 3.2**.PNDIT-hd: PBDB-T blends processed with an optimum 1% (v/v) DPE additive showed the best PCE of 6.74% with a J_{sc} = 12.18 mA/cm^2, V_{oc} = 0.83 V and FF = 0.66. Compared to the corresponding PNDIT-hd: PBDB-T blends processed without an additive, there is only a marginal improvement in performance due to a small increase in J_{sc}, a small decrease in FF and a constant V_{oc}. We found that the addition of an optimum 0.5%(v/v) DPE processing additive during the fabrication of PNDIS-hd:PBDB-T all-PSCs similarly resulted in only marginal improvement in efficiency to 8.36% PCE with J_{sc} = 14.50 mA/cm^2, V_{oc} = 0.82 V and FF = 0.71 relative to devices processed without an additive. Here too, the photovoltage was unchanged but small increases in J_{sc} and fill factor account for the observed increase in overall efficiency. Overall, these results clearly show that all-PSCs based on blends of the selenophene-containing acceptor PNDIS-hd are far superior to those based on similar blends of the thiophene-containing acceptor polymer PNDIT-hd, with or without the use of a processing additive in the fabrication of the active layers.

Figure 3.2b shows the external quantum efficiency (EQE) spectra corresponding to the optimal all-PSCs devices whose current density-voltage (*J-V*) curves are plotted in **Figure 3.2**a. The photoresponse of the PNDIT-hd:PBDB-T blends turns on at ~ 740 nm and extends to 300 nm, showing a narrow EQE peak of 70-73% at 560-580 nm. The EQE value drops significantly to only ~ 40% in the 350-450 nm range. The EQE spectra of the PNDIS-hd:PBDB-T blend devices are slightly broader than those of PNDIT-hd:PBDB-T blend devices, turning on at ~750 nm. Notably,

the EQE of the PNDIS-hd based all-PSCs have maximum values (EQE_{max}) that is significantly higher at 83-86 %, with or without the use of a DPE processing additive. The much higher EQE values exhibited by the PNDIS-hd:PBDB-T blend devices at all wavelengths compared to the PNDIT-hd:PBDB-T blend devices, clearly suggest far more efficient charge generation, dissociation, and collection in the selenophene-containing blend system. We note that the integrated EQE spectra gave calculated J_{sc} values within experimental errors (< 2-5%) of those obtained directly from the current density-voltage (*J-V*) curves.

We highlight the quite high fill factors observed in the present PNDIT-hd and PNDIS-hd based all-PSCs since low fill factor (FF) has long been considered a major drawback of all-PSCs and this has been hypothesized to be largely due to non-optimal blend morphology and associated effects on poor charge generation or transport. For example, only a small number of all-PSCs have been reported with fill factors of 0.70 or higher,[97, 110, 116-121] and most of those high FF devices have been achieved via terpolymer[116, 119, 121] or ternary blend[116-117, 119-120] strategies, and largely involved the well-studied acceptor polymer, N2200. In the present PNDIT-hd:PBDB-T and PNDIS-hd:PBDB-T all-PSC devices, FF values of 0.66-0.68 were obtained without the use of a processing additive in fabricating the active layers; the FF values of the all-PSCs reach 0.68-0.71 by using a DPE processing additive. These fill factor values are the highest observed to date for all-PSCs based on either PNDIT-hd[114, 122-124] or PNDIS-hd[24, 39, 114, 123, 125-128] as the acceptor polymer. The present high fill factors achieved for PNDIT-hd:PBDB-T and PNDIS-hd:PBDB-T all-PSC devices demonstrate that FF is not determined solely by either the acceptor or the donor component, but rather by a suitable combination of both, leading to an optimal blend morphology and associated blend photophysics and charge transport and collection.

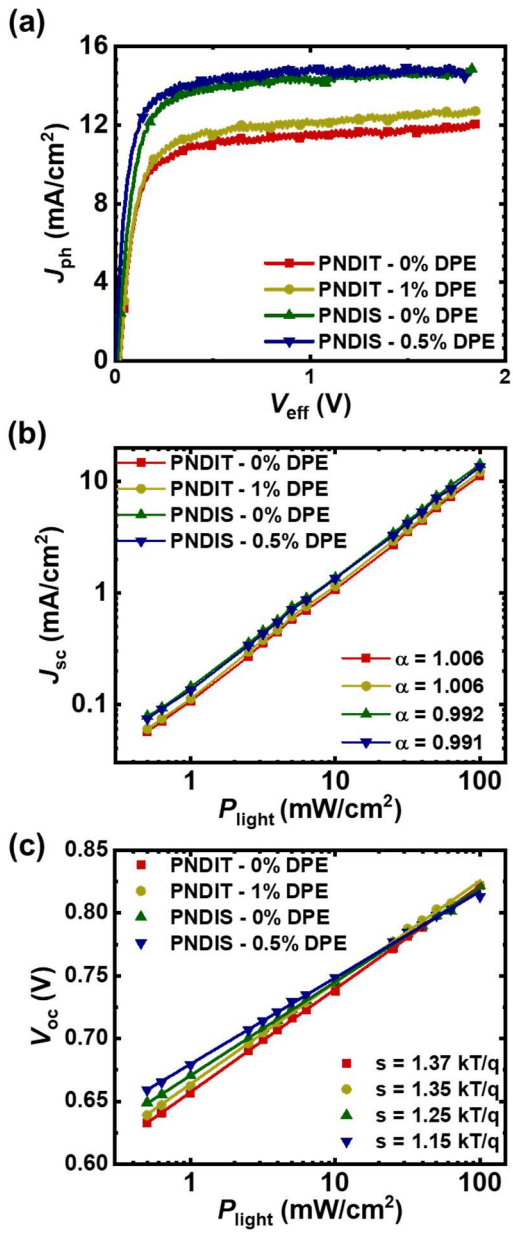

Figure 3.3. J_{ph}-V curves (a), J_{sc} versus light intensity (b), and V_{oc} versus light intensity (c) for optimized PNDIT-hd:PBDB-T and PNDIS-hd:PBDB-T blend films processed without and with DPE additive.

3.3.3 *Exciton Dissociation and Charge Collection.*

We measured the photocurrent density (J_{ph}) versus the effective voltage (V_{eff}) in order to evaluate the extent of exciton dissociation and charge collection[129-130] in the present PNDIT-hd:PBDB-T and PNDIS-hd:PBDB-T all-PSCs. **Figure 3.3**a shows a plot of $J_{ph} = J_L - J_D$, where J_L and J_D stand for current densities under illumination and in the dark, respectively, versus $V_{eff} = V_{bi} - V_{appl}$, where V_{bi} is the built-in voltage at $J_{ph} = 0$, and the V_{appl} is the applied voltage. It is seen that the J_{ph} reaches a plateau at V_{eff} of 0.5 V in all the four blend systems, indicating that free charge carriers generated in the all-PSCs are rapidly swept out. Thus, there appears to be no difference between the PNDIT-hd and PNDIS-hd devices or between those fabricated with or without the use of a processing additive.

The charge collection probability $P(E, T)$ at short-circuit condition, estimated as the ratio J_{sc}/J_{sat}, where J_{sat} the saturated J_{ph} value at high V_{eff}, was found to be generally high at 94.0% for PNDIT-hd:PBDB-T and 96.2% for PNDIS-hd:PBDB-T devices processed without the use of a processing additive. The corresponding PNDIT-hd and PNDIS-hd all-PSCs processed by using a DPE processing additive were only marginally higher with $P(E, T)$ of 94.8% and 96.5%, respectively. We conclude that the observed large difference in the photovoltaic properties of PNDIT-hd and PNDIS-hd do not originate from a significant difference in the charge dissociation and collection processes.

Table 3.3. Charge Dissociation and Recombination Parameters, Ideality Factor and Carrier Mobilities for PNDIT-hd:PBDB-T and PNDIS-hd:PBDB-T Devices.

Blend	DPE	$P(E,T)$	α	s	μ_e ($\times 10^{-5}$ $cm^2V^{-1}s^{-1}$)	μ_h ($\times 10^{-4}$ $cm^2V^{-1}s^{-1}$)	μ_h/μ_e
PNDIT-hd	-	94.0%	1.006	1.37kT/q	2.15 (1.62±0.64)	4.23 (3.74±0.33)	23.1
PNDIT-hd	1%	94.8%	1.006	1.35kT/q	3.76 (3.11±0.53)	6.46 (5.92±0.64)	19.0
PNDIS-hd	-	96.2%	0.992	1.25kT/q	2.43 (1.77±0.51)	4.98 (4.04±0.66)	22.8
PNDIS-hd	0.5%	96.5%	0.991	1.15kT/q	3.17 (3.07±0.80)	5.62 (5.20±0.48)	16.9

3.3.4 *Charge Recombination.*

The dependence of photocurrent (J_{sc}) on the incident light intensity (P_{in}) was measured to examine the bimolecular recombination within the all-PSC devices.[131] Generally, in polymer solar cells, the dependence of J_{sc} on P_{in} is expected to follow a power-law relationship: $J_{sc} \propto P_{in}^{\alpha}$, where significant deviation of the exponent from unity ($\alpha = 1$) is considered to arise from bimolecular recombination. As shown in **Figure 3.3**b and **Table 3.3**, all four all-PSCs based on PNDIT-hd and PNDIS-hd, regardless of the processing strategy, follow the power-law behavior with α values of 0.991-1.006. These results indicate that bimolecular recombination loss is negligible at short circuit condition in these all-PSCs and is thus not the limiting factor for their photovoltaic performance. We evaluated the dependence of V_{oc} on the light intensity (P_{in})[131-133] and calculated the ideality factor, $s = \frac{kT}{q}\frac{\partial V_{oc}}{\partial \ln(P_{in})}$ towards examination of monomolecular recombination as a loss mechanism in the present all-PSCs. An ideality factor of unity (s =kT/q) implies that bimolecular recombination is predominant at open circuit condition, while an s value approaching 2kT/q signifies that monomolecular or trap-assisted recombination loss dominates. From the slopes extracted from **Figure 3.3**c and presented in **Table 3.3**, we found that the ideality factor values of

PNDIS-hd devices are much closer to unity than those for PNDIT-hd devices (1.37 *kT/q* and 1.35 *kT/q*), suggesting that monomolecular or trap-assistant recombination loss is less severe in the former devices than the PNDIT-hd all-PSCs.

3.3.5 *Charge Transport Properties.*

We examined the extend that charge transport limits the performance of these PNDIT-hd and PNDIS-hd blend devices and contributes to explanation of the observed differences in photovoltaic properties by investigating single-carrier devices. The hole- and electron-only devices, analyzed by the space-charge-limited current (SCLC) method, were fabricated with the architectures: ITO/PEDOT:PSS/active layer/MoO_3/Ag (hole-only) and ITO/ZnO(PEI)/active layer/LiF/Al (electron-only), where PEDOT:PSS is the hole injection layer and ZnO(PEI) is the electron injection layer. The $J^{1/2}$-V characteristics of single-carrier devices are presented in Figure S3.12 and Figure S3.13 and the calculated carrier mobilities are summarized in **Table 3.3**.

The hole mobility (μ_h) varied from 4.2×10^{-4} $cm^2V^{-1}s^{-1}$ in the optimal PNDIT-hd:PBDB-T blend devices processed without using a processing additive to 5.0×10^{-4} $cm^2V^{-1}s^{-1}$ in the corresponding PNDIS-hd:PBDB-T devices. The use of a DPE processing additive resulted in the hole mobility improving slightly to ~ 6×10^{-4} $cm^2V^{-1}s^{-1}$ in both PNDIT-hd:PBDB-T blend devices and PNDIS-hd:PBDB-T devices. The observed hole mobility in the present all-PSC devices is comparable to other reported PBDB-T based all-PSC devices.[25, 45, 98, 134] However, the electron mobility (μ_e) varied from 2.2×10^{-5} $cm^2V^{-1}s^{-1}$ in the PNDIT-hd devices to 2.4×10^{-5} $cm^2V^{-1}s^{-1}$ in PNDIS-hd devices processed without using a processing additive. The electron mobility in devices processed by using a DPE processing additive slightly improved to 3.8×10^{-5} $cm^2V^{-1}s^{-1}$ and 3.2×10^{-5} $cm^2V^{-1}s^{-1}$ in the PNDIT-hd and PNDIS-hd devices, respectively. Among the striking features of these results include the fact that electron transport is not significantly different among the all-

PSCs based on the two different acceptor polymers. Charge transport in all the present all-PSCs is highly asymmetric with the μ_h/μ_e ratios varying from 23 in the devices fabricated without the use of a processing additive to below 17-19 in devices produced with the aid of a DPE processing additive (Table 3.3). Despite the large asymmetry in the charge transport properties of both PNDIT-hd:PBDB-T and PNDIS-hd:PBDBT blend devices, the observed high fill factors of 0.68-0.71 suggest that the all-PSCs have favorable morphology that enabled efficient charge photogeneration and collection.

We conclude that poor electron transport is an important limitation of the present all-PSC devices based on both PNDIT-hd and PNDIS-hd acceptor polymers. On the other hand, the slightly different electron mobilities in the all-PSCs based on PNDIT-hd and PNDIS-hd could not account for the observed large difference in photovoltaic properties discussed earlier.

3.3.6 *Blend Surface Morphology.*

Atomic force microscopy (AFM) imaging was used to characterize the surface morphology of the optimal PNDIT-hd:PBDB-T and PNDIS-hd:PBDB-T all-PSC devices. The height and phase images of the PNDIT-hd:PBDB-T blend films processed without and with DPE additive are presented in **Figure 3.4**a and **Figure 3.4**b, respectively. The height and phase images of the PNDIS-hd:PBDB-T blend films processed without and with DPE additive are presented in **Figure 3.4**c and **Figure 3.4**d, respectively.

The most striking feature of these images of the surface morphology of the all-PSCs is the large difference between blend films containing the two different acceptor polymers PNDIT-hd and PNDIS-hd. Blend films containing the *thiophene-linked* acceptor polymer, PNDIT-hd, generally showed a much coarser surface morphology with larger domains than those containing the *selenophene-linked* acceptor polymer, PNDIS-hd. The surface roughness as measured by the

root-mean-square (RMS) value for PNDIT-hd:PBDB-T blend films was 2.5 nm without using a processing additive and 2.1 nm for the corresponding active layers processed with aid of a DPE additive. In contrast, the RMS value for PNDIS-hd:PBDB-T blend films processed without using a processing additive was 1.5 nm, which decreases to 1.3 nm when a DPE processing additive was used in fabricating the active layer. It is also clear that the use of the DPE processing additive in processing the active layer does lead to a smaller (~13-16%) decrease in the surface roughness.

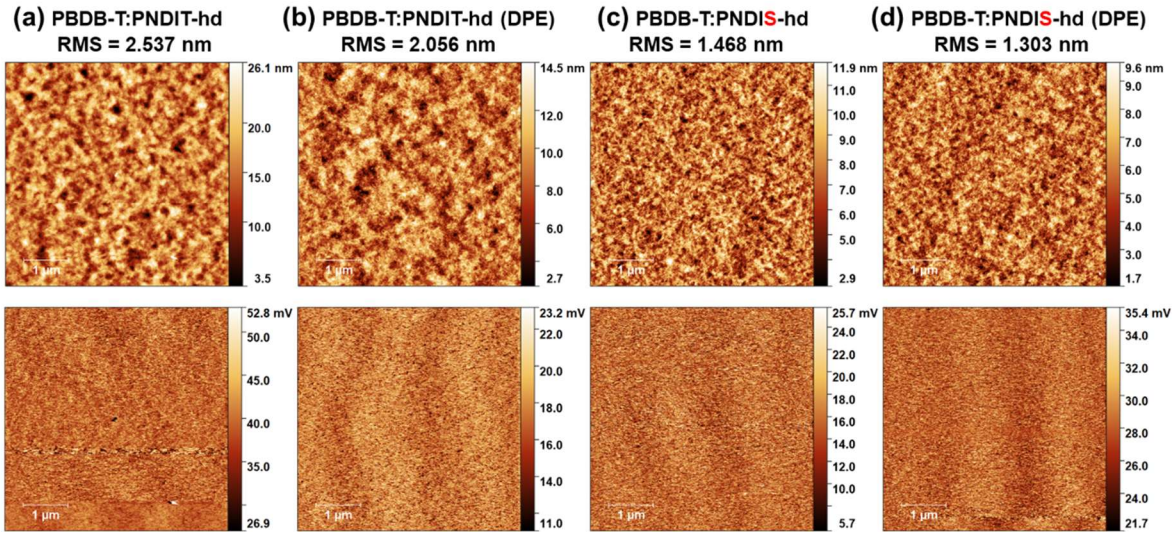

Figure 3.4. AFM height and phase images (5×5 µm) of polymer blends: (a) PBDB-T:PNDIT-hd, (b) PBDB-T:PNDIS-hd, (c) PBDB-T:PNDIT-hd processed with 1% DPE, and (d) PBDB-T:PNDIS-hd films processed with 0.5% DPE.

The surface morphology of PNDIS-hd:PBDB-T blend films processed without and with DPE additive (**Figure 3.4**c and d) show relatively uniform fine scale features across the whole surface area, indicating good intermixing between the donor and acceptor polymers with no obvious large scale phase separation. In the case of PNDIT-hd:PBDB-T blend films processed with DPE additive

(**Figure 3.4**b), some fibril-like patterns are visible whereas apparent larger scale phase-separated microstructure is seen in the corresponding blend films processed without DPE additive (**Figure 3.4**a). The fine scale microstructures observed in the surface morphology of PNDIS-hd:PBDB-T blend films are consistent with the enhanced photovoltaic properties compared to PNDIT-hd:PBDB-T blend films. We conclude that the molecular-level substitution of selenophene for thiophene in the polymer backbone when going from PNDIT-hd to PNDIS-hd has resulted in a significant and beneficial change in the blend film surface morphology than what could be achieved by the use of a processing additive.

3.3.7 *Bulk Blend Morphology.*

We used grazing-incidence wide-angle X-ray scattering (GIWAXS) measurements to characterize the thin-film microstructures of the two pristine acceptor polymers, PNDIT-hd and PNDIS-hd, and their binary blends with the donor polymer, PBDB-T. The GIWAXS investigation was focused on the pristine and blend thin films processed under the conditions used in fabricating the optimal all-PSCs *without* the use of a processing additive; as discussed earlier, only marginal changes in the blend photophysics, charge photogeneration and recombination dynamics, and photovoltaic properties were observed by using a DPE processing additive in fabricating devices. The 2D-GIWAXS images and the corresponding line cuts for the neat acceptor polymer films are presented in **Figure 3.5**. A schematic illustration of the molecular packing of PNDIT-hd and PNDIS-hd, and the relevant *d*-spacings, is shown in Figure S3.14. The peak positions, *d*-spacings, and the crystalline coherence length (L_c) for the neat polymer films are summarized in **Table 3.4**. The 2D-GIWAXS images and the corresponding line cuts for the neat donor polymer film and the photovoltaic blend films are shown in **Figure 3.6**.

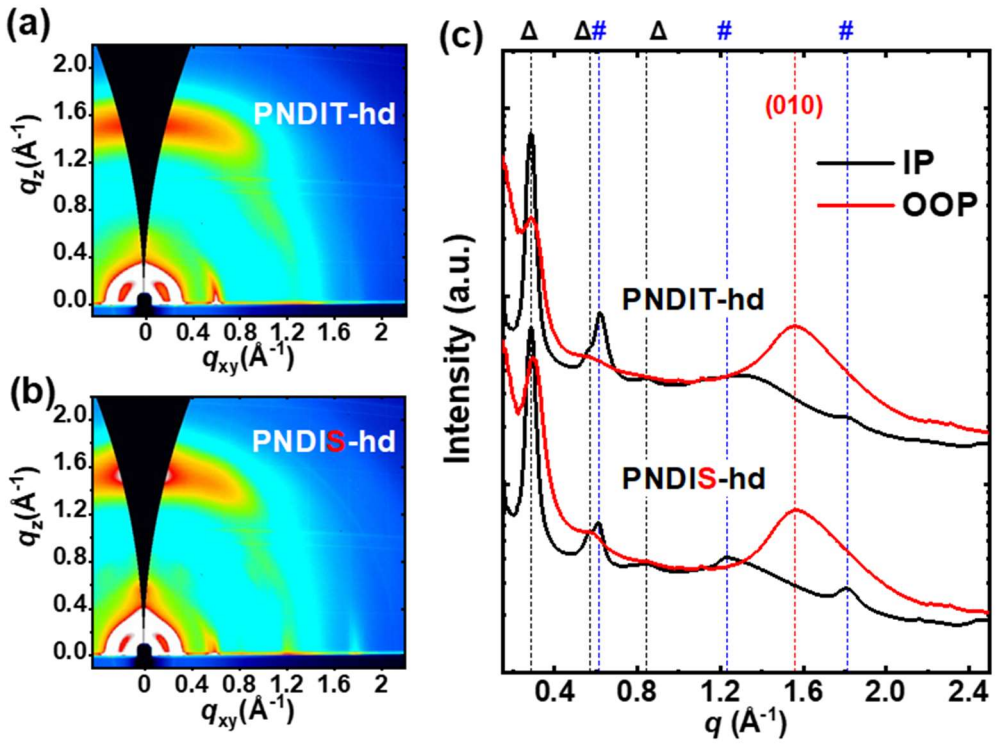

Figure 3.5. 2D GIWAXS characterization of pristine acceptor polymer thin films: (a) 2D GIWAXS pattern of PNDIT-hd; (b) 2D GIWAXS pattern of PNDIS-hd; and (c) line-cut profiles for pristine films of PNDIT-hd and PNDIS-hd. "Δ" denotes the in-plane lamellar diffraction peaks (100) (200) (300), "#" denotes the (001), (002) and (003) diffraction peaks of the backbone ordering.

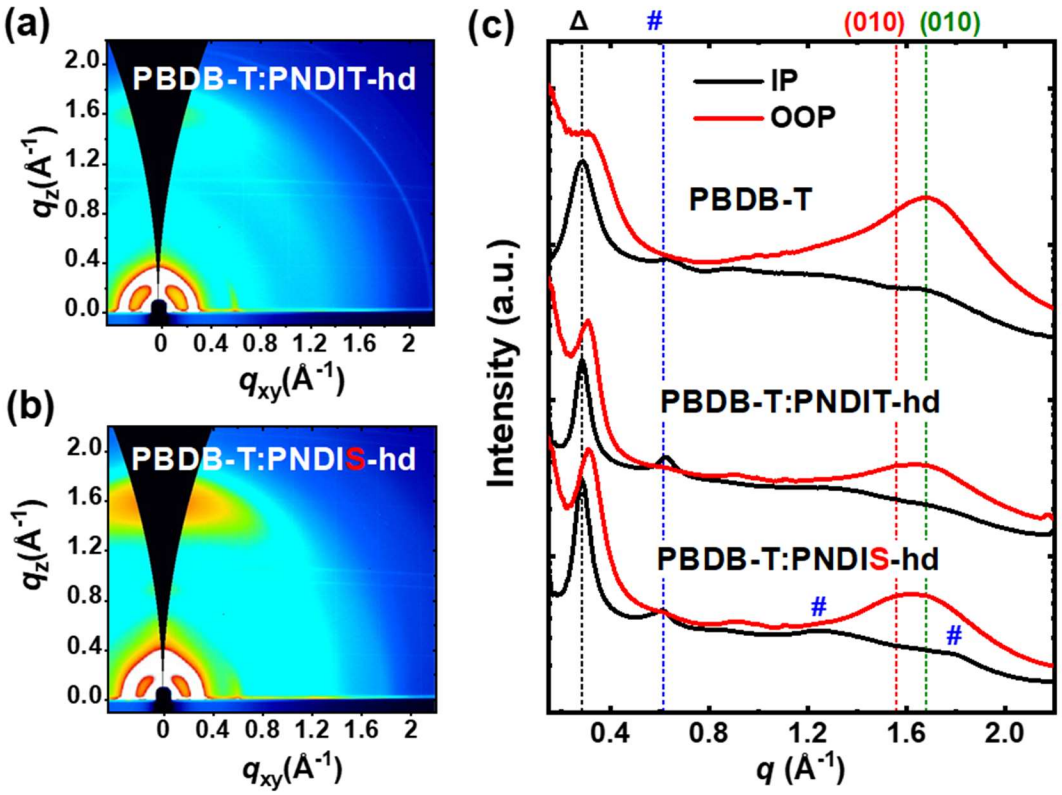

Figure 3.6. 2D GIWAXS characterizations of polymer blend thin films: (a) 2D GIWAXS image for PBDB-T:PNDIT-hd blend, (b) 2D GIWAXS image for PBDB-T:PNDIS-hd blend, and (c) line-cut profiles for pristine PBDB-T and its blends with PNDIT-hd and PNDIS-hd, respectively. "Δ" denotes the in-plane lamellar diffraction peak (100), and "#" denotes the diffraction peaks for the backbone ordering (001). The π-π stacking peak (010) positions from PBDB-T and PNDIT-hd and PNDIS-hd are also marked.

Table 3.4. Summary of In-plane (IP) and Out-of-plane (OOP) Peaks from 2D GIWAXS Data on Polymer and Blend Thin Films

Polymer	IP (100)			OOP (010)		
	q_{xy} (Å^{-1})	*d*-spacing (Å)	L_c (nm)	q_z (Å^{-1})	*d*-spacing (Å)	L_c (nm)
PBDB-T	0.290	21.69	7.01	1.68	3.74	1.47
PNDIT-hd	0.285	22.05	14.68	1.57	4.00	1.13
PNDIS-hd	0.288	21.85	17.31	1.59	3.94	1.60
PNDIT-hd: PBDB-T	0.287	21.91	10.94	1.63	3.86	1.40
PNDIS-hd: PBDB-T	0.286	21.96	11.26	1.62	3.87	1.38

Neat films of both PNDIT-hd and PNDIS-hd exhibit intense (100) diffraction peaks in the in-plane (IP) direction (q_{xy} = 0.285 – 0.290 Å^{-1}), corresponding to *d*-spacing values of 21.7 – 22.1 Å (**Table 3.4**). The comparable lamellar stacking distance observed in PNDIT-hd and PNDIS-hd is consistent with their similar molecular structures. Higher order in-plane diffraction peaks (200) (q_{xy} = 0.56 Å^{-1}) and (300) (q_{xy} = 0.84 Å^{-1}) were also observed in both neat PNDIT-hd and PNDIS-hd films (Figure 5c), suggesting the highly crystalline and well-ordered nature of the acceptor polymer chains.[135] Additionally, the (001) diffraction peaks in the IP direction were present in both acceptor polymer films at q_{xy} of 0.61-0.62 Å^{-1}, which suggest strong ordering along the polymer backbone directions. The *d*-spacing values for the IP (001) peaks are found to be 10.13 Å and 10.30 Å for PNDIT-hd and PNDIS-hd, respectively, where the larger *d*-spacing of PNDIS-hd can be explained by the slightly larger molecular width of the selenophene ring relative to the thiophene ring.

In the out-of-plane (OOP) direction, the neat PNDIT-hd and PNDIS-hd films showed pronounced and broad (010) diffraction peaks with comparable intensity at q_z of 1.57 Å^{-1} and 1.59

$Å^{-1}$ corresponding to a π-π stacking distance of 4.00 Å and 3.94 Å (**Table 3.4**), respectively. Compared to PNDIT-hd, PNDIS-hd exhibited a much more intense (100) diffraction peak in the OOP direction (Figure S3.15). Thus, the co-existence of the pronounced IP (100) peak and the distinct OOP (100) and (010) peaks in the PNDIS-hd films suggest that PNDIS-hd had mixed *face-on* and *edge-on* oriented crystallites, whereas PNDIT-hd showed preferentially *face-on* molecular orientations. The crystalline coherence length (L_c) values estimated by using the Scherrer equation[136] are presented in **Table 3.4**. The L_c values of PNDIS-hd calculated from the IP (100) and OOP (010) peaks were found to be higher than those of PNDIT-hd (**Table 3.4**), indicating that PNDIS-hd has enhanced crystallinity in both the lamellar and π-π stacking directions.

As shown in Figure 3.6c, the neat donor polymer PBDB-T films exhibit intense (100) diffraction and (010) diffraction peaks in the IP and OOP directions at q_{xy} of 0.29 $Å^{-1}$ and q_z of 1.68 $Å^{-1}$, respectively, suggesting that PBDB-T exhibited predominantly *face-on* orientated crystallites. The L_c of neat PBDB-T films was found to be 7.01 nm (**Table 3.4**). The 2D-GIWAXS results for the donor polymer PBDB-T agree well with previous reports.[25, 134]

The (010) diffraction peaks in the OOP directions of both blend films are broadened and centered at q_z values that lied between the q_z of the donor and acceptor polymers (**Table 3.4**), which indicates that there is intimate mixing between the donor and acceptor polymers. As shown in Figure 3.6b, distinct and bright OOP (010) diffraction patterns are present in the PNDIS-hd:PBDB-T blends, whereas the PNDIT-hd:PBDB-T blends showed minimal diffraction patterns in the OOP direction (Figure 3.6a). This result argues that the populations of *face-on* oriented crystallites are significantly higher in the PNDIS-hd:PBDB-T blends. The PNDIT-hd:PBDB-T blends were also found to exhibit increased populations of *edge-on* oriented crystallites compared to either of the neat component polymers as evidenced by the enhanced intensity of the (100)

diffraction peak in the OOP direction (Figure S3.16). The co-existence of *face-on* and *edge-on* oriented crystallites in PNDIT-hd:PBDB-T blends could justify the poorer photovoltaic properties as discussed above. The larger L_c value of the PNDIS-hd:PBDB-T blend films (L_c = 11.26 nm) suggest enhanced crystallinity compared to that of the thiophene-containing blend counterparts (L_c = 10.94 nm). Overall, these 2D-GIWAXS results and analysis collectively demonstrate that compared to the PNDIT-hd blend counterparts, PNDIS-hd:PBDB-T blends have a more optimal blend morphology that features predominantly *face-on* oriented crystallites with enhanced blend crystallinity; thus, corroborating the observed enhanced photovoltaic properties.

3.4 CONCLUSIONS

In summary, we have used the alternating naphthalene diimide-*thiophene* copolymer, PNDIT-hd, and naphthalene diimide-*selenophene* copolymer, PNDIS-hd, to investigate the effects of the donor moiety substitution on the intrinsic and photovoltaic blend properties of n-type semiconducting copolymers with simple donor-acceptor structure. Although both PNDIT-hd and PNDIS-hd have identical electrochemically derived HOMO/LUMO energy levels, we have found that the latter acceptor polymer has a broadened optical absorption with an optical bandgap of 1.70 eV, which is 0.07 eV narrower relative to PNDIT-hd. In binary blends with the donor polymer PBDB-T, the selenophene-containing acceptor polymer PNDIS-hd enabled all-PSCs with significantly enhanced photocurrent, external quantum efficiency (EQE) and overall photovoltaic power conversion efficiency compared to the thiophene-containing acceptor polymer. PNDIT-hd:PBDB-T based all-PSCs could thus achieve a PCE of 6.7% (J_{sc} = 12.18 mA/cm^2, FF = 0.66) whereas the corresponding PNDIS-hd:PBDB-T devices showed a higher PCE of 8.4% (J_{sc} = 14.50 mA/cm^2, FF = 0.71). The observed enhanced photovoltaic properties of the selenophene-containing polymer PNDIS-hd could largely be accounted for by its improved light harvesting,

formation of optimal blend morphology as evidenced by the 2D GIWAXS results, and reduced monomolecular recombination losses, compared to its thiophene counterpart, PNDIT-hd. These results demonstrate the many advantages in selenophene substitution for thiophene in the design of n-type semiconducting polymers with donor-acceptor architectures for applications in all-polymer solar cells.

3.5 SUPPORTING INFORMATION

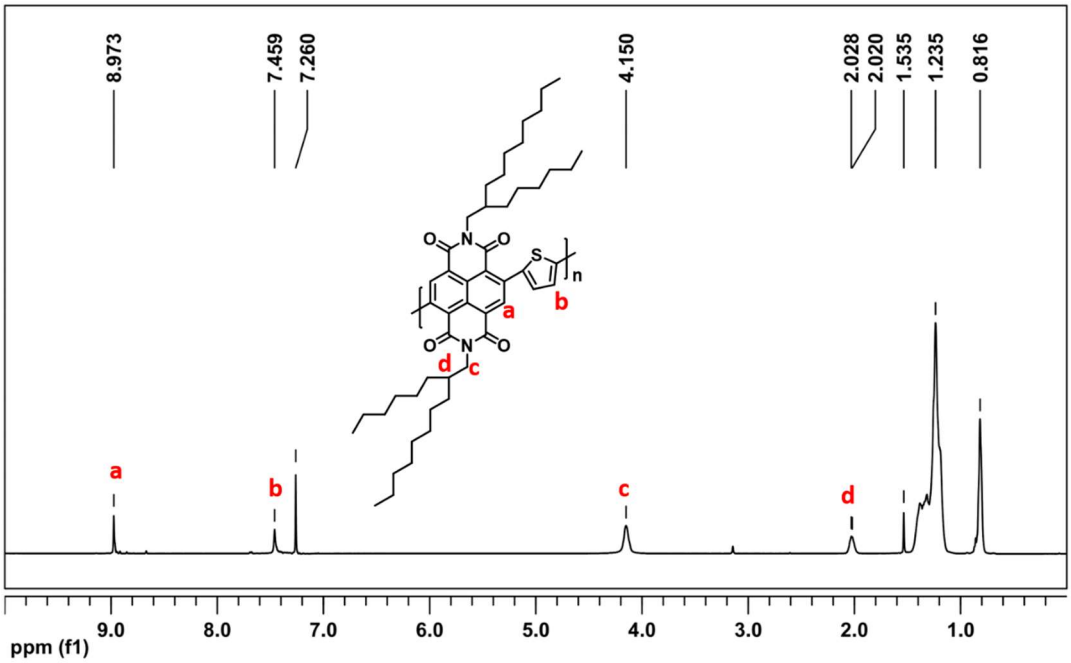

Figure S3.7. ^{1}H NMR (500 MHz, 298 K, CDCl3) spectrum of PNDIT-hd.

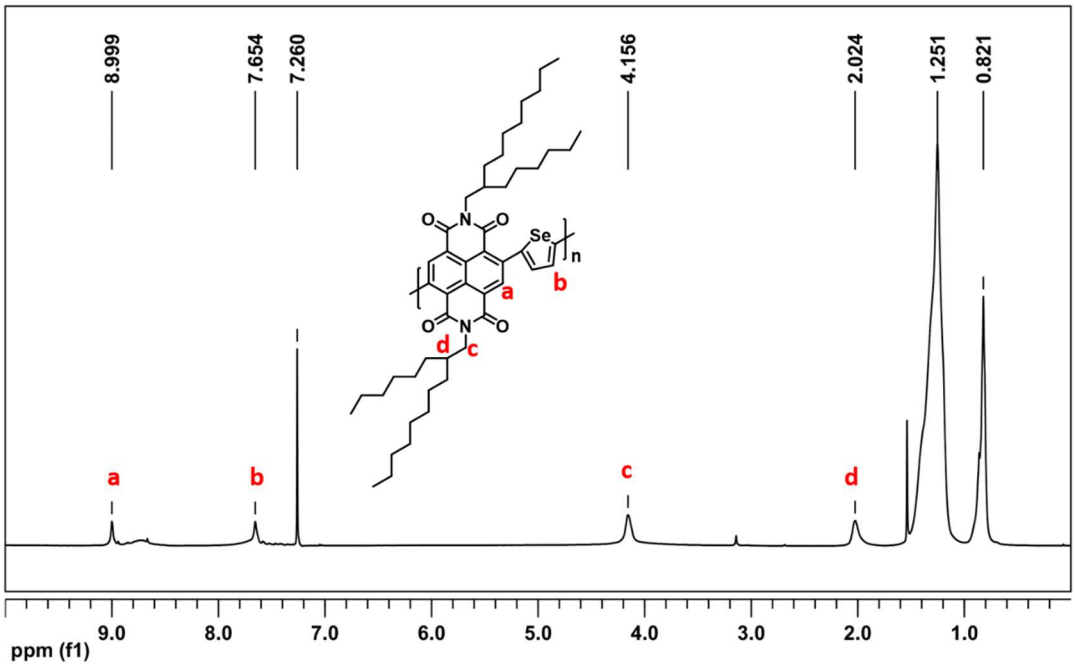

Figure S3.8. [1]H NMR (500 MHz, 298 K, CDCl3) spectrum of PNDIS-hd.

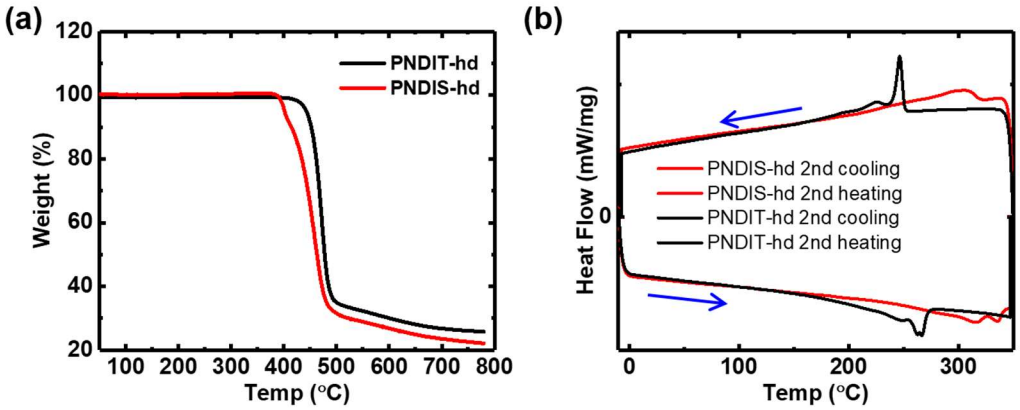

Figure S3.9. TGA thermograms (a) and DSC traces (b) of PNDIT-hd and PNDIS-hd under flowing N_2.

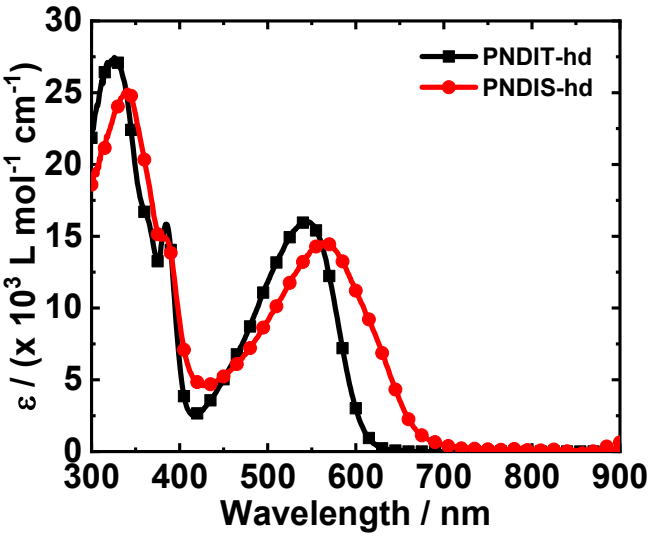

Figure S3.10. Optical absorption spectra of PNDIT-hd and PNDIS-hd in dilute chlorobenzene solutions (10^{-6} M).

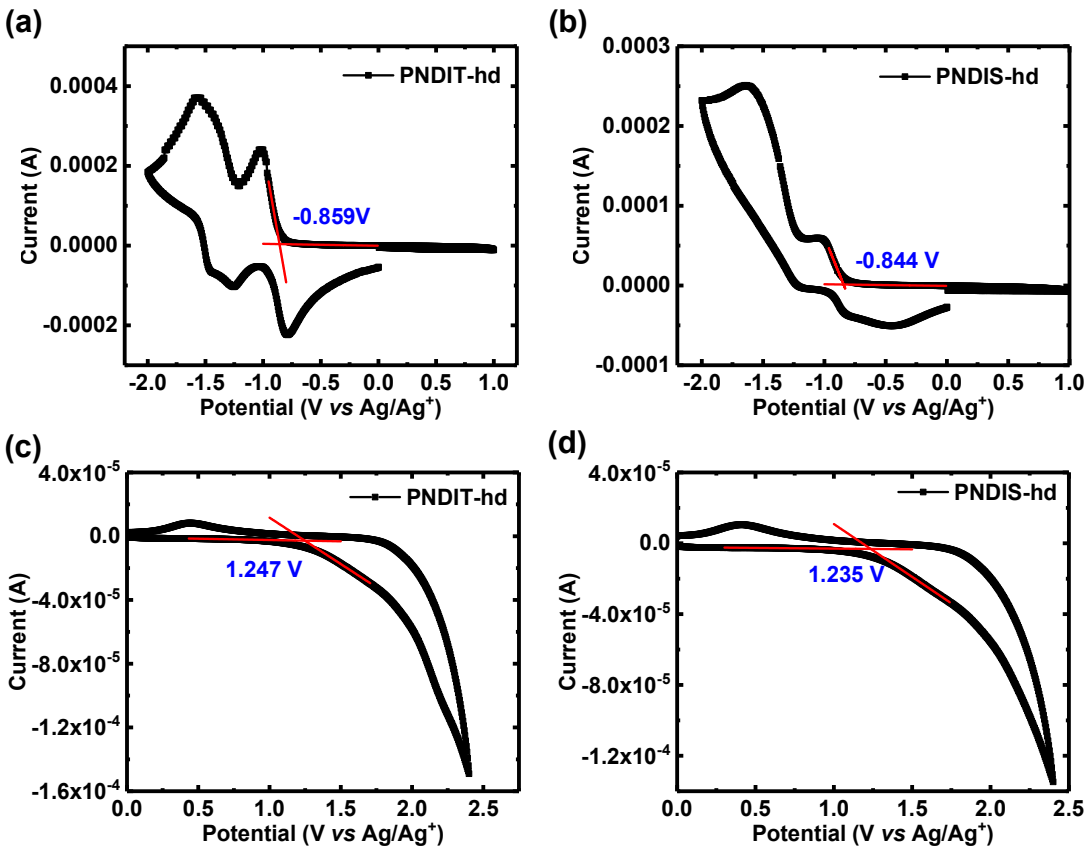

Figure S3.11. Cyclic voltammograms of PNDIT-hd and PNDIS-hd thin films: (a) (b) reduction; (c) (d) oxidation.

Table S3.5. Summary of Photovoltaic Properties of PBDB-T:PNDIT(S)-hd Blends at Various Donor Polymer/Acceptor Polymer (D/A) Ratios.

Polymer[a]	D/A	J_{sc} (mA/cm^2)	V_{oc} (V)	FF	PCE_{max} (PCE_{avg}[b]) (%)
PNDIT-hd	1:0.8	10.22	0.85	0.61	5.25 (5.11±0.12)
	1:1	10.04	0.85	0.65	5.53 (5.30±0.16)
	1:1.25	10.12	0.84	0.64	5.45 (5.35±0.09)
	1:1.5	9.97	0.84	0.65	5.44 (5.22±0.19)
PNDIS-hd	1:0.8	13.69	0.82	0.60	6.67 (6.44±0.18)
	1:1	14.14	0.81	0.59	6.68 (6.57±0.17)
	1:1.25	14.54	0.82	0.62	7.39 (7.18±0.15)
	1:1.5	14.37	0.82	0.61	7.10 (7.03±0.06)

[a] Annealed at 175 °C for 10 min. [b]Average of 4 devices.

Table S3.6. Summary of Photovoltaic Properties of PBDB-T:PNDIT(S)-hd Blends (D/A = 1:1.25) at Various Annealing Temperatures.

Polymer	Temp (°C)	J_{sc} (mA/cm^2)	V_{oc} (V)	FF	PCE_{max} (PCE_{avg}[a]) (%)
PNDIT-hd	135	11.75	0.85	0.65	6.41 (6.18±0.20)
	155	11.95	0.85	0.65	6.63 (6.42±0.16)
	175	11.73	0.84	0.60	5.90 (5.79±0.08)
PNDIS-hd	135	14.27	0.83	0.66	7.78 (7.58±0.16)
	155	13.60	0.83	0.65	7.28 (6.83±0.33)
	175	13.74	0.82	0.63	7.11 (6.75±0.43)

[a]Average of 10 devices.

Table S3.7. Summary of Photovoltaic Properties of PBDB-T:PNDIT(S)-hd Blends (D/A = 1:1.25) with Various Composition of DPE Processing Additive.

Polymer	Additive	J_{sc} (mA/cm^2)	V_{oc} (V)	FF	PCE_{max} (PCE_{avg}[c]) (%)
PNDIT-hd[a]	0.5% DPE	12.22	0.84	0.65	6.72 (6.43±0.32)
	1% DPE	12.75	0.85	0.64	6.86 (6.73±0.11)
	2% DPE	11.59	0.86	0.63	6.26 (6.13±0.11)
	1% DIO	12.00	0.86	0.65	6.77 (6.48±0.22)
PNDIS-hd[b]	0.1% DPE	12.72	0.83	0.68	7.22 (7.04±0.17)
	0.5% DPE	14.20	0.84	0.67	8.00 (7.80±0.16)
	1% DPE	14.01	0.83	0.65	7.48 (7.13±0.25)
	0.5% DIO	13.22	0.85	0.68	7.69 (7.36±0.30)

[a]Annealed at 155 °C for 10 min. [b] Annealed at 135 °C for 10 min. [c] Average of 10 devices.

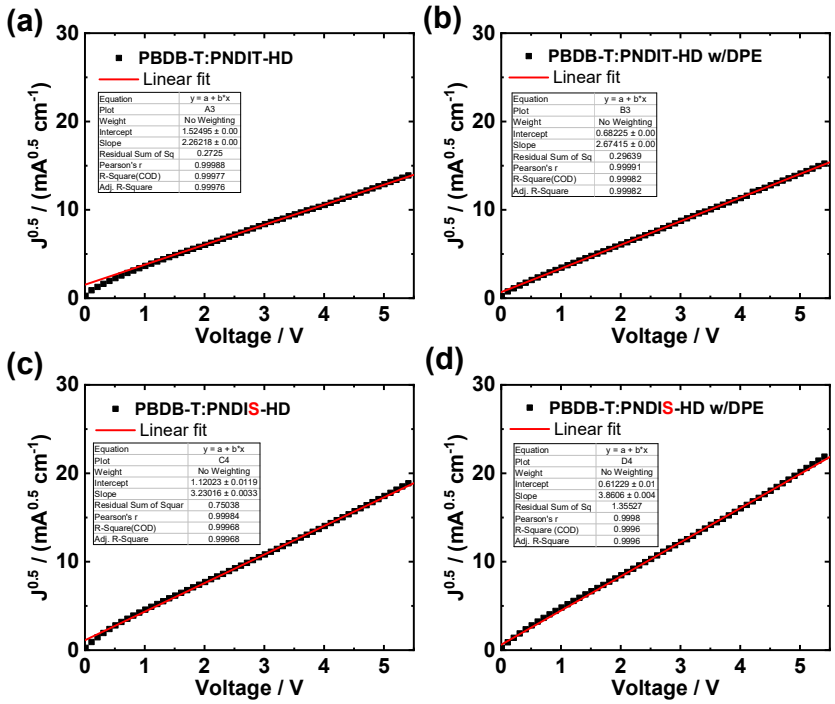

Figure S3.12. $J^{0.5}$-V plots for electron-only devices: (a)PBDB-T:PNDIT-hd, (b)PBDB-T:PNDIT-hd with 1%DPE, (c)PBDB-T:PNDIS-hd, and (d)PBDB-T:PNDIS-hd with 0.5%DPE.

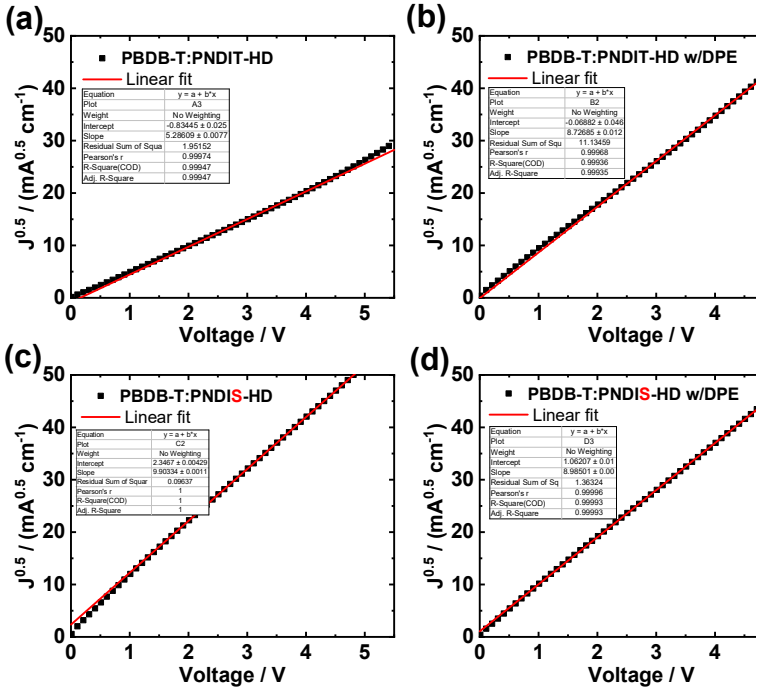

Figure S3.13. $J^{0.5}$-V plots for hole-only devices: (a)PBDB-T:PNDIT-hd, (b)PBDB-T:PNDIT-hd with 1%DPE, (c)PBDB-T:PNDIS-hd, and (d)PBDB-T:PNDIS-hd with 0.5%DPE.

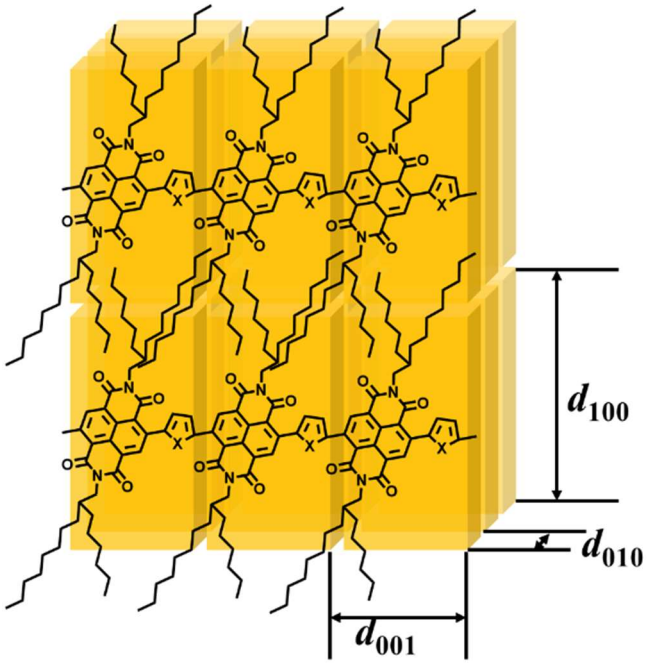

Figure S3.14. Schematic illustration of the packing characteristics of the acceptor polymers PNDIT-hd (X = T) and PNDIS-hd (X = S).

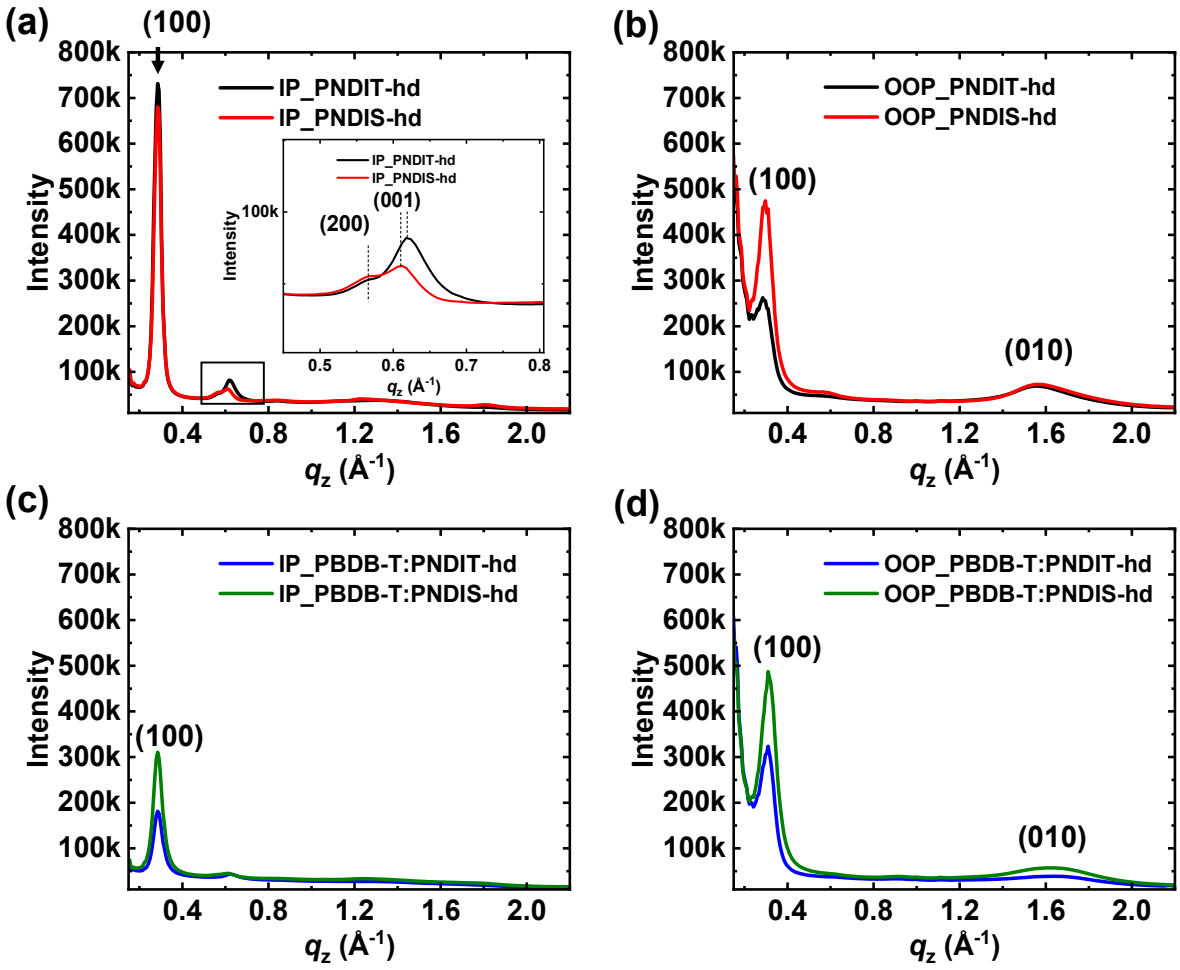

Figure S3.15. 2D-GIWAXS line-cut profiles in absolute intensities: (a) in-plane (IP) and (b) out-of-plane (OOP) for pristine films: PNDIT-hd and PNDIS-hd; and (c) in-plane (IP) and (d) out-of-plane (OOP) for blend films: PBDB-T:PNDIT-hd and PBDB-T:PNDIS-hd.

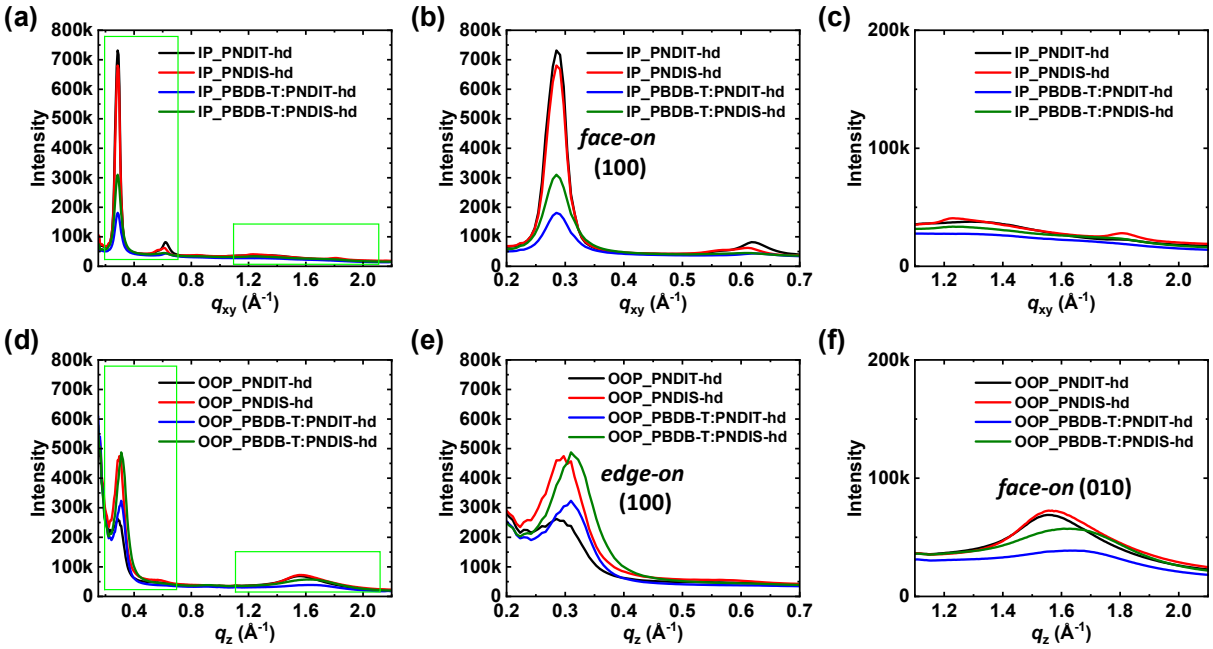

Figure S3.16. 2D-GIWAXS line-cut profiles in absolute intensities to contrast pristine films of PNDIT(S)-hd and blends of PBDB-T:PNDIT(S)-hd. (a-c) in-plane (IP) and expansions of the green area; (d-f) out-of-plane (OOP) and expansions of the green-framed area.

Chapter 4. DEVELOPMENT OF NOVEL NON-FULLENE ACCEPTORS WITH IMPROVED INTRINSIC STABILITY TOWARD FUTURE COMMERCIALLIZATION

4.1 LADDER MOLECULE ACCEPTORS FOR HIGH-PERFORMANCE ORGANIC SOLAR CELLS: DESIGN, SYNTHESIS, ENHANCED INTRINSIC STABILITY AND PHOTOVOLTAIC PROPERTIES

4.1.1 *Introduction*

Organic solar cells (OSCs) based on non-fullerene acceptors (NFAs) have made tremendous progress in the past few years.[20, 53, 137-138] Especially, the acceptor-donor-acceptor (A-D-A) small molecule acceptors (SMAs) originated from ITIC[9] have demonstrated the most noticeable success.[138] Extensive efforts have been devoted to the molecular engineering of ITIC-like derivatives, which have generated numerous plausible acceptor materials and boosted the power conversion efficiency (PCE) towards record high values of 15~18%.[68-71, 139-144] Despite the excitingly rapid progress, the *state-of-the-art* SMAs continue to revolve around the basic A-D-A structure consisted of an aromatic central core and two electron-withdrawing end groups. As illustrated in **Figure 4.1a**, these A-D-A structures were usually synthesized *via* Knoevenagel condensation between an aromatic dialdehyde building block and an active methylene compound such as 1,1-dicyanomethylene-3-indanone (DCMI), thus the resulted molecules feature the methine (=CH-) bridges connecting the donor and acceptor moieties. Recently, however, a number of studies have revealed that the current SMAs-based OSCs suffered from various degradation processes,[53] which were identified to originate from complex causes including chemical[145-147],

photo[148-150], photochemical[151-153], and morphological[154-155] instability. Taking ITIC for example, it was found out that the methine bridges in ITIC are the chemically vulnerable sites causing photocatalytic decomposition at ZnO/active layer interface.[152] In another study, ITIC derivatives were found to undergo solution-phase redistribution process between end groups (EG), i.e., EG_1-IDTT-EG_1 + EG_2-IDTT-EG_2 ⇌ 2 EG_1-IDTT-EG_2, hence high scrutiny is required when the photoactive blend is comprised of unsymmetrical structures or ternary blends with ITIC-like SMAs.[146] Therefore, as the first important step towards superior operation stability of OSCs, designing NFAs with high intrinsic stability and free of weak linkages is crucial.

Enhanced coplanarity and reduced conformational disorder have been another important pursuit in developing new NFAs. Highly coplanar structure ensures effective electronic delocalization and long effective conjugation length, which could enhance intrinsic charge transport properties. In the typical ITIC-like A-D-A structures, the methine bridges inevitably result in conformers due to rotational freedom around the single bond. Such conformational disorder would remain unresolved if the NF SMAs continue to adopt current A-D-A-type backbone architecture. In recent research, various methods have been exploited to achieve "conformation lock", such as introducing steric hinderance[156] and intramolecular noncovalent interactions[157-158] (S···O, S···F, *etc.*). It could be reasonably argued that, in order to achieve high-level coplanarity and to minimize conformational disorder, covalently fused ladder structures should be considered instead. In fact, ladder structures with fused double-stranded backbones, in the form of small molecules[159-161] and polymers[162], have been an important class of materials for application in various organic electronics, due to their unique optical, electronic and mechanical properties. Nevertheless, in the solution-processible OSCs, NF SMAs with *true* ladder structures have been extremely scarce.[163-164] Two main reasons should be taken into account: (1) there has

been lack of efficient and versatile synthetic strategy towards ring annulation; and (2) poor solubility and strong aggregation of such ladder molecules prevent formation of favorable film morphology when blended with donor polymers.

Here, we demonstrate a novel design of NF SMAs with ladder backbone to eliminate the chemically reactive and photo unstable methine bridges in the conventional A-D-A structures. As illustrated in **Figure 4.1b**, we synthesized the heretofore unreported bis(amino-aldehyde) building block, followed with Friedlander condensation with the methylene-keto-containing end groups to achieve "ladderization". It is obvious that such molecular design could be applied to a variety of central cores and end groups, thus is expected to enable high tunability in the optical absorption and electronic structures of any resulted ladder molecules. As a proof of concept, we started with the IDTT core and the DCMI end groups, also for the purpose of comparing with the well-known ITIC. A series of ladder molecule acceptors (LMAs) named as LTXs were synthesized. In these LMAs, long branched side chains, 2-hexyldecyl chains, were installed to ensure suitable solubility. Various end-groups including DCMI, its fluorinated and chlorinated derivatives were used to further tune the optical and electronic properties. The resulted LMAs were named as LTX, LTX-4F, and LTX-4Cl, respectively. (**Figure 4.1b**) The LTXs demonstrated unique dual-band optical absorption and enlarged energy bandgaps compared to their non-ladder counterpart, ITIC. The photovoltaic properties of the LTXs were investigated pairing with the widely used donor polymer PM6, yielding high PCEs of 7.2-11.5% with high V_{oc} values of 0.93-1.13 V and high fill factors of 0.63-0.75. In particular, photovoltaic devices based on PM6:LTX-4F and PM6:LTX-4Cl demonstrated superior photovoltaic performance (PCE 11.0% and 11.5%) and afforded high fill factors of 0.74-0.75. The superior performance of LTX-4F and LTX-4Cl relative to LTX was attributed to broadened optical absorption and better donor/acceptor miscibility facilitating

formation of favorable morphology. In addition, the intrinsic photochemical stability of the LTXs and the long-term operation stability of solar cell devices based on PM6:LTXs were investigated side-by-side with ITIC and corresponding devices based on PM6:ITIC. The present study is a successful attempt to address the stability issue of current mainstream non-fullerene small molecule acceptors and provides a powerful alternative synthetic strategy towards ladder molecule acceptors with high intrinsic photochemical stability as well as high photovoltaic performance.

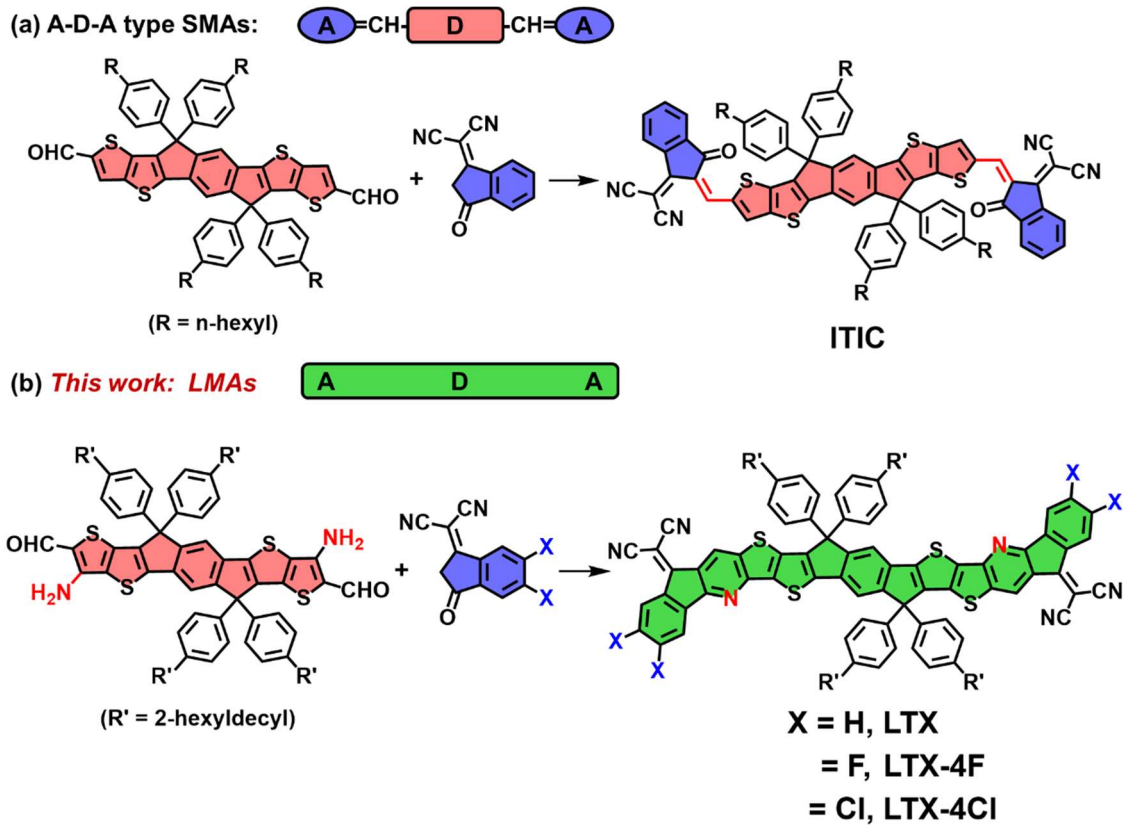

Figure 4.1. (a) Structural illustration of conventional A-D-A type SMAs, exemplified with ITIC, synthesized via Knoevenagel condensation reaction; (b) structural illustration of the ladder molecule acceptors (LMAs) introduced in this work, synthesized via Friedlander condensation reaction.

4.1.2 *Experimental Methods*

Material Synthesis and Characterization. The donor polymer PM6 and the acceptor ITIC were purchased from Solarmer, Inc. 1-bromo-4-(2-hexyldecyl)-benzene,[165] IDTT-C_6[9] and IDTT-hd[9] were synthesized according to literature procedures. Other reagents and solvents were all from commercial sources. ^{1}H NMR, ^{13}C NMR and ^{19}F NMR spectra were recorded on a Bruker DRX499 spectrometer. Mass spectrometry (MALDITOF) was performed on an Autoflex III smart beam. Thermogravimetric analysis (TGA) of the polymers was conducted on a TA Instruments model Q50 TGA at a heating rate of 10 °C/min under a flow of N_2 with scans from room temperature to 800 °C. Optical absorption spectra were obtained from a PerkinElmer Lambda 900 UV-vis/near-IR spectrophotometer.

IDTT-C_6-2Br (compound 1a). In a 250 mL round-bottom flask, IDTT (1a) (1.758g, 1.72 mmol) was dissolved in chloroform/acetic acid (50 mL/15 mL) solvent mixture. The flask was wrapped with aluminum foil to avoid light. To the stirring solution, NBS (0.629 g, 3.53 mmol, 2.05 equiv) was added in one portion. Reaction mixture was kept stirring in dark at room temperature for overnight. Resulted yellow suspension was slowly poured into water. Perform extraction with dichloromethane. The organic layer was washed with water, $NaHCO_3$ (aq) and brine. Organic fraction was then dried over Na_2SO_4, and concentrated in *vacuo*. Crude product was purifed with silica gel column, eluting with hexane/DCM (4:1 v/v). Collected product was recrystallized from DCM/MeOH, collected from filtration and further dried in vacuum oven. Yield: 1.91g, 94%, pale yellow powder. ^{1}H NMR (500 MHz, $CDCl_3$, δ): 7.52 (s, 2H), 7.27 (s, 2H), 7.17 (d, J = 6.5 Hz, 8H), 7.08 (d, J = 6.5 Hz, 8H), 2.59 (t, J = 7.8 Hz, 8H), 1.66-1.57 (m, 8H), 1.41-1.26 (br, 24H), 0.90 (t, J = 6.5 Hz, 12H). ^{13}C NMR (125 MHz, $CDCl_3$, δ): 153.23,

146.23, 142.30, 141.91, 139.92, 139.86, 135.86, 134.06, 128.53, 127.88, 122.97, 116.97, 112.49, 62.88, 35.57, 31.69, 31.24, 29.14, 22.57, 14.08. MALDI-TOF, *m*/*z*: calcd for [$C_{68}H_{72}Br_2S_4$]: 1174.288, found: 1174.427.

IDTT-hd-2Br (compound 1b). Procedures were similar to IDTT-C_6-2Br (1a). Crude product was purified with silica gel column eluting with hexane. Yield: 90%, pale yellow wax solid. ^{1}H NMR (500 MHz, $CDCl_3$, δ): 7.50 (s, 2H), 7.27 (s, 2H), 7.13 (d, *J* = 8.24 Hz, 8H), 7.05 (d, *J* = 8.25 Hz, 8H), 2.54-2.42 (m, 8H), 1.60 (d, *J* = 17.76 Hz, 4H), 1.34-1.14 (m, 96H), 0.87 (m, 24H); ^{13}C NMR (125 MHz, $CDCl_3$, δ): 153.30, 146.39, 142.28, 140.88, 139.86, 139.82, 135.89, 134.17, 129.35, 127.73, 122.94, 116.98, 112.49, 62.92, 53.40, 40.23, 39.43, 33.33, 33.31, 33.28, 33.26, 31.91, 31.86, 29.97, 29.61, 29.33, 26.59, 26.55, 26.54, 26.49, 22.69, 14.13; MALDI-TOF, *m*/*z*: calcd for [$C_{108}H_{152}Br_2S_4$]: 1734.914, found: 1735.187.

IDTT-C_6-2CHO-2Br (compound 2a). In an argon-filled 250 mL Schlenck tube, IDTT-2Br (2a) (400 mg, 1.27 mmol) was dissolved in 80 mL anhydrous THF. Solution was cooled down to -78 ºC and kept for 15 min. At -78 ºC, lithium diisopropylamide (LDA) (1M solution in THF/hexane, 2.55 mL, 5.10 mmol, 3.5 equiv) was added dropwise. Reaction mixture was first darkened, then turned greenish, and then became bright pink-red-colored. The mixture was kept at -78 ºC and allowed to gradually warm up to room temperature for overnight, and then continue to stir at room temperature for additional 12 h. Resulted yellowish brown mixture was again cooled to 0 ºC. Anhydrous DMF (1 mL, excess) was added slowly. Resulted greenish suspension was kept stirring at room temp for 2 h. Saturated NH_4Cl (aq) was added. The mixture was then extracted with dichloromethane, washed with sat. NH_4Cl (aq), brine and dried over Na_2SO_4. Crude product was purified with silica gel column eluting with hexane/DCM with increasing polarity (from 2:1 to 2:1.5 v/v), followed with precipitation into methanol. Product was then filtered and dried in

vacuum oven. Yield: 500 mg, %, lightly-greenish yellow powder. ^{1}H NMR (500 MHz, $CDCl_3$, δ): 9.96 (s, 2H), 7.65 (s, 2H), 7.12 (m, 16H), 2.57 (t, *J* = 7.8 Hz, 8H), 1.59 (m, 8H), 1.40-1.22 (br, 24H), 0.88 (t, *J* = 6.5 Hz, 12H). ^{13}C NMR (125 MHz, $CDCl_3$, δ): 182.80, 154.61, 148.88, 147.24, 143.97, 142.51, 138.86, 138.33, 136.60, 136.46, 128.82, 127.68, 118.18, 113.87, 63.34, 35.54, 31.66, 31.23, 29.09, 22.55, 14.06. MALDI-TOF, *m*/*z*: calcd for [$C_{70}H_{72}Br_2O_2S_4$]: 1230.278, found: 1230.465.

IDTT-hd-2CHO-2Br (compound 2b). Procedures similar to IDTT-C_6-2CHO-2Br (2a). Crude product was purified with silica gel column eluting with hexane/DCM (2.5:1 v/v). Collected pure fraction was concentrated and competely dried under high vacuum. Yield: 500 mg, %, yellow wax solid. ^{1}H NMR (500 MHz, $CDCl_3$, δ): 9.97 (s, 2H), 7.68 (s, 2H), 7.14 (d, *J* = 8.23 Hz, 8H), 7.09 (d, *J* = 8.28 Hz, 8H), 2.57-2.43 (m, 8H), 1.61 (s, 4H), 1.24 (m, 96H), 0.93-0.82 (m, 24H); ^{13}C NMR (125 MHz, $CDCl_3$, δ): 182.70, 154.65, 148.87, 147.31, 143.91, 141.48, 138.82, 138.38, 136.63, 136.47, 129.62, 127.52, 118.18, 113.76, 63.39, 40.17, 39.40, 33.26, 33.20, 31.89, 31.84, 29.95, 29.60, 29.30, 26.54, 26.47, 22.67, 22.64, 14.11; MALDI-TOF, *m*/*z*: calcd for [$C_{110}H_{152}Br_2O_2S_4$]: 1790.904, found: 1791.474.

IDTT-C_6-2CHO-2NH_2 (compound 5a). IDTT-C_6-2CHO-2Br (3a) (262 mg, 0.21 mmol), NaN_3 (138 mg, 2.1 mmol, 10 equiv) and a stirrer was added into a 20 mL vial. Anhydrous DMPU (4 mL) was added and vial was capped. Reaction mixture was left stirring at room temperature for 24 h. Resulted dark solution was then precipitated into 150 mL MeOH and filtered. Dark yellow solid was collected and was used for next step without further purification. Analytical sample of IDTT-C_6-2CHO-2N_3 (4a) was collected from column purification, dried in vacuum oven at room temp to remove residual solvent completely and was then used to obtain ^{1}H NMR and ^{13}C NMR spectra. IDTT-C_6-2CHO-2N_3 (4a): ^{1}H NMR (500 MHz, $CDCl_3$, δ): 9.92 (s, 2H), 7.62 (s, 2H), 7.11

(m, 16H), 2.56 (t, 8H), 1.58 (m, 8H), 1.29 (br, 24H), 0.87 (t, 12H). ^{13}C NMR (125 MHz, $CDCl_3$, δ): 180.21, 154.90, 149.01, 146.97, 142.53, 138.99, 138.69, 137.62, 136.16, 134.05, 128.80, 127.70, 118.16, 63.18, 35.54, 31.66, 31.22, 29.08, 22.55, 14.06. Crude solid IDTT-C_6-2CHO-2N_3 (4a) was redissolved in 5 mL chloroform in a vial. 40% ammonium sulfide (1 mL, excess) was added dropwise. Mixture was stirred for 30 min at room temperature until gas evolution had ceased. Perform extraction with ether, wash with brine and dry over Na_2SO_4. Crude product was purified with a short silica gel column, eluting first with hexane and then DCM and DCM with drops of MeOH. Collected pure fraction was concentrated on rotary evaporator and was recrystallized from hexane at r.t.. Product was then filtered and dried in vacuum oven. Overall yield from 3a: 180 mg, 76%, yellow solid with typical odor of amines. ^{1}H NMR (500 MHz, $CDCl_3$, δ): 9.47 (s, 2H), 7.60 (s, 2H), 7.16 (d, J = 7.64 Hz, 8H), 7.12 (d, J = 7.90 Hz, 8H), 6.29 (s, 4H), 2.58 (t, 8H), 1.60 (td, J = 15.28, 7.51 Hz, 8H), 1.32 (br, 24H), 0.88 (t, J = 6.42 Hz, 12H). ^{13}C NMR (not available due to low solubility). MALDI-TOF, m/z: calcd for [$C_{70}H_{76}N_2O_2S_4$]: 1104.479, found: 1104.577.

IDTT-hd-2CHO-2NH_2 (compound 5b). Procedures were similar to IDTT-C_6-2CHO-2NH_2 (5a). Crude product was purified with a short silica gel column, eluting first with hexane and then DCM. Collected pure fraction was concentrated on rotary evaporator and completely dried under high vacuum. Two-step yield from 3b: 75%, orange-red solid with typical odor of amines. ^{1}H NMR (500 MHz, $CDCl_3$, δ): 7.64 (s, 2H), 9.48 (s, 2H), 7.18 (d, J = 8.25 Hz, 8H), 7.11 (d, J = 8.28 Hz, 8H), 6.33 (s, 4H), 2.63-2.42 (m, 8H), 1.62 (br, 4H), 1.38-1.18 (m, 96H), 0.89 (m, 24H). ^{13}C NMR (125 MHz, $CDCl_3$, δ): 182.85, 154.62, 147.87, 147.28, 147.24, 141.22, 139.76, 139.03, 136.19, 130.99, 129.40, 127.72, 117.80, 114.21, 63.18, 40.18, 39.39, 33.28, 33.22, 33.21,

31.87, 31.82, 29.94, 29.57, 29.29, 26.54, 26.51, 26.48, 26.44, 22.65, 22.63, 14.09; MALDI-TOF, *m*/*z*: calcd for [$C_{110}H_{156}N_2O_2S_4$]: 1665.105, found: 1665.569.

General Procedures for Friedlander Condensation Reactions. In a round bottom flask, bis(amino-aldehyde) (1 equiv) was dissolved into anhydrous toluene and purged with Argon for 20 min. On the side, DCMI end group (5 equiv) and diphenyl phosphate (20 equiv) was dissolved in anhydrous toluene in an argon-filled Schlenck tube. The bis(amino-aldehyde)/toluene solution was then slowly transfered into Schlenck tube via syringe/needle or cannula. Reaction mixture was heated to 90-100 °C and kept stirring for 24 h. After cooling to room temperature, remove toluene under high vacuum. Crude product was redissolved with chloroform, absorbed onto silica gel and loaded onto silica gel column. Product was then purified eluting with hexane:DCM (2.5:1), followed with preparative TLC plates. Collected pure fraction was concentrated and recrystallized with CF/MeOH bilayer method. Pure solid product was then filtered and dried in vacuum oven.

LTX-C_6 (compound 6a). Yield: 80 mg, 30%, dark solid. ^{1}H NMR (500 MHz, $CDCl_3$), δ: 8.91 (s, 2H; Ar H), 8.42 (d, *J* = 7.76 Hz, 2H; Ar H), 8.02 (d, *J* = 7.40 Hz, 2H; Ar H), 7.71 (s, 2H; Ar H), 7.60 (t, *J* = 7.47 Hz, 2H; Ar H), 7.44 (t, *J* = 7.60 Hz, 2H; Ar H), 7.23 (d, *J* = 8.30 Hz, 8H; Ar H), 7.15 (d, *J* = 8.31 Hz, 8H; Ar H), 2.59 (t, 8H; CH), 1.60 (td, *J* = 15.42, 7.58 Hz, 8H; CH_2), 1.41-1.22 (br, 24H), 0.86 (t, *J* = 6.73 Hz, 12H; CH_3). ^{13}C NMR (not available due to low solubility). MALDI-TOF, *m*/*z*: calcd for [$C_{94}H_{80}N_6S_4$]: 1420.533, found: 1420.836.

LTX (compound 6b). Yield: 117 mg, 32%, dark solid. ^{1}H NMR (500 MHz, $CDCl_3$), δ: 8.91 (s, 2H), 8.42 (d, *J* = 7.78 Hz, 2H), 8.02 (d, *J* = 7.36 Hz, 2H), 7.72 (s, 2H), 7.61 (t, *J* = 7.48 Hz, 2H), 7.45 (dt, *J* = 7.71, 1.03 Hz, 2H), 7.22 (d, *J* = 8.32 Hz, 8H), 7.11 (d, *J* = 8.36 Hz, 8H), 2.50 (d, *J* = 6.76 Hz, 8H), 1.65-1.55 (m, 4H), 1.19 (m, 96H), 0.84 (m, 24H); ^{13}C NMR (125 MHz, $CDCl_3$, δ): 159.68, 158.33, 154.89, 152.14, 149.27, 147.82, 141.49, 140.50, 139.51, 139.10,

137.52, 136.71, 135.37, 135.10, 134.66, 130.94, 129.60, 128.49, 127.78, 126.14, 123.43, 121.81, 118.22, 113.44, 113.17, 74.55, 63.25, 40.23, 39.46, 33.32, 33.28, 33.25, 33.22, 31.9, 31.8, 29.97, 29.60, 29.30, 26.57, 26.55, 26.49, 22.66, 22.64, 14.09; MALDI-TOF, *m*/*z*: calcd for [$C_{134}H_{160}N_6S_4$]: 1981.159, found: 1981.673.

LTX-4F (compound 7b). Yield: 120 mg, 31%, dark solid. ^{1}H NMR (500 MHz, $CDCl_3$, δ): 8.89 (s, 2H), 8.32-8.26 (m, 2H), 7.83 (m, 2H), 7.73 (s, 2H), 7.11 (d, *J* = 8.33 Hz, 8H), 7.20 (d, *J* = 8.31 Hz, 8H), 2.50 (d, *J* = 6.94 Hz, 8H), 1.58 (s, 4H), 1.32-1.14 (br, 96H), 0.84 (m, 24H); ^{13}C NMR (125 MHz, $CDCl_3$, δ): 157.74, 156.40, 155.05, 153.76, 153.65, 152.84, 152.73, 152.24, 150.81, 150.70, 149.76, 147.94, 141.55, 140.03, 138.91, 137.47, 136.72, 135.41, 131.59, 129.63, 128.78, 128.52, 127.71, 126.31, 123.34, 118.30, 116.16, 115.99, 112.91, 112.74, 111.45, 111.29, 77.25, 77.00, 76.75, 75.46, 63.27, 40.22, 39.44, 33.31, 33.28, 33.23, 31.88, 31.84, 29.96, 29.59, 29.30, 26.55, 26.48, 22.66, 22.64, 14.09; ^{19}F NMR (470 MHz, $CDCl_3$, δ: -131.13 (d, *J* = 19.10 Hz,2F), -124.73 (d, *J* = 18.72 Hz,2F); MALDI-TOF, *m*/*z*: calcd for [$C_{134}H_{156}F_4N_6S_4$]: 2053.121, found: 2053.471.

LTX-4Cl (compound 8b). Yield: 140 mg, 35%, dark solid. ^{1}H NMR (500 MHz, $CDCl_3$, δ): 8.88 (s, 2H), 8.43 (s, 2H), 8.05 (d, *J* = 7.36 Hz, 2H), 7.76 (d, *J* = 5.80 Hz, 2H), 7.26-7.21 (m, 8H), 7.13 (d, *J* = 8.29 Hz, 8H), 2.62-2.45 (m, 8H), 1.60 (d, *J* = 11.69 Hz, 5H), 1.24 (br, 96H), 0.88-0.81 (m, 24H). ^{13}C NMR (125 MHz, $CDCl_3$, δ): 157.79, 156.37, 155.08, 152.35, 149.91, 147.95, 141.59, 140.19, 140.14, 139.54, 138.87, 137.48, 136.75, 135.89, 135.17, 134.64, 129.64, 128.80, 127.82, 127.71, 123.62, 123.32, 118.33, 113.01, 112.79, 75.69, 63.25, 53.40, 40.21, 39.44, 33.31, 33.28, 33.22, 31.88, 31.84, 29.97, 29.60, 29.31, 26.56, 26.54, 26.48, 22.67, 22.65, 14.10; MALDI-TOF, *m*/*z*: calcd for [$C_{134}H_{156}Cl_4N_6S_4$]: 2117.003, found: 2117.658.

Cyclic voltammetry measurements. Cyclic voltammetry (CV) measurements were performed on an EG&G Princeton Applied Research potentiostat/galvanostat (model 273A). A three-electrode cell was used, using platinum (Pt) wires as both counter and working electrodes. Silver/silver ion (Ag in 0.01 M $AgNO_3$ solution) was used as the reference electrode. For thin films, the working electrode was a Pt wire coated with the synthesized small molecules, dip-coated from concentrated solution in chloroform and air dried for overnight. CV measurements of thin films were carried out in 0.1 M tetrabutylammonium hexafluorophosphate (Bu_4NPF_6) solution in acetonitrile at a scan rate of 50 mV/s. For solutions, the working electrode was a bare Pt wire. CV measurements of solutions were carried out in 1,2-dichlorobenzene/acetonitrile (10:1) (0.1 mM LTXs) containing 0.1 M tetrabutylammonium hexafluorophosphate (Bu_4NPF_6) as supporting electrolyte. Scan rate was 100 mV/s. Solutions were purged with inert gas for 20 min before measurements. All recorded reduction and oxidation potentials were calibrated with the ferrocene/ferrocenium (Fc/Fc^+) couple.

Solar Cell Fabrication and Testing. The inverted device structure fabricated and evaluated was: ITO/ZnO/PEI/blend active layer/ MoO_3(0.5 nm)/Ag(100 nm), where PEI or polyethylenimine is a cathode buffer layer.[79] The ITO glass substrates were sequentially sonicated in acetone, deionized (DI) water and isopropanol for 20 min each and then plasma cleaned for 10 min. The ZnO layer (~30 nm) was spin-coated from the precursor solution (0.5 g of zinc acetate dihydrate, 0.14 g of ethanolamine and 5 mL of 2-methoxyethanol) and baked at 250 ºC for 30 min in open air. Solution of PEI (M_w = 25k, Aldrich 408727) in 2-methoxyethanol (0.05 wt%) was then spin-coated onto the ZnO layer and dried at 120 ºC for additional 10 min. The resulting substrates were then stored in an argon-filled glovebox for deposition of active layers. The active layer blend solution was prepared by mixing a chlorobenzene solution of the donor polymer PM6 respectively

with a chlorobenzene solution of acceptors, LTX, LTX-4F, and LTX-4Cl; various solution volumes of the component polymers were mixed in the right proportions to afford the desired blend film compositions. In cases where a processing additive was used, the chlorobenzene:additive (v/v %) mixed solvent was achieved by adding CN to a prepared blend solution. The blend solutions were stirred overnight with low heating to achieve a homogeneous mixture. Each blend solution was then spin-coated onto the cleaned substrate and annealed on a hot plate for 10 min to afford dried thin films with a thickness of 95 ± 5 nm. Finally, the MoO_3 layer and Ag electrode were deposited within a thermal evaporator. Defined active area of 0.0314 cm^2 was achieved for individual devices through a shadow mask. The photovoltaic cells were tested under AM 1.5G solar illumination at 100 mW/cm^2 in ambient air using a Solar Simulator (model 16S, Solar Light Co., Philadelphia, PA) with a 200W Xenon Lamp Power Supply (Model XPS 200, Solar Light Co., Philadelphia, PA) calibrated by NREL certified Si photodiode (Model 1787–04, Hamamatsu Photonics K.K., Japan) and a HP4155A semiconductor parameter analyzer (Yokogawa Hewlett-Packard, Japan). After the *J–V* measurement, the EQE was measured by using a solar cell quantum efficiency measurement system (Model QEX10, PV Measurements, Inc., Boulder, CO) with a 2 mm^2 (2 × 1 mm) size masked incident light source and TF Mini Super measurement apparatus for multiple devices in a single substrate.

SCLC Device Fabrication and Testing. The space charge limited current (SCLC)[80] devices fabricated and evaluated had the structures: ITO/PEDOT:PSS/blend/MoO_3/Ag (hole-only), where poly(3,4-ethylenedioxythiophene):poly(styrenesulfonate) (PEDOT:PSS) is a hole injection layer; and ITO/ZnO/PEI/active layer/PFN-Br/Al (electron-only). The blend active layers in these SCLC devices had the same composition as the corresponding photovoltaic devices. Current-voltage (*J-V*) characteristics of the SCLC devices were plotted as $J^{0.5}$ versus *V* and fitted

by using the following formula: $J = 9\ \varepsilon_0\ \varepsilon_r\ \mu V^2/8d^3$, where J is the current density, ε_0 is the permittivity of free space, ε_r is the relative dielectric constant of the transport medium, μ is the carrier mobility, V is the applied voltage, d is the thickness of blend active layer.

Atomic Force Microscopy (AFM) Imaging. The surfaces of the actual all-polymer solar cell devices were imaged by using the atomic force microscope (Model: Bruker Dimension ICON).

2D GIXD Measurements. Two-dimensional (2D) Grazing incidence X-ray scattering (GIXD) experiments were conducted at the Japan Synchrotron Radiation Facility SPring-8 by using the beamline BL46XU. The thin-film samples investigated were prepared in the same manner as the corresponding photovoltaic devices on ZnO-coated ITO substrates, without the thermal deposition of top MO_3/Ag electrodes. The X-ray beam was monochromatized by a double-crystal Si(111) monochromator, and the X-ray energy in this experiment was 12.40 keV (λ = 0.1 nm). The angle of incident X-ray to sample surface was 0.12° with a Huber diffractometer. The scattered profile from the film sample was detected using an area detector (PILATUS 300K) for 5 s at room temperature, and the distance between the sample and detector was 174.4 mm. The crystal coherence length (L_c) of samples was determined by using the Scherrer equation: $L_c = 2\pi K/\Delta q$, where K is a shape factor (typically 0.89) and Δq is the full width at half-maximum (FWHM) of the diffraction peak.

4.1.3 *Results and Discussion*

4.1.3.1 Synthesis of Ladder Molecule Acceptors.

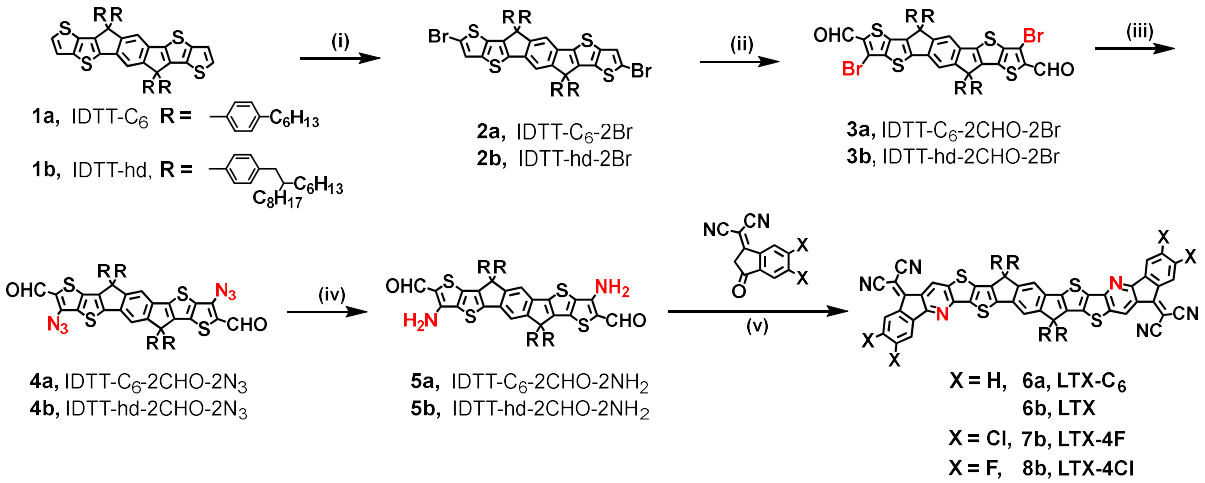

Scheme 4.1. Synthesis of ladder molecule acceptors: LTX-C_6, LTX, LTX-4F and LTX-4Cl. Reagents and conditions: (i) NBS (2.0 equiv), S: $CHCl_3$/AcOH (v:v 3:1), r.t., overnight; (ii) 1) LDA(3.0 equiv), S: THF, -78 ºC→r.t., 24 h; 2) DMF (excess), 0 ºC →r.t. for 2 h; (iii) NaN_3 (10 equiv), S: DMPU, r.t., 24 h; (iv) $(NH_4)_2S$ (aq, excess), S: $CHCl_3$/MeOH, r.t. for 30 min; (v) diphenyl phosphine, S: Toluene, 90 ºC, 24h.

Since ITIC has n-hexyl side chains, we initially synthesized bis(amino-aldehyde) based on IDTT-C_6 for comparison purposes. However, it was soon found out that the resulted product, LTX-C_6 (6a), had low solubility in common organic solvents (dichloromenthane, chloroform, chlorobenzene) and it could not be used for proper solution-processing. The drastic decrease in solubility after "ladderization" is caused by loss of rotational freedom. **Figure S1** showed the contrast of ^{1}H NMR spectra of ITIC and LTX-C_6 in the aromatic regions at the same concentration in $CDCl_3$ and the assignment of important peaks are labeled. In the spectrum of ITIC, the singlet

at 8.22 ppm (peak *c*) representing the protons on thiophenes showed clear broadening, indicating the existence of rotamers in solution for ITIC. Of course, there is no corresponding peak *c* in LTX-C_6 due to annulation. To improve solubility, we proceeded to increase the length of alkyl chains, from n-hexyl to 2-hexyldecyl chains. In addition to the DCMI end group, the fluorinated and chlorinated analogues, 2-(5,6-difluoro-3-oxo-2,3-dihydro-1H-inden-1-ylidene)malononitrile and 2-(5,6-dichloro-3-oxo-2,3-dihydro-1H-inden-1-ylidene)malononitrile, were also used to condense with the bis(amino-aldehyde) intermediate, leading to three ladder molecules noted as LTX, LTX-4F and LTX-4Cl. (**Scheme 4.1**) These three were later applied as the acceptors in photovoltaic devices.

Synthesis of IDTT-hd followed the same procedures as IDTT-C_6,[9] except replacing 1-bromo-4-hexylbenzene with 1-bromo-4-(2-hexyldecyl)benzene during the cyclization step. Lithiation of the dibromides by lithium diisopropylamide (LDA) followed with quenching with dimethylformamide (DMF) gave bis(bromo-aldehyde)s *via* "halogen dance" mechanism.[141] Subsequently, the bis(bromo-aldehyde) were converted to bis(azido-aldehyde) with NaN_3 in N, N′-dimethylpropyleneurea (DMPU) solvent, which then could be readily reduced to bis(amino-aldehyde) with commercial ammonium sulfide aqueous solution, $(NH_4)S$ (*aq*) (40%).[166-169] The bis(amino-aldehyde) was purified with silica gel column. Finally, Friedlander condensations of bis(amino-aldehyde) with various end-groups were conducted with diphenyl phosphate (DPP) as acid catalyst and toluene as solvent, following similar procedures previously reported from our group.[170-171]

During the course of developing efficient and grams-scale synthesis, we encountered several problems and adjusted our methods accordingly: (1) Halogen dance (HD) reaction has been frequently reported on other smaller fused-cores (such as IDT) generally using 2 equiv LDA per

functional group (-Br) and high yields (70 – 90%) were reported.[141] However, our HD reactions on IDTT core under literature conditions always gave complex mixture of products, including intermediates and several byproducts, leading to low yields (<30%). To maximize yield of target product, we adjusted equivalence of LDA to 1.5 equiv per functional group (-Br) and extended the time endurance of cryogenic temperature to slow down lithiation process (12h, total reaction time 24 h). The yields varied in the range of 55-80%. (2) Procedures for the conversion of bis(bromo-aldehyde) to bis(azido-aldehyde) and then to bis(amino-aldehyde) were adapted from early research on simple heterocyle azido compounds.[166-169] Our initial attempt to run the azido reaction in dimethyl sulfoxide (DMSO) failed to give target product, but DMPU as solvent worked out very well. Purification of bis(azido-aldehyde)s with silica gel column is not recommended and also unnecessary, as they showed certain interaction with silica gel which likely led to partial reduction and/or decomposition. Instead, crude product of bis(azido-aldehyde) was used directly for the next step. (3) The byproduct of the reduction towards bis(amino-aldehyde)s is sulfur. While in early literatures,[166-169] solid sulfur was reported to be easily removed with simple filtration, we found that sulfur co-existed with bis(amino-aldehyde)s since both are soluble in common organic solvents such as dichloromethane and chloroform. (4) Removal of the polar solvent DMPU (b.p.247 °C) with rotary evaporator was ineffective. However, extraction with ether from aqueous mixture could effectively separate DMPU from crude product. Subsequently, bis(amino-aldehyde)s were further purified with silica gel columns eluting with dichloromethane or with additional methanol if needed. Yields of the two-step conversion from bis(bromo-aldehyde)s to bis(amino-aldehyde)s were fairly high (~75%). More details on synthetic procedures and related characterization data are included in Supporting Information. Thermogravimetric analysis (TGA) showed that these ladder molecules have extraordinary thermal stability with high decomposition

temperatures (T_d) (determined at 5% weight loss) all above 400 ºC: LTX (418 ºC), LTX-4F (423 ºC) and LTX-4Cl (417 ºC). (**Figure S1**)

4.1.3.2 Optical absorption.

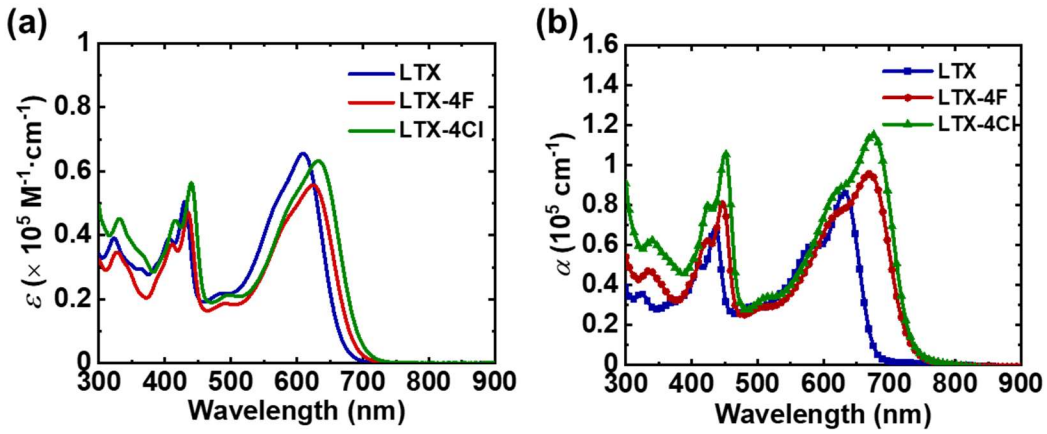

Figure 4.2. UV-vis absorption of LTX, LTX-4F and LTX-4Cl in (a) dilute solutions (10-5 M) in chloroform and (b) thin films.

Table 4.1. Optical Absorption and Energy Levels of LTX, LTX-4F and LTX-4Cl

Acceptors	λ_{max}^{sol} [nm]	λ_{max}^{film} [nm]	λ_{onset}^{film} [nm]	$E_g^{opt, a}$ [eV]	HOMO[b] [eV]	LUMO[b] [eV]	E_g^{b} [eV]	HOMO[c] [eV]	LUMO[c] [eV]	E_g^{c} [eV]
LTX	430, 610	435, 631	680	1.82	-5.60	-3.65	1.95	-5.51	-3.35	2.16
LTX-4F	435, 625	446, 668	722	1.72	-5.63	-3.74	1.89	-5.64	-3.53	2.11
LTX-4Cl	440, 633	450, 675	726	1.71	-5.64	-3.79	1.85	-5.69	-3.61	2.07

[a] $E_g^{opt} = 1240 / \lambda_{onset}^{film}$
[b] Estimated from cyclic voltammetry in solutions with reference to Fc/Fc^+ following the formula: $E_{HOMO/LUMO} = -(4.8+E_{ox/red}^{1/2})$ eV.
[c] Calculated with DFT with B3LYP 6-31G(d) basis set.

The optical absorption spectra of these ladder molecules in dilute solutions in chloroform (10^{-5} M) and in thin films are presented in **Figure 4.2**, and the corresponding data regarding the absorption maxima and the determined onset values are listed in **Table 4.1**. The most striking feature is that these ladder molecules have dual-band absorption, which is not seen in the common A-D-A-type SMAs such as ITIC. In the range of 500-800 nm, a strong and broad absorption band appeared, primarily due to the intramolecular charge transfer (ICT) between the electron-rich core and the electron-withdrawing end-groups. In addition, a relatively weaker absorption band is present in the short-wavelength region (380-450 nm). This short-wavelength absorption band is located close to the absorption of the bis(amino-aldehyde), IDTT-hd-2CHO-2NH_2 (**Figure S4**). Thus, it could be deduced that the short-wavelength band originated from the p-p* transition of the fully fused ladder backbone without the cyano (-CN) groups. Time-dependent density function theory (TD-DFT) calculations (*vide infra*) further confirmed that this short-wavelength absorption band comes from the HOMO→LUMU+2 transitions, where both molecular orbitals (MO) are spreading within the ladder framework. (**Figure S6**b) Despite the broad optical absorption range, it should be pointed out that the LTXs have relatively lower absorption coefficients compared to their non-ladder counterpart, ITIC. This is also reflected in DFT calculations that LTX has lower oscillator strength than ITIC. In addition, for each of the ladder molecules, the absorption spectrum of thin film (**Figure 4.2**) showed bathochromic shift of 20~50 nm in both absorption bands compared to that of the corresponding solution, indicating backbone aggregation and p-p interaction in solid state. LTX-4F and LTX-4Cl showed larger shift relative to LTX. Fluorination and chlorination gradually broadened the absorption ranges, which would benefit overall light harvest when applied in photovoltaic blends.

4.1.3.3 Electrochemical properties and DFT calculations.

The redox properties of the LTXs were investigated with cyclic voltammetry (CV) in solutions. The three molecules all exhibited two reversible reduction waves (**Figure S5**) and could sustain multiple cycles, demonstrating excellent redox stability. The half-wave oxidation potentials ($E_{ox}^{1/2}$) and the first half-wave reduction potentials ($E_{red}^{1/2}$) were used to derive the HOMO and LUMO energy levels, respectively, assuming that the vacuum level energy of ferrocene/ferrocenium (Fc/Fc^{+}) is -4.8 eV. The following formula was used: $E_{HOMO/LUMO} = -(4.8+E_{ox/red}^{1/2})$ eV. Based on the electrochemical data extracted from cyclic voltammograms, the estimated HOMO/LUMO energy levels are as follows: LTX (-5.60/-3.65 eV), LTX-4F (-5.63/-3.74 eV) and LTX-4Cl (-5.64/-3.79 eV). (**Table 4.1**) The results also showed that fluorination and chlorination of LTX led to lowered HOMO/LUMO energy levels and smaller band gaps, consistent with the observation from optical absorption.

To better understand the electronic structures and optical properties of these ladder molecules, density functional theory (DFT, B3LYP6-31G(d)) calculations were performed on the model structure, LTX, along with ITIC for comparison purposes. Long alkyl chains in both structures were replaced with methyl groups for simplification. The calculated energy diagrams and frontier molecular orbital profiles are presented in **Figure S7**. Results indicate that "ladderization" would raise the LUMO level and lower the HOMO level simultaneously, causing enlarged bandgap, (**Figure S7**a) consistent with the results from cyclic voltammetry. Another significant change caused by "ladderization" is the spatial distribution of the molecular orbitals. As depicted in **Figure S7**b, ITIC has HOMO mainly localized in the central fused core and LUMO fairly delocalized through the conjugated backbone, whereas LTX has HOMO similar to that of ITIC, but the LUMO of LTX is mainly localized on the end-group regions, which explains weaker

oscillator strength of LTX due to poor orbital overlap. TD-DFT calculations predicted that, unlike ITIC, LTX has two major absorption bands (**Figure S8, 9**) where the long-wavelength absorption band (500-700 nm) originates from HOMO→LUMO transitions (657.26 nm, f = 1.1278) and the short-wavelength absorption band (380 – 460 nm) is mainly from HOMO→LUMO+2 transitions (435.58 nm, f = 1.0356). (**Table S1, S2**) Transition of HOMO→LUMO+1 is symmetry forbidden for LTX. Further calculations on LTX-4F and LTX-4Cl (**Figure S10, S11**) revealed that the halogenations, from fluorination to chlorination, gradually lowered HOMO/LUMO energy levels and shrank the band gaps, consistent with results from optical spectra and cyclic voltammetry.

4.1.3.4 Intrinsic Photochemical Stability.

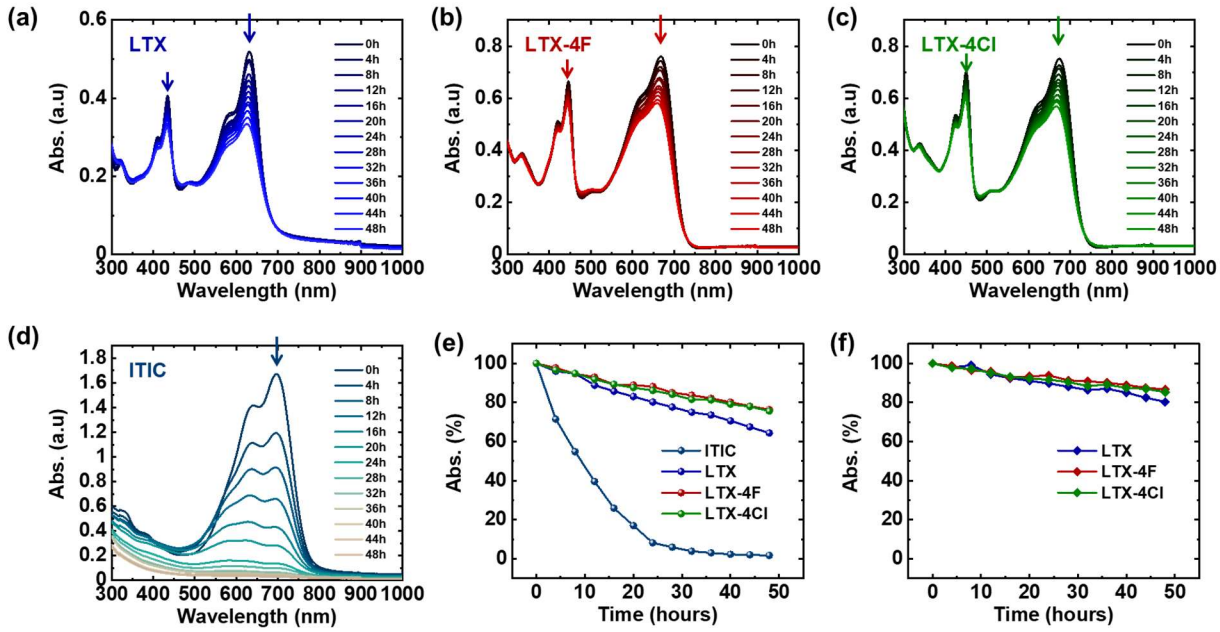

Figure 4.3. Progression of optical absorption spectra for (b) LTX, (c) LTX-4F, (d) LTX-4Cl, and (e) ITIC; (f) percentage loss of maximum absorbance over time for the intra-molecular charge transfer (ICT) bands (550 – 750 nm) of the four acceptors; (g) percentage loss of maximum

absorbance over time for the HOMO → LUMO+2 transitions (380 – 480 nm) of the three ladder molecule acceptors.

To validate the intrinsic photochemical stability of the LTXs, we traced the optical absorption spectra of the neat films, as well as the neat film of ITIC, under continuous 1 sun illumination in ambient environment with controlled temperature. **Figure 4.3a** exhibited the photos of the neat films of LTX, LTX-4F, LTX-4Cl and ITIC recorded at every 4 hours. The corresponding absorption spectra for each film is plotted in **Figure 4.3b-e**. The absorption peaks of ITIC decreased rapidly upon illumination and the neat film became transparent beyond 32 h, indicating complete disintegration of conjugation backbone. In contrast, the LTXs demonstrated much slower photodegradation progress. As plotted in **Figure 4.3f**, in the major absorption band at 550-750 nm, LTX retained 65% of the initial maximum absorbance, whereas LTX-4F and LTX-4Cl retained 75-76% of their initial maxima. The secondary absorption band at 380 – 480 nm showed even more slower degradation, with LTX retaining 80% of the initial maximum absorbance and LTX-4F and LTX-4Cl retaining 86-87%. (**Figure 4.3g**) The different photodegradation rate of the two bands indicated that the minor bond breakage might have happened at different sites of the ladder structure. The results also revealed that fluorination and chlorination were beneficial to further enhance the intrinsic photochemical stability.

4.1.3.5 Contact Angle Measurements

Table 4.2. Contact Angles and Calculated Surface Energy Parameters of the Neat Films.

Neat film	θ_{water} (°)	θ_{oil} (°)[a]	γ^d (mN/m)[b]	γ^p (mN/m)[b]	γ (mN/m)[b]	χ[c]
PM6	106.7	67.42	24.33	0.17	24.49	-
LTX	109.5	42.34	38.41	0.43	38.85	1.65k
LTX-4F	104.28	47.16	35.84	0.01	35.85	1.08k
LTX-4Cl	99.81	49.67	34.46	0.15	34.61	0.87k

[a] θ_{oil} represents the contact angle of 1,8-diiodomethane;
[b] γ values are calculated by the Owens-Wendt-Rabel-Kaelble (OWRK) method, where γ^d and γ^p represent the surface free energies generated from the dispersion forces and the polar forces, respectively, and γ represents the surface energy ($\gamma = \gamma^d + \gamma^p$).
[c] $\chi = k(\sqrt{\gamma_D} - \sqrt{\gamma_A})^2$, where k is a constant.

To predict the mixing behaviors in the blend systems, contact angle measurements were performed on the individual neat films of the polymer donor and the LMAs, using water and diiodomethane as wetting solvents. The relevant images are shown in **Figure S10** and the calculated surface energy parameters are summarized in **Table 4.2**. All four neat films showed water contact angles greater than 90° (99.42°-106.70°) and diiodomethane contact angles much smaller than 90° (30.75°-67.42°), suggesting that both the polymer donor and the acceptors are hydrophobic-oleophilic. According to the surface tension (γ) calculated based on the widely used Wu model,[172] the involved donor and acceptors stand in the following order: LTX (38.85 mN·m^{-1}) > LTX-4F (35.85 mN·m^{-1}) > LTX-4Cl (34.61 mN·m^{-1}) > PM6 (24.49 mN·m^{-1}). Fluorination and chlorination decreased the surface energy of the acceptor, bringing it closer to that of PM6, thus increasing the donor/acceptor miscibility: PM6:LTX < PM6:LTX-4F < PM6:LTX-4Cl. Overall, the surface tensions of the three acceptors are similar to each other but are significantly higher than

that of PM6. As a result, vertical composition gradient could be formed within the blend films, where the acceptors with higher surface energies would enrich at the bottom and the polymer donor PM6 enrich on the surface. In an inverted device architecture where ZnO serves as the bottom electron-transporting layer, such vertical composition gradient is advantageous for vertical charge transport and collection, therefore benefit device performance.

In addition, Flory-Huggins interaction parameter ($\chi_{D,A}$) could be used to evaluate the miscibility of the donor and acceptor components in BHJ blend films.[116] $\chi_{D,A}$ is estimated using the empirical formula: $\chi_{D,A} = K(\sqrt{\gamma_D} - \sqrt{\gamma_A})^2$, where K is a positive constant and γ_D and γ_A are the surface energies of the neat films of donor and acceptor, respectively.[173] Generally, a low value of $\chi_{D,A}$ indicates high miscibility of donor and acceptor, while a high value of $\chi_{D,A}$ leads to phase separation in the blend films. As listed in **Table 4.2**, the $\chi_{D,A}$ values of the three blend systems stand in the descending order: PM6:LTX (1.65K) > PM6:LTX-4F (1.08K) > PM6:LTX-4Cl (0.87K). Thus, among the three blend systems, PM6:LTX is expected to have the lowest miscibility and the greatest phase separation, while PM6:LTX-4Cl is expected to have the best miscibility and the finest phase separation.

4.1.3.6 Photovoltaic Properties.

The photovoltaic properties of LTXs were investigated by fabricating solar cell devices with inverted architecture: ITO/ZnO/PEI/photoactive layer/MoO_3/Ag, where PEI was used as a cathode interlayer. The photoactive layer was a binary blend of the donor polymer PM6 and the synthesized LMAs: LTX, LTX-4F and LTX-4Cl. For each PM6:LMA combination, devices were individually optimized by varying the donor:acceptor (D:A) weight ratios, the annealing temperature, and the usage of processing additives. For PM6:LTX, the optimal conditions were

found to be with D:A ratio of 1:1.2 (wt:wt) and aging inside the Argon filled glovebox at room temperature for 2 h after spin-coating, with 2 vol% chloronaphthalene (CN) as processing additive, while for PM6:LTX-4F and PM6:LTX-4Cl, the optimal conditions were with D:A ratio of 1:1.5 (wt:wt) and thermal annealing at 110 °C for 10 min after spin-coating, with 0.5 vol% CN as processing additive.

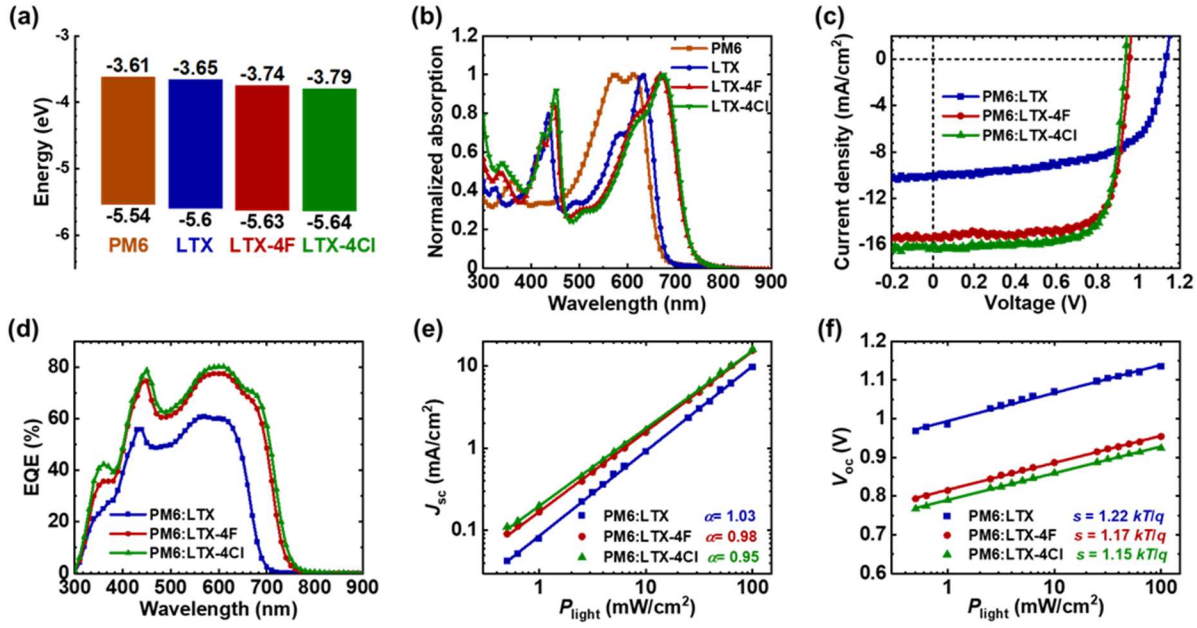

Figure 4.4. (a) Energy levels and (b) thin film optical absorption of the donor polymer PM6 and the ladder molecule acceptors: LTX, LTX-4F and LTX-4Cl; (c) J-V response curves and (d) EQE spectra, (e) charge photogeneration, (f) light intensity dependence of short-circuit current (J_{sc}), and (g) light intensity dependence of open-circuit voltage (V_{oc}) for the blend films of PM6:LTXs under optimized conditions.

Table 4.3. Summary of Photovoltaic Parameters and Charge Transport Properties of the Optimized Devices of PM6:LTXs

Blends	J_{sc} (mA/cm^2)	V_{oc} (V)	FF	PCE [a] (%)	$J_{sc}^{calc.}$ (mA/cm^2)	μ_h (10^{-4} cm^2/Vs)	μ_e (10^{-4} cm^2/Vs)	μ_h/μ_e
PM6:LTX	10.02 (9.72 ± 0.21)	1.13 (1.13 ± 0.00)	0.63 (0.61 ± 0.01)	7.17 (6.69 ± 0.24)	9.51	4.09	4.40	0.93
PM6:LTX-4F	15.49 (15.10 ± 0.35)	0.954 (0.950 ± 0.004)	0.74 (0.74 ± 0.01)	10.98 (10.55 ± 0.21)	14.32	4.12	3.58	1.15
PM6:LTX-4Cl	16.39 (15.78 ± 0.55)	0.935 (0.924 ± 0.010)	0.75 (0.74 ± 0.01)	11.48 (10.83 ± 0.46)	15.48	4.87	3.84	1.27

[a] Average values of over 15 devices.

The current density-voltage (*J-V*) curves of the best performing devices are presented in **Figure 4.4**. The detailed photovoltaic parameters including open-circuit voltage (V_{oc}), short-circuit current density (J_{sc}), fill factor (FF) and power conversion efficiency (PCE) are summarized in **Table 4.3**. It is noteworthy that all three blends demonstrated fairly high V_{oc}: PM6:LTX (1.13 V), PM6:LTX-4F (0.954 V) and PM6:LTX-4Cl (0.935 V). Such V_{oc} values are among the highest for polymer solar cells in general. The high V_{oc} values of PM6:LTXs are consistent with previous findings from DFT calculations (**Figure S6**a) showing that the LTXs have relatively high-lying LUMO energy levels compared to their non-ladder counterpart, ITIC. Furthermore, we observed the trend that halogenations led to decreased V_{oc}, which is also consistent with previous results showing gradually lowered LUMO energy levels from fluorination to chlorination. (**Table 1**) Compared to the PM6:LTX blend, the PM6:LTX-4F and PM6:LTX-4Cl blends produced significantly higher J_{sc}: PM6:LTX (9.72 ± 0.21 mA/cm^2), PM6:LTX-4F (15.10 ± 0.35 mA/cm^2), PM6:LTX-4Cl (15.78 ± 0.55 mA/cm^2). This is partly due to the fact that LTX-4F and LTX-4Cl have red-shifted absorption bands relative to LTX.(**Figure 4.4**) Besides, the PM6:LTX-4F and PM6:LTX-4Cl blends demonstrated far better fill factors than the PM6:LTX blend: PM6:LTX (FF = 0.61 ± 0.01), PM6:LTX-4F (FF = 0.74 ± 0.01) and PM6:LTX-4Cl (FF = 0.74 ± 0.01), indicating

formation of more favorable blend morphology with the halogenated derivatives. The observed enhancement in both J_{sc} and FF suggest that the halogenations is an effective method to improve light harvest and induce formation of favorable blend morphology, thereby improve photovoltaic performance. Summarized in **Table 4.3**, these photovoltaic parameters combined led to the champion devices: PM6:LTX (PCE = 7.17%), PM6:LTX-4F (PCE = 10.98%), and PM6:LTX-4Cl (PCE = 11.48%). The corresponding EQE spectra of the optimized devices based on PM6:LTXs are shown in **Figure 4.4**.

The photo responses of the PM6:LTXs blend devices spanned over a broad range from 300 nm to 700-770 nm, contributed by the absorption from both the donor polymer and the LMAs. In correspondence to the individual optical absorption of the donor and the acceptors, the EQE responses in the range of 390-480 nm and 625-770 nm originated primarily from the photoinduced hole transfer of the acceptors LTXs, whereas the EQE responses in the range of 480-620 nm was largely contributed by the photoinduced electron transfer of the donor polymer PM6. The maximum EQE were found to be 60.8%, 77.5%, and 80.2% for PM6:LTX, PM6:LTX-4F, and PM6:LTX-4Cl, respectively, in the range of 570-610 nm. The calculated J_{sc} ($J_{sc}^{calc.}$) (**Table 4.3**) obtained by integrating the EQE spectra were within 3-5% error with the J_{sc} extracted from the *J-V* curves.

We highlight the high fill factors and high PCEs achieved from the blends of PM6:LTX-4F (FF = 0.74 ± 0.01, PCE = 10.55 ± 0.21%) and PM6:LTX-4Cl (FF = 0.74 ± 0.01, PCE = 10.83 ± 0.46%), as these are the highest values achieved for ladder molecules so far. In previous literatures, the LMAs were mostly based on fused perylene diimide (PDI) and bithiophene imide (BTI) where the resulted blend films with donor polymers often suffered from poor morphology, causing low fill factors and low PCEs. We think that the LTXs are inspiring examples that

overcame those drawbacks and demonstrated feasibility and potential of LMAs in polymer solar cells.

4.1.3.7 Charge Photogeneration, Recombination and Charge Transport.

The dependence of J_{sc} and V_{oc} on the incident light intensity (P_{light}) were characterized to investigate the charge recombination mechanism. (**Figure 4.4**) The relationship between J_{sc} and P_{light} follows the power law: $J_{sc} \propto {P_{light}}^{\alpha}$. Under short-circuit conditions, when bimolecular recombination within the photoactive layer is negligible, α approaching 1 should be observed. Deviation from 1 indicates loss from bimolecular recombination. We observe α values as follows: PM6:LTX (1.03), PM6:LTX-4F (0.98), PM6:LTX-4Cl (0.95), suggesting minor bimolecular recombination loss. On the other hand, we evaluated the correlation between V_{oc} and P_{light}, where the ideality factor s was extracted with the following equation: $s = \frac{kT}{q}\frac{\partial V_{oc}}{\partial \ln (P_{light})}$. Under open-circuit conditions, when bimolecular recombination is predominant, an ideality factor of unity (s = kT/q) should be observed, while an s value approaching 2kT/q signifies monomolecular or trap-assisted recombination loss. We observed relatively low s values: PM6:LTX (1.22 kT/q), PM6:LTX-4F (1.17 kT/q) and PM6:LTX-4Cl (1.15 kT/q). The PM6:LTX blend demonstrated relatively higher s value, indicating less optimal charge collection processes compared to the PM6:LTX-4F and PM6:LTX-4Cl blends.

The bulk charge transport properties of the LTXs neat films and the PM6:LTXs blend films were characterized by extracting the space-charge limited current (SCLC) carrier mobilities from single-carrier diodes. The device architecture for the hole-only diode is: ITO/PEDOT:PSS/active layer/MoO_3/Ag, and for the electron-only diode: ITO/ZnO/PEI/active layer/PFN-Br/Al. The LTXs neat films were thermally annealed at 110ºC for 10 min. The PM6:LTXs blend films were

processed under the same optimized conditions as used in the corresponding solar cell devices. The corresponding *J-V* curves and SCLC fittings for the neat and blend films are presented in **Figure SX-X.** The neat films of LTX, LTX-4F and LTX-4Cl exhibited high electron mobilities (μ_e) of 1.02 × 10^{-4} cm^2/Vs, 3.40 × 10^{-4} cm^2/Vs and 2.94 × 10^{-4} cm^2/Vs, respectively.(**Table S4**) Results suggest that fluorination and chlorination led to ~ 3-fold enhancement in electron transport for the neat films. The blend films of PM6:LTXs demonstrated highly symmetrical hole/electron transport, where the μ_h/μ_e ratios for the blends of PM6:LTX, PM6:LTX-4F and PM6:LTX-4Cl were found to be 0.93, 1.15 and 1.27, respectively. (**Table 4.3**) The electron mobilities for the PM6:LTXs blends were higher (3.58 × 10^{-4} -4.40 ×10^{-4} cm^2/Vs) than those for the corresponding LTXs neat films (1.02 × 10^{-4} - 3.40 × 10^{-4} cm^2/Vs), suggesting that the combination of PM6 and LTXs could produce favorable local fields arising from the permanent dipole moments in these conjugated molecules which in turn facilitated efficient electron transport across the electrodes.[174] Furthermore, the influence of fluorination and chlorination on the charge transport properties of blend films was not significant and no clear trend could be established.

4.1.3.8 Surface Morphology and Bulk Blend Morphology.

Surface morphology of the PM6:LTXs blend films under optimal conditions were presented in **Figure S17.** The bulk morphology of the LTXs neat films and the PM6:LTXs blend films were characterized using synchrotron-based two-dimension grazing incidence X-ray scattering (2D-GIXD). **Figure 4.5** presented the 2D diffraction patterns and the corresponding 1D line-cut profiles in the in-plane (IP) (q_{xy}) and the out-of-plane (OOP) (q_z) directions for all relevant neat and blend films. The extracted data for peak positions, *d*-spacing, and the calculated crystalline coherence length (L_c) for each of the neat and blend films are summarized in **Table 4**.

The 2D diffraction patterns for PM6 are included in **Figure S14**. The IP and OOP line-cuts of PM6 are plotted within **Figure 4.5g-h** for better visualization.

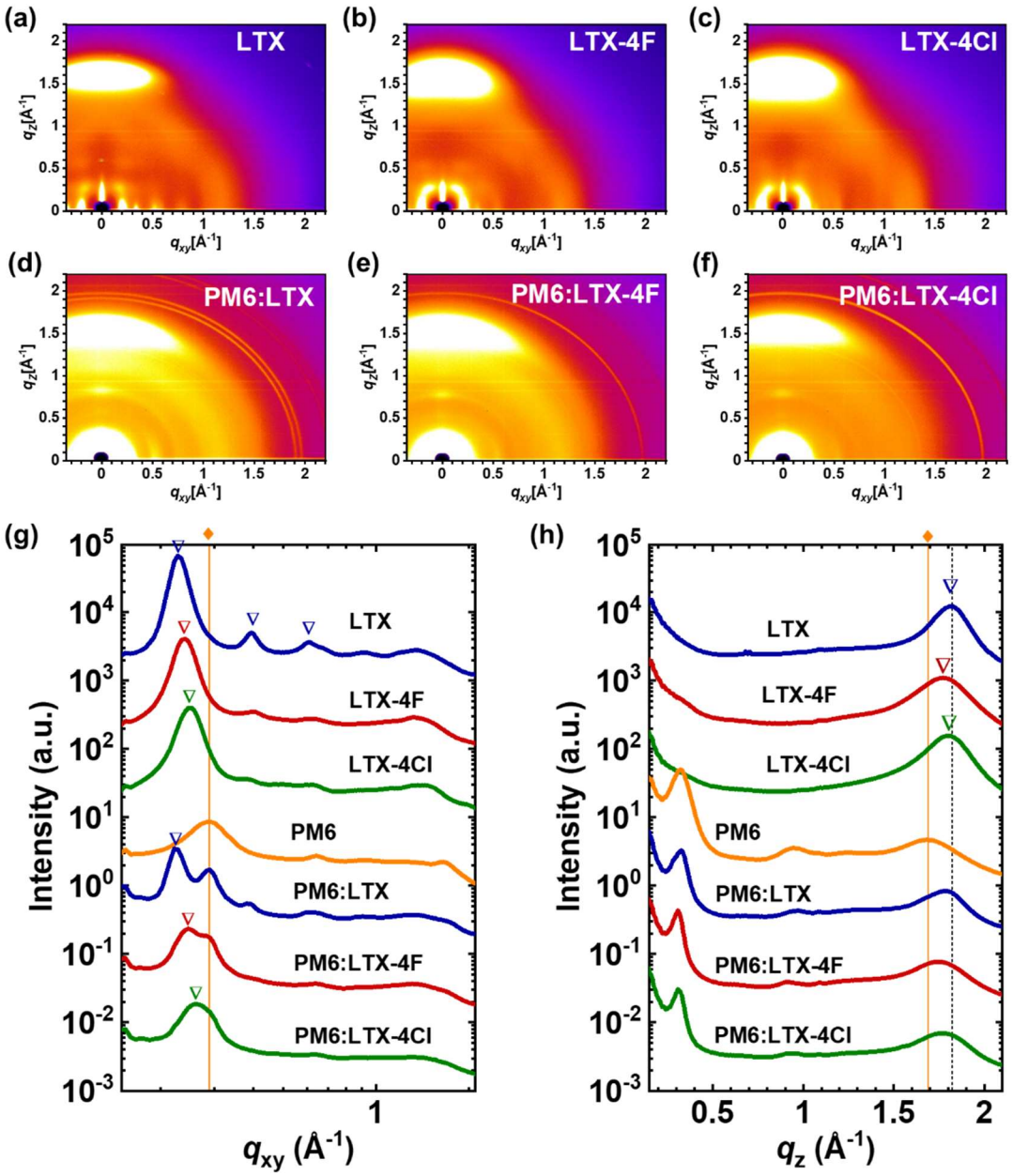

Figure 4.5. 2D GIXD patterns for the LTXs neat films and the PM6:LTXs blend films: (a) LTX; (b) LTX-4F; (c) LTX-4Cl; (d) PM6:LTX; (d) PM6:LTX-4F; (e) PM6:LTX-4Cl; and 1D line cuts for all neat and blend films in (g) in-plane (IP) and (h) out-of-plane (OOP) directions, where "♦" denotes peaks from the donor polymer PM6 and "▽" denotes peaks from ladder molecule acceptors LTXs.

As shown in **Figure 4.5**a-c, 2D GIXD patterns of the neat films for LTX, LTX-4F and LTX-4Cl showed similar features: strong π-π diffraction patterns in the OOP direction, associated with lamellar diffractions in the lower q_{xy} region in the IP direction. Such diffraction patterns suggest that the ladder molecules adopted preferentially *face-on* orientation in the neat films, where the ladder conjugation backbones are parallel to the substrate and the π-π stacking is in the vertical direction. In the IP direction, lamellar peak positions at the lower q_{xy} region were determined at: LTX (0.228 $Å^{-1}$), LTX-4F (0.240 $Å^{-1}$), and LTX-4Cl (0.249 $Å^{-1}$), corresponding to the *d*-spacing distances of 27.6 Å, 26.2 Å, and 25.3 Å, respectively. (**Figure 4.5g**) This *d*-spacing distance is corresponding to the crystal parameter, *b*/2, as illustrated in **Figure S4.16**. In addition, LTX also showed weak and broad peaks at q_{xy} = ~ 0.40 $Å^{-1}$ (d ~ 15 Å) and ~0.60 Å (d ~ 10 Å) in the IP direction, seemingly representing different types of in-plane structural ordering. LTX-4F and LTX-4Cl have similar peaks at identical positions but with significantly reduced peak intensities, indicating that LTX had the highest crystallinity among the three acceptors and the halogenations decreased crystallinity. Calculated from the lamellar peaks in the IP directions, the estimated crystalline coherence length (L_c) of the LTXs neat films were in the descending order: LTX (21.8 nm) > LTX-4F (15.5 nm) > LTX-4Cl (13.8 nm). In the OOP direction, (**Figure 4.5**h) the π-π peak positions at q_z were estimated to be: LTX (1.81 $Å^{-1}$), LTX-4F (1.77 $Å^{-1}$), and LTX-4Cl (1.80 $Å^{-1}$), corresponding to the π-π stacking distances of 3.47 Å, 3.54 Å, and 3.49 Å, respectively.(**Table S5**)

In the blend films of PM6:LTXs, the 2D GIXD diffraction patterns (**Figure 4.5d-f**) preserved strong π-π (010) diffractions in the OOP direction, suggesting largely populated *face-on*-oriented crystallites. The corresponding 1D line-cut profiles of the blend films in both the IP and OOP directions were much like the overlay of the line-cuts from the respective donor and acceptor components, as marked in **Figure 4.5g-h**. It is worth noting that the three acceptors, LTX,

LTX-4F and LTX-4Cl, behaved differently when blended with the donor polymer PM6. As shown in **Figure 4.5g** for the IP direction, in the blend of PM6:LTX, we observed well separated peaks at lower q_{xy} region, originated from PM6 and LTX respectively, indicating distinct phase separation with high domain purity. Correspondingly, in the blend of PM6:LTX-4F, the two peaks started to merge as a main peak at 0.246 $Å^{-1}$ along with a shoulder peak at 0.289 $Å^{-1}$, whereas in the blend of PM6:LTX-4Cl, the peaks appeared as one broad peak centered at median q_{xy} of 0.258 $Å^{-1}$. As listed in **Table S4**, the estimated L_c values for the blend of PM6:LTX were identical to that of the respective neat components, whereas for the blends of PM6:LTX-4F and PM6:LTX-4Cl, calculated L_c values decreased to 9.2 nm and 7.6 nm, respectively, due to peak broadening. The evident progression of the IP lamellar diffraction peaks going from PM6:LTX to PM6:LTX-4F and PM6:LTX-4Cl suggested that the fluorination and chlorination enhanced the miscibility between the donor polymer and the acceptor molecules and promoted donor/acceptor intermixing within the blend films. In the OOP direction, the three blend films showed similar patterns, featuring bright π-π diffraction patterns at the higher q_z region (**Figure 4.5**d-f) and weak lamellar peaks at the lower q_z region resembling that of PM6 (**Figure 4.5**h). There were subtle differences in the OOP diffractions going from PM6:LTX-hd to PM6:LTX-hd-4F and PM6:LTX-hd-4Cl. In the blend of PM6:LTX-hd, the broad π- π diffraction peak maximized at q_z close to that of LTX-hd, whereas in the blend films of PM6:LTX-hd-4F and PM6:LTX-hd-4Cl, the broad π- π diffraction peak centered at median q_z values. (**Figure 4.5**h) These observations are consistent with the analysis of the IP diffractions that PM6:LTX-hd had distinct phase separation while PM6:LTX-hd-4F and PM6:LTX-hd-4Cl had enhanced donor/acceptor miscibility and intermixing. The results are also consistent with previous predictions based on contact angle measurements. More importantly, the increasing donor/acceptor intermixing in the blend films going from PM6:LTX to

PM6:LTX-4F and PM6:LTX-4F coincided with the observed improvement in their photovoltaic parameters (both J_s and FF), suggesting that such enhancement of donor/acceptor miscibility and intermixing as a result of fluorination and chlorination was advantageous for the photovoltaic performance of the blend films.

4.1.4 *Conclusions*

In this paper, we have demonstrated an alternative molecular design of NF SMAs in an attempt to address the issue of intrinsic photochemical stability. A series of ladder molecule acceptors (LMAs), namely LTX, LTX-4F and LTX-4Cl, were successfully synthesized via Friedlander condensation reactions and characterized side-by-side in comparison with ITIC. Owing to the completely fused ladder backbones, the LTXs indeed demonstrated superior intrinsic photochemical stability under continuous 1 sun illumination in ambient atmosphere. More importantly, high photovoltaic performance was well preserved: PM6:LTX (PCE 7.2%), PM6:LTX-4F (PCE 10.5%) and PM6:LTX-4Cl (PCE 11.5%).

The LTXs have distinctive dual-band optical absorption. Compared with ITIC, the LTXs generally have enlarged bandgaps with lower-lying HOMO energy levels and higher-lying LUMO energy levels. Thus, relatively high V_{oc} values of 0.93-1.13 V were achieved in the photovoltaic blends of PM6:LTXs. Moreover, the blend of PM6:LTX had relatively low fill factor of 0.63, whereas the blends of PM6:LTX-4F and PM6:LTX-4Cl showed high fill factors of 0.74-0.75. Contact angle measurements suggested that fluorination and chlorination helped to lower the surface energies of the LTXs, therefore could afford better donor /acceptor miscibility when blended with PM6. Meanwhile, results from 2D GIXD analysis clearly showed that the blend of PM6:LTX had distinct phase separation, whereas the blends of PM6:LTX-4F and PM6:LTX-4Cl have enhanced donor/acceptor intermixing. These observations suggested that the halogenations

were very effective strategy not only to broaden the optical absorption, but also to induce formation of favorable blend morphology.

Furthermore, we would also like to point out that, compared with ITIC-like NFAs, the LTXs lacked the optical absorption in the 700 – 900 nm range, which may have greatly limited their photocurrent. Further molecular engineering that would enable broadened optical absorption extending into the near infrared region should be explored.

4.1.5 *Supporting Information*

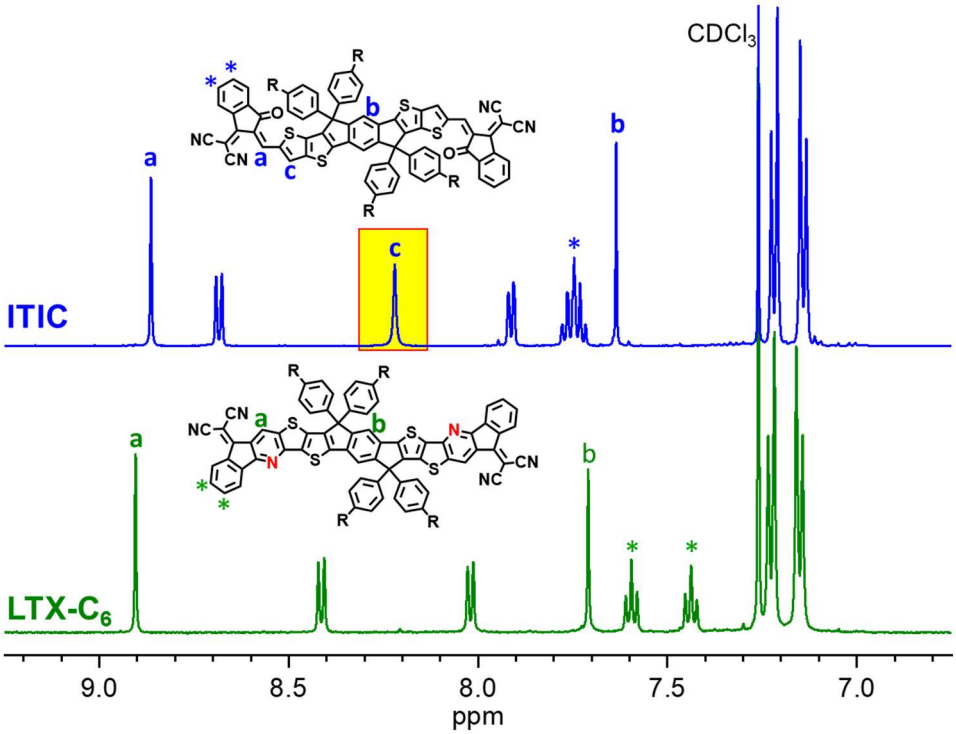

Figure S4.6. Comparison of ^{1}H NMR ($CDCl_3$, 500 MHz, 298K) spectra for ITIC and LTX-C_6 at the same concentrations.

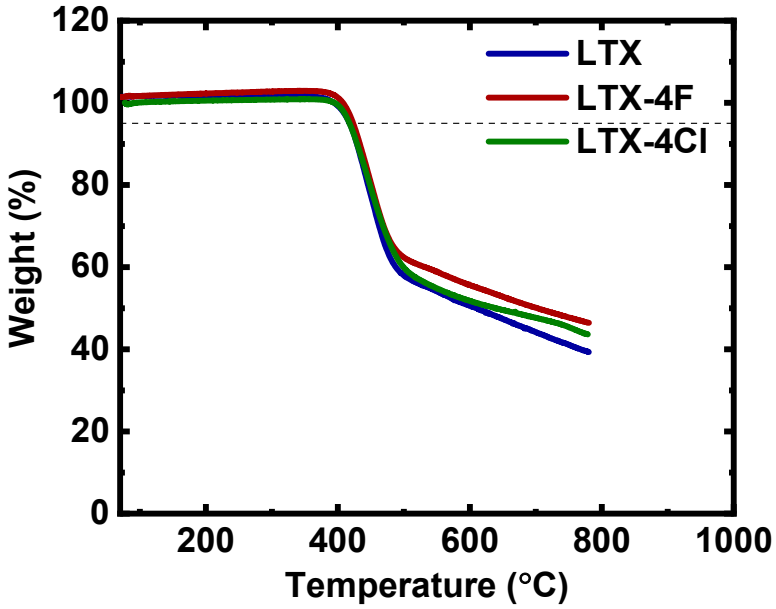

Figure S4.7. TGA traces of LTX, LTX-4F and LTX-4Cl.

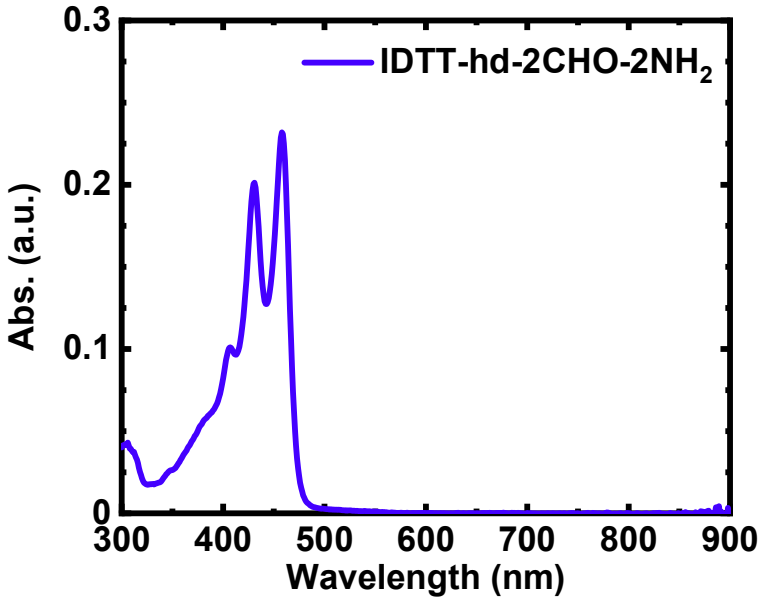

Figure S4.8. UV-vis absorption of IDTT-hd-2CHO-2NH_2 as dilute solution in chloroform.

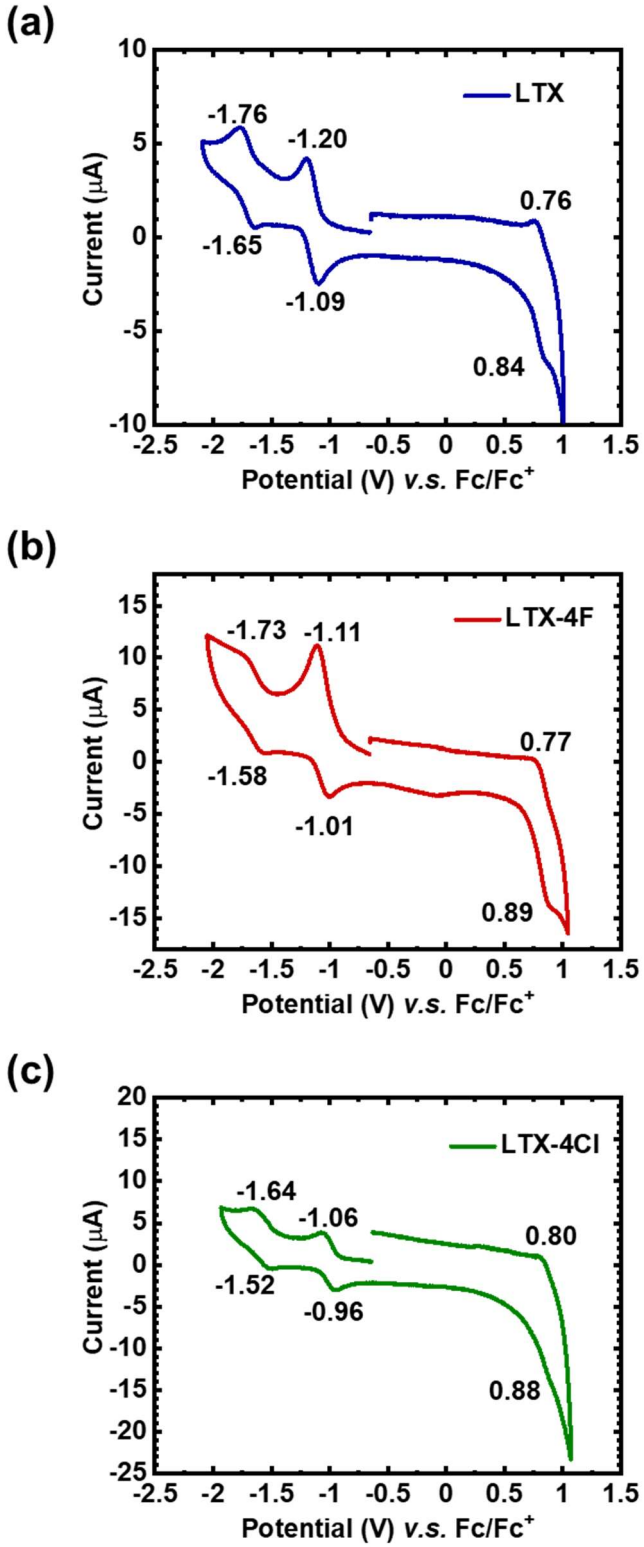

Figure S4.9. Cyclic voltammograms of dilute solutions: (a) LTX, (b) LTX-4F and (c) LTX-4Cl.

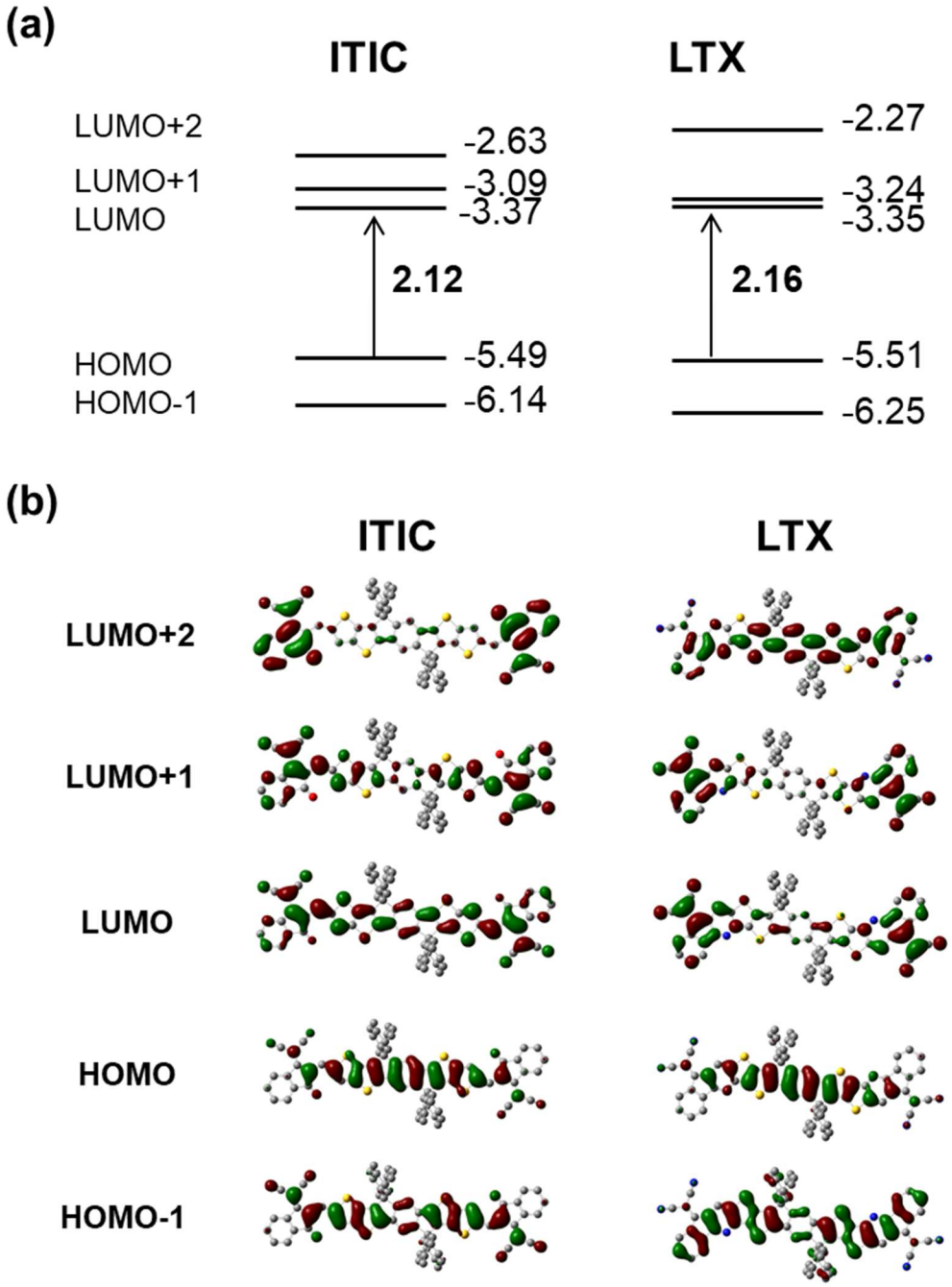

Figure S4.10. (a) Calculated energy diagrams and (b) visualization of molecular orbitals of ITIC and LTX with DFT (B3LYP(6-31G(d)). All alkyl chains were replaced with methyl groups for simplification.

Table S4.4. Selected TD-DFT (B3LYP/6-31G(d)) Calculated Energies, Oscillator Strength and Cmpositions of Major Electronic Transitions of LTX.

No.	Wavelength (nm)	Oscillator Strength (*f*)	Major Contributions
1	**657.26**	**1.1278**	**HOMO → LUMO (96%)**
2	494.27	0.1266	HOMO-1 → LUMO+1(50%) HOMO-2 → LUMO (32%)
3	444.46	0.1683	HOMO-2 → LUMO (54%) HOMO-1→ LUMO+1 (30%)
4	438.71	0.0835	HOMO-4 → LUMO (84%)
5	**435.58**	**1.0356**	**HOMO → LUMO+2 (91%)**
6	426.62	0.1402	HOMO-6 → LUMO (64%)
7	351.34	0.3055	HOMO-10 → LUMO (63%)
8	339.45	0.1332	HOMO-13 → LUMO+1 (48%) HOMO → LUMO+4 (34%)

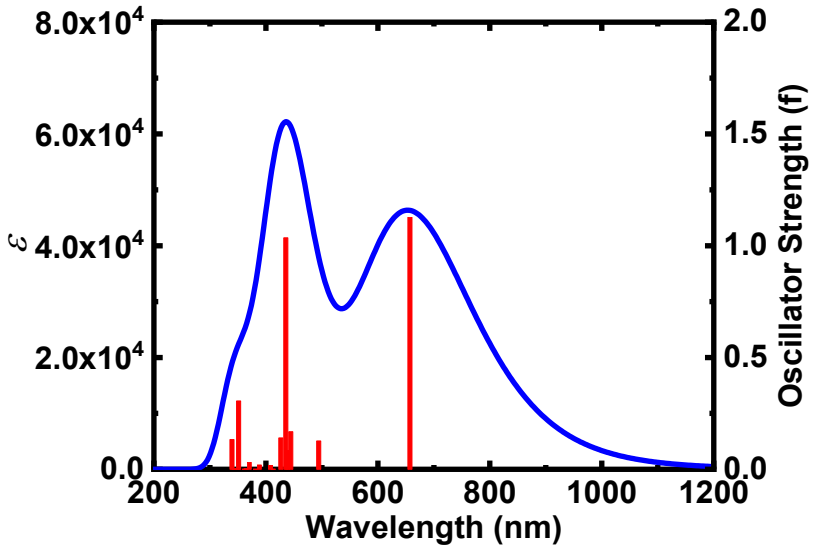

Figure S4.11. Calculated UV-vis absorption spectrum of LTX with DFT (B3LYP(6-31G(d)).

Table S4.5. Selected TD-DFT (B3LYP/6-31G(d)) Calculated Energies, Oscillator Strength and Compositions of Major Electronic Transitions of ITIC.

No.	Wavelength (nm)	Oscillator Strength (*f*)	Major Contributions
1	**648.73**	**2.5293**	**HOMO → LUMO (99%)**
2	488.35	0.1934	HOMO → LUMO+2 (94%)
3	441.16	0.0402	HOMO-1 → LUMO+1 (66%) HOMO-4 → LUMO (28%)
4	**435.34**	**0.4446**	**HOMO-4 → LUMO (65%)** **HOMO-1 → LUMO+1 (28%)**
5	375.3	0.0955	HOMO-1 → LUMO+3 (53%)
6	364.59	0.0664	HOMO → LUMO+4 (66%)

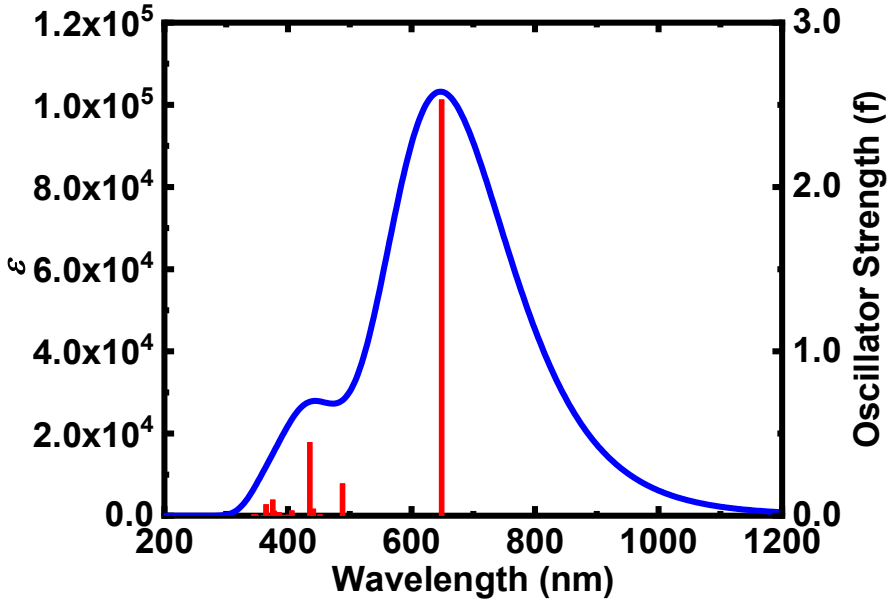

Figure S4.12. Calculated UV-vis absorption spectrum of ITIC with DFT (B3LYP(6-31G(d)).

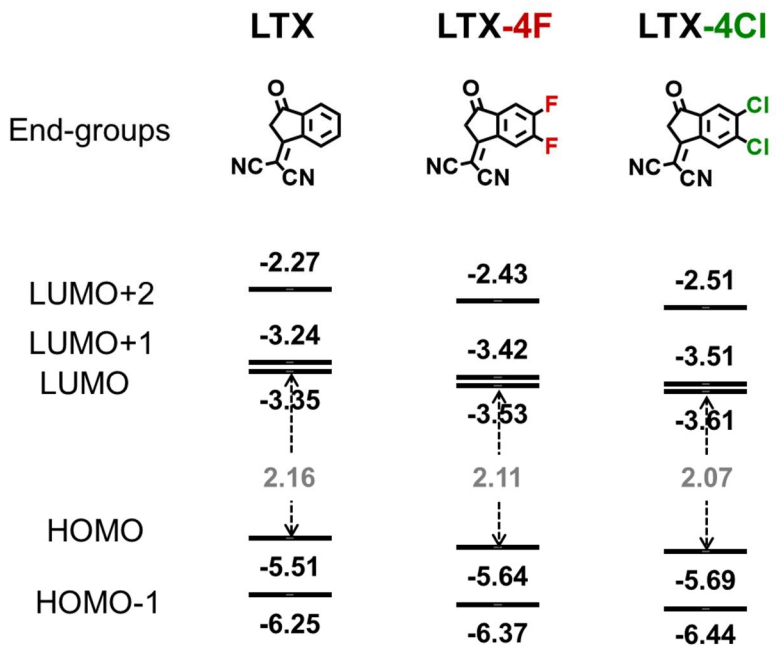

Figure S4.13. Calculated energy levels and band gaps of LTX, LTX-4F and LTX-4Cl with DFT (B3LYP/6-31G(d)).

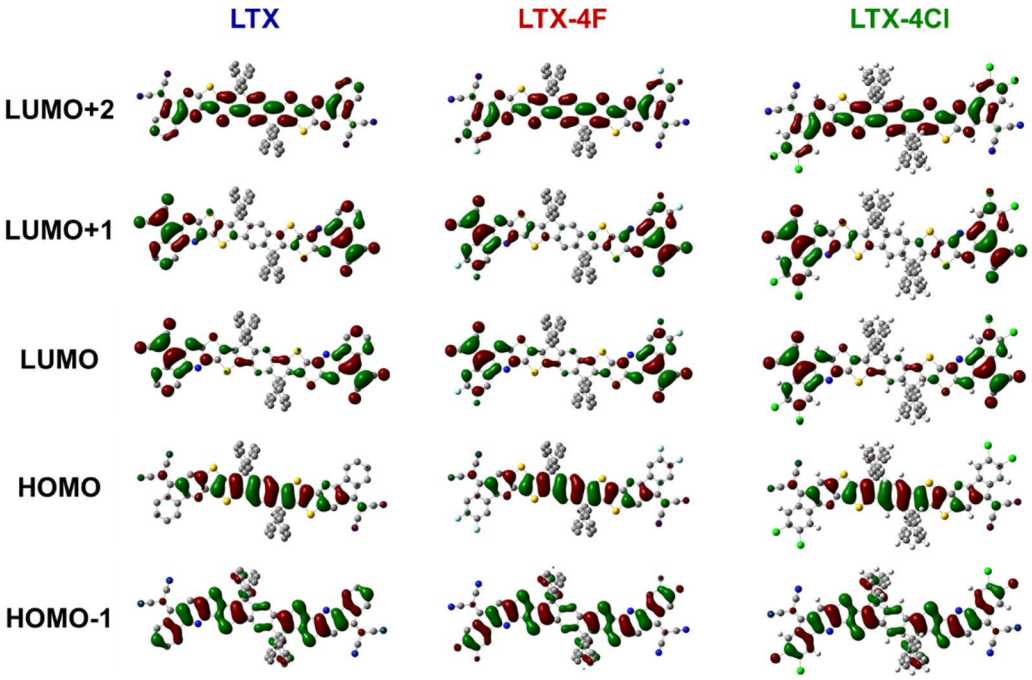

Figure S4.14. Molecular orbitals of LTX, LTX-4F and LTX-4Cl.

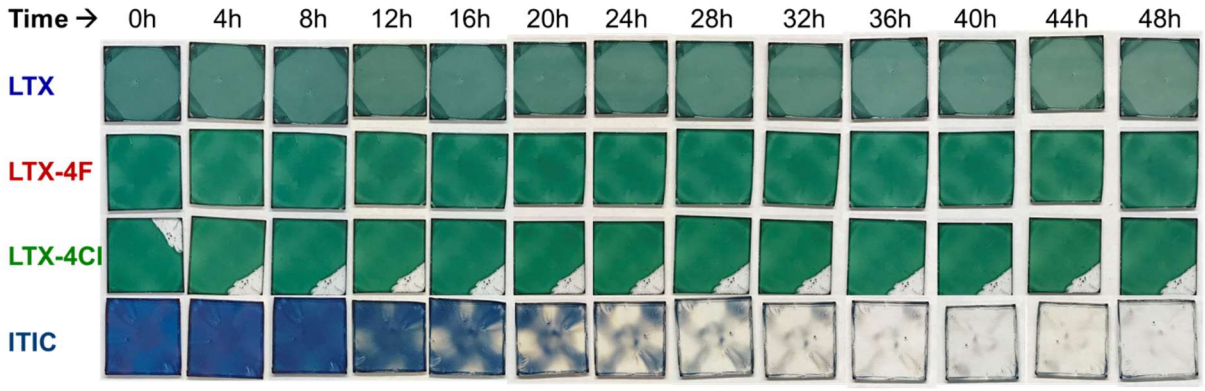

Figure S4.15. Photos of neat films of LTX, LTX-4F, LTX-4Cl and ITIC under continuous 1 sun illumination for up to 48 h.

Table S4.6. Extracted Data of Absorbance at Peak Positions During Photodegradation for Thin Films of LTX, LTX-4F, LTX-4Cl and ITIC

Time (hours)	LTX				LTX-4F				LTX-4Cl				ITIC	
	380-480 nm		550-750 nm		380-480 nm		550-750 nm		380-480 nm		550-750 nm		695 nm	
	Abs.	Abs. (%)	Abs.	Abs. (%)	Abs.	Abs. (%)	Abs.	Abs. (%)	Abs.	Abs. (%)	Abs.	Abs. (%)	Abs.	Abs. (%)
0	0.41	100	0.52	100	0.66	100	0.76	100	0.70	100	0.75	100	1.67	100
4	0.40	97.99	0.50	96.02	0.66	98.75	0.74	97.70	0.69	97.74	0.73	96.62	1.19	71.47
8	0.40	99.10	0.49	94.88	0.64	96.48	0.72	94.73	0.68	97.22	0.71	94.90	0.92	54.79
12	0.38	94.44	0.46	88.83	0.64	95.85	0.71	93.00	0.67	95.20	0.69	91.91	0.66	39.55
16	0.38	92.44	0.45	85.76	0.62	92.68	0.68	89.23	0.65	93.21	0.67	89.30	0.43	25.86
20	0.37	91.15	0.43	83.03	0.62	93.44	0.68	88.93	0.65	92.31	0.66	87.63	0.28	16.95
24	0.36	89.74	0.42	80.23	0.62	93.79	0.67	88.16	0.64	91.68	0.65	86.14	0.14	8.13
28	0.36	88.10	0.40	77.65	0.61	91.35	0.65	85.06	0.63	90.43	0.63	84.14	0.10	5.92
32	0.35	86.44	0.39	74.99	0.60	90.87	0.64	83.72	0.62	88.52	0.61	81.56	0.06	3.87
36	0.35	87.00	0.38	73.57	0.60	90.16	0.62	82.14	0.63	89.18	0.61	81.32	0.05	3.02
40	0.35	85.01	0.37	70.61	0.59	88.97	0.61	80.19	0.61	87.50	0.59	79.09	0.04	2.26
44	0.33	82.49	0.35	67.44	0.58	87.57	0.59	78.10	0.61	86.97	0.59	77.90	0.03	1.99
48	0.33	80.28	0.33	64.38	0.58	86.71	0.58	76.40	0.60	85.31	0.57	75.59	0.03	1.72

X-ray Crystallography of LTX. A black prism, measuring 0.30 × 0.25 × 0.10 mm^3 was mounted on a loop with oil. Data was collected at -173ºC on a Bruker APEX II single crystal X-ray diffractometer, Mo-radiation.

Crystal-to-detector distance was 40 mm and exposure time was 150 seconds per frame for all sets. The scan width was 0.75º. Data collection was 100% complete to 20.816º in ϑ. A total of 13825 reflections were collected covering the indices, $-35 \leq h \leq 30$, $0 \leq k \leq 66$, $0 \leq l \leq 22$, R_{int} = 0.1893 indicated that the data was very weak. Indexing and unit cell refinement indicated a C-centered monoclinic lattice. The space group was found to be Cc (No. 9).

The data was integrated and scaled using SAINT, SADABS within the APEX2 software package by Bruker.[90]

Solution by direct methods (SHELXS, SIR97[90]) produced a complete heavy atom phasing model consistent with the proposed structure. The structure was completed by difference Fourier synthesis with SHELXL97.[91-93] Scattering factors are from Waasmair and Kirfel.[94] Hydrogen atoms were placed in geometrically idealised positions and constrained to ride on their parent atoms with C---H distances in the range 0.95-1.00 Angstrom. Isotropic thermal parameters U_{eq} were fixed such that they were $1.2U_{eq}$ of their parent atom U_{eq} for CH's and $1.5U_{eq}$ of their parent atom U_{eq} in case of methyl groups. All non-hydrogen atoms were refined anisotropically by full-matrix least-squares.

Data were summaried in **Table S4.7**.

Table S4.7. Crystallographic data for ladder molecule acceptor, LTX.

Empirical formula	C134 H160 N6 S4	
Formula weight	1982.91	
Temperature	100(2) K	
Wavelength	0.71073 Å	
Crystal system	Monoclinic	
Space group	C c	
Unit cell dimensions	a = 29.872(4) Å	α= 90°.
	b = 55.816(9) Å	β= 122.556(7)°.
	c = 18.769(2) Å	γ = 90°.
Volume	26377(7) $Å^3$	
Z	8	
Density (calculated)	0.999 Mg/m^3	
Absorption coefficient	0.118 mm^{-1}	
F(000)	8560	
Crystal size	0.300 x 0.150 x 0.100 mm^3	
Theta range for data collection	1.361 to 20.816°.	
Index ranges	-35<=h<=30, 0<=k<=66, 0<=l<=22	
Reflections collected	13825	
Independent reflections	13825 [R(int) = 0.1893]	
Completeness to theta = 20.816°	100.0 %	
Refinement method	Full-matrix least-squares on F^2	
Data / restraints / parameters	13825 / 6861 / 2449	
Goodness-of-fit on F^2	1.082	
Final R indices [I>2sigma(I)]	R1 = 0.2014, wR2 = 0.4160	
R indices (all data)	R1 = 0.4699, wR2 = 0.5770	
Absolute structure parameter	0.8(6)	
Largest diff. peak and hole	0.592 and -0.446 $e.Å^{-3}$	

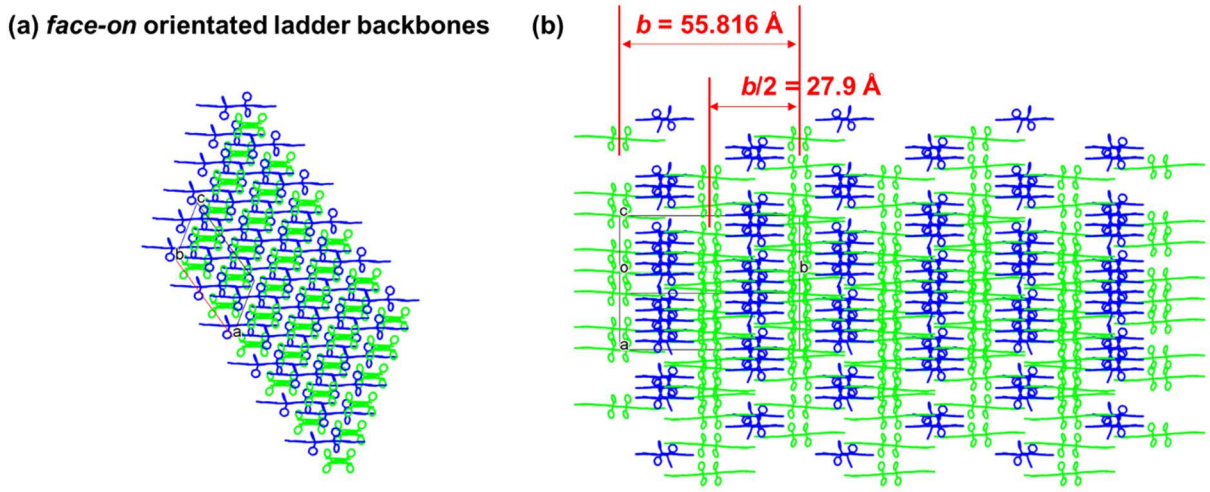

Figure S4.16. Crystal packing of LTX, viewing in the horizontal direction of *face-on* oriented ladder backbones. Alkyl side chains are omitted for clarity.

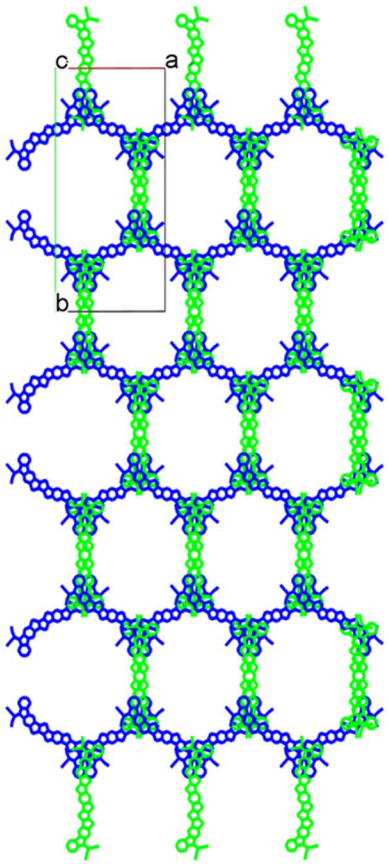

Figure S4.17. Crystal packing of LTX (top view, along *c*). Alkyl side chains are omitted for clarity.

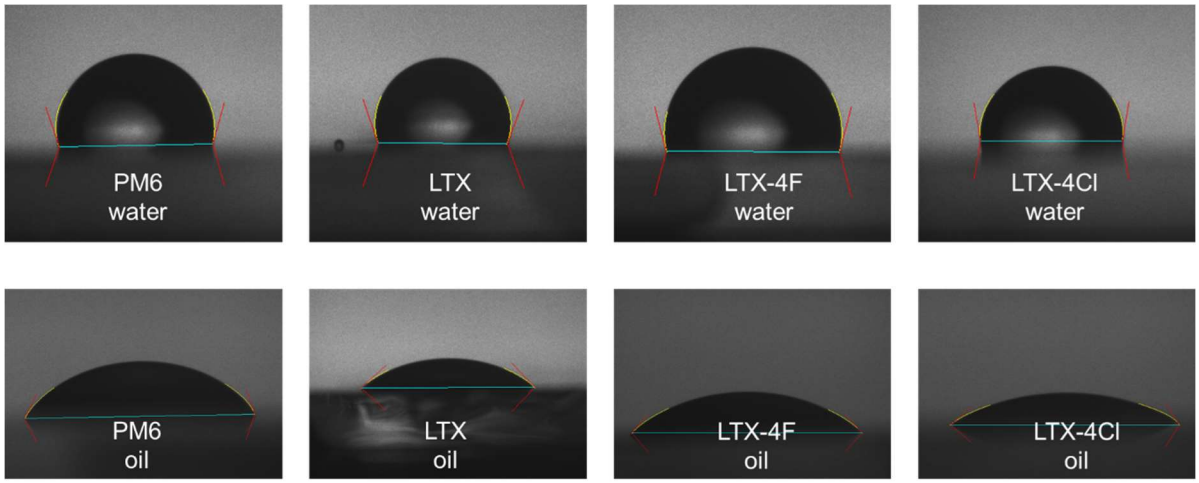

Figure S4.18. Views of surface contact measurements for the neat films of PM6 and the ladder small molecule acceptors: LTX, LTX-4F and LTX-4Cl, using water and diiodomethane as the wetting liquid.

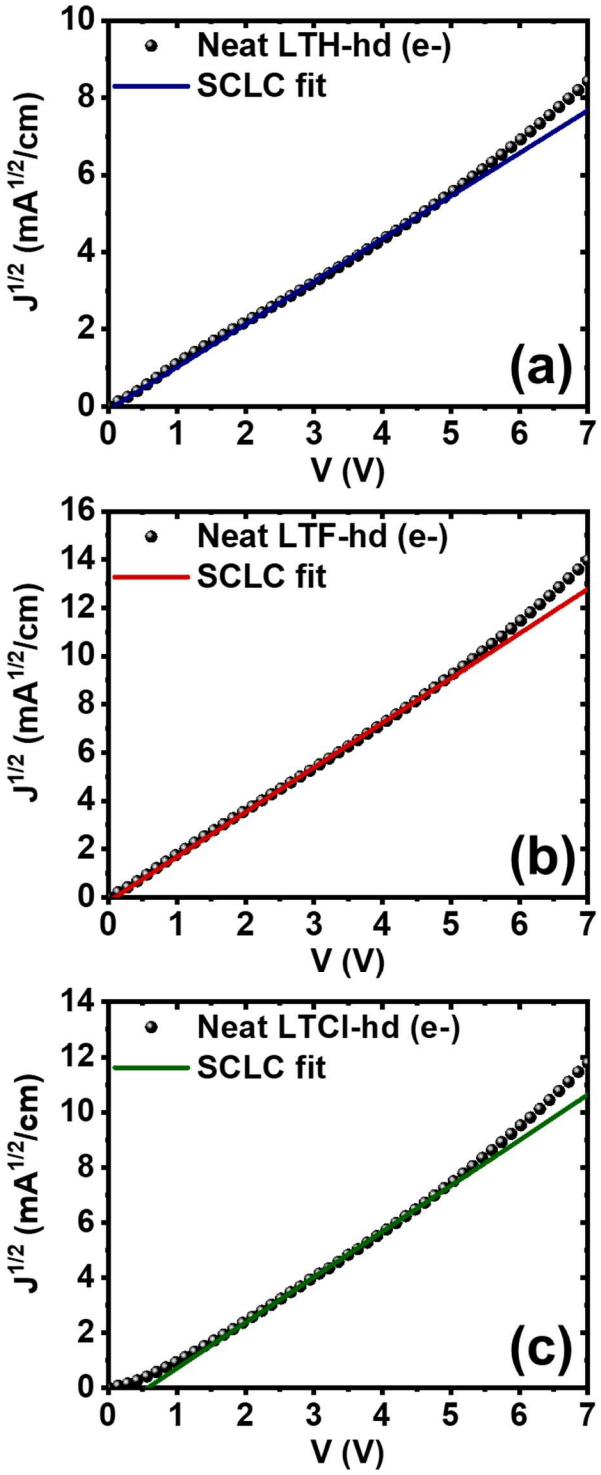

Figure S4.19. SCLC fitting for electron-only devices based on neat films of: (a) LTX; (b) LTX-4F; and (c) LTX-4Cl.

Table S4.8. SCLC Electron Mobilities of the LTXs Neat Films

Acceptors	μ_e (10^{-4} cm^2/Vs)
LTX-hd	1.02 (± 0.12)
LTX-hd-4F	3.40 (± 1.07)
LTX-hd-4Cl	2.94 (± 0.30)

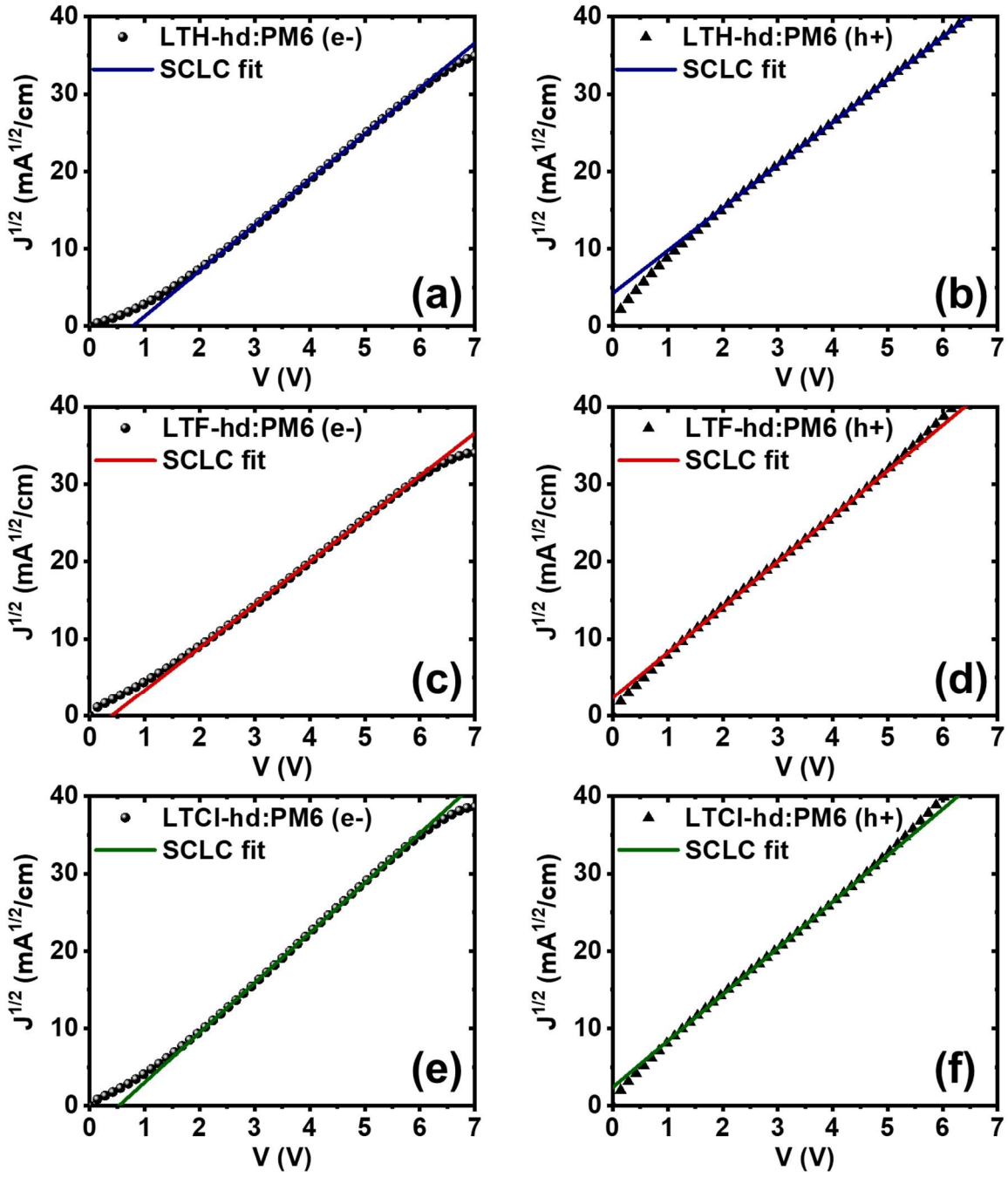

Figure S4.20. SCLC fitting for single-carrier devices of the PM6:LTXs blend films: (a) PM6:LTX (electron-only); (b) PM6:LTX (hole-only); (c) PM6:LTX-4F (electron-only); (d) PM6:LTX-4F (hole-only); (e) PM6:LTX-4Cl (electron-only); and (f) PM6:LTX-4Cl (hole-only).

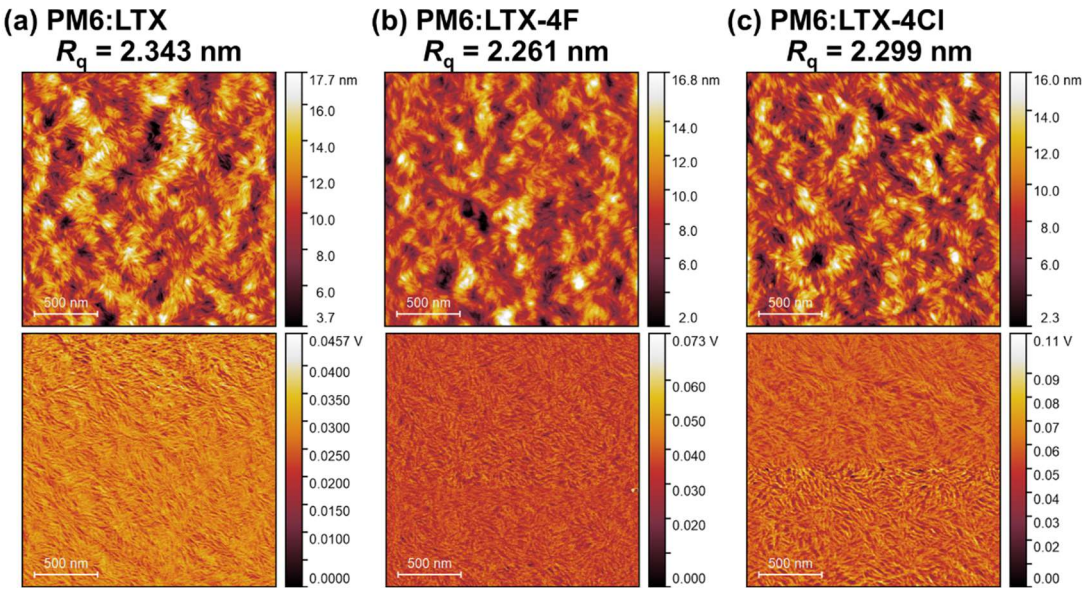

Figure S4.21. AFM images height and phase images (2 μm × 2 μm) of blend films based on (a) PM6:LTX, (b) PM6:LTX-4F and (c) PM6:LTX-4Cl, under optimal processing conditions.

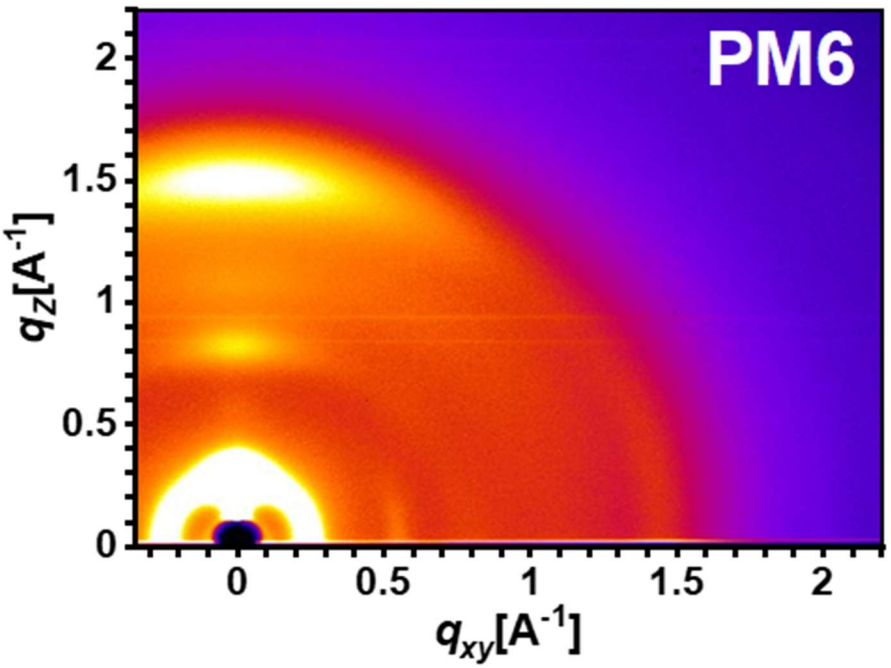

Figure S4.22. 2D GIXD diffraction pattern for the neat film of PM6.

Table S4.9. Summary of Major In-Plane (IP) and Out-of-Plane (OOP) Peaks from 2D GIXD and the Corresponding d-Spacing Distances and Crystalline Coherence Length (L_c)

Films	IP (100)			OOP (001)					
	q_{xy} [Å^{-1}]	d-spacing [Å]	L_c [nm]	q_z [Å^{-1}]	d-spacing [Å]	L_c [nm]	q_z [Å^{-1}]	d-spacing [Å]	L_c [nm]
LTX	0.228, 0.393	27.6, 16.0	20.55	-	-	-	1.81	3.47	2.95
LTX-4F	0.240	26.2	15.27	-	-	-	1.77	3.54	2.10
LTX-4Cl	0.249	25.3	13.42	-	-	-	1.80	3.49	2.47
PM6	0.289	21.7	7.23	3.259	19.28	6.25	1.69	3.72	2.09
PM6:LTX	0.222, 0.289	28.4, 21.7	21.33, 11.85	3.256	19.28	6.96	1.79	3.51	2.54
PM6:LTX-4F	0.246 (shoulder)	25.5	7.64	3.075	20.43	9.43	1.76	3.58	2.03
PM6:LTX-4Cl	0.258 (broad)	24.3	8.71	3.075	20.43	8.74	1.77	3.56	2.06

Below are ^{1}H NMR, ^{13}C NMR, ^{17}F NMR and MALDI-TOF spectra for synthesized compounds:

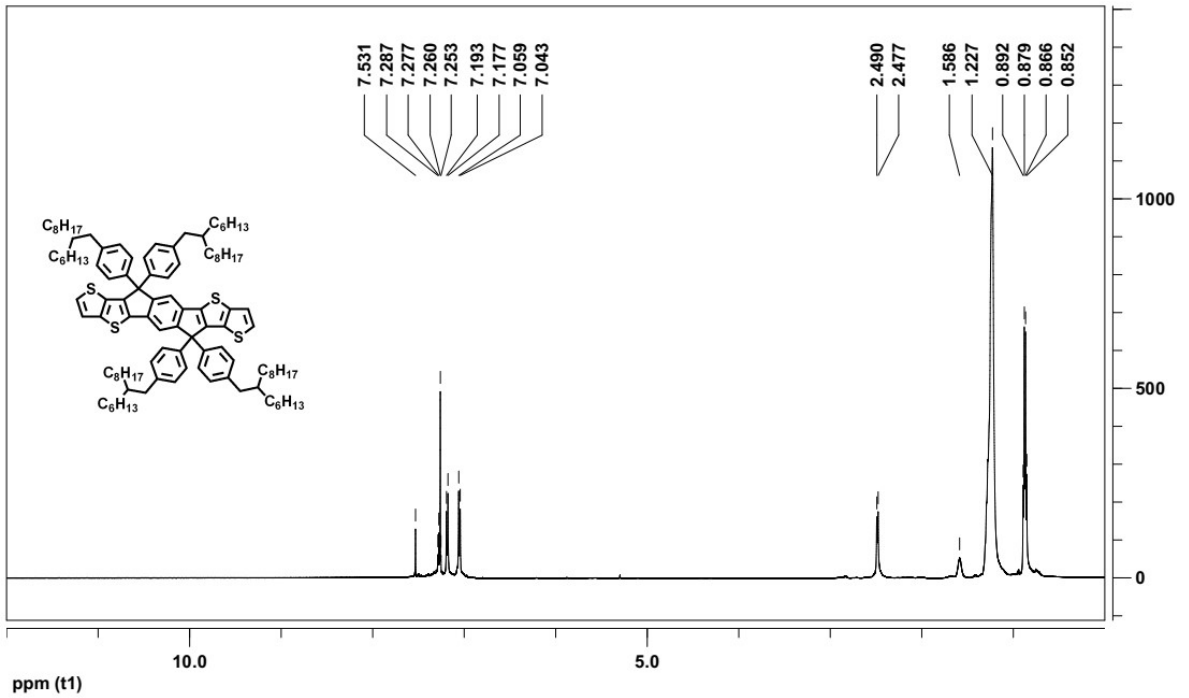

Figure S4.23. ^{1}H NMR (500 MHz, $CDCl_3$) spectrum of IDTT-hd.

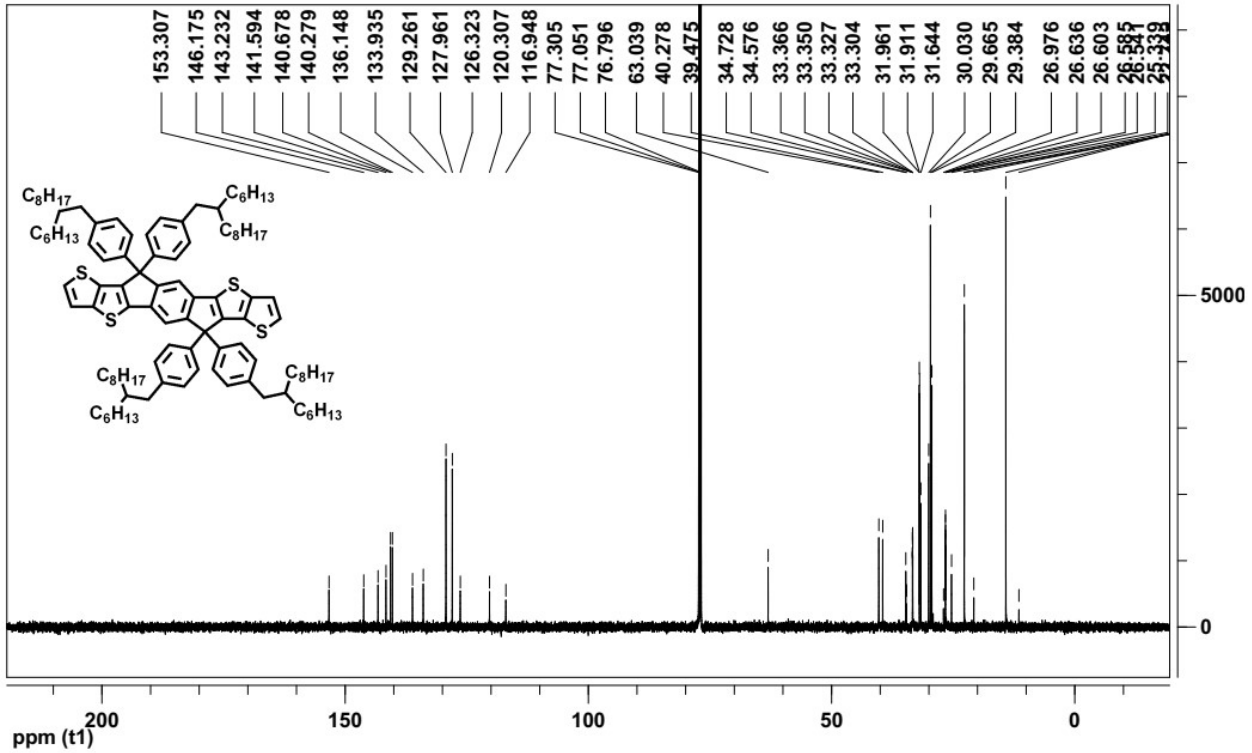

Figure S4.24. ^{13}C NMR (125 MHz, $CDCl_3$) spectrum of IDTT-hd.

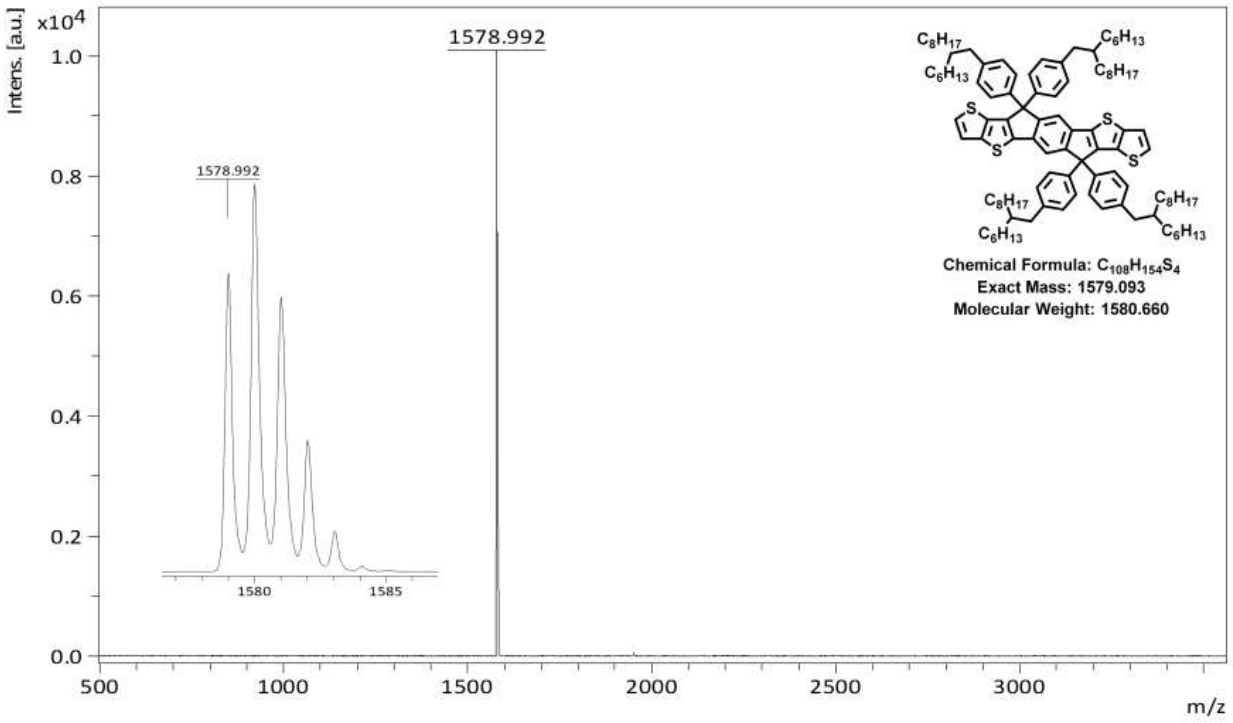

Figure S4.25. MALDI-TOF mass spectrum of IDTT-hd.

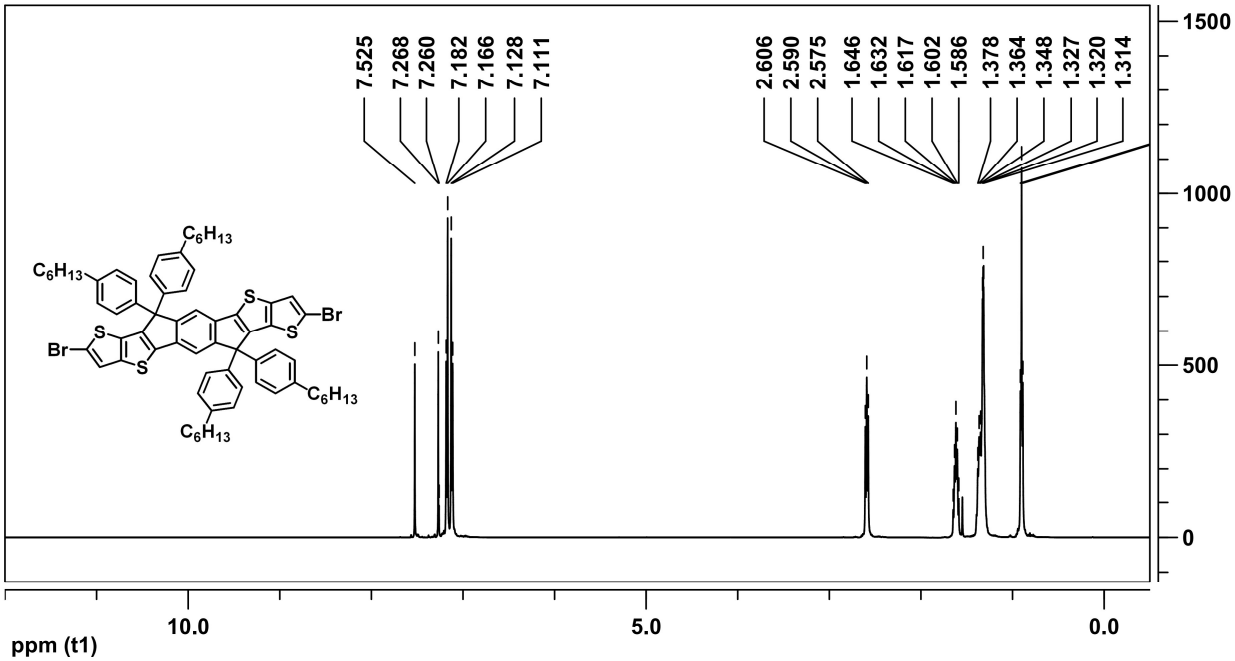

Figure S4.26. ^{1}H NMR (500 MHz, $CDCl_3$) spectrum of IDTT-C_6-2Br.

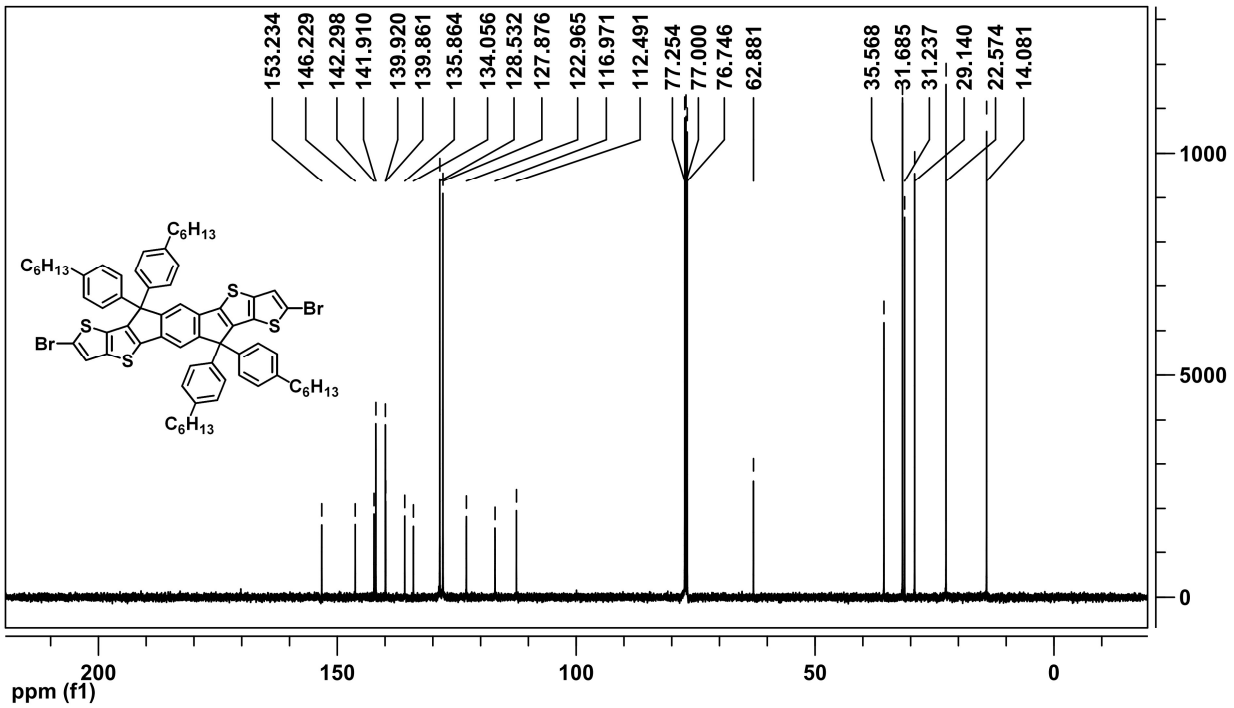

Figure S4.27. ^{13}C NMR (125 MHz, $CDCl_3$) spectrum of IDTT-C_6-2Br.

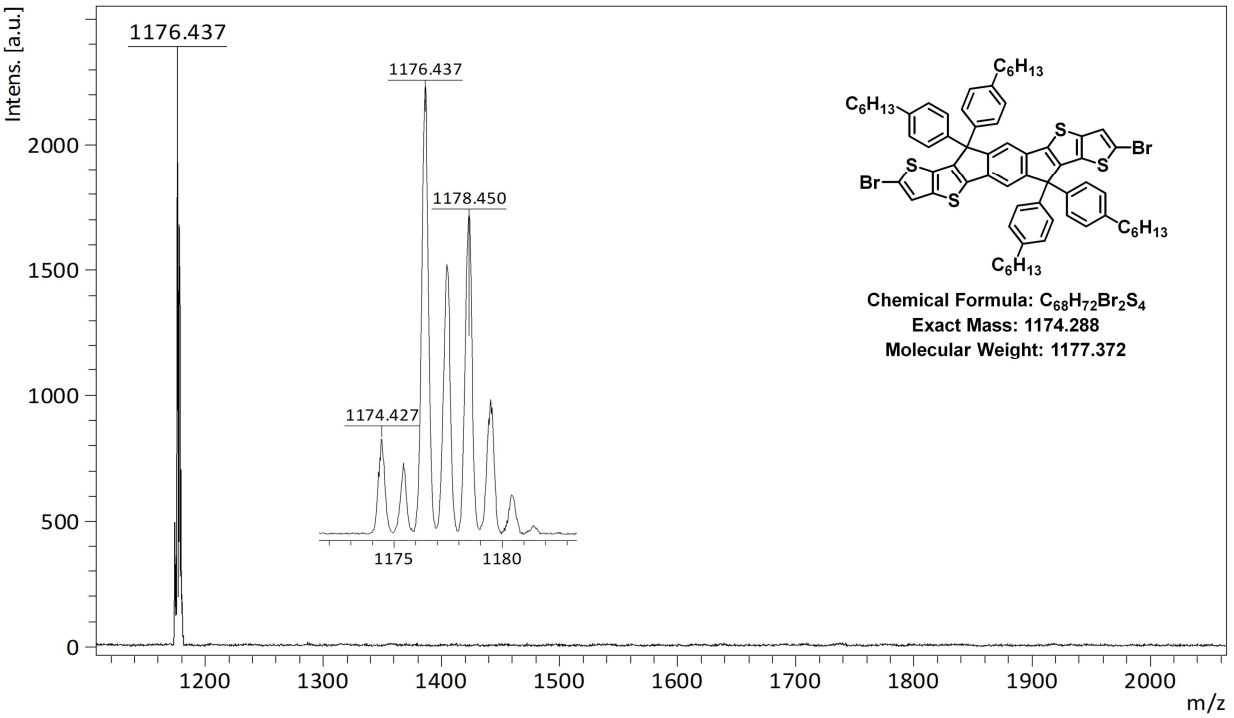

Figure S4.28. MALDI-TOF mass spectrum of IDTT-C_6-2Br.

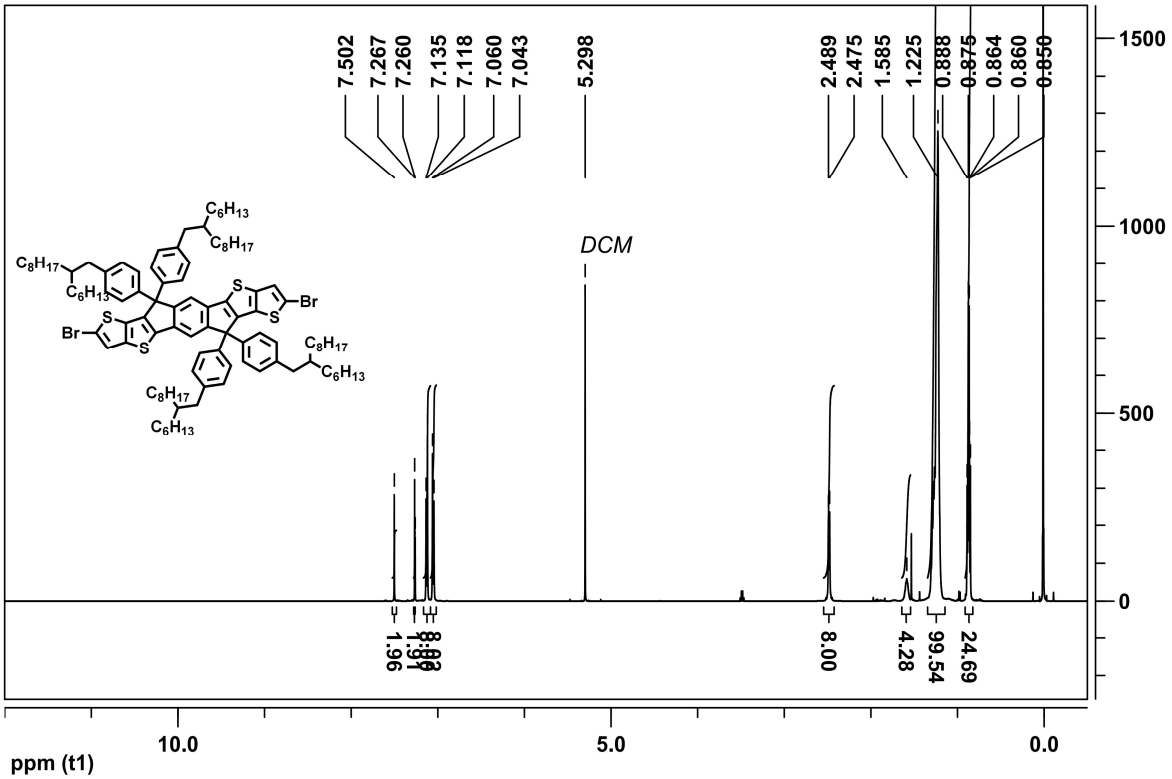

Figure S4.29. ^{1}H NMR (500 MHz, $CDCl_3$) spectrum of IDTT-hd-2Br.

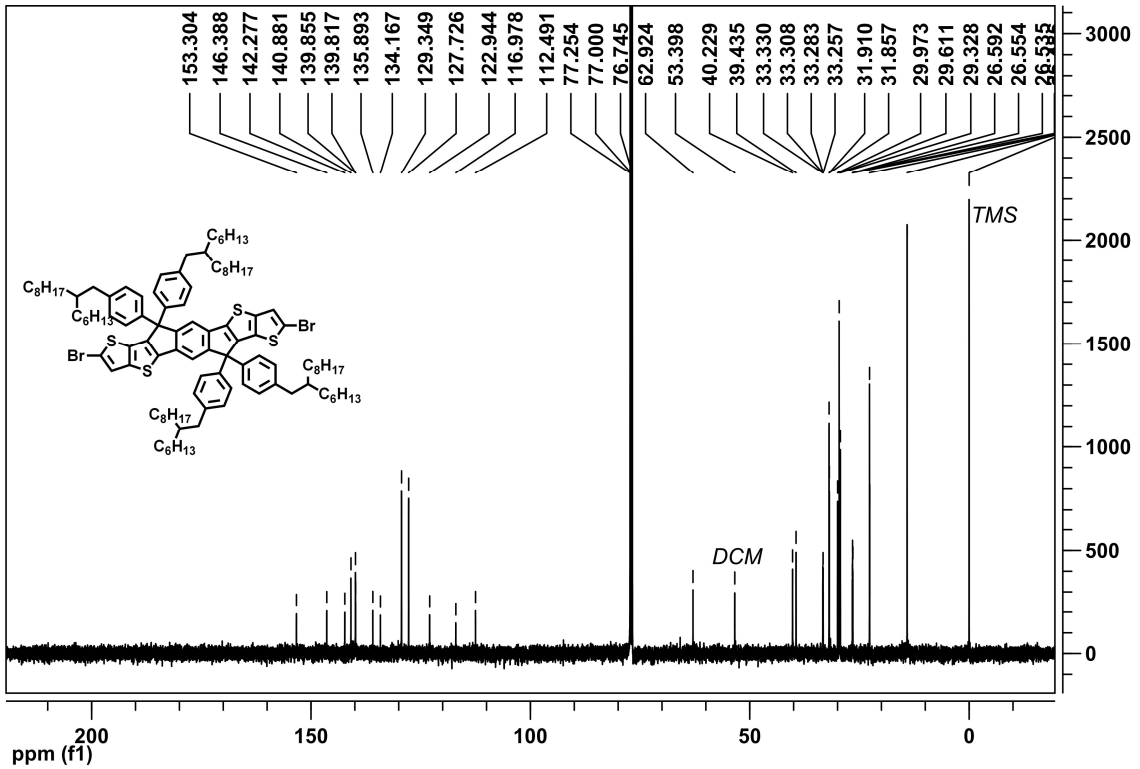

Figure S4.30. ^{13}C NMR (125 MHz, $CDCl_3$) spectrum of IDTT-hd-2Br.

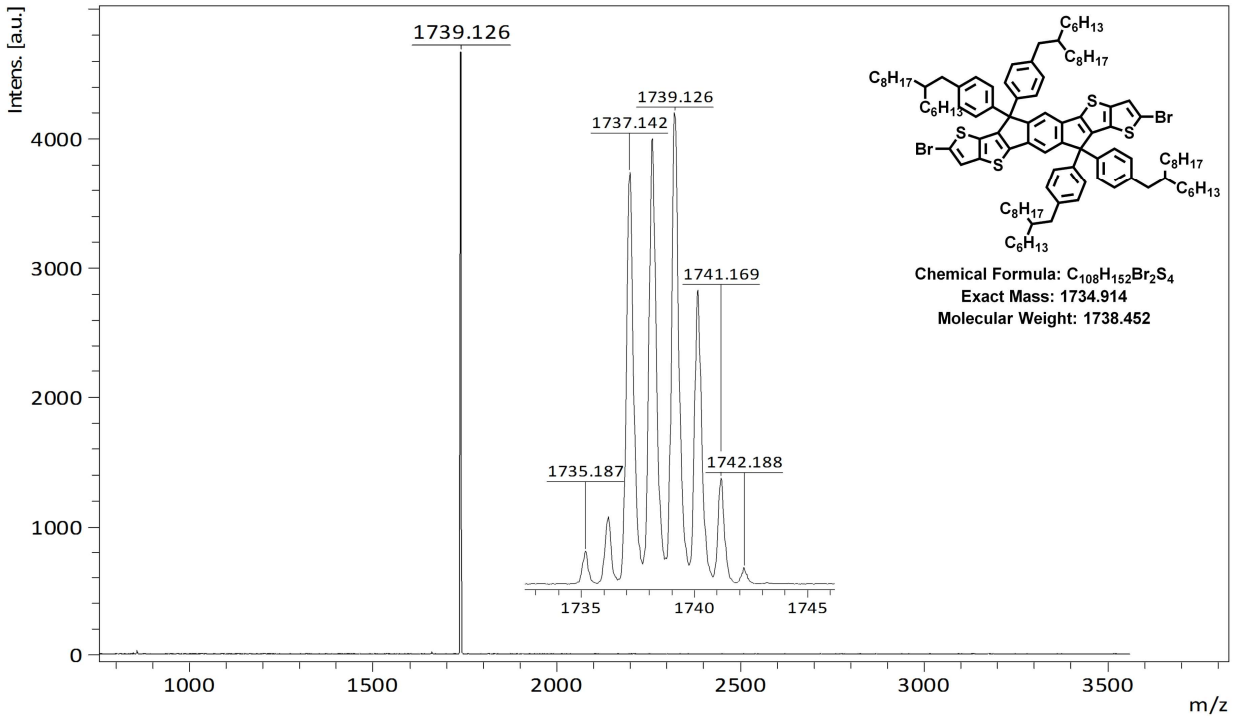

Figure S4.31. MALDI-TOF mass spectrum of IDTT-hd-2Br.

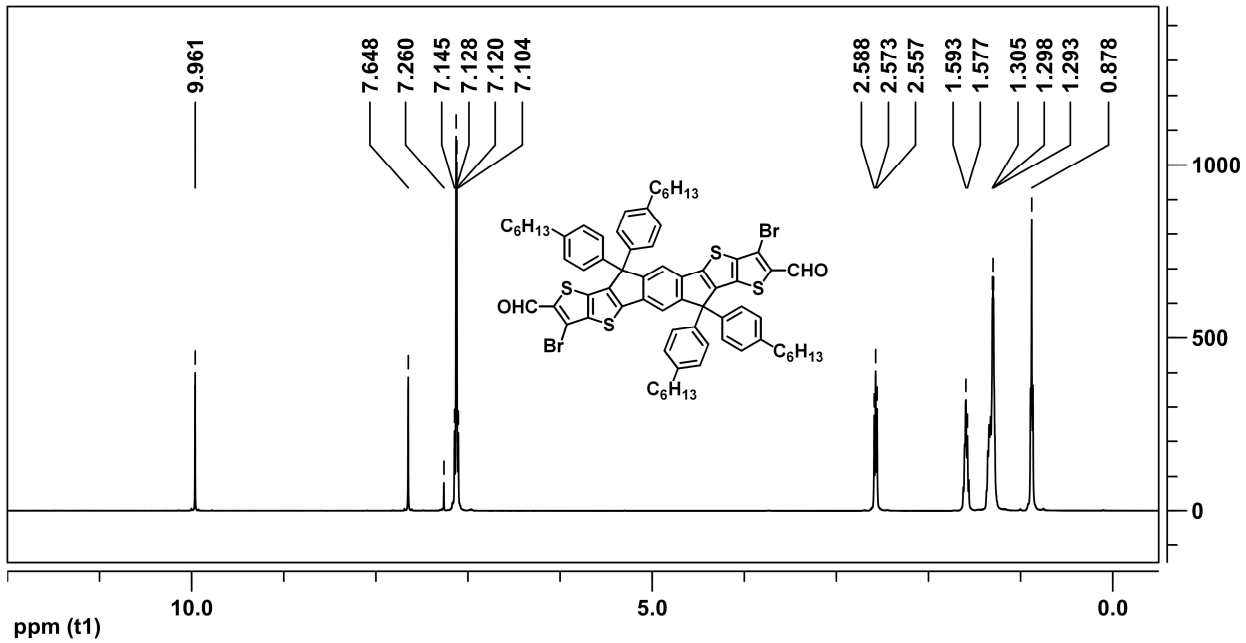

Figure S4.32. ^{1}H NMR (500 MHz, $CDCl_3$) spectrum of IDTT-C_6-2CHO-2Br.

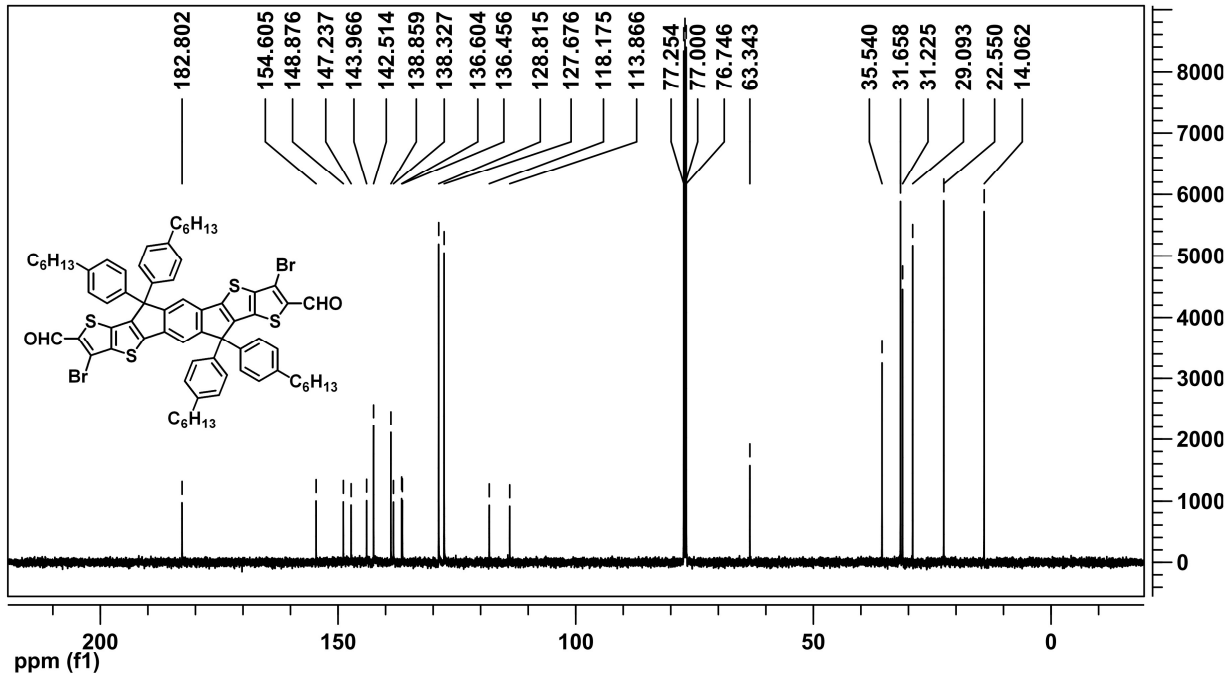

Figure S4.33. ^{13}C NMR (125 MHz, $CDCl_3$) spectrum of IDTT-C_6-2CHO-2Br.

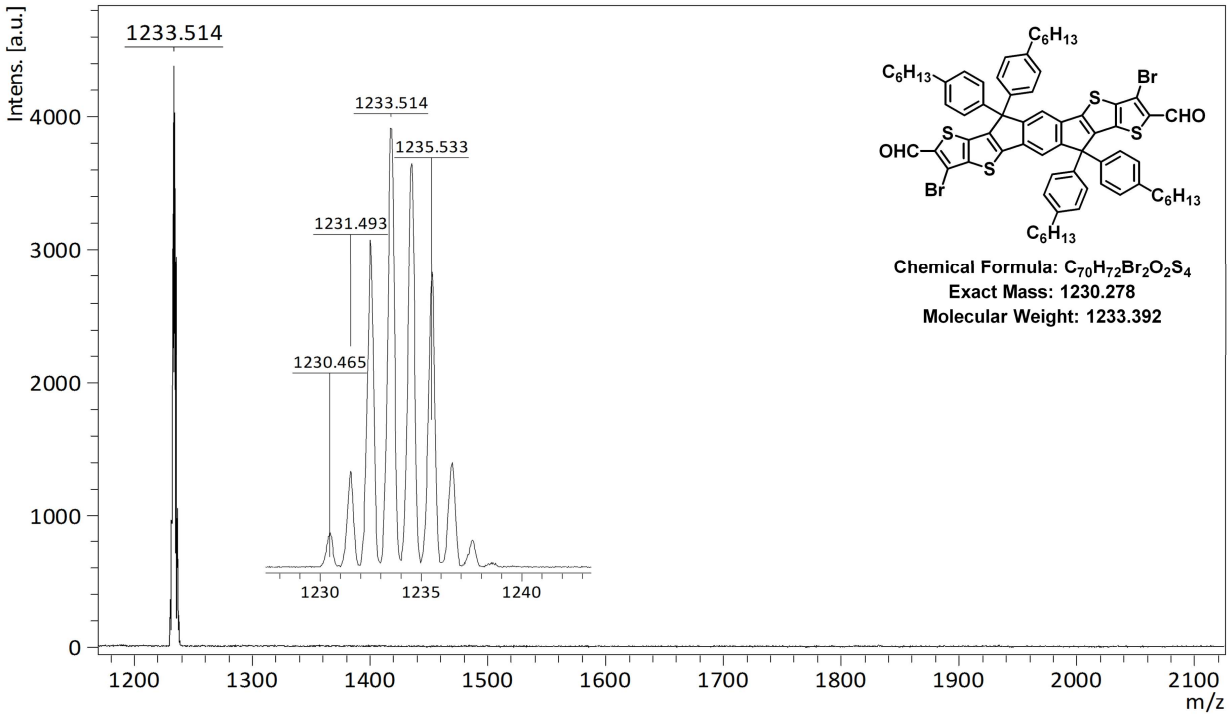

Figure S4.34. MALDI-TOF mass spectrum of IDTT-C_6-2CHO-2Br.

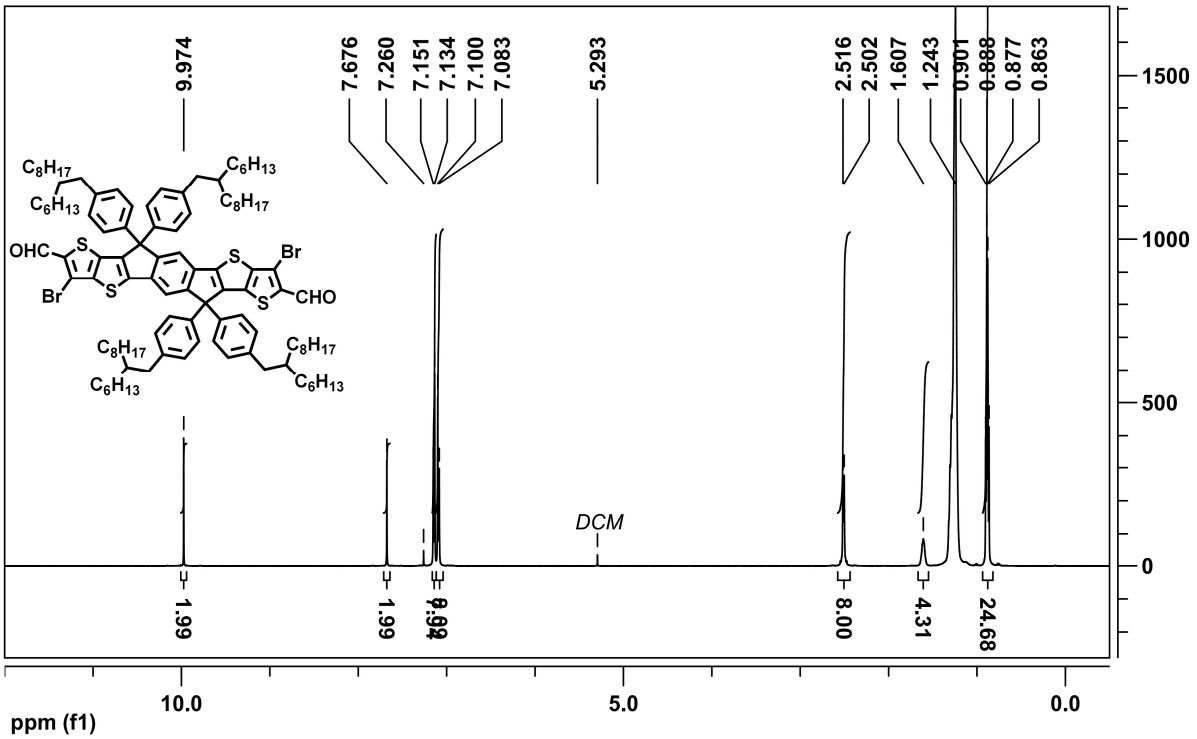

Figure S4.35. ^{1}H NMR (500 MHz, $CDCl_3$) spectrum of IDTT-hd-2CHO-2Br.

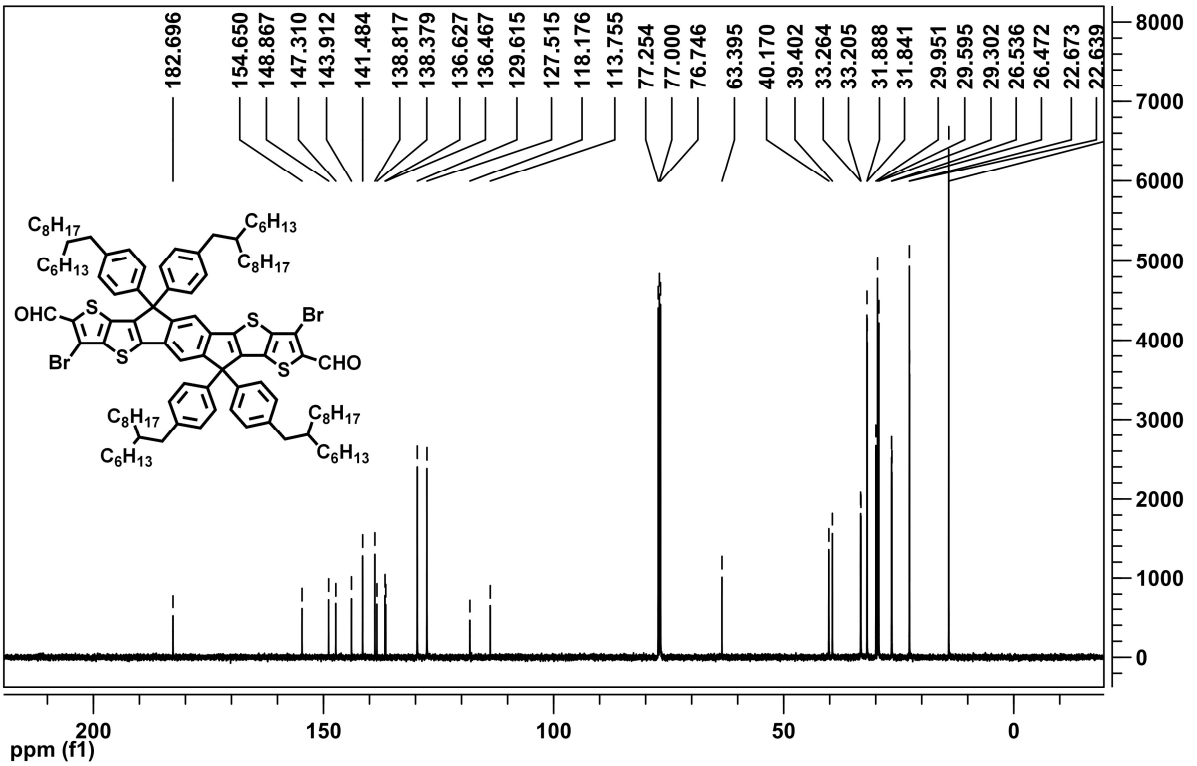

Figure S4.36. ^{13}C NMR (125 MHz, $CDCl_3$) spectrum of IDTT-hd-2CHO-2Br.

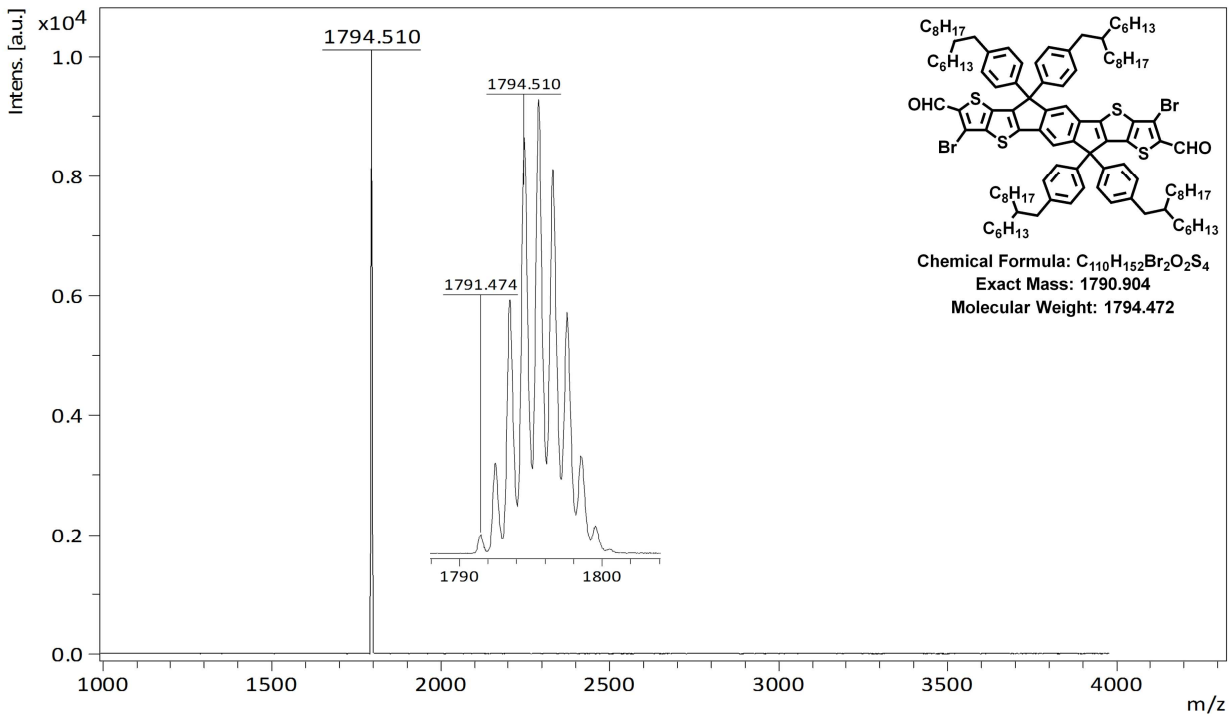

Figure S4.37. MALDI-TOF mass spectrum of IDTT-hd-2CHO-2Br.

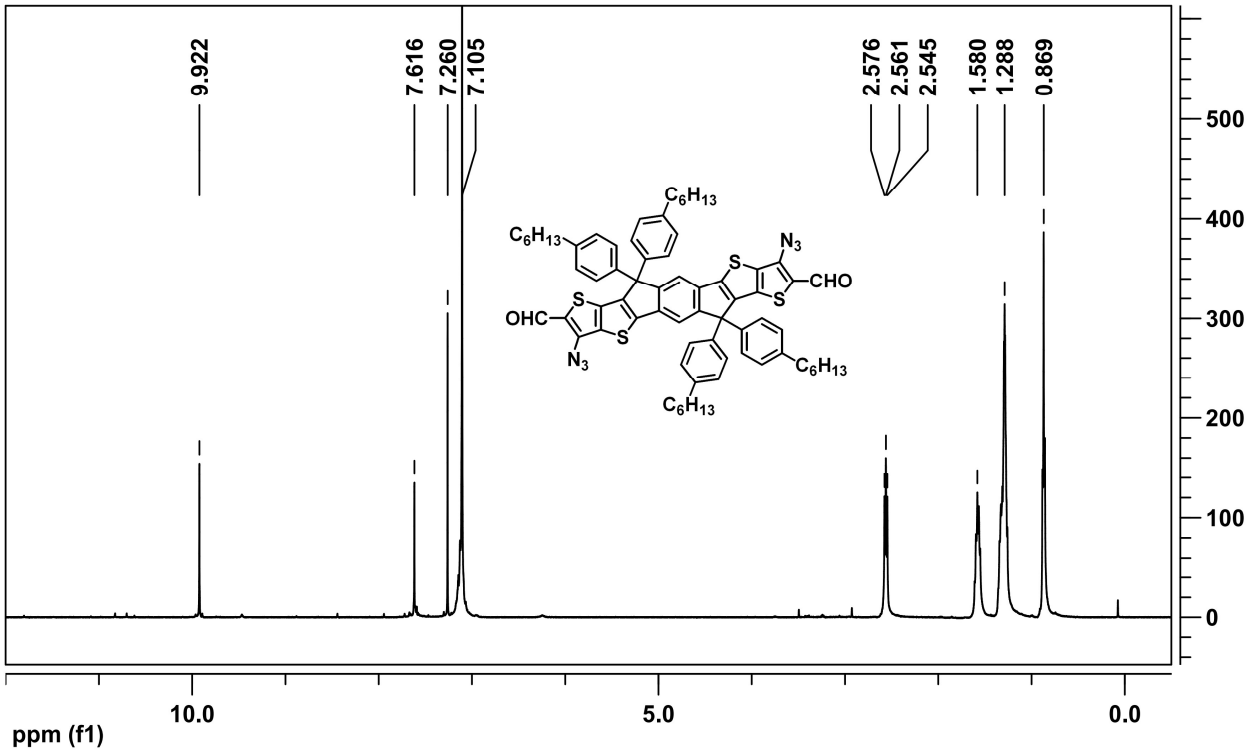

Figure S4.38. ^{1}H NMR (500 MHz, $CDCl_3$) spectrum of IDTT-C_6-2CHO-2N_3.

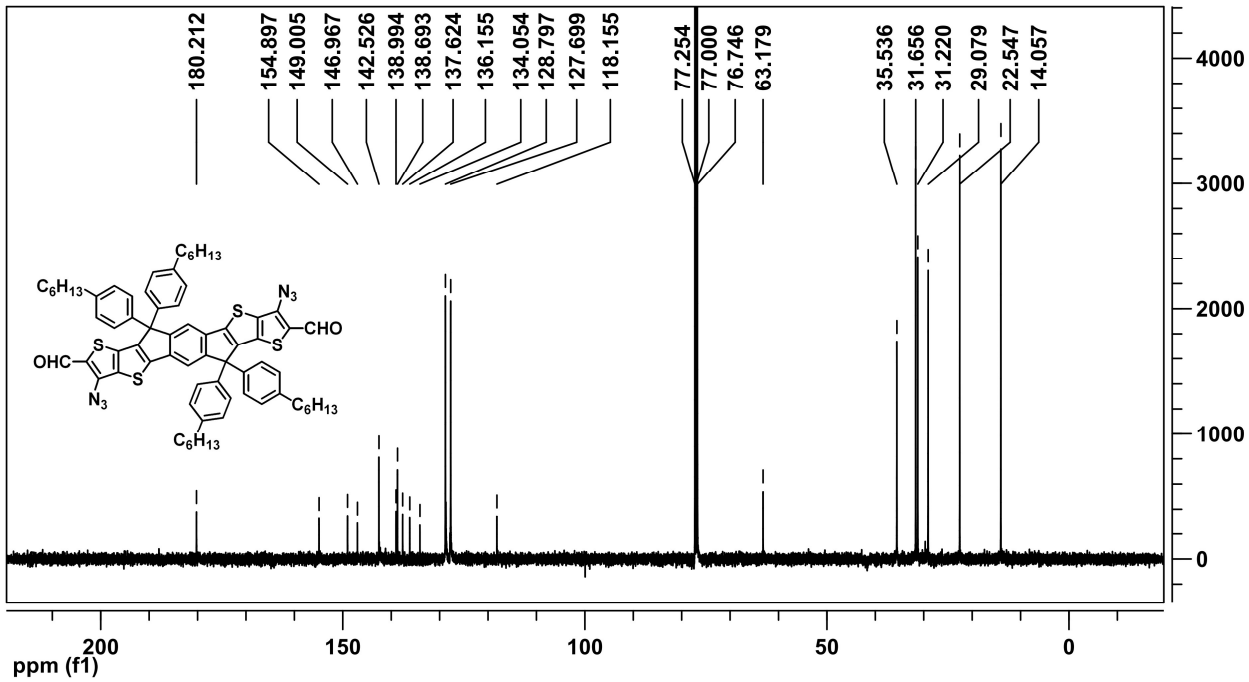

Figure S4.39. ^{13}C NMR (125 MHz, $CDCl_3$) spectrum of IDTT-C_6-2CHO-2N_3..

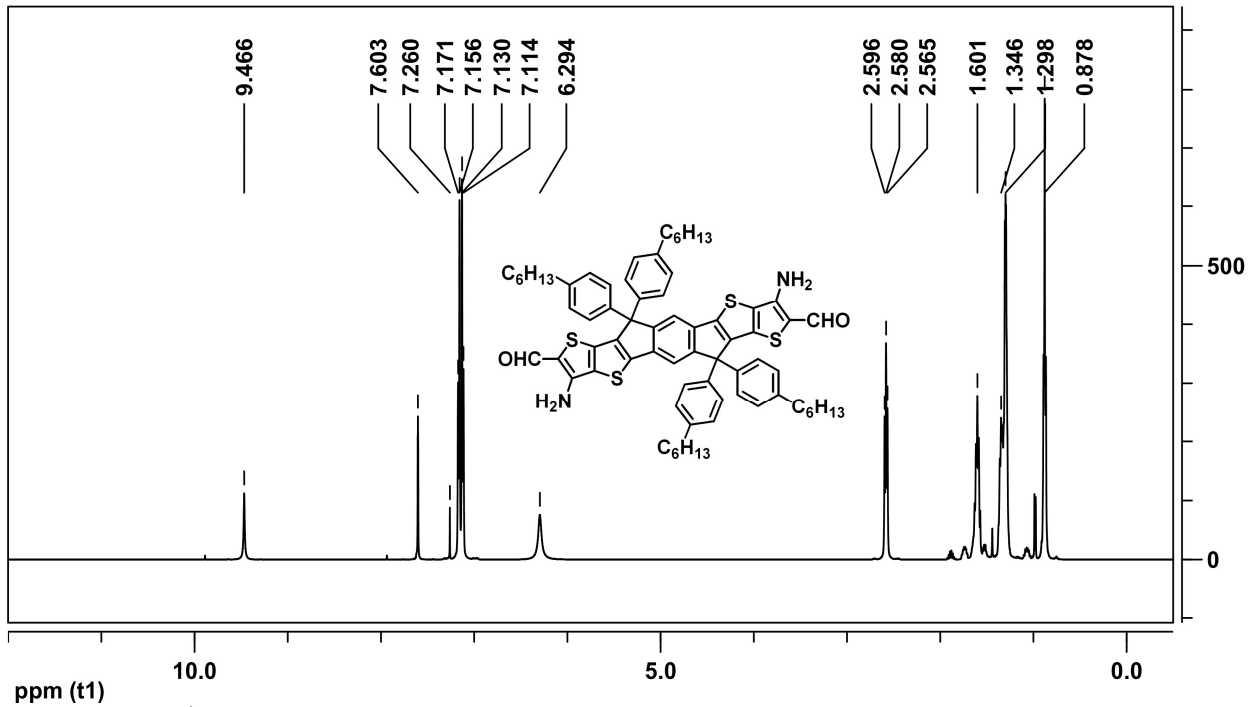

Figure S4.40. ^{1}H NMR (500 MHz, $CDCl_3$) spectrum of IDTT-C_6-2CHO-2NH_2.

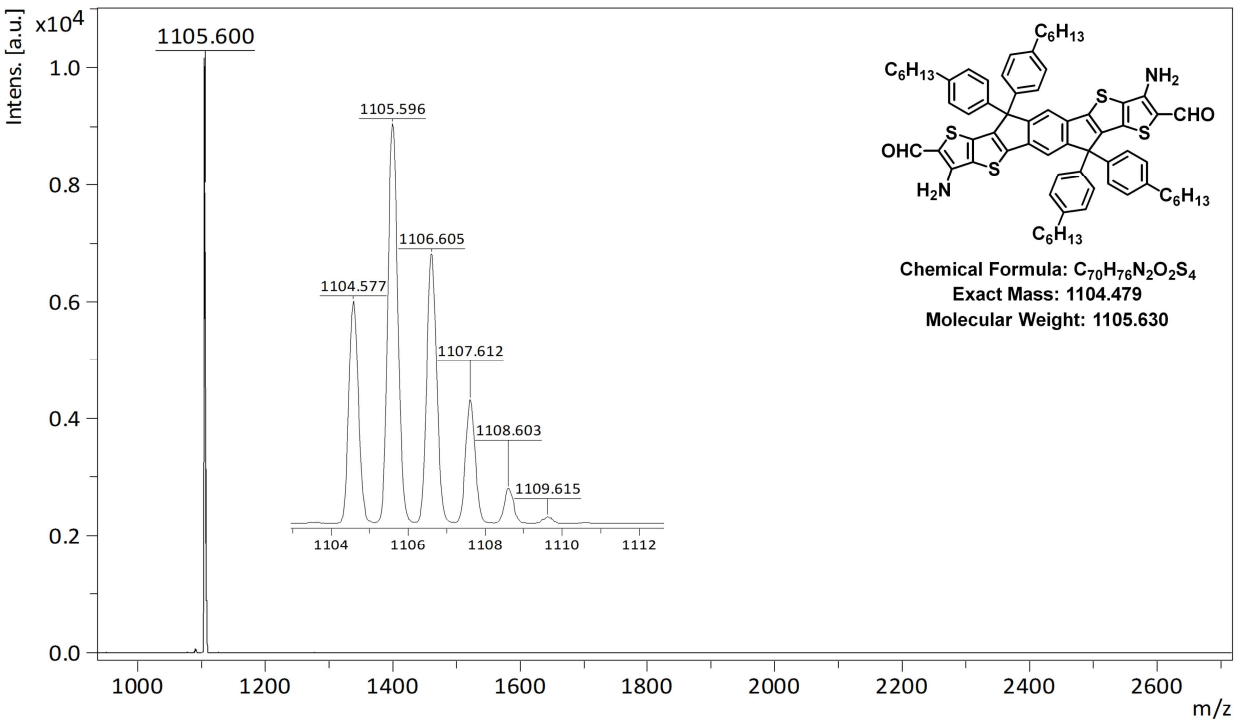

Figure S4.41. MALDI-TOF mass spectrum of IDTT-C_6-2CHO-2NH_2.

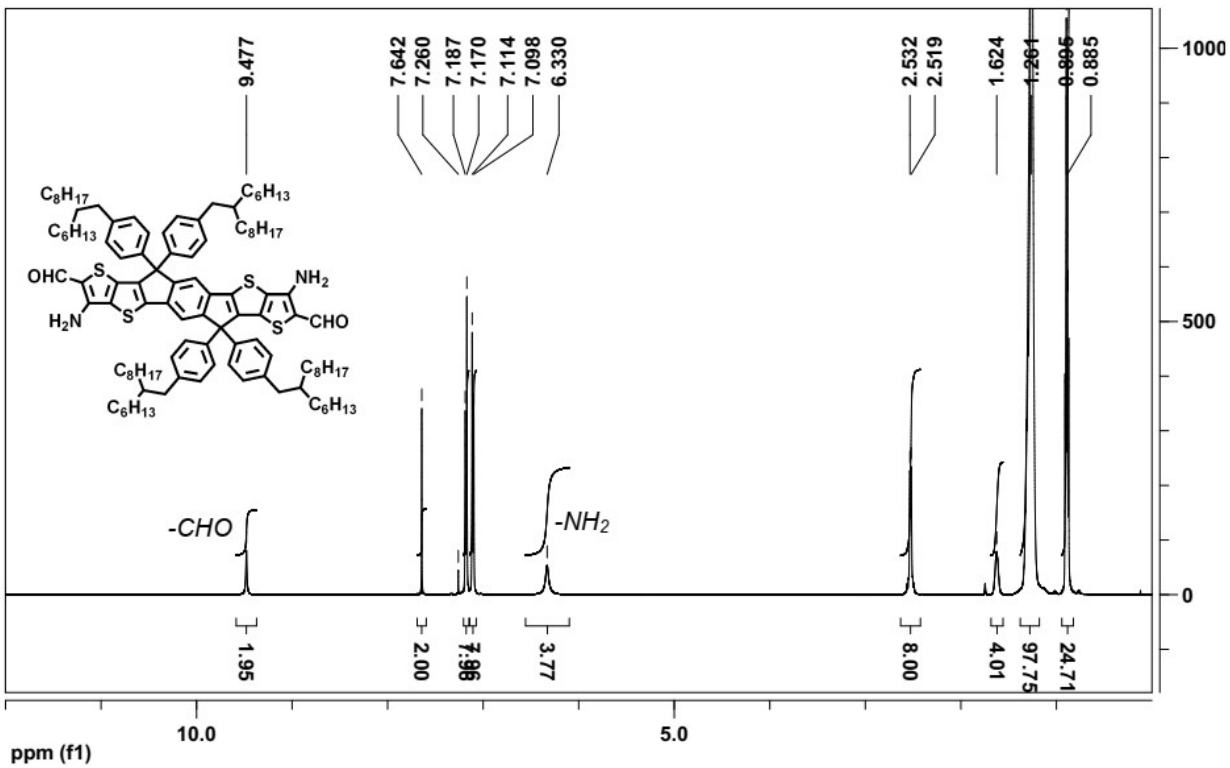

Figure S4.42. ^{1}H NMR (500 MHz, $CDCl_3$) spectrum of IDTT-hd-2CHO-2NH_2.

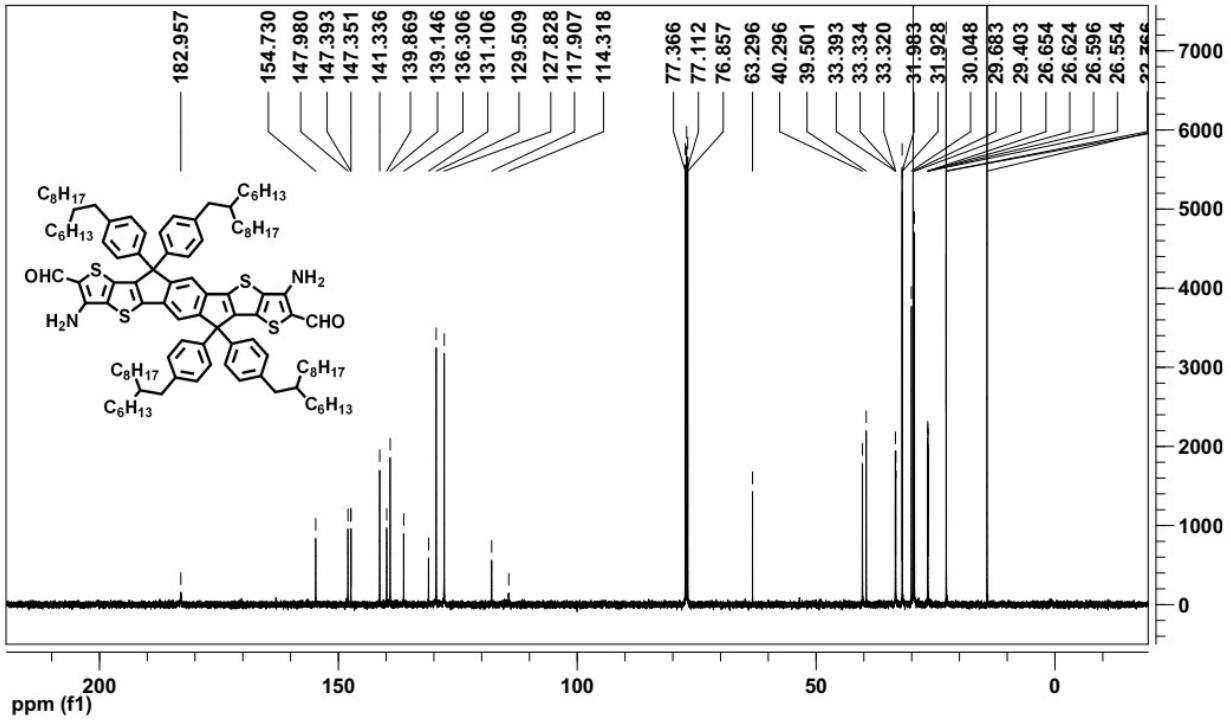

Figure S4.43. ^{13}C NMR (125 MHz, $CDCl_3$) spectrum of IDTT-hd-2CHO-2NH_2.

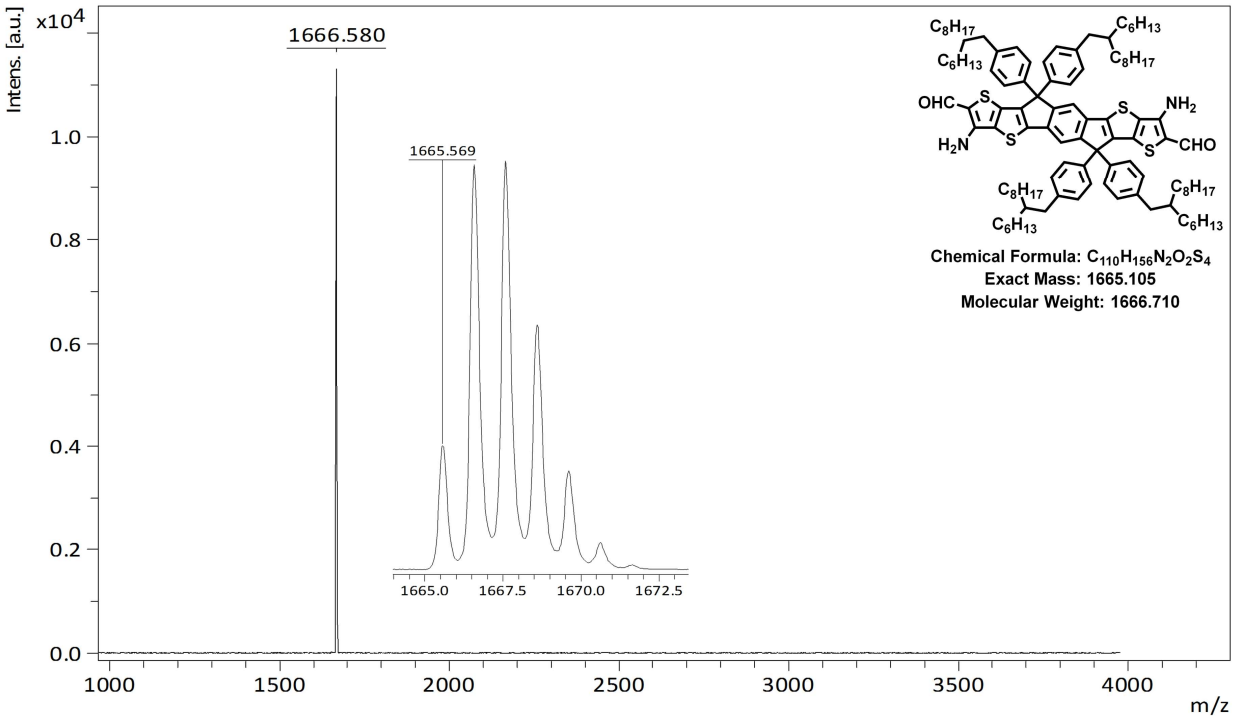

Figure S4.44. MALDI-TOF mass spectrum of IDTT-hd-2CHO-2NH_2.

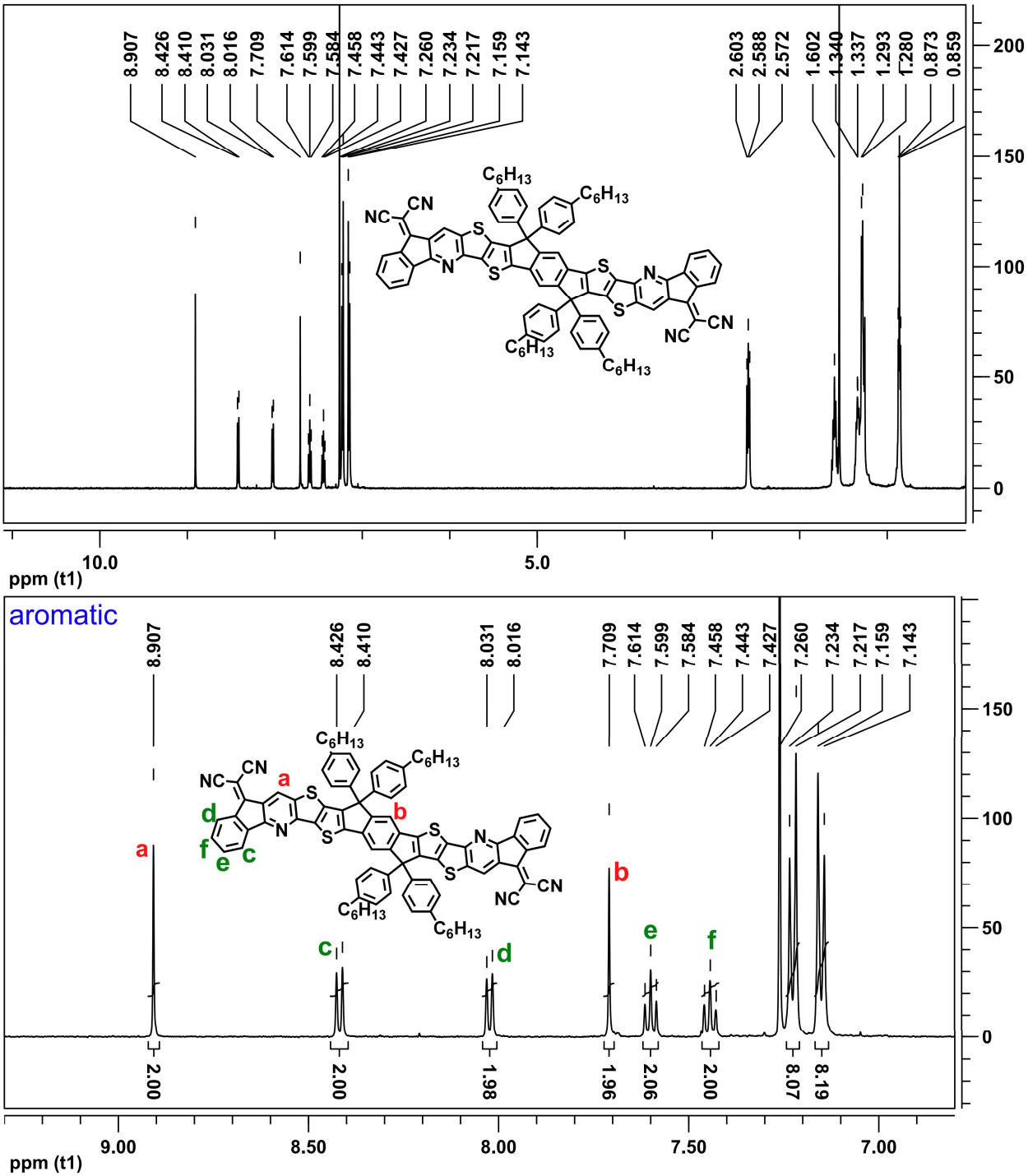

Figure S4.45. ^{1}H NMR (500 MHz, $CDCl_3$) spectrum of LTX-C_6 and the expansion of the aromatic region.

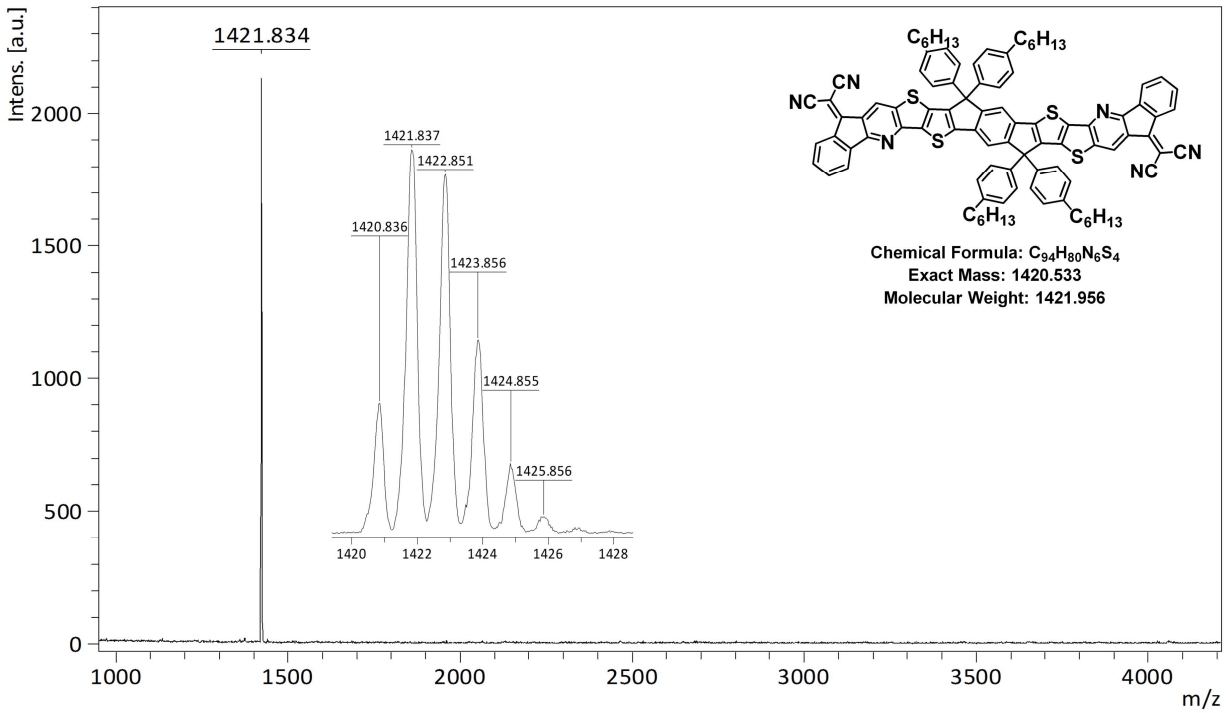

Figure S4.46. MALDI-TOF mass spectrum of LTX-C_6.

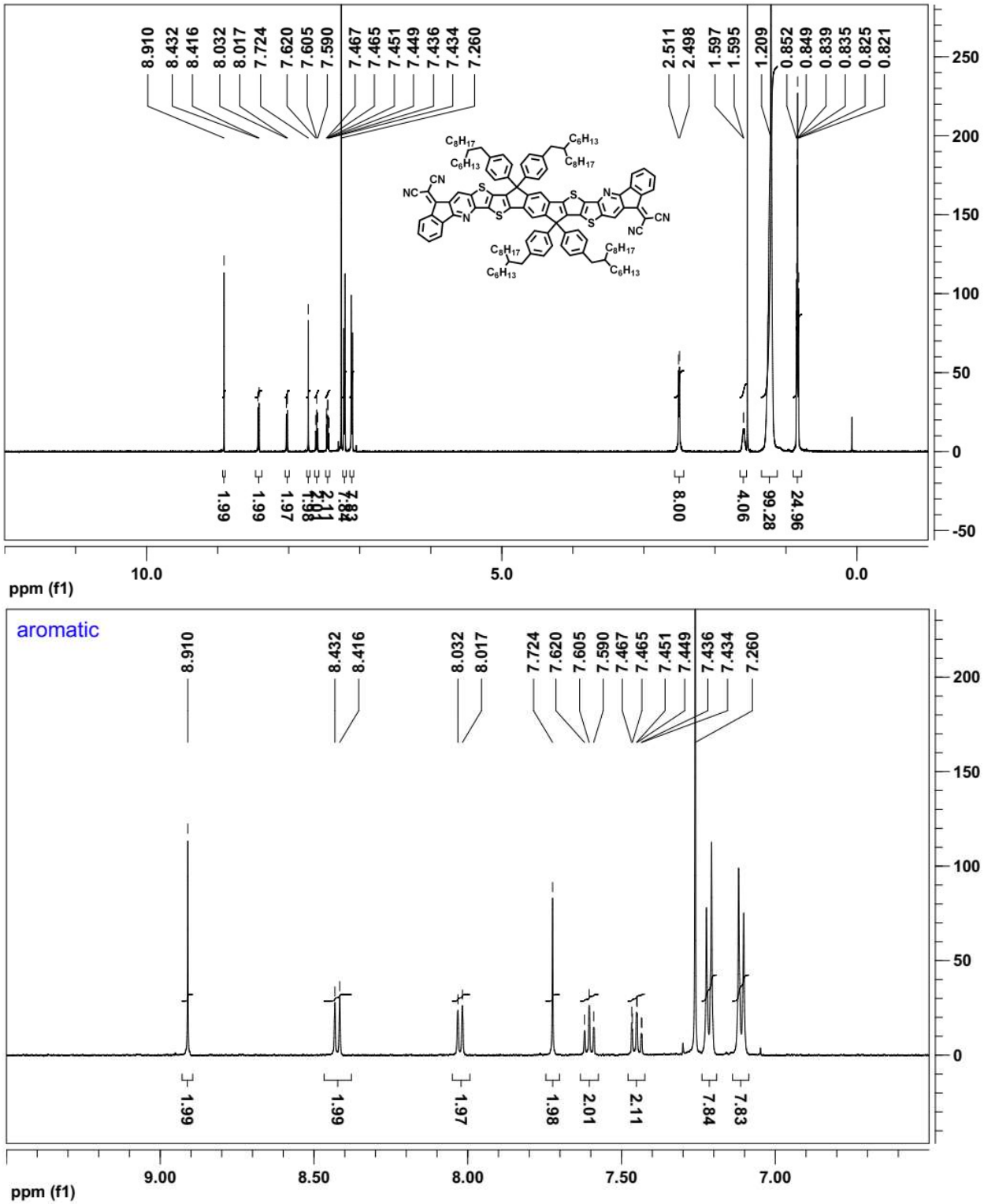

Figure S4.47. ^{1}H NMR (500 MHz, $CDCl_3$) spectrum of LTX and the expansion of the aromatic region.

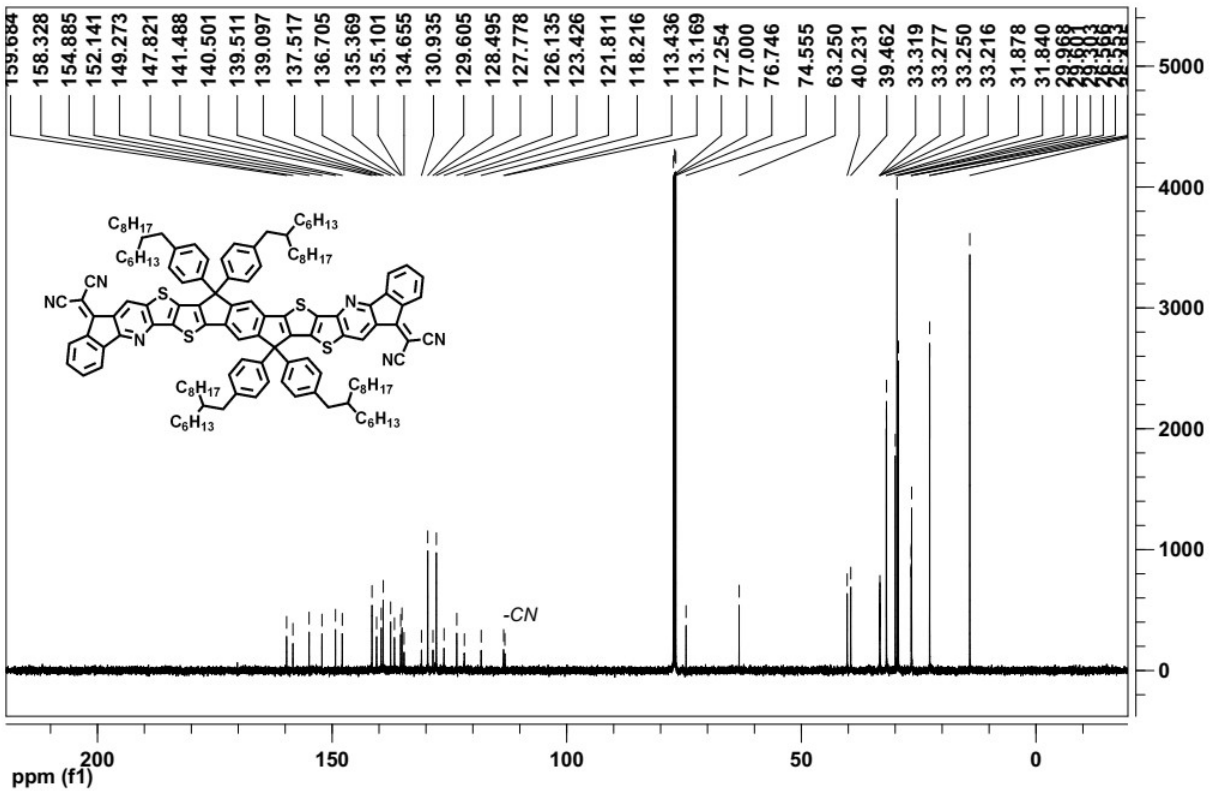

Figure S4.48. ^{13}C NMR (125 MHz, $CDCl_3$) spectrum of LTX.

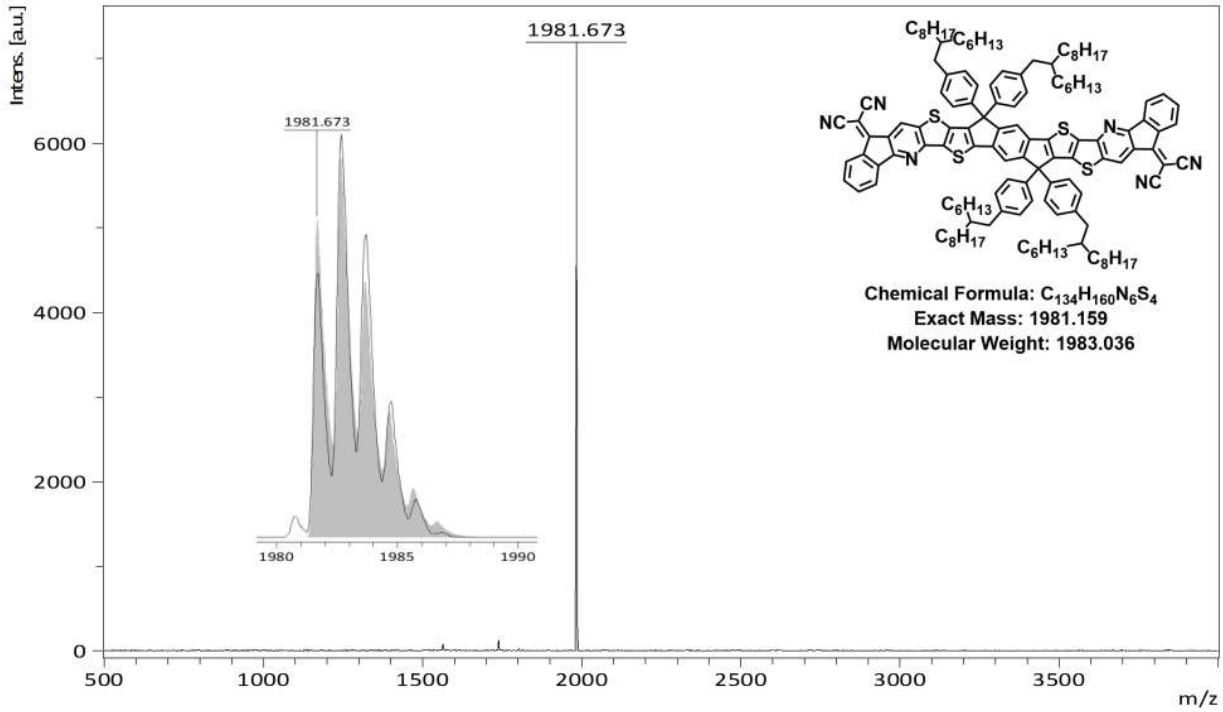

Figure S4.49. MALDI-TOF mass spectrum of LTX.

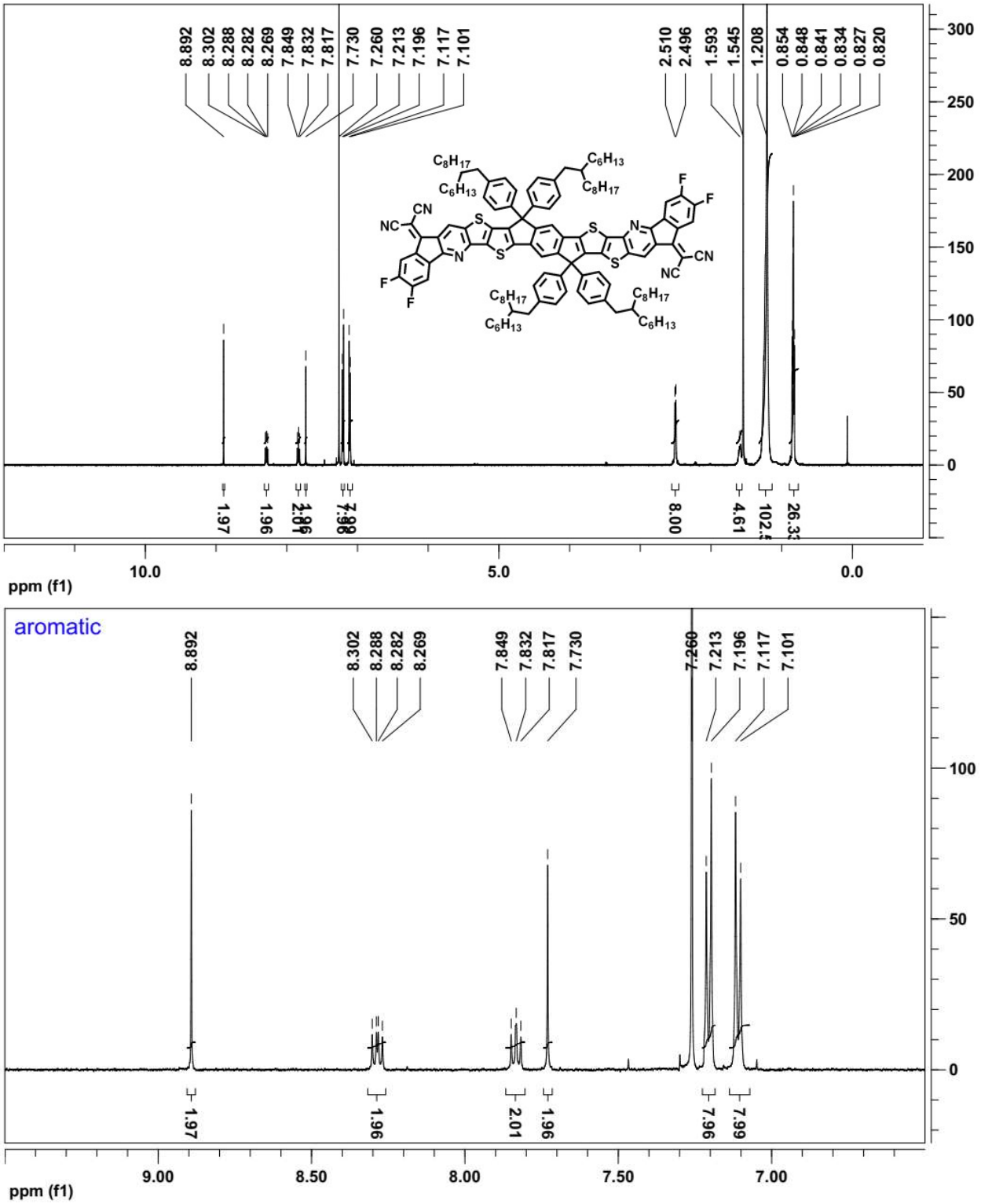

Figure S4.50. ^{1}H NMR (500 MHz, $CDCl_3$) spectrum of LTX-4F and the expansion of the aromatic region.

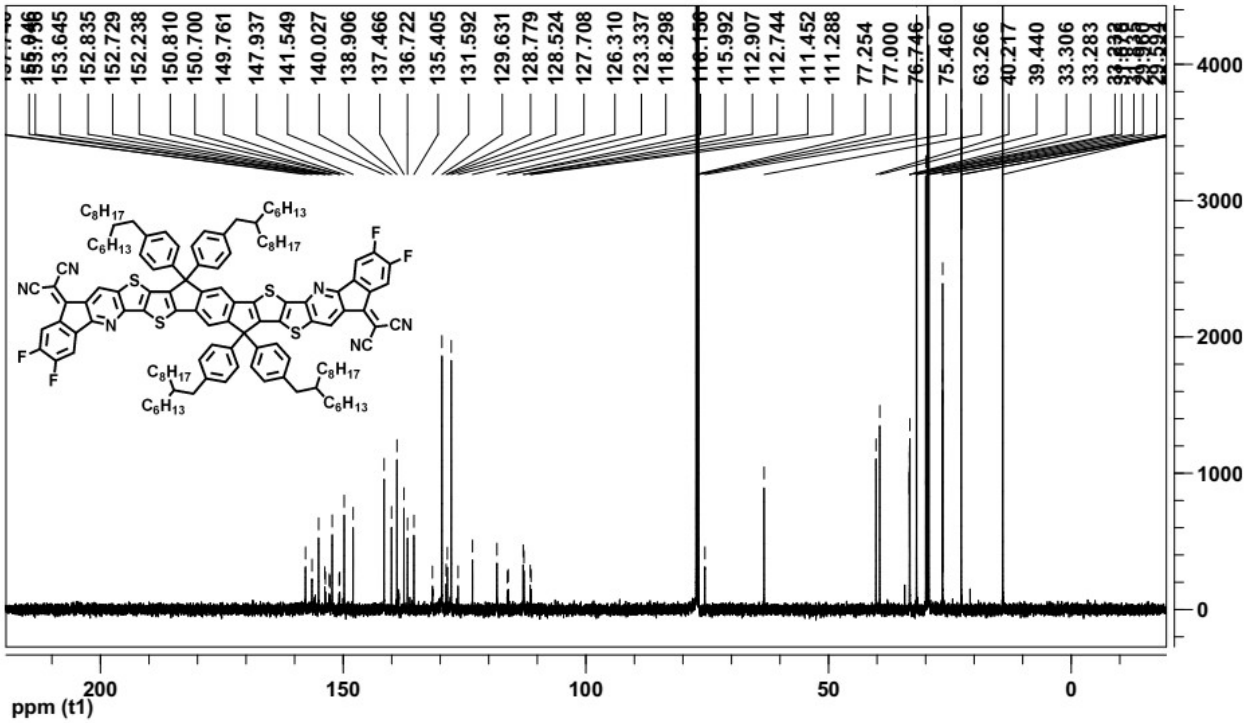

Figure S4.51. ^{13}C NMR (125 MHz, $CDCl_3$) spectrum of LTX-4F.

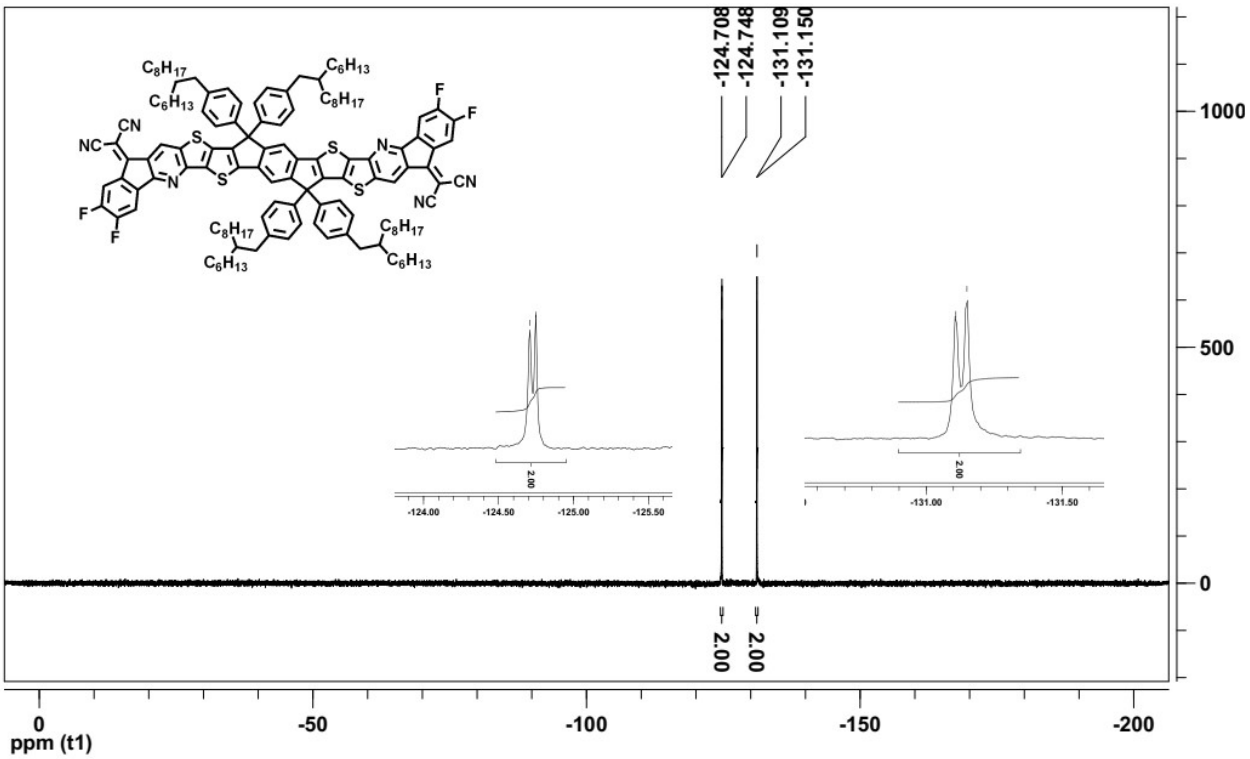

Figure S4.52. ^{19}F NMR (470 MHz, $CDCl_3$) spectrum of LTX-4F.

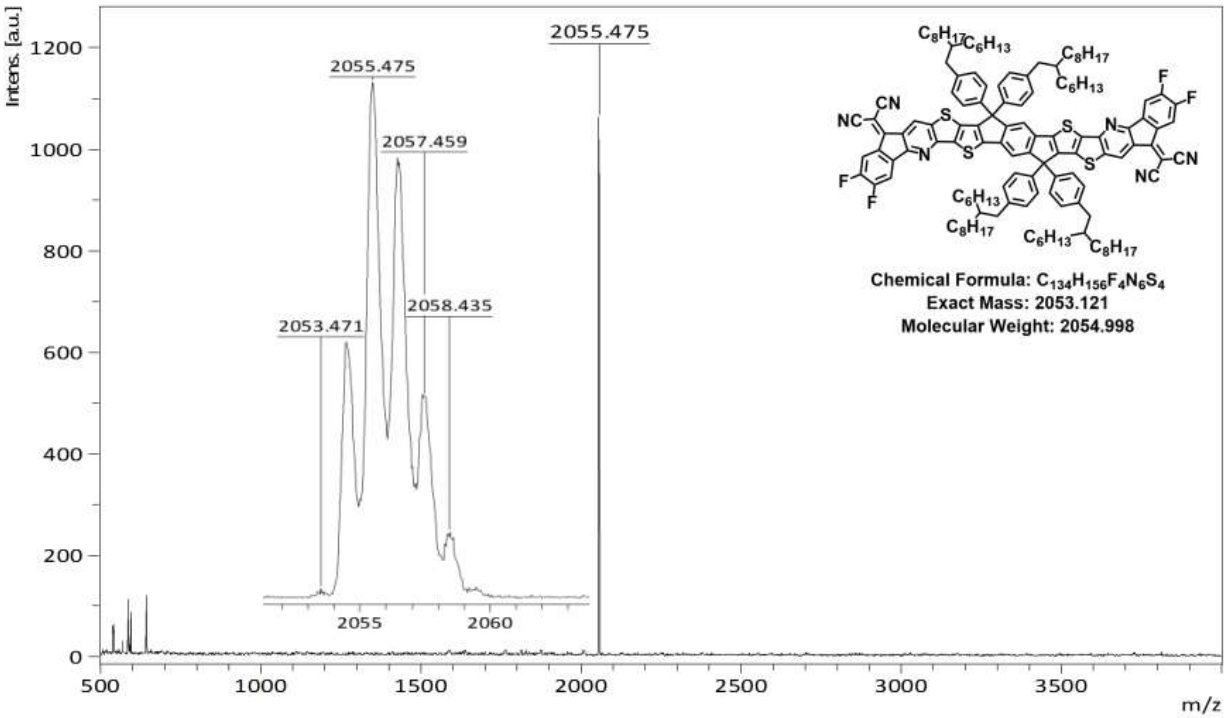

Figure S4.53. MALDI-TOF mass spectrum of LTX-4F.

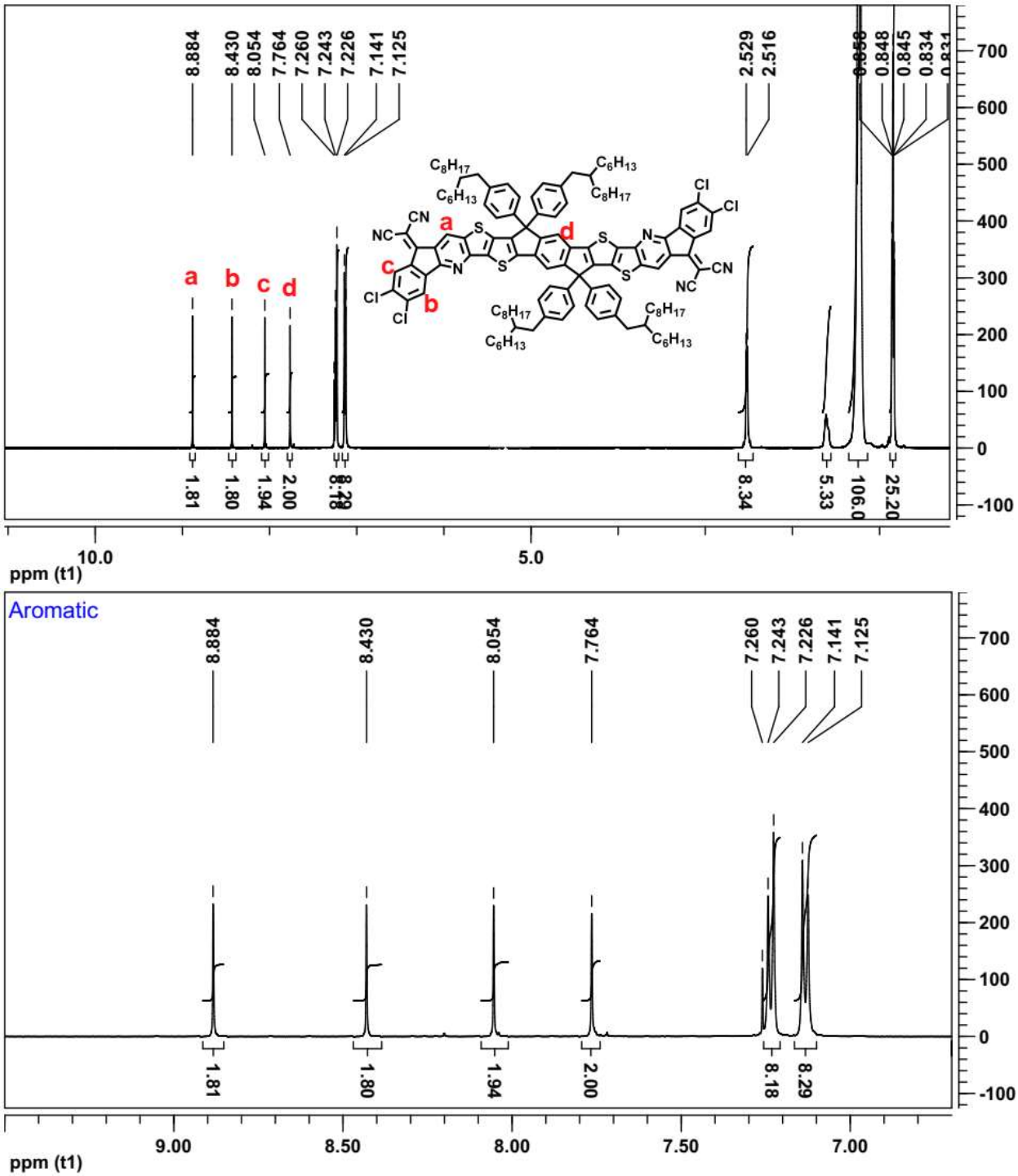

Figure S4.54. ^{1}H NMR (500 MHz, $CDCl_3$) spectrum of LTX-4Cl and the expansion of the aromatic region.

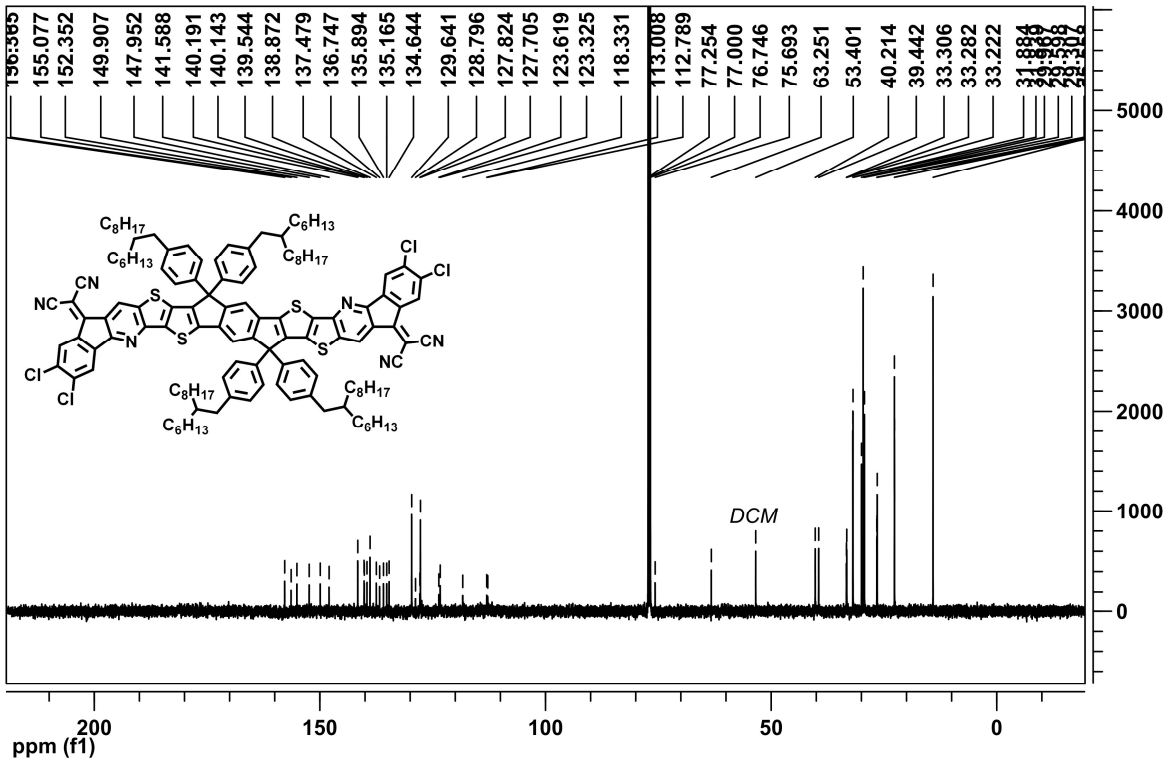

Figure S4.55. ^{13}C NMR (125 MHz, $CDCl_3$) spectrum of LTX-4Cl.

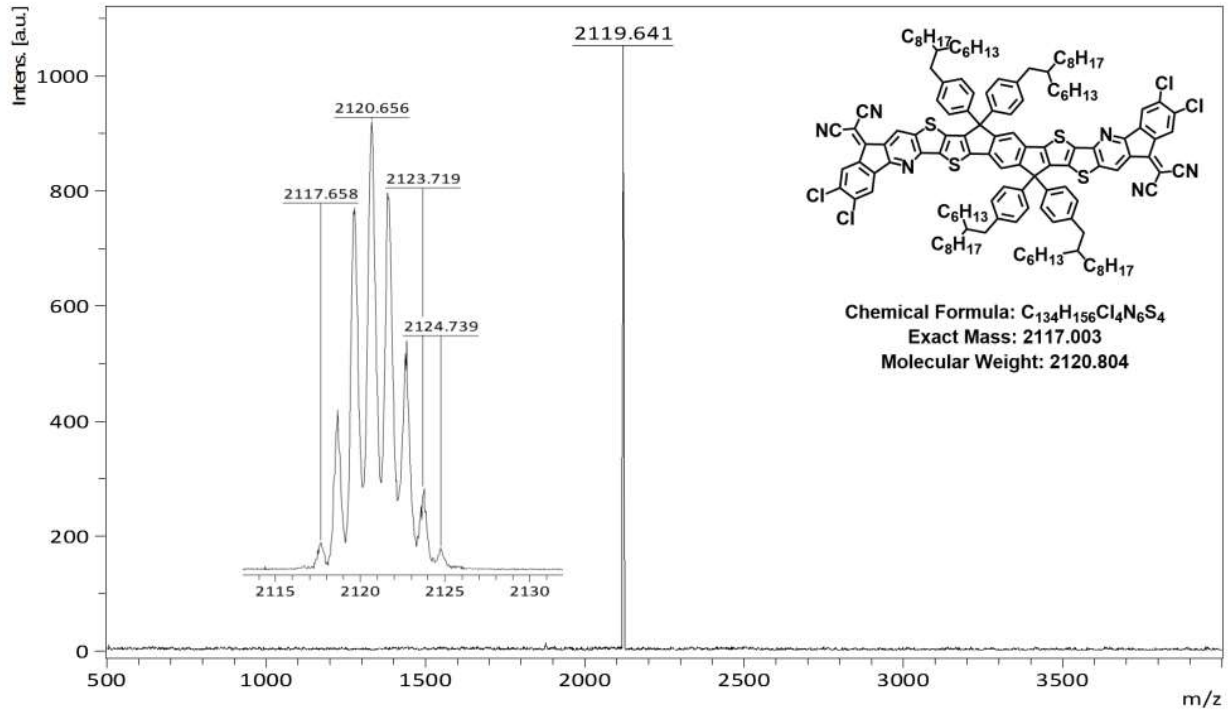

Figure S4.56. MALDI-TOF mass spectrum of LTX-4Cl.

4.2 Effects of Side Chains and Halogenations on Ladder Molecule Acceptors

4.2.1 *Introduction*

Organic solar cells (OSCs) have emerged as one of the promising photovoltaic (PV) technologies moving towards commercialization, demonstrating *state-of-the-art* power conversion efficiency (PCE) as high as 18% in single junction devices.[54] With the photoactive layers comprised of organic semiconductors, OSCs provide unique characteristics compared with their inorganic counterparts, including synthetic accessibility, tunability in optical and electronic properties, light weight, and mechanical flexibility. In recent years, rapid development in non-fullerene acceptors (NFAs) have contributed most to boost the photovoltaic performance of polymer:NFA-based OSCs *via* rigorous molecular and device engineering. The most important classes of NFAs are the ITIC, IDTBR and Y6 families[139], which in nature share similar acceptor-donor-aceptor (A-D-A) backbone architecture and were synthesized in similar fashion.

Currently, however, the intrinsic stability of individual photoactive components and the long-term device operation stability are under critical considerations in order to achieve the ultimate goal of commercialization.[64] It has been recognized that the root causes of degradation processes in OSCs are multifaceted, ranging from intrinsic photochemical stabilities inherent in the molecular design of photoactive materials to the morphological changes within blends under stress conditions. Little has been achieved so far to revolutionize the molecular design of current mainstream NFAs.

Previously, we developed a series of ladder molecule acceptors (LMAs), which adopted novel double-stranded tridecacyclic backbones, thereby possessed extraordinary thermal stability, defined conformation, and enhanced intrinsic stability. It was found that “ladderization” led to

raised LUMO energy levels, therefore contributed to high V_{oc} values. The LMAs demonstrated unique dual-band absorption spanning from 300 – 750 nm. Especially, extra-long branched alkyl (2-hexyldecyl) chains were installed to ensure solution-processibility.

To follow up, we here present a new series of LMAs with relatively shorter alkyl (n-decyl) chains to probe the "sweet spot" between solubilizing groups and device performance. The new LMAs, namely LTX10, LTX10-4F and LTX10-4Cl, (**Figure 4.57**a) were synthesized with our developed chemistry, and they showed optical absorption and electronic structures highly similar to their counterparts with long branched alkyl chains. (**Figure 4.57**b, c) Binary blend solar cells based on the blend of PM6:LTX10, PM6:LTX10-4F and PM6:LTX10-4Cl demonstrated moderately high PCEs of 6.1%, 9.0% and 9.3%, respectively. Compared to their counterparts with long branched chains in previous report, these blends were found to have relatively lower and more unbalanced charge transport properties, suggesting that reducing the length of alkyl chains negatively impacted the bulk charge transport in blend films. Furthermore, 2D GIWAXS studies revealed that LTX10 adopted *edge-on* orientation, whereas LTX10-4F were *tilted* and LTX10-4Cl were *face-on* oriented.

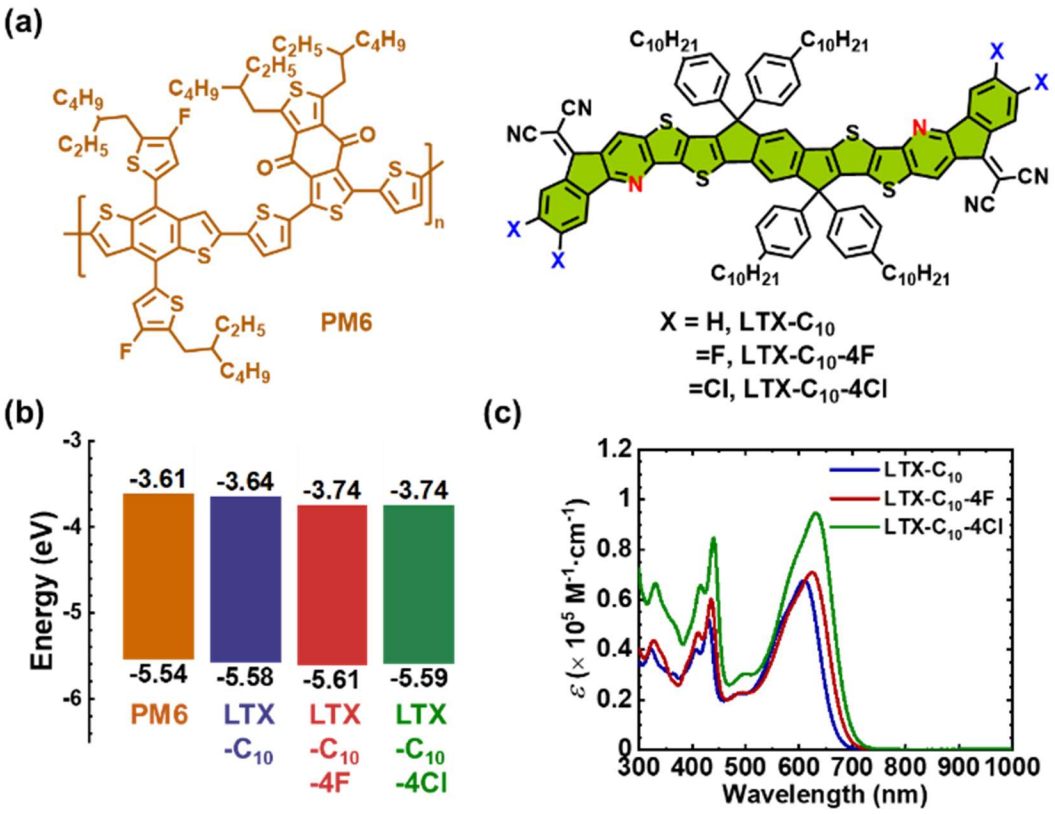

Figure 4.57. (a) Chemical structures, (b) HOMO/LUMO energy levels of the polymer donor, and (c) optical absorption spectra of PM6 and the ladder molecule acceptors: LTX10, LTX10-4F and LTX10-4Cl;

4.2.2 *Experimental Methods*

Synthetic procedures.

IDTT10-2Br. In a 250 mL round-bottom flask, **IDTT10 (1a)** (1.758g, 1.72 mmol) was completely dissolved in chloroform/acetic acid (50 mL/15 mL) solvent mixture. The flask was wrapped with aluminum foil to avoid light. To the stirring solution, NBS (0.629 g, 3.53 mmol, 2.05 equiv) was added in one portion. Reaction was kept stirring in dark at room temperature for overnight. Resulted yellow suspension was slowly poured into water. Perform extraction with

dichloromethane. The organic layer was washed with water, $NaHCO_3$ (aq) and brine. Organic fraction was then dried over Na_2SO_4, and concentrated in *vacuo*. Crude product was absorbed in silica gel and loaded onto column, eluting with hexane/DCM (4:1 v/v). Collected product was recrystallized from DCM/MeOH, collected from filtration and further dried in vacuum oven. Yield: 1.91g, 94%, pale yellow powder.

IDTT10-2CHO-2Br. In an argon-filled 250 mL two-neck round-bottom flask, **IDTT10-2Br (2a)** (400 mg, 1.27 mmol) was dissolved in 80 mL anhydrous THF. Solution was cooled down to -78 ºC and kept for 15 min. At -78 ºC, lithium diisopropylamide (LDA) (1M solution in THF/hexane, 2.55 mL, 5.10 mmol, 4 equiv) was added dropwise. Reaction mixture turned into redolored solution. The mixture was kept at -78 ºC and allowed to gradually warm up to room temperature for overnight. Resulted yellowish brown mixture was again cooled to 0 ºC. Anhydrous DMF (1 mL, excess) was added slowly. Resulted suspension was kept stirring at room temp for 1 h. Saturated NH_4Cl (aq) was added. The mixture was then extracted with dichloromethane, washed with sat. NH_4Cl (aq), brine and dried over Na_2SO_4. Crude product was purified with silica gel column eluting with hexane/DCM with increasing polarity (from 2:1 to 2:1.5 v/v), followed with precipitation into methanol. Product was then filtered and dried in vacuum oven. Yield: 500 mg, %, lightly-greenish yellow powder.

IDTT10-2CHO-2NH_2. Crude solid **IDTT-2CHO-2N_3 (4a)** from previous step was redissolved in 5 mL chloroform in a vial. 40% ammonium sulfide (1 mL, excess) was added dropwise. Mixture was stirred for 30 min at room temperature until gas evolution had ceased. Perform extraction with chloroform, wash with brine and dry over Na_2SO_4. Crude product was purified with short silica gel column, eluting with DCM. Collected fraction was concentrated on

rotary evaporator and was recrystallized from hexane at r.t.. Product was then filtered and dried in vacuum oven. Overall yield from **3a**: 180 mg, 76%, yellow solid.

General Procedures for Friedlander Condensation Reactions. In an argon-filled Schlenck tube, bis(amino-aldehyde) (1 equiv), end group (5 equiv) and diphenyl phosphate (20 equiv) was dissolved into anhydrous toluene. Reaction mixture was heated up and kept refluxing for overnight. After cooling to room temperature, resulted dark mixture was precipitated into 10% Et_3N/MeOH and kept stirring for 2 h. After filtration, dark crude product was collected and redissolved with chloroform, and further purified with silica gel column and preparative TLC plates. Collected fraction was concentrated and recrystallized with CF/MeOH. Pure product was then filtered and dried in vacuum oven. Yield: ~30%.

Cyclic voltammetry measurements. Cyclic voltammetry (CV) measurements were performed on an EG&G Princeton Applied Research potentiostat/galvanostat (model 273A). A three-electrode cell was used, using platinum (Pt) wires as both counter and working electrodes. Silver/silver ion (Ag in 0.01 M $AgNO_3$ solution) was used as the reference electrode. For thin films, the working electrode was a Pt wire coated with the synthesized small molecules, dipoated from concentrated solution in chloroform and air dried for overnight. CV measurements of thin films were carried out in 0.1 M tetrabutylammonium hexafluorophosphate (Bu_4NPF_6) solution in acetonitrile at a scan rate of 50 mV/s. For solutions, the working electrode was a bare Pt wire. CV measurements of solutions were carried out in 1,2-dichlorobenzene/acetonitrile (10:1) (0.1 mM) containing 0.1 M tetrabutylammonium hexafluorophosphate (Bu_4NPF_6) as supporting electrolyte. Scan rate was 100 mV/s. Solutions were purged with inert gas before measurements. All recorded reduction and oxidation potentials were calibrated with the ferrocene/ferrocenium (Fc/Fc^+) couple.

Solar Cell Fabrication and Testing. The inverted device structure fabricated and evaluated was: ITO/ZnO/PEI/blend active layer/ MoO_3(0.5 nm)/Ag(100 nm), where PEI or polyethylenimine is a cathode buffer layer.[79] The ITO glass substrates were sequentially sonicated in acetone, deionized (DI) water and isopropanol for 20 min each and then plasma cleaned for 10 min. The ZnO layer (~30 nm) was spin-coated from the precursor solution (0.5 g of zinc acetate dihydrate, 0.14 g of ethanolamine and 5 mL of 2-methoxyethanol) and baked at 250 ºC for 30 min in open air. Solution of PEI (M_w = 25k, Aldrich 408727) in 2-methoxyethanol (0.05 wt%) was then spin-coated onto the ZnO layer and dried at 120 ºC for additional 10 min. The resulting substrates were then stored in an argon-filled glovebox for deposition of active layers. The active layer blend solution was prepared by mixing a chlorobenzene solution of the donor polymer PM6 respectively with a chlorobenzene solution of acceptors: LTX10, LTX10-4F, LTX10-4Cl. Various solution volumes of the component polymers were mixed in the right proportions to afford the desired blend film compositions. In cases where a processing additive was used, the chlorobenzene:additive (v/v %) mixed solvent was achieved by adding CN to a prepared blend solution. The blend solutions were stirred overnight with low heating to achieve a homogeneous mixture. Each blend solution was then spin-coated onto the cleaned substrate and annealed on a hot plate for 10 min to afford dried thin films with a thickness of 95 ± 5 nm. Finally, the MoO_3 layer and Ag electrode were deposited within a thermal evaporator. Defined active area of 0.0314 cm^2 was achieved for individual devices through a shadow mask. The photovoltaic cells were tested under AM 1.5G solar illumination at 100 mW/cm^2 in ambient air using a Solar Simulator (model 16S, Solar Light Co., Philadelphia, PA) with a 200W Xenon Lamp Power Supply (Model XPS 200, Solar Light Co., Philadelphia, PA) calibrated by NREL certified Si photodiode (Model 1787–04, Hamamatsu Photonics K.K., Japan) and a HP4155A semiconductor parameter analyzer (Yokogawa Hewlett-

Packard, Japan). After the *J–V* measurement, the EQE was measured by using a solar cell quantum efficiency measurement system (Model QEX10, PV Measurements, Inc., Boulder, CO) with a 2 mm^2 (2 × 1 mm) size masked incident light source and TF Mini Super measurement apparatus for multiple devices in a single substrate.

SCLC Device Fabrication and Testing. The space charge limited current (SCLC)[80] devices fabricated and evaluated had the structures: ITO/PEDOT:PSS/blend/MoO_3/Ag (hole-only), where poly(3,4-ethylenedioxythiophene):poly(styrenesulfonate) (PEDOT:PSS) is a hole injection layer; and ITO/ZnO/PEI/active layer/PFN-Br/Al (electron-only). The blend active layers in these SCLC devices had the same composition as the corresponding photovoltaic devices. Current-voltage (*J-V*) characteristics of the SCLC devices were plotted as $J^{0.5}$ versus V and fitted by using the following formula: $J = 9\ \varepsilon_0\ \varepsilon_r\ \mu V^2/8d^3$, where J is the current density, ε_0 is the permittivity of free space, ε_r is the relative dielectric constant of the transport medium, μ is the carrier mobility, V is the applied voltage, d is the thickness of blend active layer.

Atomic Force Microscopy (AFM) Imaging. The surfaces of the actual all-polymer solar cell devices were imaged by using the atomic force microscope (Model: Bruker Dimension ICON).

2D GIXD Measurements. Two-dimensional (2D) Grazing incidence X-ray scattering (GIXD) experiments were conducted at the Japan Synchrotron Radiation Facility SPring-8 by using the beamline BL46XU. The thin-film samples investigated were prepared in the same manner as the corresponding photovoltaic devices on ZnO-coated ITO substrates, without the thermal deposition of top MO_3/Ag electrodes. The X-ray beam was monochromatized by a double-crystal Si(111) monochromator, and the X-ray energy in this experiment was 12.40 keV (λ = 0.1 nm). The angle of incident X-ray to sample surface was 0.12° with a Huber diffractometer. The scattered profile from the film sample was detected using an area detector (PILATUS 300K) for 5

s at room temperature, and the distance between the sample and detector was 174.4 mm. The crystal coherence length (L_c) of samples was determined by using the Scherrer equation: $L_c = 2\pi K/\Delta q$, where K is a shape factor (typically 0.89) and Δq is the full width at half-maximum (FWHM) of the diffraction peak.

4.2.3 *Results and Discussion*

4.2.3.1 Materials synthesis and characterization.

The ladder molecule acceptors, LTX10, LTX10-4F and LTX10-4Cl, were synthesized following the synthetic route developed previously in our lab. (**Scheme 4.2**) Details in synthetic procedures and characterization data in ^{1}H NMR, ^{13}C NMR and mass spectrometry are provided in **Supporting Information**. Due to the shorter n-decyl chains, the solubility of LTX10, LTX10-4F and LTX10-4Cl in common organic solvents (e.g. dichloromethane, chloroform, chlorobenzene) decreased significantly relative to their precedents with long branched 2-hexyldecyl chains, which posed some difficulty in purification processes. Nevertheless, pure compounds were eventually obtained from column purification followed with preparative TLC plates. The solubility of the three LMAs stands in the ascending order: LTX10 < LTX10-4F < LTX10-4Cl. Thermogravimetric analysis (TGA) showed that these ladder molecules have high decomposition temperatures (T_d): LTX10 (418 °C), LTX10-4F (432 °C) and LTX10-4Cl (435 °C). (**Figure S4.63**) LTX10, LTX10-4F and LTX10-4Cl showed similar dual-band optical absorption, (**Figure 4.57**c) as expected based on our previous studies. The redox properties of the LTXs were investigated with cyclic voltammetry (CV) in solutions and in thin films. (**Figure S4.64)**The HOMO/LUMO energy levels extracted from cyclic voltammograms in solutions are: LTX10 (-5.58/-3.64 eV), LTX10-4F (-

5.61/-3.74 eV) and LTX10-4Cl (-5.59/-3.74 eV). (**Figure 4.57**b). Going from 2-hexyldecyl chains to n-decyl chains, the HOMO/LUMO energy levels were raised very slightly (0.01 – 0.05 eV).

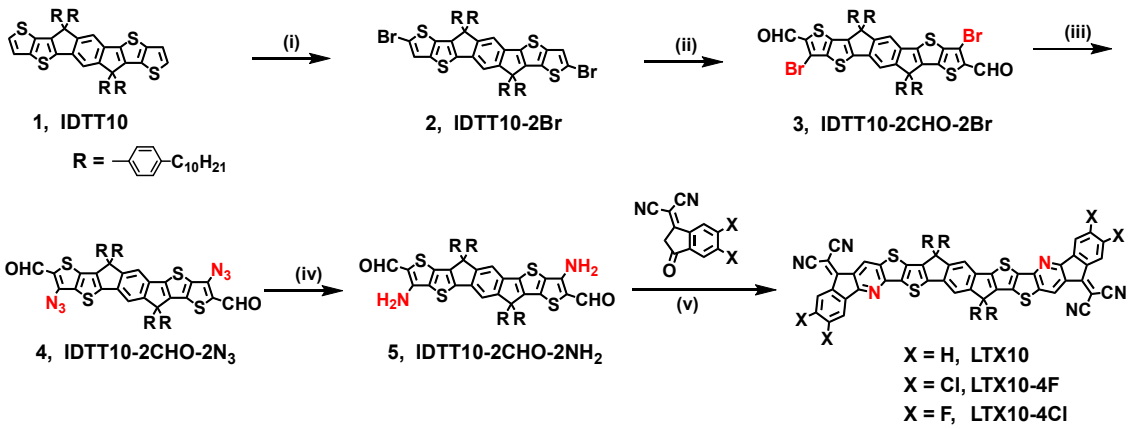

Scheme 4.2. Synthesis of the ladder molecule acceptors: LTX10, LTX10-4F and LTX10-4Cl.

4.2.3.2 Crystal analysis of IDTT10-2CHO-2NH_2.

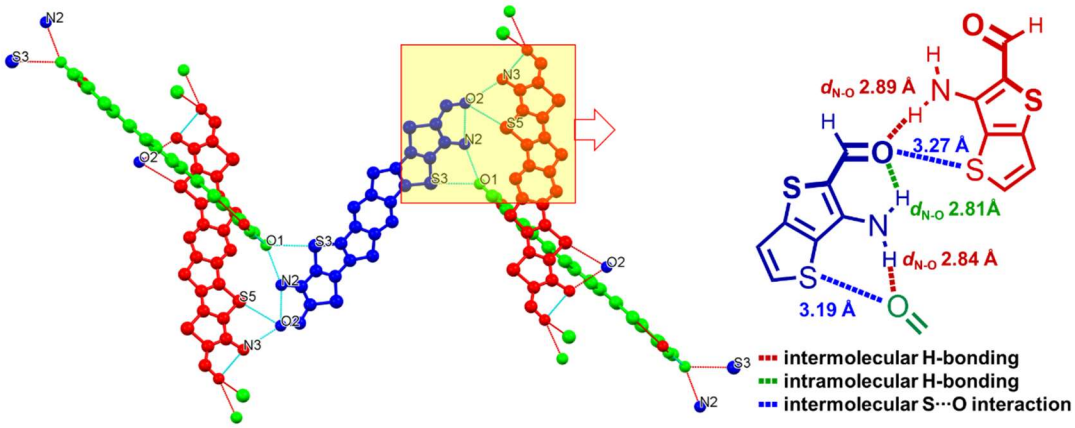

Figure 4.58. Crystal structure of bis(amino-aldehyde), IDTT10-2CHO-2NH_2, and the intermolecular and intramolecular interactions. Molecules are colored by symmetry equivalence. All hydrogen atoms and n-decylphenyl chains are omitted for clarity.

We here report the very first single crystal for the novel heptacyclic bis(amino-aldehyde) building block, IDTT10-2CHO-2NH_2. The orange-colored needle crystals appeared from a solution of IDTT10-2CHO-2NH_2 in dichloromethane/methanol mixed solvent, after the vessel was left open in fume hood for a few days. The crystal has a monoclinic packing system, and the space group is $P2_{1/c}$. The unit cell parameters are a = 22.3804(16) Å, α = 90°; b = 18.6922(14) Å, β = 109.494(5)°; c = 28.469(2) Å, γ = 90°. As illustrated in **Figure 4.58**, each bis(amino-aldehyde) molecule interacts with four neighboring molecules mainly *via* N-H···O hydrogen-bonding (H-bonding), where the amine (N2) interacts with the carbonyl oxygen (O1) from one neighboring molecule, and the carbonyl oxygen (O2) interacts with the amine (N3) from another neighboring molecule. The intermolecular H-bonding has N-O distances of 2.84 Å and 2.89 Å, thus are considered moderate[175] strength. Meanwhile, intermolecular S···O interactions are also present, with S-O distances of 3.19 Å and 3.27 Å which are smaller than the sum of their Van der Waals radii (r_S =1.89 Å, r_O = 1.50 Å). In addition to the intermolecular interactions, the bis(amino-aldehyde) also showed intramolecular H-bonding between its own amine and carbonyl oxygen, leading to exclusive S,O-*trans* conformation similar to 3-amino-2-formylthiophene[166] reported in early literature.

Photovoltaic Properties. The photovoltaic properties of LMAs were investigated pairing with the polymer donor, PM6. Inverted device architecture was adopted: ITO/ZnO/PEI/photoactive layer/MoO_3/Ag, where PEI was cathode interlayer. For each PM6:LMA combination, devices were individually optimized by varying the donor:acceptor (D:A) weight ratios, the annealing temperature, and addition of processing additives. The optimal processing conditions for PM6:LTX10, PM6:LTX10-4F, and PM6:LTX10-4Cl were found to be with D:A ratio of 1:0.8 (wt:wt) and aging inside the Argon filled glovebox at room temperature

for 2 h after spin-coating, with 2 vol% chloronapthalene (CN), 1.5 vol% CN, and 1 vol% CN as processing additive, respectively. The current density-voltage (*J-V*) curves and the EQE spectra of the best performing devices are presented in **Figure 4.59.** The detailed photovoltaic parameters including open-circuit voltage (V_{oc}), short-circuit current density (J_{sc}), fill factor (FF) and power conversion efficiency (PCE) are summarized in **Table 4.10**. The optimized PM6:LTX10 devices exhibited an average J_{sc} of 8.58 mA/cm^2, a large V_{oc} of 1.09 V, and a relatively low FF of 0.59, leading to an average PCE of 5.47%. Compared to PM6:LTX10, the optimized PM6: LTX10-4F and PM6: LTX10-4Cl devices showed increased average J_{sc} of 12.92 mA/cm^2 and 13.15 mA/cm^2, respectively. The improvement of J_{sc} in PM6: LTX10-4F and PM6: LTX10-4Cl blends are consistent with the stronger light harvesting ability of LTX10-4F and LTX10-4Cl, which showed higher absorption coefficients and red-shifted absorption bands compared to LTX10. (**Figure 4.57**) The PM6:LTX10-4F and PM6:LTX10-4Cl devices also demonstrated significantly increased FF of 0.70 and 0.71, respectively, compared to PM6:LTX10 (FF = 0.60), indicating formation of more favorable blend morphology with halogenations. It is noteworthy that all three blends, PM6:LTX10, PM6:LTX10-4F and PM6:LTX10-4Cl, demonstrated high V_{oc} of 1.09 V, 0.973 V and 0.966 V, respectively. As listed in **Table 4.10**, the champion devices of PM6:LTX10, PM6:LTX10-4F, and PM6:LTX10-4Cl demonstrated maximum PCE of 6.05%, 9.02% and 9.33%, respectively. The EQE spectra of the optimized PM6:LTXs blend devices are shown in **Figure 4.59b**. The maximum EQE for the devices based on the LTX10 series were found to be 56.3%, 69.8%, and 71.2% for PM6:LTX10, PM6:LTX10-4F, and PM6:LTX10-4Cl, respectively, in the range of 560-580 nm. The calculated J_{sc} ($J_{sc}^{calc.}$) (**Table 4.10**) obtained by integrating the EQE spectra were within 3-5% error with the J_{sc} extracted from the *J-V* curves.

Table 4.10. Summarized Photovoltaic Parameters of the Optimized PM6:LMAs Blend Devices.

Blends	J_{sc} (mA/cm^2)	V_{oc} (V)	FF	PCE [(a)] (%)	$J_{sc}^{calc.}$ (mA/cm^2)	μ_h (10^{-3} cm2/Vs)	μ_e (10^{-4} cm^2/Vs)	μ_h/μ_e
PM6:LTX10	9.22 (8.58 ± 0.26)	1.09 (1.09 ± 0.01)	0.60 (0.59 ± 0.02)	6.05 (5.47 ± 0.35)	8.60	1.51	1.55	9.75
PM6:LTX10-4F	13.29 (12.92 ± 0.27)	0.973 (0.973 ± 0.002)	0.70 (0.68 ± 0.02)	9.02 (8.49 ± 0.29)	12.48	1.03	1.09	9.42
PM6:LTX10-4Cl	13.61 (13.15 ± 0.23)	0.966 (0.962 ± 0.005)	0.71 (0.70 ± 0.02)	9.33 (8.81 ± 0.26)	13.16	0.83	1.73	4.79

[(a)] Average values of over 15 devices.

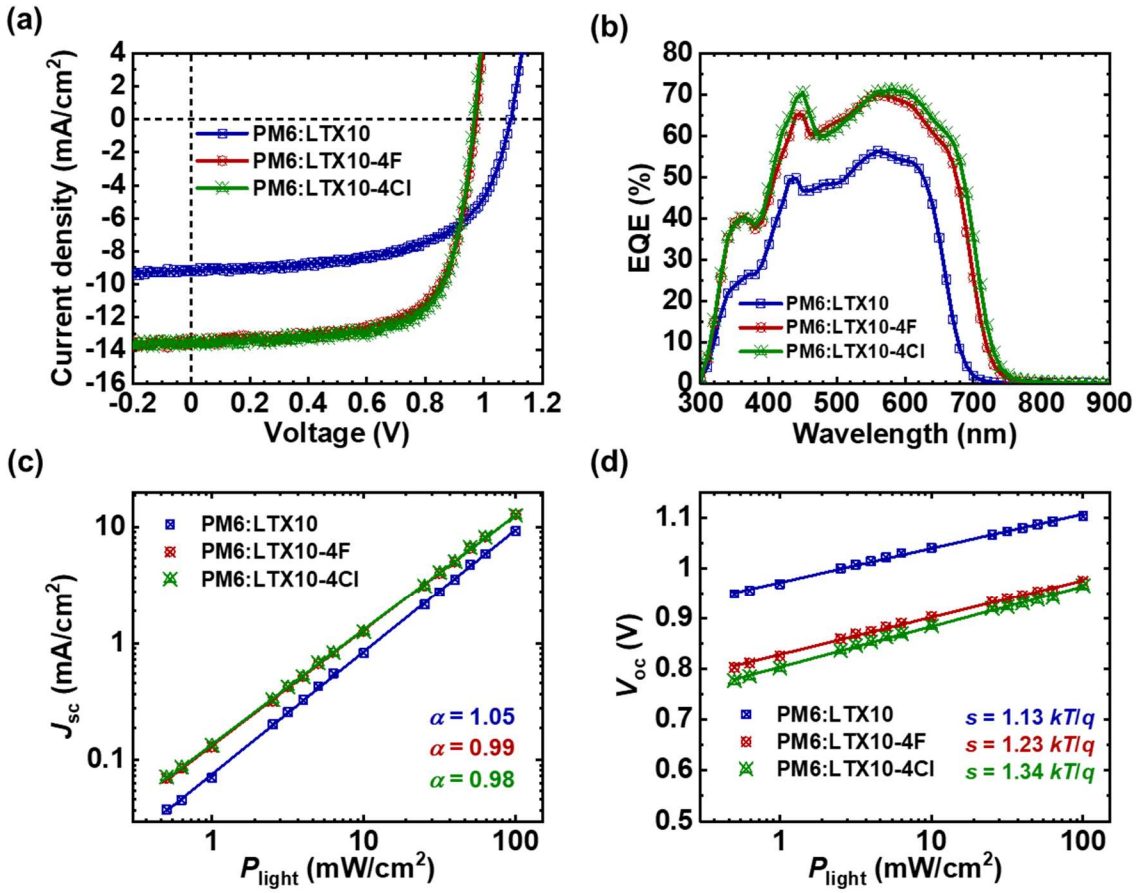

Figure 4.59. (a) *J-V* response curves, (b) EQE spectra, (c) light intensity dependence of short-circuit current (J_{sc}) and (d) light intensity dependence of open-circuit voltage (V_{oc}) for devices based on blend of PM6:LTX10, PM6:LTX10-4F and PM6:LTX10-4Cl.

4.2.3.3 Charge Photogeneration, Recombination and Charge Transport.

The dependence of J_{sc} and V_{oc} on the incident light intensity (P_{light}) were characterized to investigate the charge recombination mechanism. (**Figure 4.59**) The relationship between J_{sc} and P_{light} follows the power law: $J_{sc} \propto P_{ligh}{}^{\alpha}$. Under shortircuit conditions, when bimolecular recombination within the photoactive layer is negligible, *a* approaching 1 should be observed. Deviation from 1 indicates loss from bimolecular recombination. We observe *a* values of the three blends to be 1.05, 0.99 and 0.98, suggesting minimum bimolecular recombination loss. On the other hand, we evaluated the correlation between V_{oc} and P_{light}, where the ideality factor *s* was extracted with the following equation: $s = \frac{kT}{q}\frac{\partial V_{oc}}{\partial \ln (P_{light})}$. Under openircuit conditions, when bimolecular recombination is predominant, an ideality factor of unity (s = kT/q) should be observed, while an *s* value approaching 2kT/q signifies monomolecular or trap-assisted recombination loss. We obtained *s* values of 1.13kT/q, 1.23kT/q and 1.34kT/q for PM6:LTX10, PM6:LTX10-4F and PM6:LTX10-4Cl, respectively, suggesting increased presence of traps with fluorination and chlorination.

The bulk charge transport properties of the neat films of LMAs and the blend films of PM6:LMAs were characterized by extracting the space-charge limited current (SCLC) carrier mobilities from single-carrier diodes: ITO/PEDOT:PSS/active layer/MoO_3/Ag (hole-only) and ITO/ZnO/PEI/active layer/PFN-Br/Al (electron-only). The neat films of LMAs were thermally annealed at 110°C for 10 min. The blend films of PM6:LMAs were processed under the same optimized conditions as in the corresponding solar cell devices. The *J-V* curves and SCLC fittings for the hole-only and the electron-only devices of the blend films of PM6:LMAs are presented in **Figure S4.66**. The extracted hole mobility (m_h), electron mobility (m_e), and the m_h/m_e ratio of the blend films are summarized in **Table 4.10**. For the neat films, this series of LMAs with n-decyl

side chains formed poor-quality films with macroscopic aggregates across the film, due to limited solubility. For the blend films of PM6:LMAs, we observed highly unbalanced hole/electron transport, where the μ_h/μ_e ratios for PM6:LTX10, PM6:LTX10-4F and PM6:LTX10-4Cl were found to be 9.75, 9.42 and 4.79, respectively. These μ_h/μ_e ratios suggested that chlorination is beneficial for more symmetrical charge transport. Previously we have demonstrated that with long branched sidechains, symmetrical hole/electron transport in PM6:LMAs blends could be achieved. Thus, here we ascribe the asymmetrical hole/electron transport to the negative effects of shorter side chains in LTX10, LTX10-4F and LTX10-4Cl.

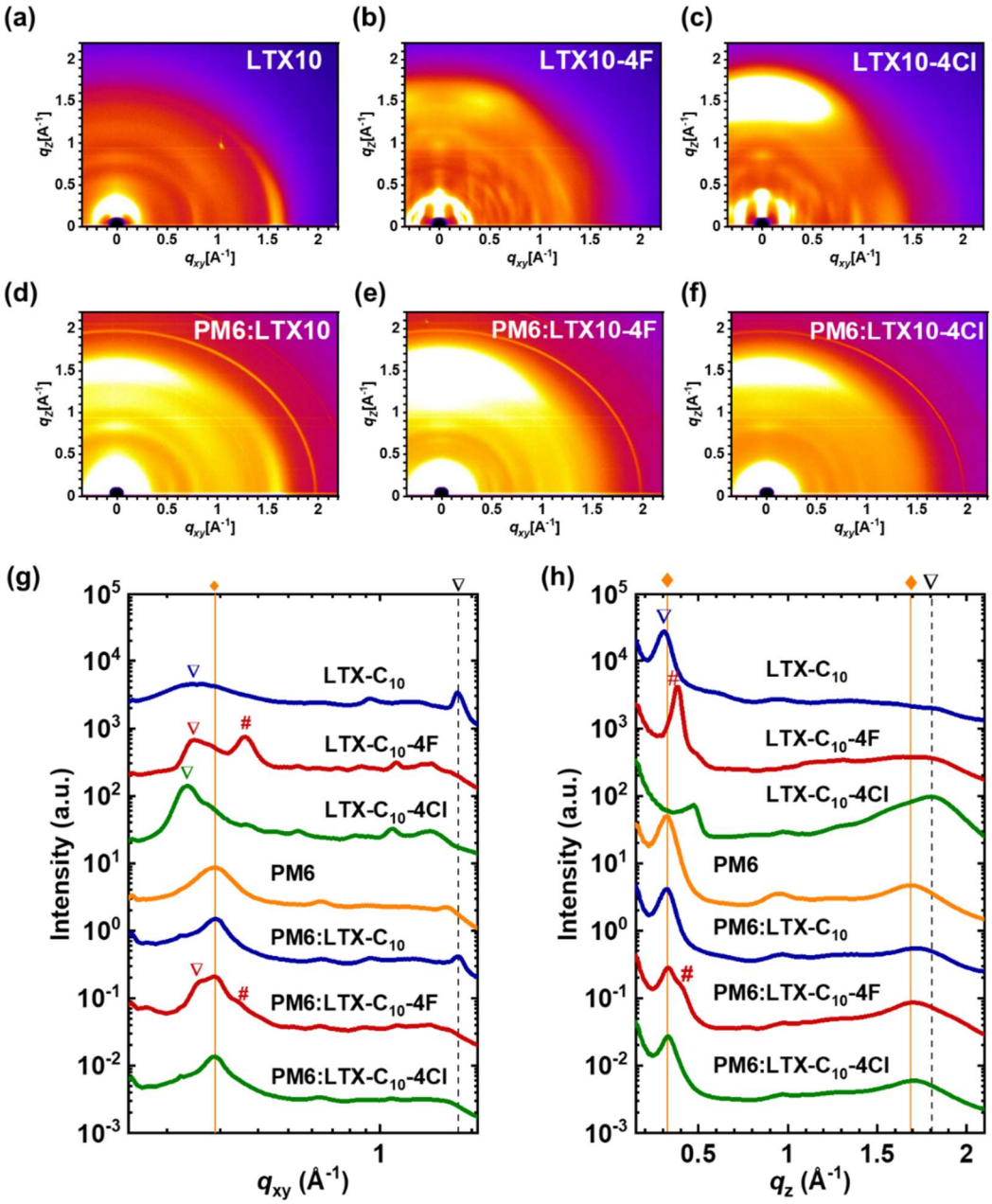

Figure 4.60. 2D GIXD patterns for the neat and blend films: (a) LTX10; (b) LTX10-4F; (c) LTX10-4Cl; (d) PM6:LTX; (d) PM6:LTX10-4F; (e) PM6:LTX10-4Cl; and 1D line cuts for all neat and blend films in (g) in-plane (IP) and (h) out-of-plane (OOP) directions, where "♦" denotes peaks from the donor polymer PM6 and "▽" and "#" denotes peaks from the ladder molecule acceptors.

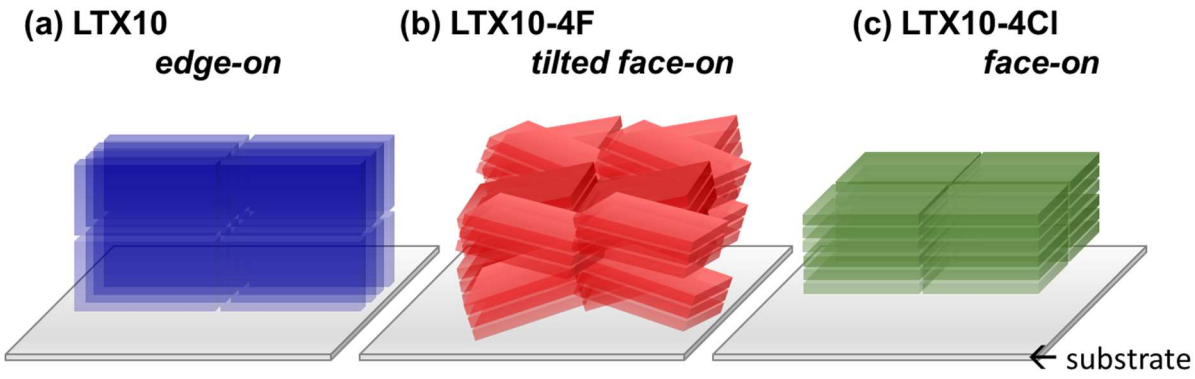

Figure 4.61. Simplified illustration of molecular packing characteristics for (a) LTX10, (b) LTX10-4F and (c) LTX10-4Cl in neat and blend films deduced from 2D GIWAXS analysis.

4.2.3.4 2D GIWAXS Analysis.

The bulk morphology of the neat films of LMAs and the blend films of PM6:LMAs were characterized using synchrotron-based two-dimension grazing incidence wide angle X-ray scattering (2D-GIWAXS). **Figure 4.60** presented the 2D diffraction patterns and the corresponding 1D lineut profiles in the in-plane (IP) (q_{xy}) and the out-of-plane (OOP) (q_z) directions for all neat and blend films. The extracted data for peak positions, *d*-spacing, and the calculated crystalline coherence length (L_c) for each of the neat and blend films are summarized in **Table S4.13**. The 2D diffraction patterns for PM6 are presented in **Figure S4.22.** 2D GIXD diffraction pattern for the neat film of PM6., and the IP and OOP line-cuts of PM6 are plotted within **Figure 4.60g-h**.

The neat films of LTX10, LTX10-4F and LTX10-4Cl showed drastically different 2D diffraction patterns. For the neat film of LTX10, (**Figure 4.60a**) π-π diffraction pattern appeared in the IP direction at q_{xy} of 1.80 $Å^{-1}$ (d = 3.49 Å) with a crystalline coherence length (L_c) of 4.05 nm, while in the OOP direction, an intense lamellar peak at q_z of 0.31 $Å^{-1}$ (d = 20.43 Å, L_c = 7.28 nm) was

identified. Such diffraction patterns represent distinct *edge-on* orientation of LTX10, where the ladder backbones are perpendicular to the substrate with the lamellar packing in the vertical direction and the π-π stacking in the horizontal direction (**Figure 4.61**a). In contrast, the neat film of LTX10-4Cl showed π-π diffraction in the OOP direction at q_z of 1.80 Å^{-1} (d = 3.49 Å, L_c = 1.41 nm) and associated IP diffraction at q_{xy} of 0.234 Å^{-1} (d = 26.87 Å, L_c = 12.86 nm), representing distinct *face-on* orientation, where the ladder backbones are parallel to the substrate with the π-π stacking in the vertical direction (**Figure 4.61**c). For the neat film of LTX10-4F, however, the 2D diffraction patterns were more complex. There is off-axis π-π diffractions at q_z of 1.78 Å^{-1} (d = 3.54 Å), suggesting existence of somewhat *tilted face-on* π-π stacking. In the IP direction, two peaks were identified at lower q_{xy} of 0.25 Å^{-1} (d = 25.53 Å, L_c = 8.01 nm) and 0.36 Å^{-1} (d = 17.32 Å, L_c = 9.97 nm). (**Figure 4.60**h, "▽") In the OOP direction, a very intense peak appeared at q_z of 0.38 Å^{-1} (d = 16.42 Å, L_c = 12.10 nm), (**Figure 4.60**h, "#"), representing a unidentified structural ordering with *d*-spacing of ~16-17 Å with rather random orientations (**Figure 4.61**c).

The neat film of PM6 clearly showed mixed *face-on* and *edge-on* orientation, where the *face-on* oriented crystallites were reflected as the OOP π-π diffraction at q_z of 1.69 Å^{-1} (d = 3.72 Å, L_c = 2.09 nm) associated with the IP lamellar peak at q_{xy} of 0.289 Å^{-1} (d = 21.7 Å, L_c = 7.23 nm) and the *edge-on* oriented crystallites were represented with intense lamellar peak at q_z of 0.326 Å^{-1} (d = 19.3 Å, L_c = 6.25 nm). In the blend films of PM6:LMAs, all three blends showed π-π diffraction patterns in the OOP direction, indicating existence of *face-on* orientated crystallites. (**Figure 4.60**d-f**)** Given that the blends of PM6:LTX10-series had the donor/acceptor weight ratio (D:A) of 1:0.8, the distinct diffraction features of the acceptors were weakened in the blends relative to the signals from individual neat films. The blend of PM6:LTX10 preserved weak π-π diffraction peak in the IP direction originated from *edge-on* oriented LTX10. The blend of

PM6:LTX10-4F have shoulder peaks in the lower q_{xy} and q_z regions that were originally present in neat film of LTX10-4F. In addition, the blend of PM6:LTX10-4Cl mostly resembled diffractions of PM6 neat film and the features of LTX10-4Cl became indistinguishable. In summary, from PM6:LTX10 to PM6:LTX10-4F and further to PM6:LTX10-4Cl, while the donor polymer adopts a mixed *face-on*/*edge-on* orientations, the orientation of the LMAs varied from *edge-on* for LTX10, to *tilted face-on* for LTX10-4F, and further towards *face-on* for LTX10-4Cl, therefore positively affecting photovoltaic performance.

4.2.4 *Conclusions*

In summary, we present a new series of ladder molecule acceptors (LMAs) based on Friedlander condensation of IDTT core with n-decyl side chains (IDTT10) and various end-groups, namely, LTX10, LTX10-4F and LTX10-4Cl. The new series of LMAs demonstrated optical and electronic properties similar to the reported precedents with 2-hexyldecyl side chains. However, compared with long branched side chains, the shorter n-decyl chains did compromise the solubility, thus posed extra difficulty in synthesis and purification, and had negative effects on film-forming qualities when blending LMAs with the polymer donor, PM6. Nevertheless, decent photovoltaic performance was obtained from the optimized devices based on PM6:LMAs blends with PCE ranging from 6.1% to 9.3% and high V_{oc} values of 0.97 – 1.1 V. Furthermore, 2D GIXD analysis revealed the LTX10 adopted preferentially *edge-on* orientation, whereas LTX10-4Cl was preferentially *face-on*. LTX10-4F demonstrated significant structural ordering in multiple directions with somewhat tilted *face-on* π-π stacked crystallites.

4.2.5 *Supporting Information*

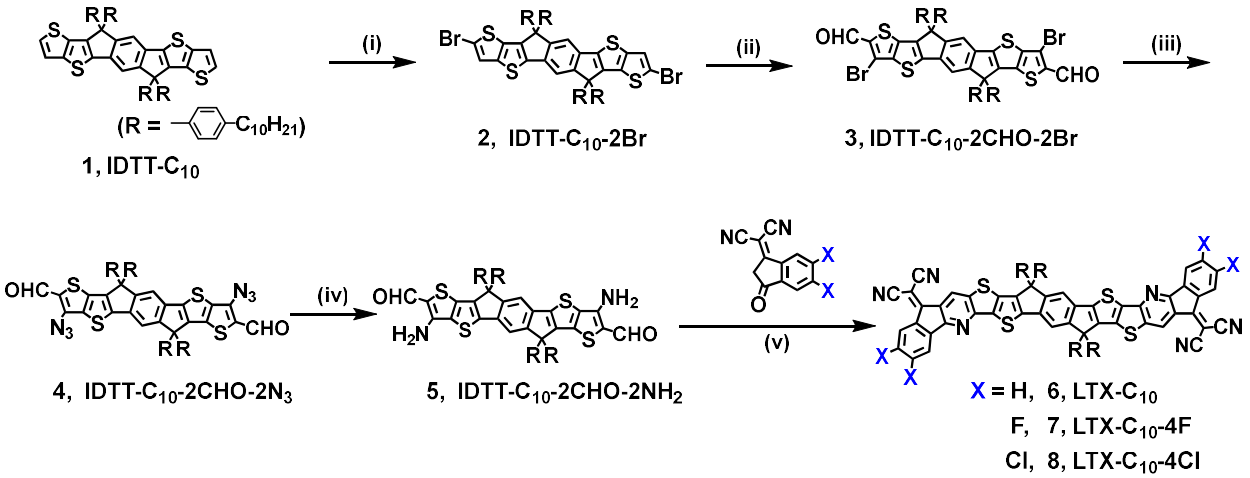

Scheme S4.3. Synthesis of ladder molecule acceptors: LTX-C_{10}, LTX-C_{10}-4F and LTX-C_{10}-4Cl. Reagents and conditions: (i) NBS (2.0 equiv), S: $CHCl_3$/AcOH (v:v 3:1), r.t., overnight; (ii) 1) LDA(3.0 equiv), S: THF, -78 ºC→r.t., 24 h; 2) DMF (excess), 0 ºC →r.t. for 2 h; (iii) NaN_3 (10 equiv), S: DMPU, r.t., 24 h; (iv) $(NH_4)_2S$ (aq, excess), S: $CHCl_3$/MeOH, r.t. for 30 min; (v) diphenyl phosphate, S: Toluene, 90 ºC, 24h.

X-ray Crystallography of IDTT10-2CHO-2NH$_2$. A very tiny yellow needle, measuring 0.22 x 0.05 x 0.05 mm^3 was mounted on a loop with oil. Data was collected at -173ºC on a Bruker APEX II single crystal X-ray diffractometer, Mo-radiation.

Crystal-to-detector distance was 40 mm and exposure time was 300 seconds per frame for all sets. The scan width was 0.5º. Data collection was 99.5% complete to 25º in ϑ. A total of 19726 unique reflections were collected covering the indices, -27<=h<=27, -22<=k<=22, -34<=l<=34 with a R_{int} of 0.2097. Indexing and unit cell refinement indicated a primitive monoclinic lattice. The space group was found to be P 2_1/c (No. 14).

The data was integrated and scaled using SAINT, SADABS within the APEX2 software package by Bruker.[90] Solution by direct methods (SHELXS, SIR97[90]) produced a complete heavy atom phasing model consistent with the proposed structure. The structure was completed by difference Fourier synthesis with SHELXL97.[91-93] Scattering factors are from Waasmair and Kirfel.[94] Hydrogen atoms were placed in geometrically idealised positions and constrained to ride on their parent atoms with C---H distances in the range 0.95-1.00 Angstrom. Isotropic thermal parameters U_{eq} were fixed such that they were 1.2U_{eq} of their parent atom U_{eq} for CH's and 1.5U_{eq} of their parent atom U_{eq} in case of methyl groups. All non-hydrogen atoms were refined anisotropically by full-matrix least-squares.

The crystals started to fracture the moment they were removed from solution. Thus, a relatively small sample examined.

The asymmetric unit contains 3 half molecules. One of those halves sees its n-pentane groups disordered.

The structure is of high quality and ready for publication.

Data were summarized in **Table S4.11**.

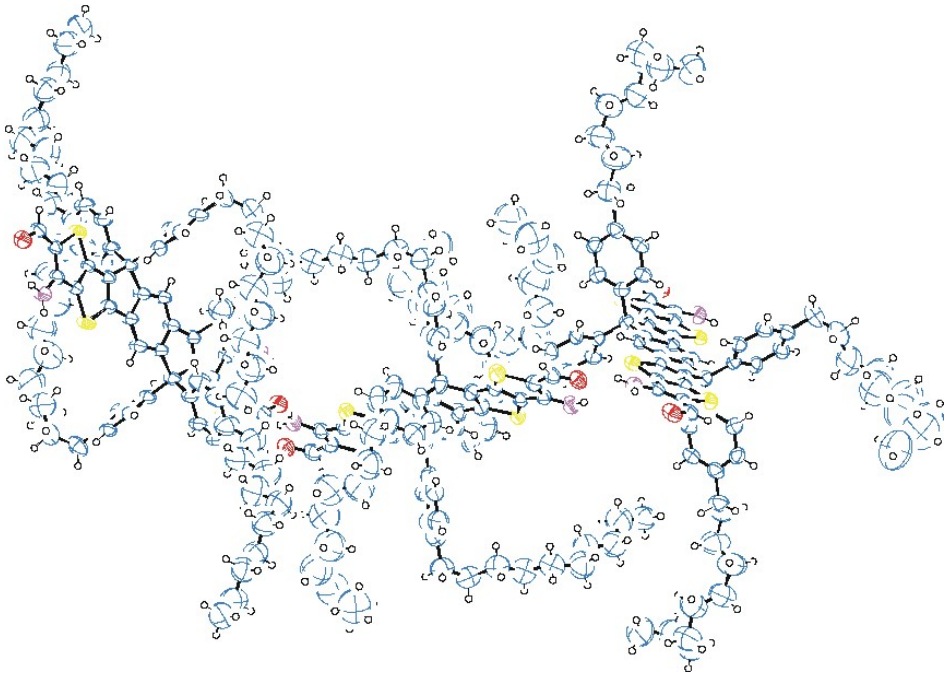

Figure S4.62. ORTEP of the extended structure for IDTT10-2CHO-2NH_2 with thermal ellipsoids at the 50% probability level. Disorder omitted for clarity.

Table S4.11. Crystallographic Data and Structural Refinement for IDTT10-2CHO-2NH_2

	IDTT-2CHO-2NH_2
Empirical formula	C_{86} H_{108} N_2 O_2 S_4
Formula weight	1329.98
Temperature	100(2) K
Wavelength	0.71073 Å
Crystal system	Monoclinic
Space group	P $2_{1/c}$
Unit cell dimensions	a = 22.3804(16) Å, α= 90°
	b = 18.6922(14) Å, β=109.494(5)°
	c = 28.469(2) Å, γ = 90°
Volume	11227.2(15) $Å^3$
Z	6
Density (calculated)	1.180 Mg/m^3
Absorption coefficient	0.176 mm^{-1}
F(000)	4308
Crystal size	0.220 × 0.050 × 0.050 mm^3
Theta range for data collection	1.455 to 25.027°
Index ranges	$-27 \le h \le 27$, $-22 \le k \le 22$, $-34 \le l \le 34$
Reflections collected	19726
Independent reflections	19726 [R(int) = 0.2097]
Completeness to theta = 25.000°	99.5 %
Refinement method	Full-matrix least-squares on F^2
Data / restraints / parameters	19726 / 2246 / 1260
Goodness-of-fit on F^2	0.836
Final R indices [I>2sigma(I)]	R1 = 0.1053, wR2 = 0.2392
R indices (all data)	R1 = 0.3937, wR2 = 0.3435
Largest diff. peak and hole	0.393 and -0.363 $e.Å^{-3}$

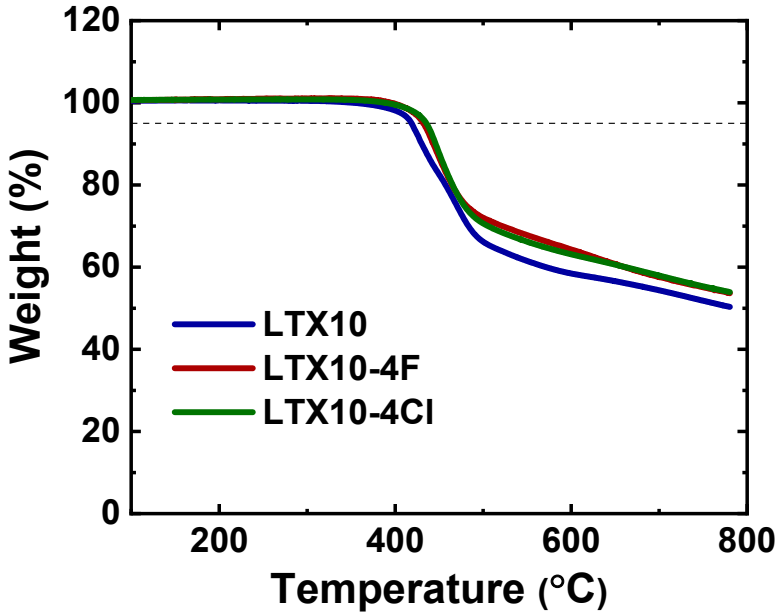

Figure S4.63. TGA traces of the ladder molecule acceptors: LTX10, LTX10-4F and LTX10-4Cl.

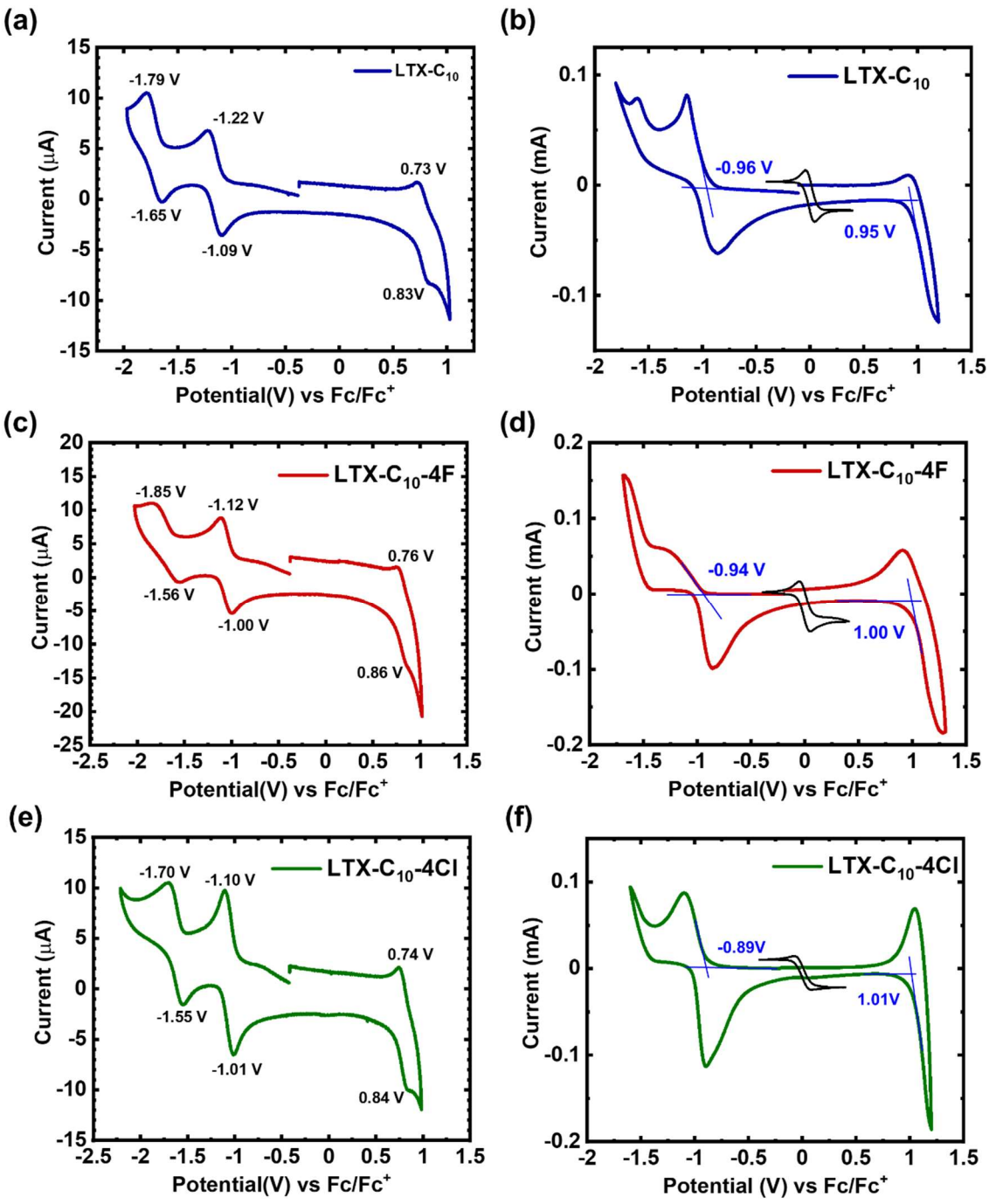

Figure S4.64. Cyclic voltammograms of solutions and thin films for the ladder molecule acceptors: (a) LTX-C_{10} (solution); (b) LTX-C_{10} (thin film); (c) LTX-C_{10}-4F (solution); (d) LTX-C_{10}-4F (thin film); (e) LTX-C_{10}-4Cl (solution); (f) LTX-C_{10}-4Cl (thin film).

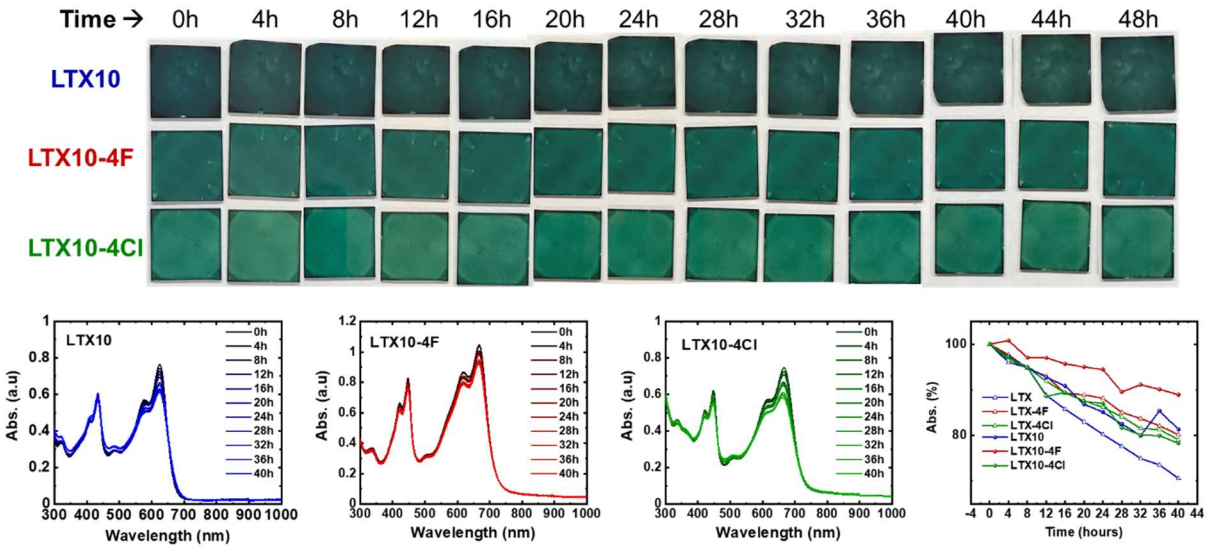

Figure S4.65. Images of thin films of LTX, LTX-4F and LTX10-4Cl under continuous 1 sun illumination for up to 48 h and the progression of the optical absorbance.

Table S4.12. Charge Transport Properties of Neat Films for the Ladder Molecule Acceptors

Acceptors	μ_e (cm^2/Vs)
LTX10	$8.98 \times 10^{-5} \pm 1.03 \times 10^{-4}$
LTX10-4F	$1.36 \times 10^{-4} \pm 1.61 \times 10^{-4}$
LTX10-4Cl	$2.11 \times 10^{-5} \pm 1.35 \times 10^{-5}$

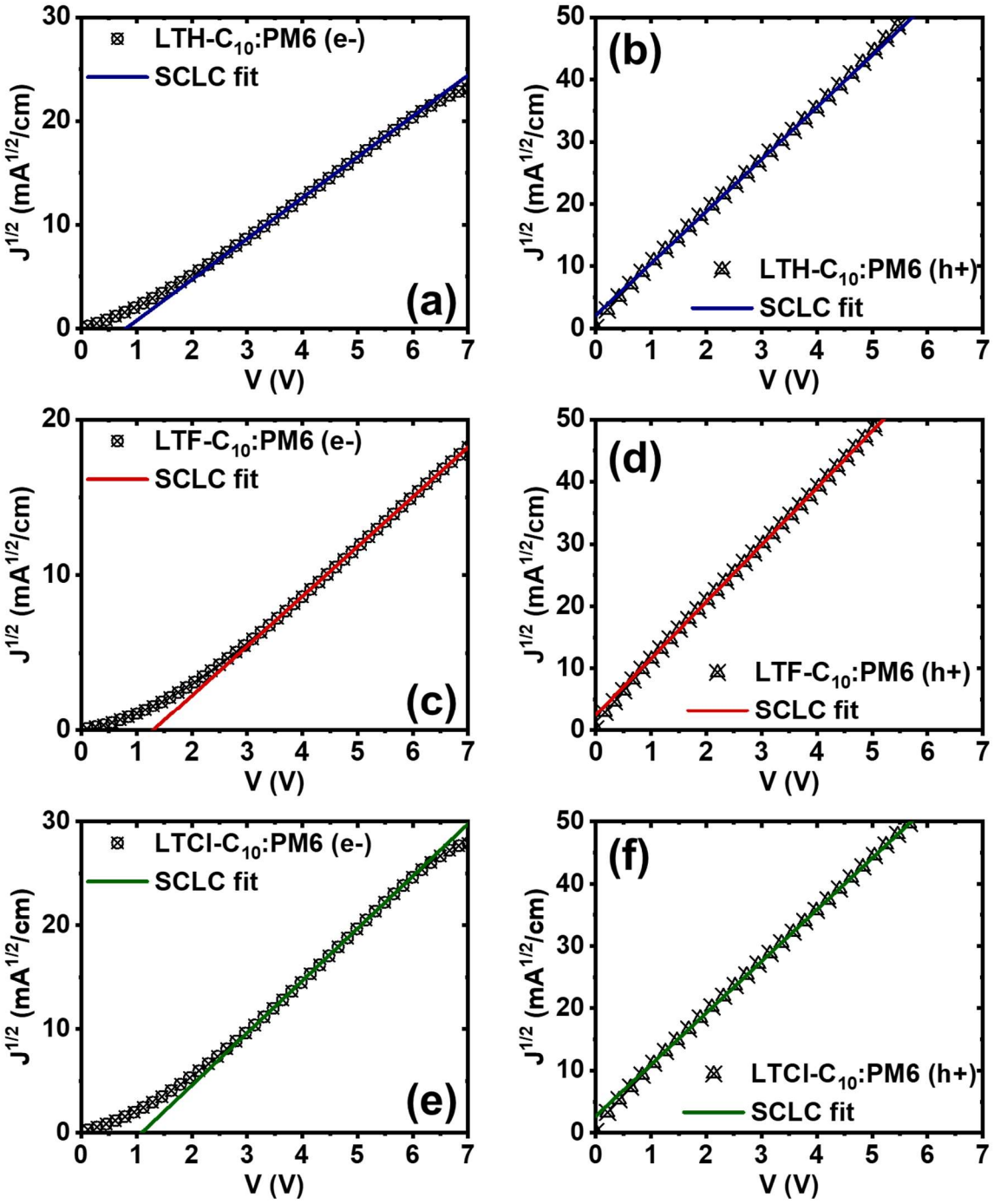

Figure S4.66. SCLC fitting of PM6:LMAs: (a) PM6:LTX10 (electron-only); (b) PM6:LTX10 (hole-only); (c) PM6:LTX10-4F (electron-only); (b) PM6:LTX10-4F (hole-only); (a) PM6:LTX10-4Cl (electron-only); (b) PM6:LTX10-4Cl (hole-only).

Table S4.13. Peak Positions Extracted from 1D Line-Cut Profiles in the In-Plane (IP) Direction and the Out-of-Plane (OOP) Direction for Neat Films and PM6:LMA Blend Films.

Film component	q_{xy} (Å^{-1})	*d*-spacing (Å)	L_c (nm)	q_z (Å^{-1})	*d*-spacing (Å)	L_c (nm)	q_z (Å^{-1})	*d*-spacing (π-π)	L_c (nm)
LTX10	0.258[a], 1.80	24.3, 3.49	4.03, 4.05	0.308	20.4	7.28	N/A	N/A	N/A
LTX10-4F	0.246, 0.363	25.5, 17.3	8.01, 9.97	0.383	16.4	12.10	1.78	3.54	1.39
LTX10-4Cl	0.234 (0.270[b])	26.9	12.86	0.470	13.4	N/A	1.80	3.49	1.41
PM6	0.289	21.7	7.23	0.326	19.3	6.25	1.69	3.72	2.09
PM6:LTX10	0.289, 1.82	21.7	10.96, 3.42	0.326	19.3	6.51	1.73	3.64	1.66
PM6:LTX10-4F	0.289 (0.258[b])	21.7	8.72	0.332, 0.383[b]	18.9	5.30	1.71[b]	3.67	1.43
PM6:LTX10-4Cl	0.289	21.7	10.45	0.332	18.9	6.75	1.70	3.70	1.66

[a] broad peak. [b] shoulder peak.

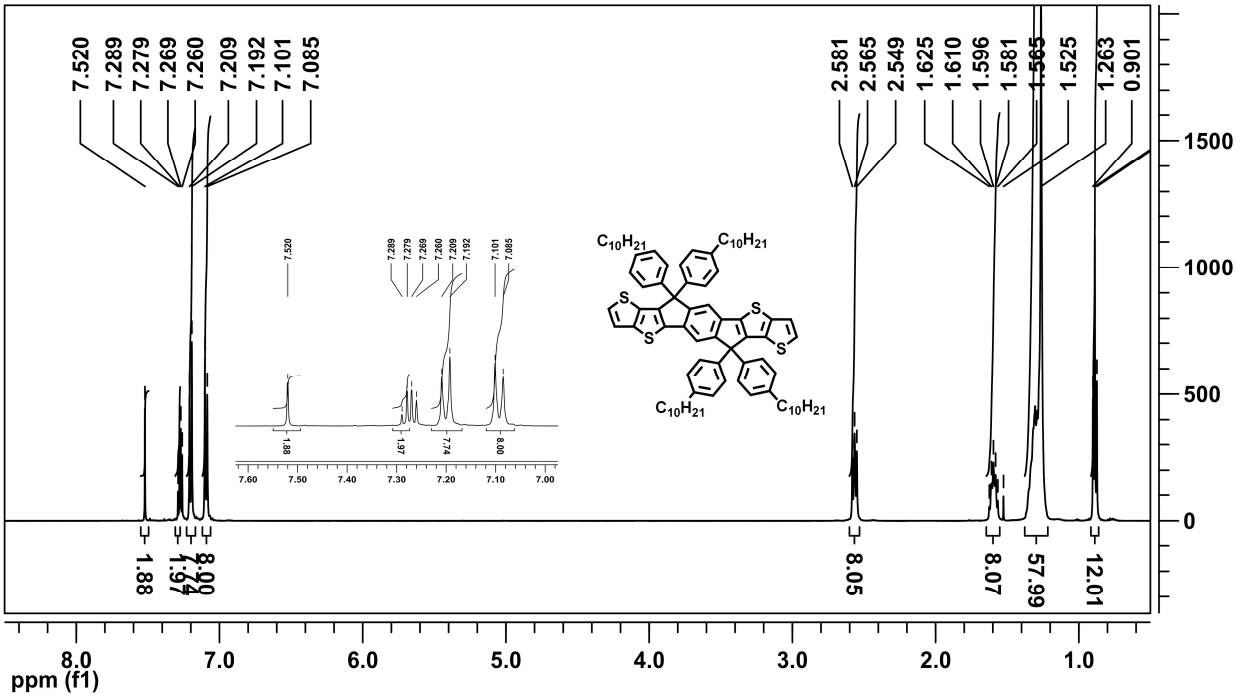

Figure S4.67. ^{1}H NMR (500 MHz, $CDCl_3$) spectrum of IDTT10.

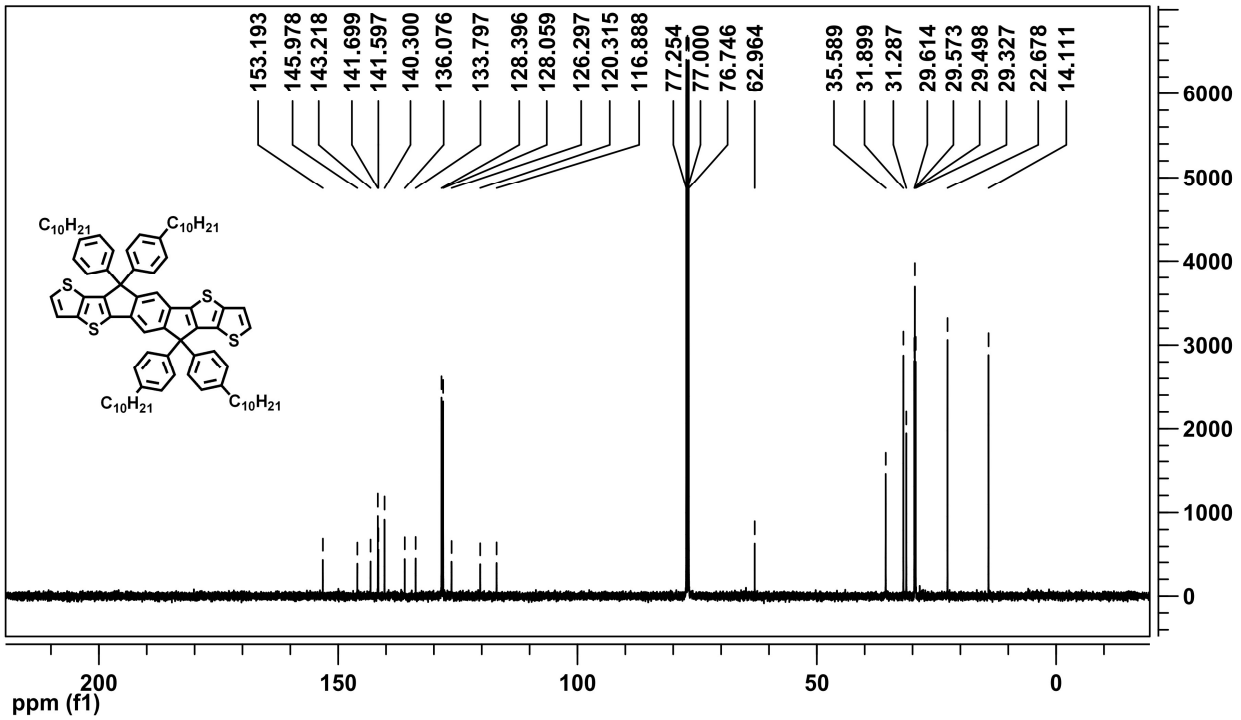

Figure S4.68. ^{13}C NMR (125 MHz, $CDCl_3$) spectrum of IDTT10.

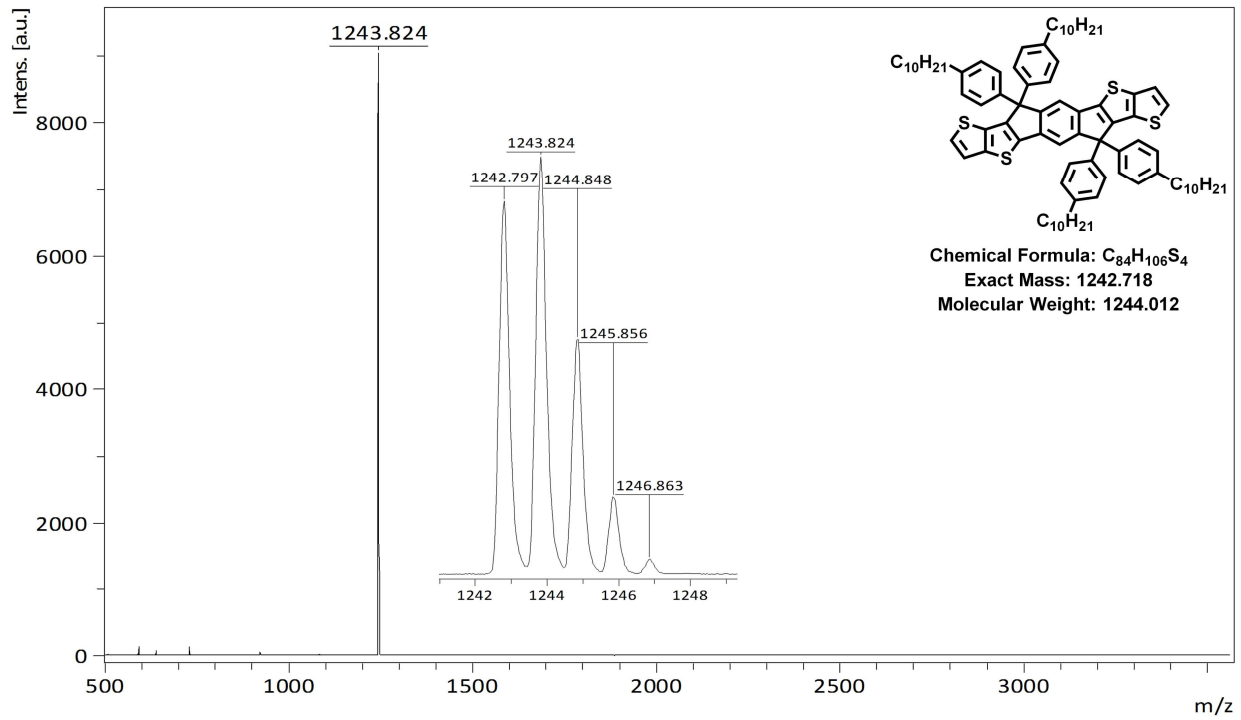

Figure S4.69. MALDI-TOF mass spectrum of IDTT10.

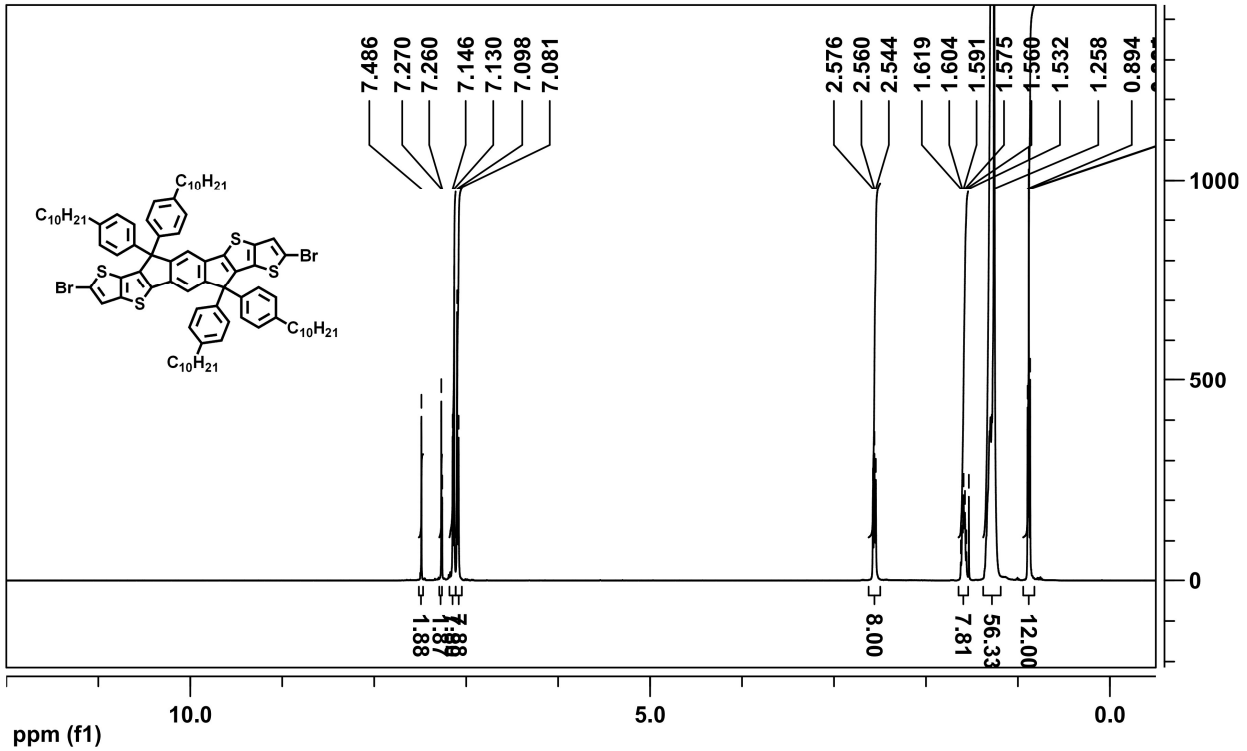

Figure S4.70. ^{1}H NMR (500 MHz, $CDCl_3$) spectrum of IDTT10-2Br.

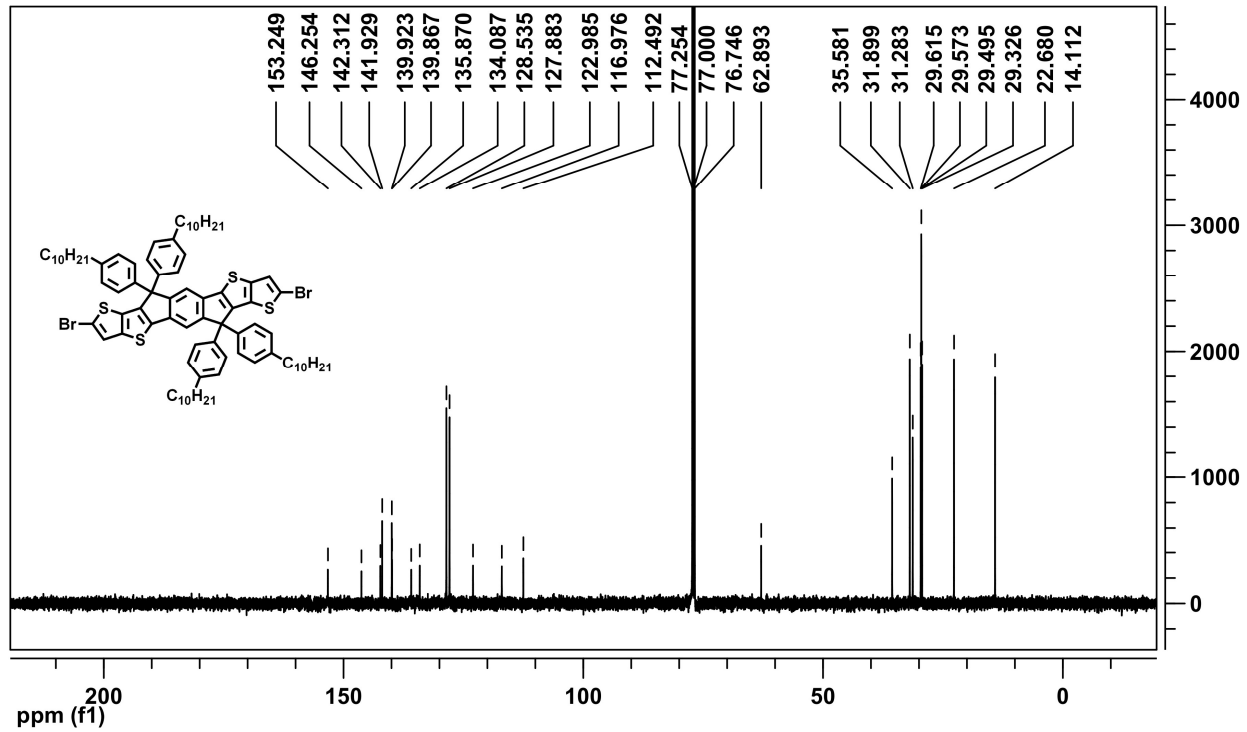

Figure S4.71. ^{13}C NMR (125 MHz, $CDCl_3$) spectrum of IDTT10-2Br.

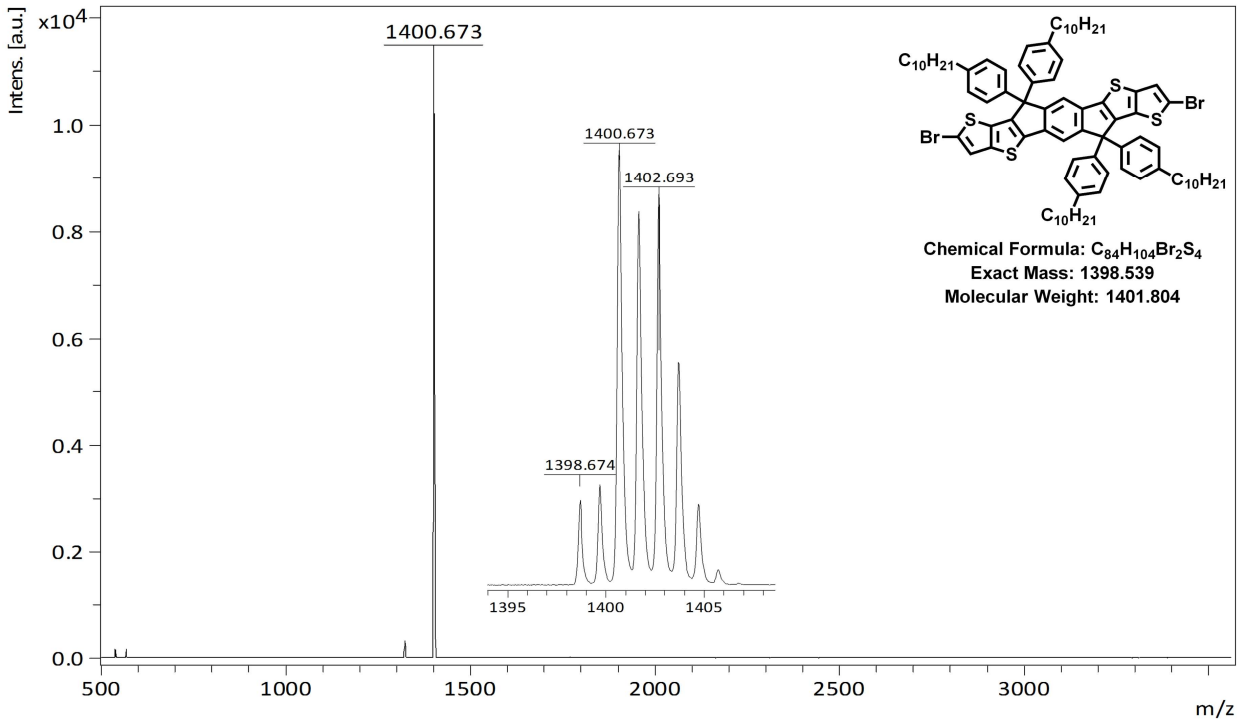

Figure S4.72. MALDI-TOF mass spectrum of IDTT10-2Br.

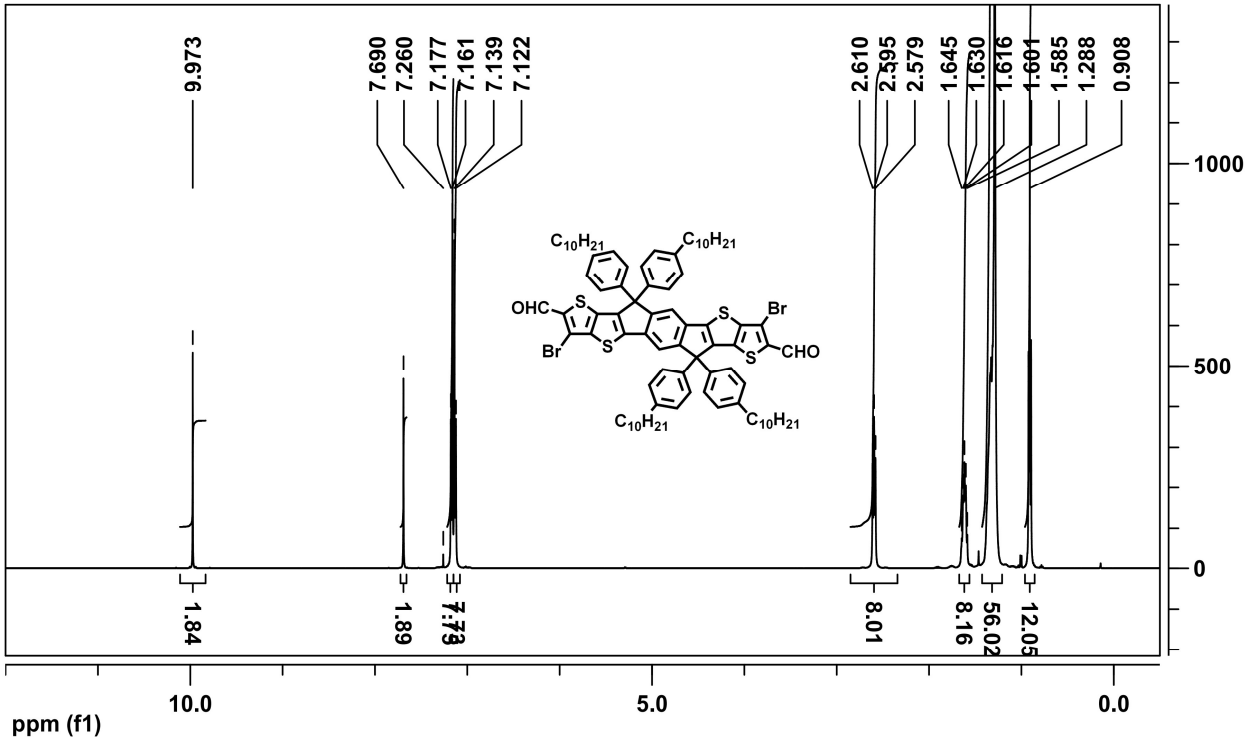

Figure S4.73. ^{1}H NMR (500 MHz, $CDCl_3$) spectrum of IDTT10-2CHO-2Br.

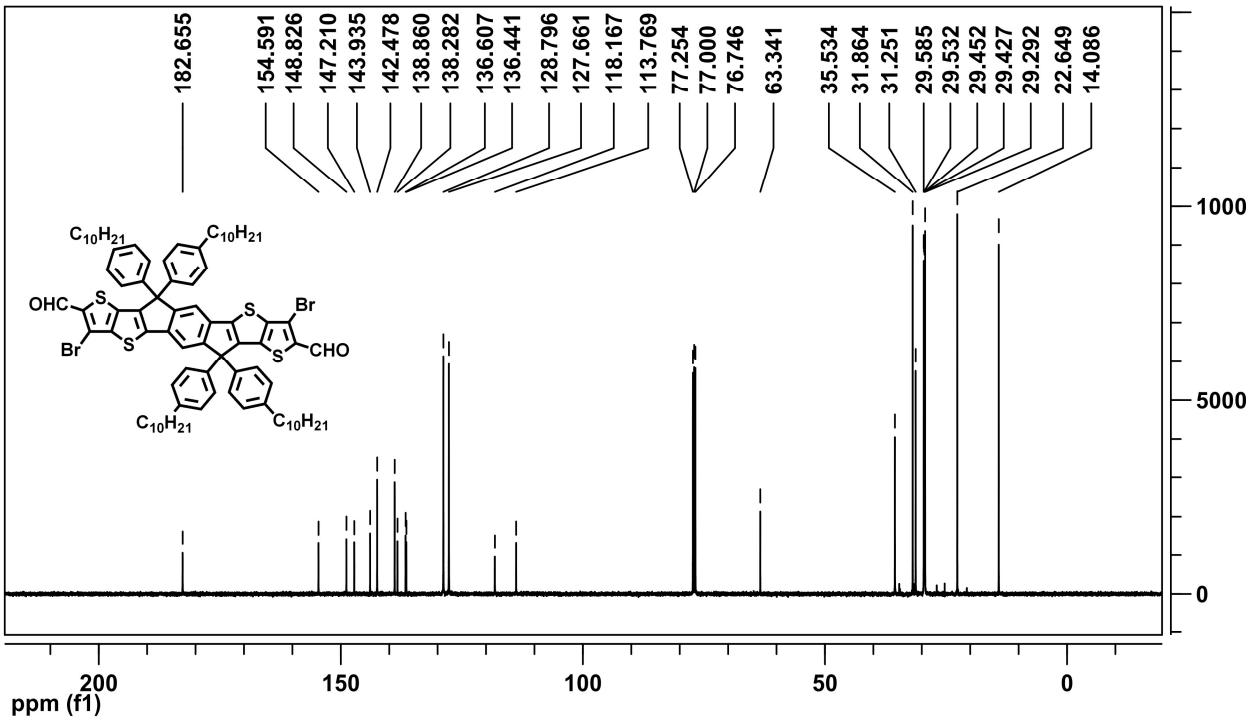

Figure S4.74. ^{13}C NMR (125 MHz, $CDCl_3$) spectrum of IDTT10-2CHO-2Br.

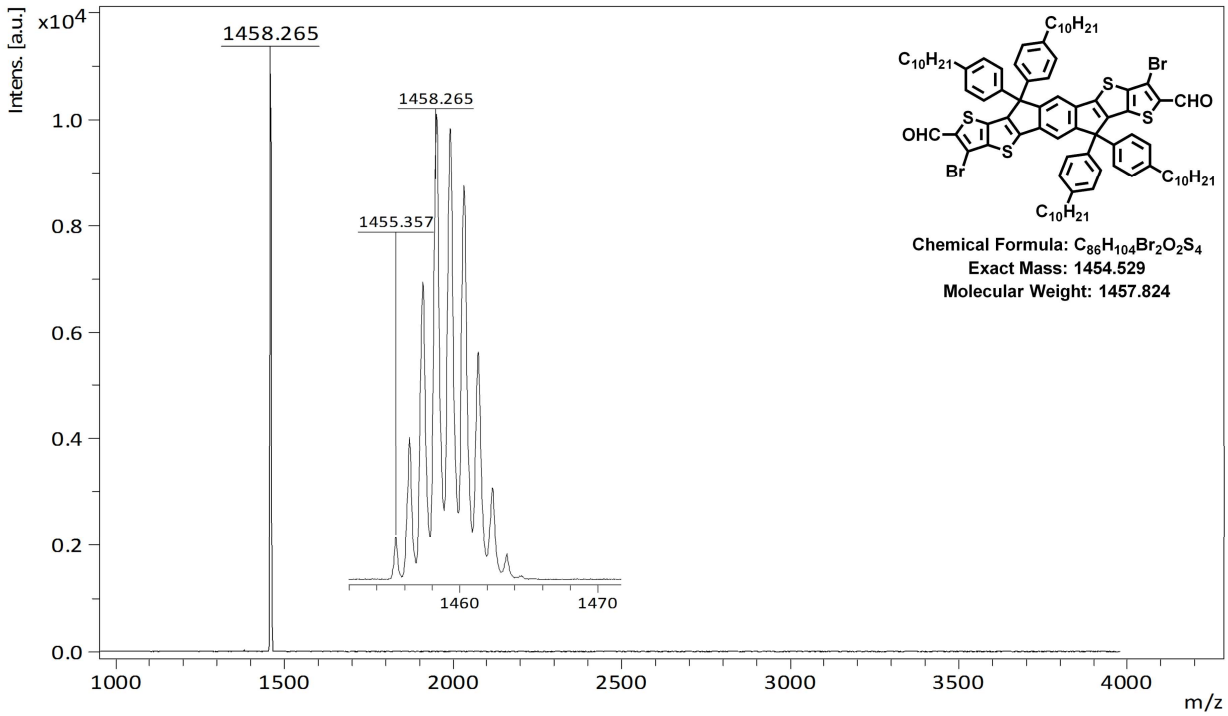

Figure S4.75. MALDI-TOF mass spectrum of IDTT10-2CHO-2Br.

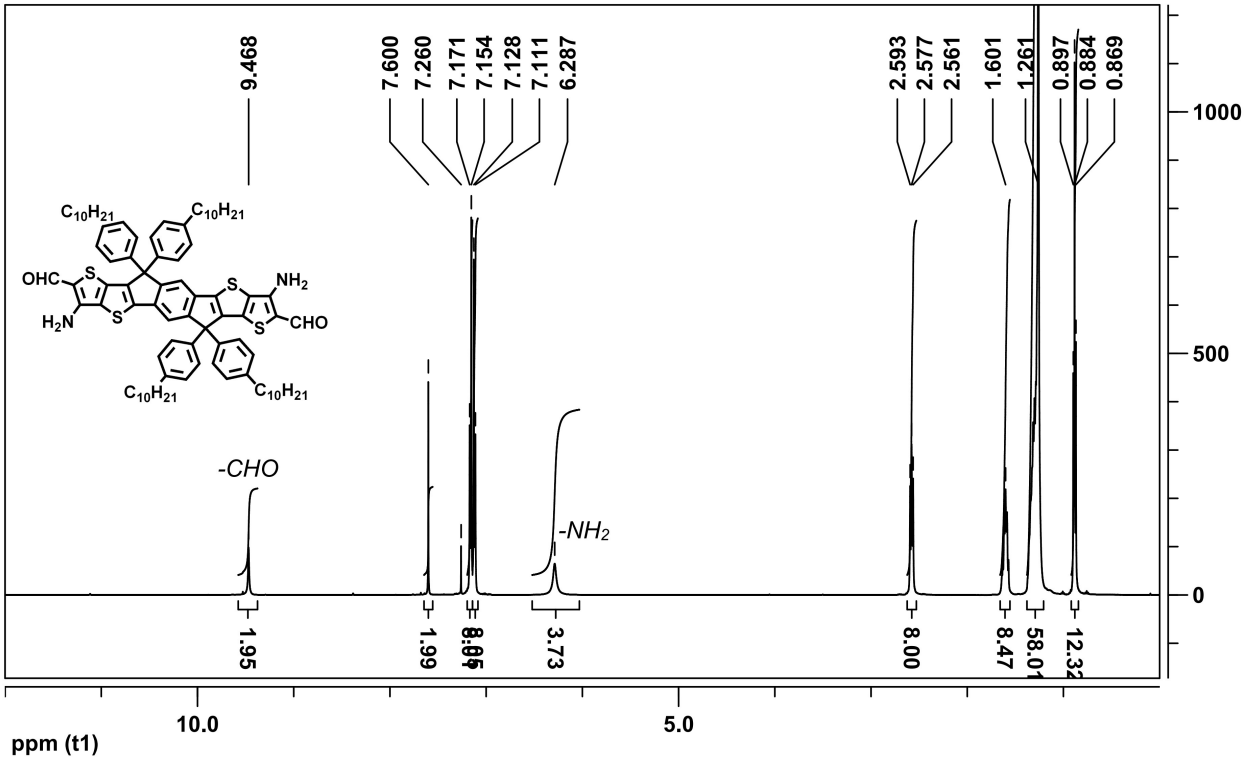

Figure S4.76. ^{1}H NMR (500 MHz, $CDCl_3$) spectrum of IDTT10-2CHO-2NH_2.

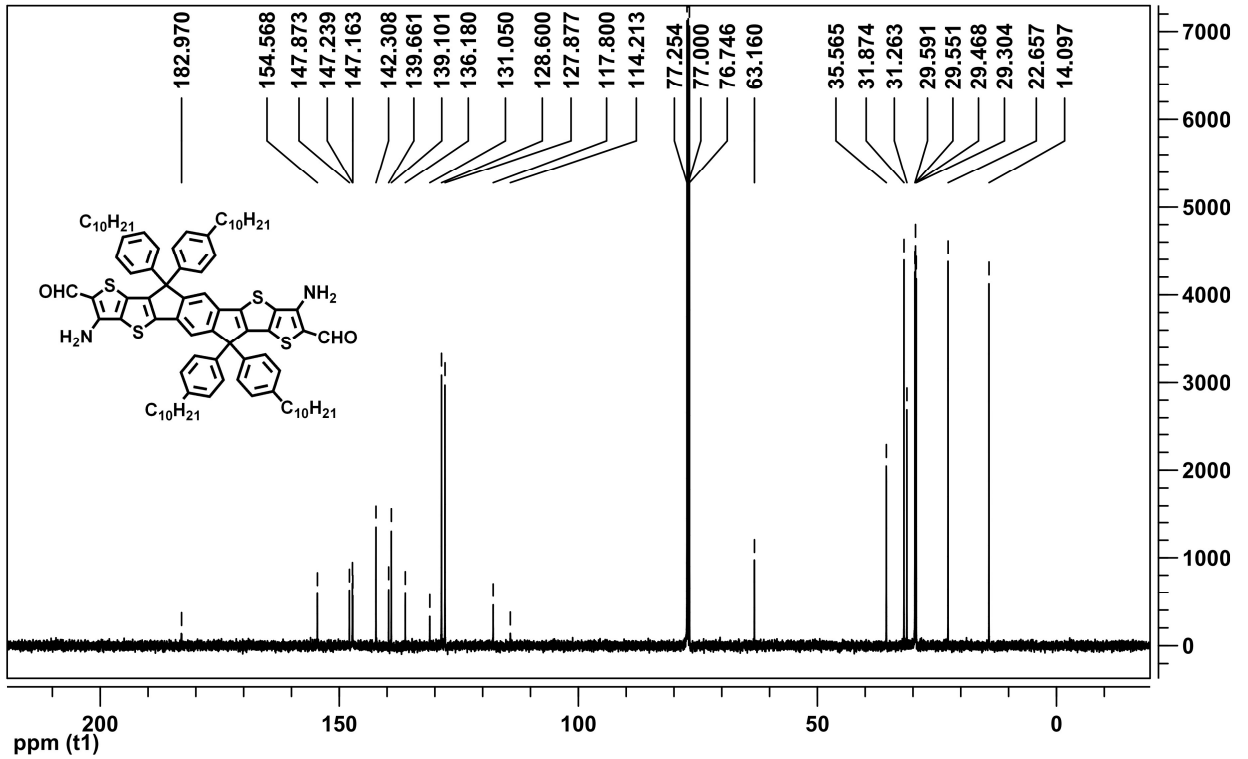

Figure S4.77. ^{13}C NMR (125 MHz, $CDCl_3$) spectrum of IDTT10-2CHO-2NH_2.

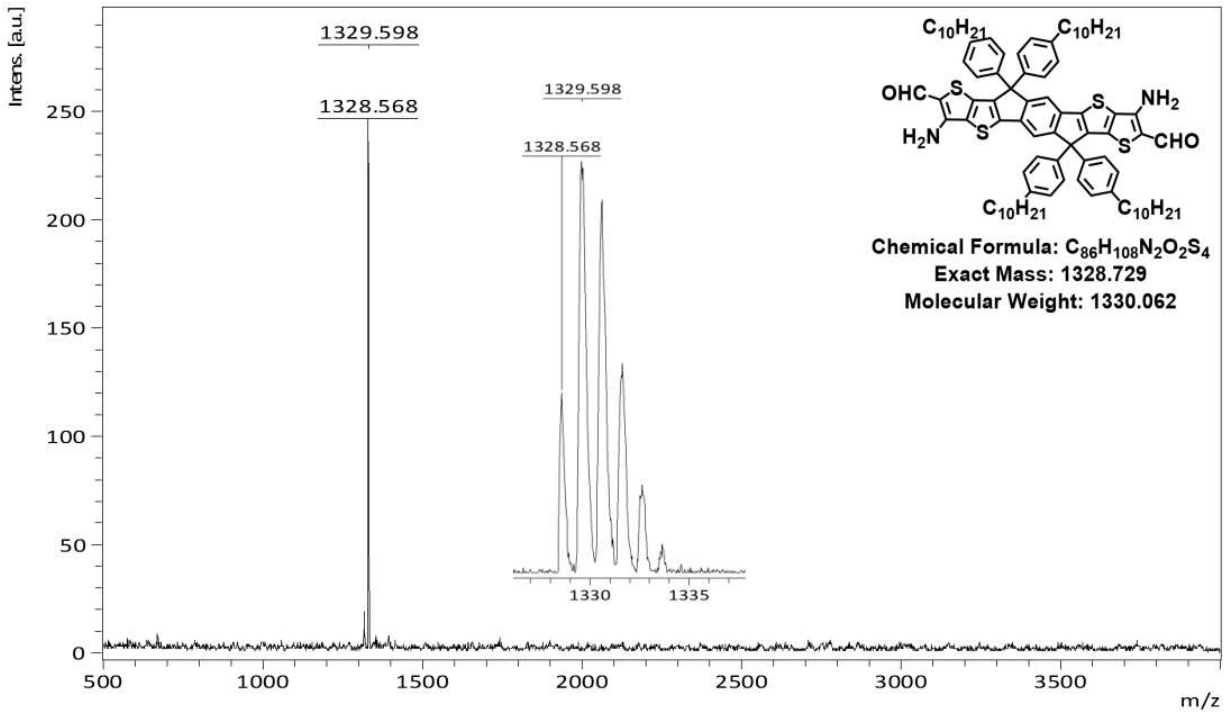

Figure S4.78. MALDI-TOF mass spectrum of IDTT10-2CHO-2NH_2.

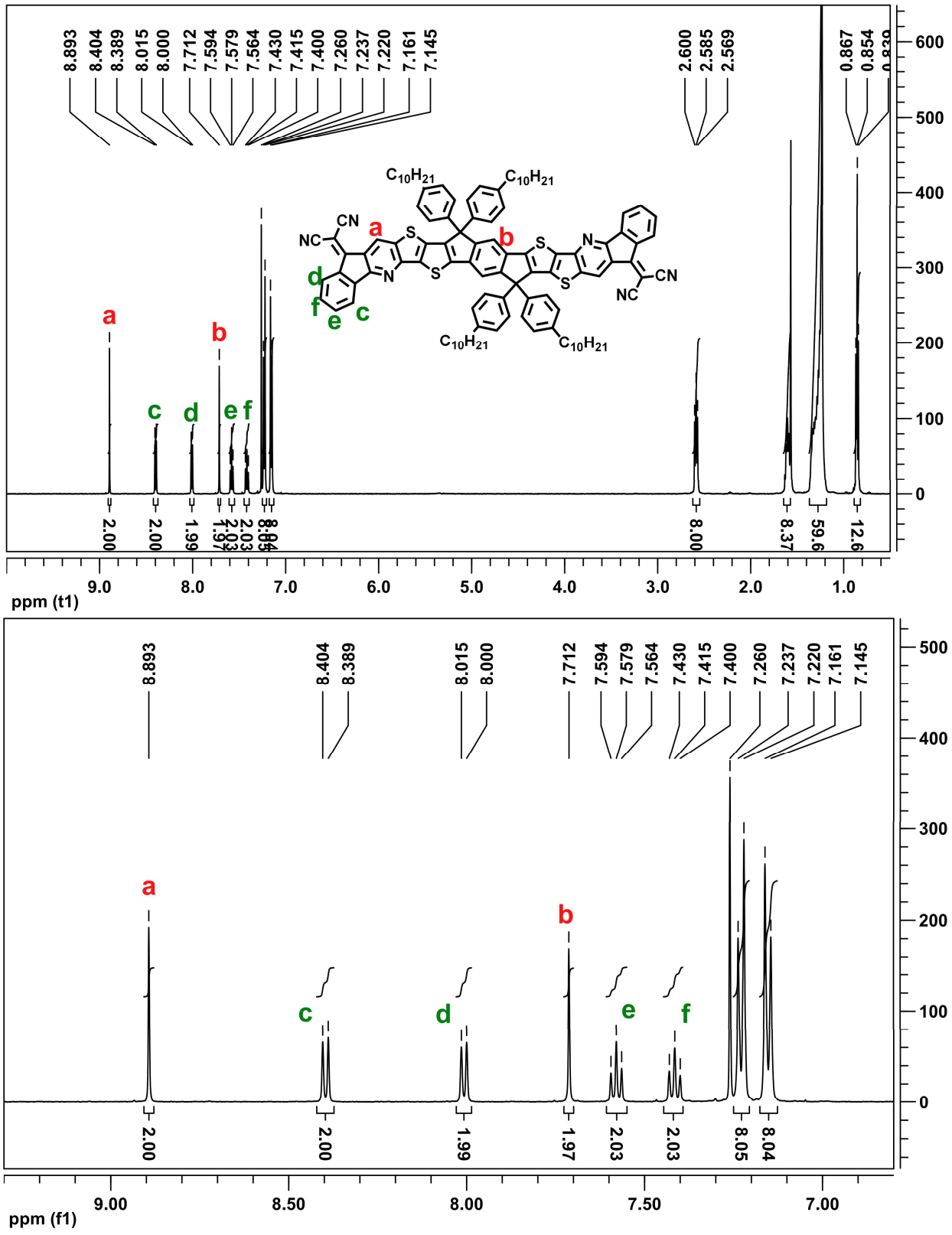
8.893
8.404
8.389
8.015
8.000
7.712
7.594
7.579
7.564
7.430
7.415
7.400
7.260
7.237
7.220
7.161
7.145
2.600
2.585
2.569
0.867
0.854
a
b
c
d
e
f
NC
CN
$C_{10}H_{21}$
2.00
2.00
1.99
1.97
2.03
8.00
8.37
59.6
12.6
ppm (t1)
ppm (f1)

Figure S4.79. ^{1}H NMR (500 MHz, $CDCl_3$) spectrum of LTX10, and the expansion of the aromatic region.

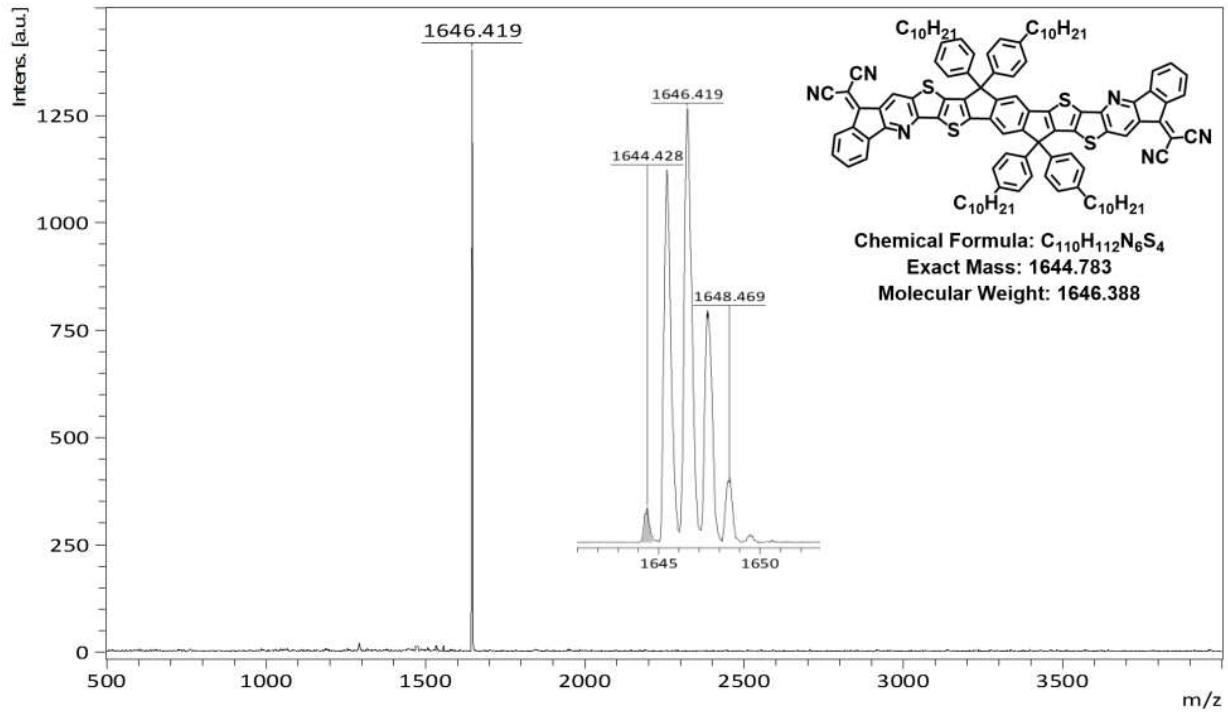

Figure S4.80. MALDI-TOF mass spectrum of LTX10.

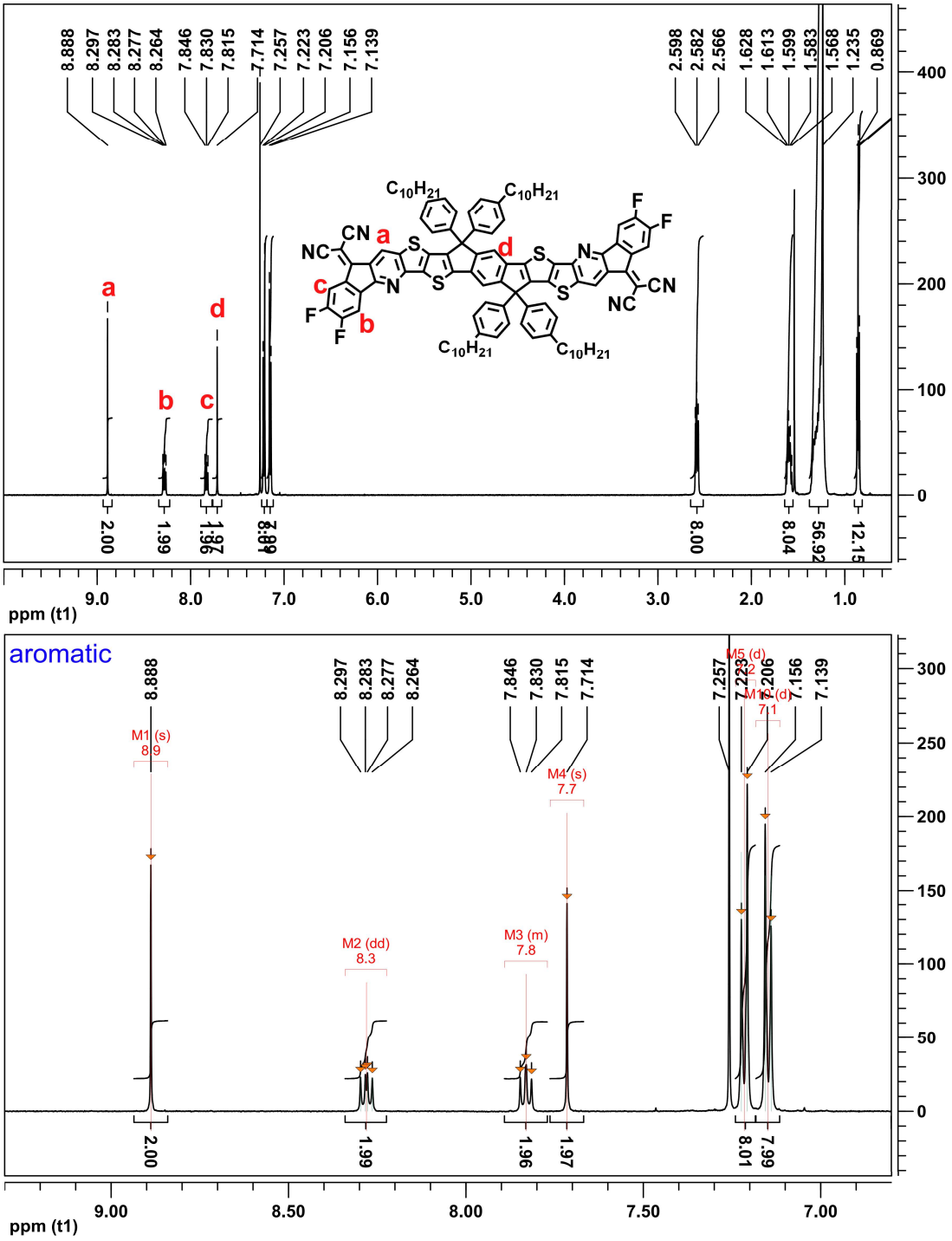

Figure S4.81. ^{1}H NMR (500 MHz, $CDCl_3$) spectrum of LTX10-4F, and the expansion of the aromatic region.

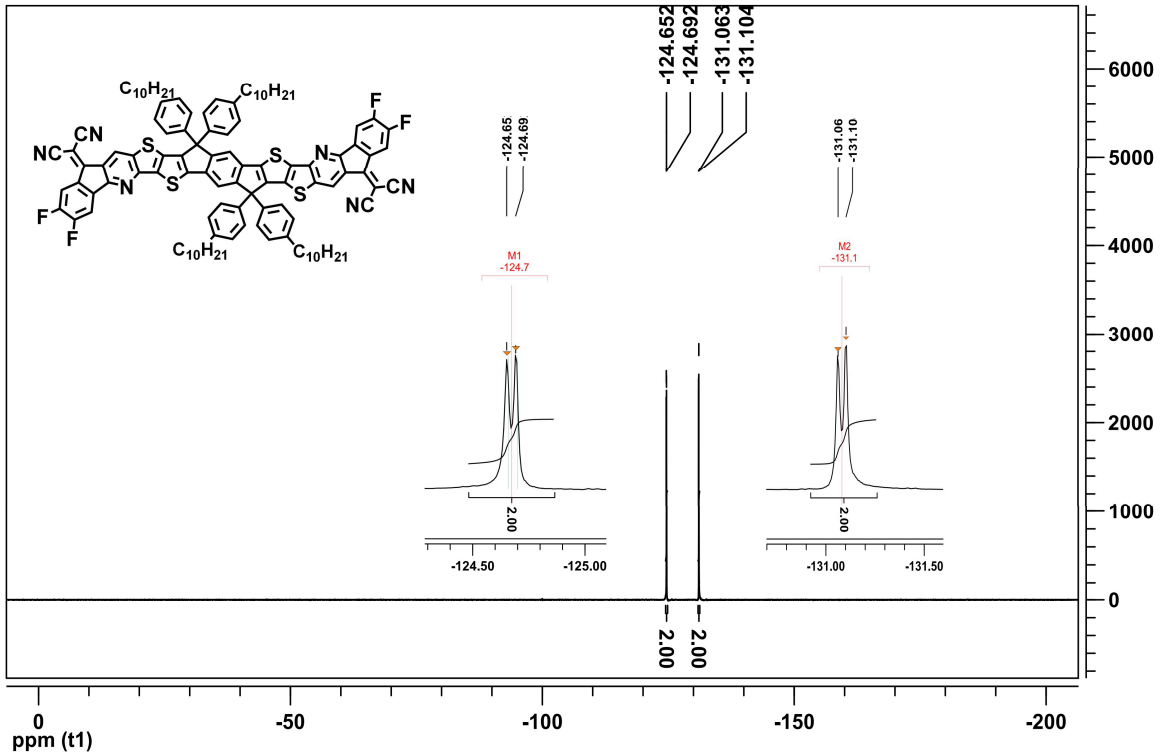

Figure S4.82. ^{19}F NMR spectrum of LTX10-4F.

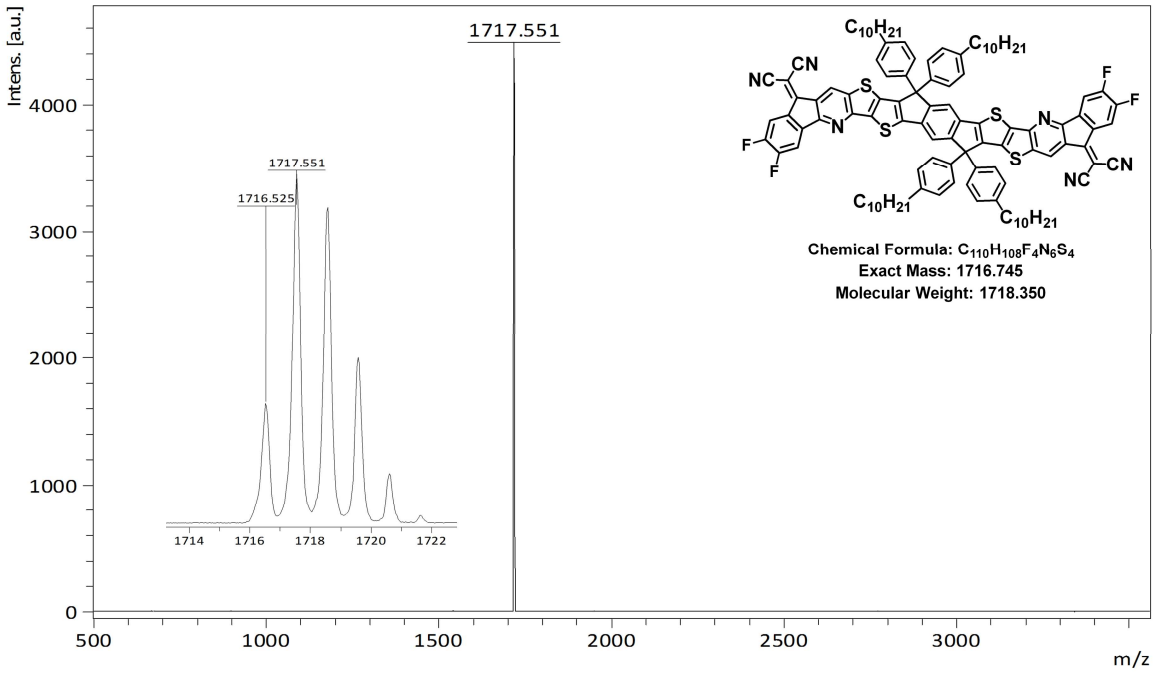

Figure S4.83. MALDI-TOF mass spectrum of LTX10-4F.

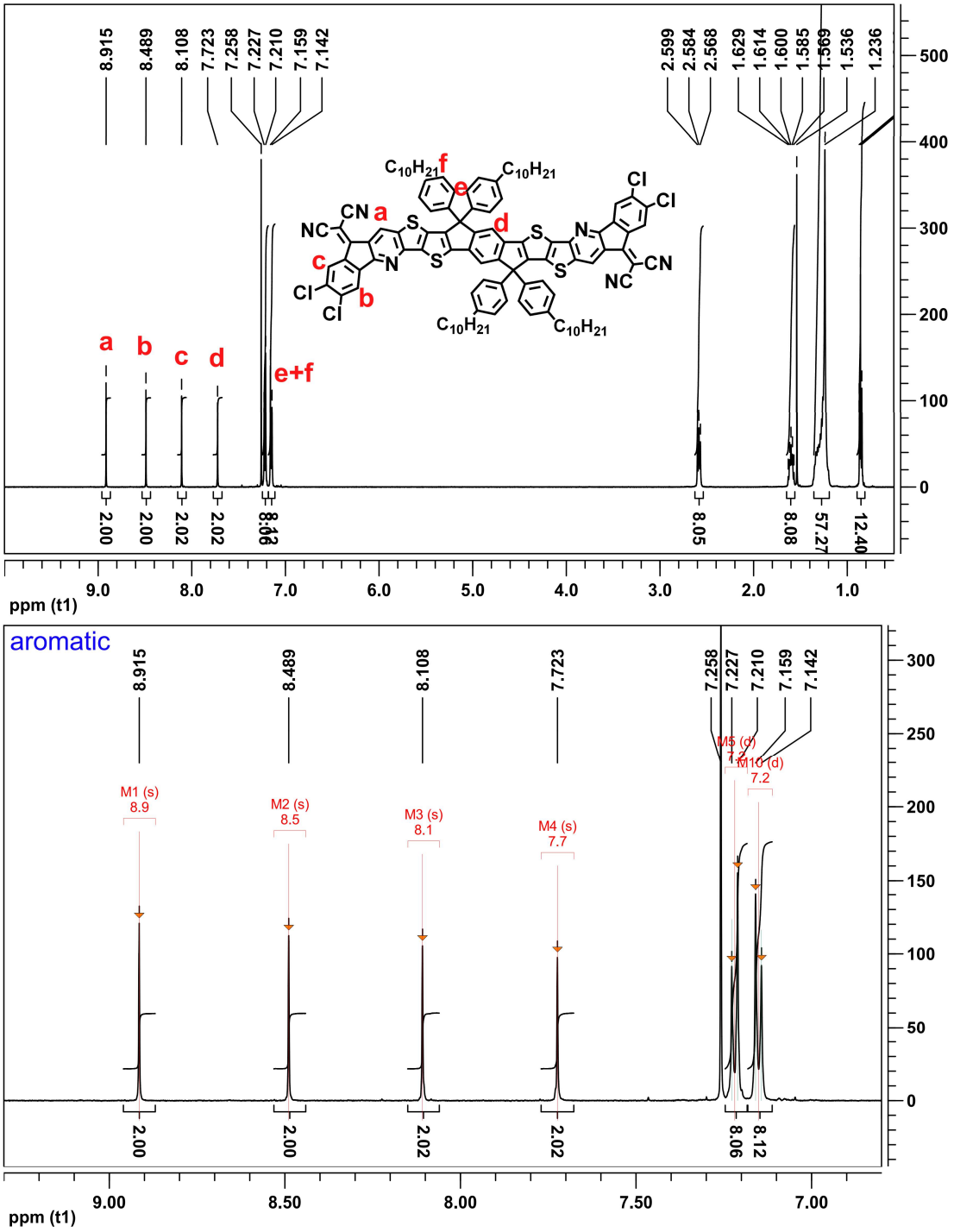

Figure S4.84. ^{1}H NMR (500 MHz, $CDCl_3$) spectrum of LTX10-4Cl, and the expansion of the aromatic region.

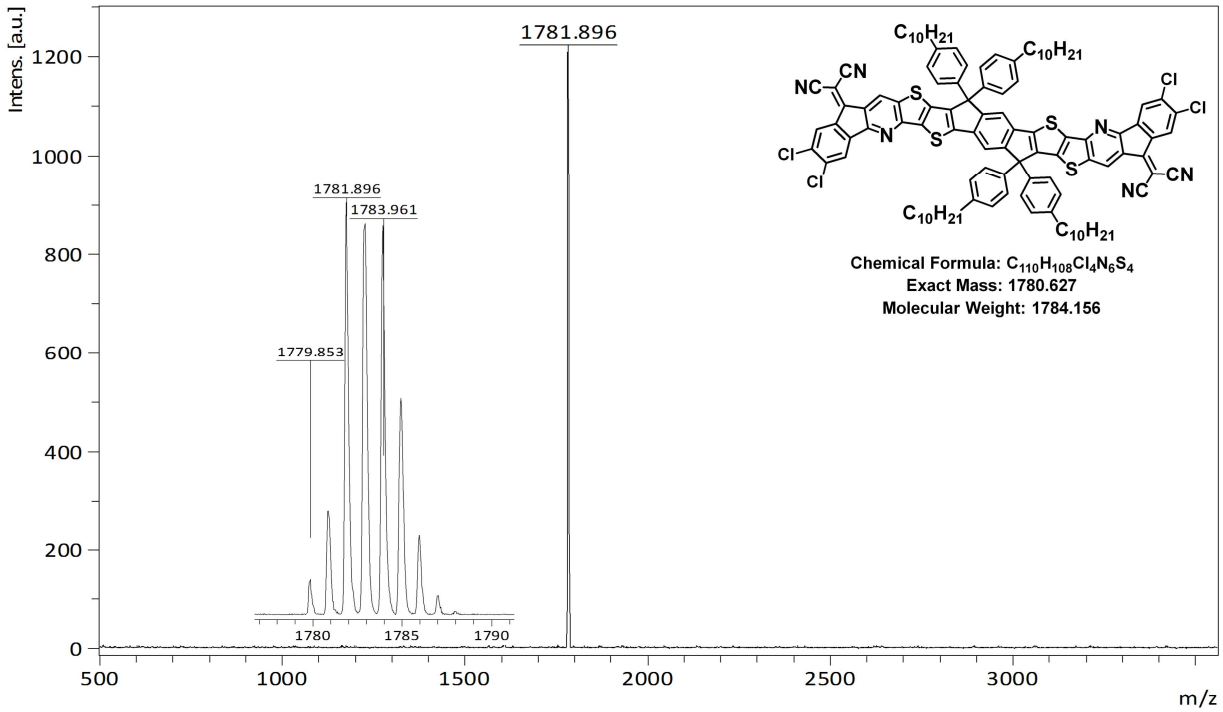

Figure S4.85. MALDI-TOF mass spectrum of LTX10-4Cl.

Chapter 5. CONCLUSIONS AND OUTLOOK

5.1 CONCLUSIONS

Throughout this dissertation, my work has been involved with the three most important components in organic solar cells: p-type polymers, n-type polymers, and non-fullerene small molecule acceptors. The underlying *structure-property-processing-performance* relationships of these materials were carefully investigated.

In **Chapter 2**, I explored the strategy of selenophene substitution as a potential method to improve performance of the regular thiophene-based p-type polymers. Three new selenophene-containing polymers, PBDB-S, PBDBS-T and PBDBS-S were synthesized based on a widely used polymer, PBDB-T, where the original thiophene units in various side chain and backbone positions were substituted with selenophene. It was found that selenophene substitution in the side chain positions had minimal impact on the optical absorption and the electronic structures, whereas selenophene substitution in the backbone positions led to red-shifted absorption by ~40 nm and raised HOMO energy levels by ~0.1 eV. High PCE of 10.41% was demonstrated with PBDB-S:Y6 blend, better than the 8.59% PCE for the thiophene counterpart, PBDB-T:Y6 blend. The PBDB-S:Y6 blend showed enhanced J_{sc} and FF, as well as superior hole and electron mobilities compared to the PBDB-T:Y6 blend, which was attributed to enhanced light-harvesting ability and higher crystallinity resulted from selenophene substitution in the side chain positions. On the other hand, due to strong Se···O intramolecular interactions and strong intermolecular π-π interactions, PBDBS-T and PBDBS-S experienced unique "gel up" phenomenon during polymerization and had low solubility and poor solution-processibility. Devices based on PBDBS-T:Y6 and PBDBS-S:Y6 blends showed relatively low PCE of 6.28% and 5.32%, respectively. To conclude, while

the strategy of selenophene substitution has demonstrated potential to improve the regular thiophene-based polymers in light-harvesting ability, charge transport properties and photovoltaic performance, it is important to also recognize various intramolecular and intermolecular interactions as well as the potential consequences in reduced solubility and solution-processibility.

In **Chapter 3**, a comparative study was conducted to investigate the effects of selenophene substitution on the intrinsic and photovoltaic blend properties of n-type semiconducting polymers, using the alternating naphthalene diimide-*thiophene* copolymer, PNDIT-hd, and naphthalene diimide-*selenophene* copolymer, PNDIS-hd. It was found that the latter acceptor polymer has slightly broadened optical absorption with an optical bandgap of 1.70 eV, which is 0.07 eV narrower relative to PNDIT-hd, even though both polymers have identical electrochemically derived HOMO/LUMO energy levels. In binary blends with the donor polymer PBDB-T, the selenophene-containing acceptor polymer PNDIS-hd enabled all-PSCs with significantly enhanced photocurrent, external quantum efficiency (EQE) and overall photovoltaic power conversion efficiency compared to the thiophene-containing counterpart. All-PSCs based on PNDIT-hd:PBDB-T could achieve a PCE of 6.7% (J_{sc} = 12.18 mA/cm^2, FF = 0.66) whereas the corresponding PNDIS-hd:PBDB-T devices showed a higher PCE of 8.4% (J_{sc} = 14.50 mA/cm^2, FF = 0.71). The observed enhanced photovoltaic properties of the selenophene-containing polymer PNDIS-hd could largely be accounted for by its improved light harvesting, formation of optimal blend morphology as evidenced by the 2D GIWAXS results and reduced monomolecular recombination losses. These results demonstrate the many advantages in selenophene substitution in the design of n-type semiconducting polymers with donor-acceptor architectures for applications in all-polymer solar cells.

Chapter 4 demonstrated a novel molecular design of non-fullerene small molecule acceptors in an attempt to address the issue of intrinsic photochemical stability of current mainstream NFAs. The heretofore unreported bis(amino-aldehyde) building block based on the IDTT core was developed and was reacted with the methylene-keto containing end groups *via* Friedlander condensation to achieve the designed ladder structures.

Chapter 4.1 presented a series of ladder molecule acceptors (LMAs) with long branched 2-hexyldecyl side chains to ensure solubility, named as LTX, LTX-4F and LTX-4Cl. The three LMAs were characterized side-by-side in comparison with ITIC. Owing to the covalently fused ladder backbones, the LMAs indeed demonstrated superior intrinsic photochemical stability under continuous 1 sun illumination in ambient atmosphere. High photovoltaic performance was well preserved: PM6:LTX (PCE 7.2%), PM6:LTX-4F (PCE 10.5%) and PM6:LTX-4Cl (PCE 11.5%). The LMAs have distinctive dual-band optical. Compared to ITIC, the LMAs generally have enlarged bandgaps with lower-lying HOMO energy levels and higher-lying LUMO energy levels, leading to high V_{oc} values of 0.93-1.13 V in photovoltaic devices. In particular, the blend of PM6:LTX had relatively low fill factor of 0.63, whereas the blends of PM6:LTX-4F and PM6:LTX-4Cl showed high fill factors of 0.74-0.75. 2D GIWAXS analysis and contact angle measurement suggested that fluorination and chlorination promoted better donor/acceptor intermixing, thus contributed to formation of favorable blend morphology and enhanced fill factors.

Chapter 4.2 presented a second series of ladder molecule acceptors based on Friedlander condensation of IDTT core with n-decyl side chains and various end-groups, named as LTX10, LTX10-4F and LTX10-4Cl. The new series of LMAs demonstrated optical and electronic properties similar to the precedents with 2-hexyldecyl side chains. However, compared with the

long branched side chains, the shorter n-decyl chains compromised the solubility, thus posed extra difficulty in synthesis and purification, and had negative effects on film-forming qualities when blended with the polymer donor, PM6. Nevertheless, decent photovoltaic performance was obtained from the optimized devices based on PM6:LMAs blends with PCE ranging from 6.1% to 9.3% and high V_{oc} values of 0.97 – 1.1 V. 2D GIWAXS analysis revealed that LTX10 adopted preferentially *edge-on* orientation, whereas LTX10-4Cl was preferentially *face-on*. LTX10-4F demonstrated significant structural ordering in multiple dimensions with somewhat *tilted face-on* π-π stacked crystallites.

The findings from the two series of LMAs included in **Chapter 4** validated the feasibility and potential of the ladder structural design for non-fullerene acceptors with better intrinsic stabilities and high photovoltaic performance. In the meantime, the results also demonstrated the significant impact of side chains and halogenations on the solubility, optical absorption, molecular packing, backbone orientation and blend film morphology of these ladder molecules, therefore, provided important guidelines for future material development toward commercialization of organic photovoltaics technology.

Each of the above sections revealed some important aspects regarding the development of organic semiconductors for the application of organic solar cells. The results from these studies contributed new knowledge to the greater community of organic optoelectronics research. The molecular design strategies and the new chemistry developed in this dissertation shall continue to be exploited in pursuit of better understanding of fundamental material science and engineering as well as better performing materials for broader applications beyond organic solar cells.

5.2 OUTLOOK

In the past decade, the field of organic solar cells has made the greatest transition from the fullerene era to the current non-fullerene era. At the beginning of my graduate school, non-fullerene acceptors (NFAs), including small molecule acceptors and n-type polymers, were relatively scarce and the PCE of polymer:NFA devices was nowhere to compete with fullerene-based devices. As mentioned earlier, the emergence of ITIC in 2015 and the following ITIC-like derivatives have been the most important milestone in organic photovoltaics research. Today, publications on numerous small molecule acceptors and n-type polymers (mostly based on ITIC-like derivatives) are reporting record PCE as high as 18%. I believe new material discoveries will continue to be the key driving force to further improve performance of organic solar cells. Efforts should continue to be directed towards revolutionizing the molecular design of current organic semiconductors.

I have demonstrated in Chapter 4 as proof-of-concept that the novel ladder structures could be an effective molecular design to afford extraordinary thermal stability and enhanced intrinsic photochemical stability while retaining high photovoltaic performance with high fill factors. The developed synthetic method is highly versatile. Thus, it could enable great flexibility in tuning optical absorption and electronic structures if applied to various bis(amino-aldehyde) and methylene-keto-containing building blocks. Therefore, in the near future, the potential of ladder structures composed of vastly different electron-rich and electron-deficient building blocks shall be further explored. On the other hand, the ladder molecule acceptor itself could serve as the electron-deficient moiety in an alternating donor-acceptor copolymer, thus could lead to a variety of p-type or n-type semi-ladder polymers, which are an intriguing class of materials for organic optoelectronics but are currently scarce. Furthermore, with improved yield for the Friedlander

condensation reactions, the synthetic strategy developed here could be applied towards green polymerizations as they would eliminate the necessity of organometallic reagents used in the common Stille or Suzuki polymerizations. As a result, semi-ladder or full-ladder conjugated polymers could potentially be realized. Additionally, other cyclization strategies to achieve ladder structures may also be exploited with considerations in the ease of synthesis and upscaling production.

Last but not least, organic solar cells have yet to be commercialized, due to many challenges in material development, material stability, device lifetime, manufacture *etc*. Multifaceted efforts are required to achieve the lab-to-fab transfer. In recent years, organic photovoltaics have also been more and more envisioned as future indoor light-harvesting technology for powering low-power electronics and portable/wearable electronics for the Internet of Things (IoT) ecosystem.[176] Though without knowing for certain where the organic photovoltaics technology will eventually land in future marketplace, it is of high priority for material scientists and engineers to understand the degradation mechanisms of individual photoactive components and the morphological and interfacial changes within the multilayer devices.

BIBLIOGRAPHY

[1] Shirakawa, H.; Louis, E. J.; MacDiarmid, A. G.; Chiang, C. K.; Heeger, A. J. Synthesis of electrically conducting organic polymers: halogen derivatives of polyacetylene, (CH). *J. Chem. Soc., Chem. Commun.* **1977**, 578-580.

[2] Chiang, C. K.; Fincher, C. R.; Park, Y. W.; Heeger, A. J.; Shirakawa, H.; Louis, E. J.; Gau, S. C.; MacDiarmid, A. G. Electrical Conductivity in Doped Polyacetylene. *Phys. Rev. Lett.* **1977**, *39*, 1098-1101.

[3] Spanggaard, H.; Krebs, F. C. A brief history of the development of organic and polymeric photovoltaics. *Sol. Energy Mater. Sol. Cells* **2004**, *83*, 125-146.

[4] Tang, C. W. Multilayer organic photovoltaic elements, US Patent 4164431A. **1979**.

[5] Tang, C. W. Two‐layer organic photovoltaic cell. *Appl. Phys. Lett.* **1986**, *48*, 183-185.

[6] Hiramoto, M.; Fujiwara, H.; Yokoyama, M. p‐i‐n like behavior in three‐layered organic solar cells having a co‐deposited interlayer of pigments. *J. Appl. Phys.* **1992**, *72*, 3781-3787.

[7] Yu, G.; Gao, J.; Hummelen, J. C.; Wudl, F.; Heeger, A. J. Polymer Photovoltaic Cells: Enhanced Efficiencies via a Network of Internal Donor-Acceptor Heterojunctions. *Science* **1995**, *270*, 1789.

[8] Halls, J. J. M.; Walsh, C. A.; Greenham, N. C.; Marseglia, E. A.; Friend, R. H.; Moratti, S. C.; Holmes, A. B. Efficient Photodiodes from Interpenetrating Polymer Networks. *Nature* **1995**, *376*, 498-500.

[9] Lin, Y.; Wang, J.; Zhang, Z. G.; Bai, H.; Li, Y.; Zhu, D.; Zhan, X. An electron acceptor challenging fullerenes for efficient polymer solar cells. *Adv. Mater.* **2015**, *27*, 1170-4.

[10] Li, G.; Zhu, R.; Yang, Y. Polymer solar cells. *Nat. Photonics* **2012**, *6*, 153-161.

[11] Fred Wudl, G. S. Conducting polymer formed of poly(2-methoxy,5-(2'-ethyl-hexyloxy)-p-phenylenevinylene), US Patent 5189136A. **1993**.

[12] Brabec, C. J.; Shaheen, S. E.; Winder, C.; Sariciftci, N. S.; Denk, P. Effect of LiF/metal electrodes on the performance of plastic solar cells. *Appl. Phys. Lett.* **2002**, *80*, 1288-1290.

[13] Wienk, M. M.; Kroon, J. M.; Verhees, W. J. H.; Knol, J.; Hummelen, J. C.; van Hal, P. A.; Janssen, R. A. J. Efficient Methano[70]fullerene/MDMO-PPV Bulk Heterojunction Photovoltaic Cells. *Angew. Chem. Int. Ed.* **2003**, *42*, 3371-3375.

[14] Li, G.; Shrotriya, V.; Huang, J. S.; Yao, Y.; Moriarty, T.; Emery, K.; Yang, Y. High-efficiency solution processable polymer photovoltaic cells by self-organization of polymer blends. *Nature Materials* **2005**, *4*, 864-868.

[15] Ma, W. L.; Yang, C. Y.; Gong, X.; Lee, K.; Heeger, A. J. Thermally stable, efficient polymer solar cells with nanoscale control of the interpenetrating network morphology. *Adv. Funct. Mater.* **2005**, *15*, 1617-1622.

[16] Liao, S. H.; Jhuo, H. J.; Cheng, Y. S.; Chen, S. A. Fullerene derivative-doped zinc oxide nanofilm as the cathode of inverted polymer solar cells with low-bandgap polymer (PTB7-Th) for high performance. *Adv. Mater.* **2013**, *25*, 4766-71.

[17] Zhang, S.; Ye, L.; Zhao, W.; Liu, D.; Yao, H.; Hou, J. Side Chain Selection for Designing Highly Efficient Photovoltaic Polymers with 2D-Conjugated Structure. *Macromolecules* **2014**, *47*, 4653-4659.

[18] Zheng, Z.; Yao, H.; Ye, L.; Xu, Y.; Zhang, S.; Hou, J. PBDB-T and its derivatives: A family of polymer donors enables over 17% efficiency in organic photovoltaics. *Mater. Today* **2020**, *35*, 115-130.

[19] Facchetti, A. Polymer donor–polymer acceptor (all-polymer) solar cells. *Mater. Today* **2013**, *16*, 123-132.

[20] Hou, J.; Inganas, O.; Friend, R. H.; Gao, F. Organic solar cells based on non-fullerene acceptors. *Nat. Mater.* **2018**, *17*, 119-128.

[21] Yang, J.; Xiao, B.; Tang, A.; Li, J.; Wang, X.; Zhou, E. Aromatic-Diimide-Based n-Type Conjugated Polymers for All-Polymer Solar Cell Applications. *Adv. Mater.* **2019**, *31*, 1804699.

[22] Zhou, N.; Facchetti, A. Naphthalenediimide (NDI) polymers for all-polymer photovoltaics. *Mater. Today* **2018**, *21*, 377-390.

[23] Hwang, Y. J.; Earmme, T.; Courtright, B. A.; Eberle, F. N.; Jenekhe, S. A. n-Type semiconducting naphthalene diimide-perylene diimide copolymers: controlling crystallinity, blend morphology, and compatibility toward high-performance all-polymer solar cells. *J. Am. Chem. Soc.* **2015**, *137*, 4424-4434.

[24] Hwang, Y. J.; Courtright, B. A.; Ferreira, A. S.; Tolbert, S. H.; Jenekhe, S. A. 7.7% Efficient All-Polymer Solar Cells. *Adv. Mater.* **2015**, *27*, 4578-4584.

[25] Kolhe, N. B.; Lee, H.; Kuzuhara, D.; Yoshimoto, N.; Koganezawa, T.; Jenekhe, S. A. All-Polymer Solar Cells with 9.4% Efficiency from Naphthalene Diimide-Biselenophene Copolymer Acceptor. *Chem. Mater.* **2018**, *30*, 6540-6548.

[26] Li, H.; Kim, F. S.; Ren, G.; Hollenbeck, E. C.; Subramaniyan, S.; Jenekhe, S. A. Tetraazabenzodifluoranthene diimides: building blocks for solution-processable n-type organic semiconductors. *Angew. Chem. Int. Ed. Engl.* **2013**, *52*, 5513-5517.

[27] Li, H.; Kim, F. S.; Ren, G.; Jenekhe, S. A. High-mobility n-type conjugated polymers based on electron-deficient tetraazabenzodifluoranthene diimide for organic electronics. *J. Am. Chem. Soc.* **2013**, *135*, 14920-14923.

[28] Li, H.; Hwang, Y. J.; Earmme, T.; Huber, R. C.; Courtright, B. A. E.; O'Brien, C.; Tolbert, S. H.; Jenekhe, S. A. Polymer/Polymer Blend Solar Cells Using Tetraazabenzodifluoranthene Diimide Conjugated Polymers as Electron Acceptors. *Macromolecules* **2015**, *48*, 1759-1766.

[29] Fukutomi, Y.; Nakano, M.; Hu, J. Y.; Osaka, I.; Takimiya, K. Naphthodithiophenediimide (NDTI): synthesis, structure, and applications. *J. Am. Chem. Soc.* **2013**, *135*, 11445-11448.

[30] Yang, J.; Xiao, B.; Tajima, K.; Nakano, M.; Takimiya, K.; Tang, A.; Zhou, E. Comparison among Perylene Diimide (PDI), Naphthalene Diimide (NDI), and Naphthodithiophene Diimide (NDTI) Based n-Type Polymers for All-Polymer Solar Cells Application. *Macromolecules* **2017**, *50*, 3179-3185.

[31] Zhou, E.; Nakano, M.; Izawa, S.; Cong, J.; Osaka, I.; Takimiya, K.; Tajima, K. All-Polymer Solar Cell with High Near-Infrared Response Based on a Naphthodithiophene Diimide (NDTI) Copolymer. *ACS Macro Lett.* **2014**, *3*, 872-875.

[32] Sun, H.; Liu, B.; Wang, Z.; Ling, S.; Zhang, Y.; Zhang, G.; Wang, Y.; Zhang, M.; Li, B.; Yang, W.; Wang, J.; Guo, H.; Liu, F.; Guo, X. Side chain engineering of polymer acceptors for all-polymer solar cells with enhanced efficiency. *J. Mater. Chem. C* **2020**, *8*, 4012-4020.

[33] Sun, H.; Tang, Y.; Koh, C. W.; Ling, S.; Wang, R.; Yang, K.; Yu, J.; Shi, Y.; Wang, Y.; Woo, H. Y.; Guo, X. High-Performance All-Polymer Solar Cells Enabled by an n-Type Polymer Based on a Fluorinated Imide-Functionalized Arene. *Adv. Mater.* **2019**, 1807220.

[34] Wang, Y.; Guo, H.; Harbuzaru, A.; Uddin, M. A.; Arrechea-Marcos, I.; Ling, S.; Yu, J.; Tang, Y.; Sun, H.; López Navarrete, J. T.; Ortiz, R. P.; Woo, H. Y.; Guo, X. (Semi)ladder-Type Bithiophene Imide-Based All-Acceptor Semiconductors: Synthesis, Structure–Property Correlations, and Unipolar n-Type Transistor Performance. *J. Am. Chem. Soc.* **2018**, *140*, 6095-6108.

[35] Lee, C.; Lee, S.; Kim, G. U.; Lee, W.; Kim, B. J. Recent Advances, Design Guidelines, and Prospects of All-Polymer Solar Cells. *Chem. Rev.* **2019**, *119*, 8028-8086.

[36] Wang, G.; Melkonyan, F. S.; Facchetti, A.; Marks, T. J. All-Polymer Solar Cells: Recent Progress, Challenges, and Prospects. *Angew. Chem. Int. Ed.* **2019**, *58*, 4129-4142.

[37] Genene, Z.; Mammo, W.; Wang, E.; Andersson, M. R. Recent Advances in n-Type Polymers for All-Polymer Solar Cells. *Adv. Mater.* **2019**, *31*, 1807275.

[38] Benten, H.; Mori, D.; Ohkita, H.; Ito, S. Recent research progress of polymer donor/polymer acceptor blend solar cells. *J. Mater. Chem. A* **2016**, *4*, 5340-5365.

[39] Earmme, T.; Hwang, Y. J.; Murari, N. M.; Subramaniyan, S.; Jenekhe, S. A. All-polymer solar cells with 3.3% efficiency based on naphthalene diimide-selenophene copolymer acceptor. *J. Am. Chem. Soc.* **2013**, *135*, 14960-14963.

[40] Yao, H.; Bai, F.; Hu, H.; Arunagiri, L.; Zhang, J.; Chen, Y.; Yu, H.; Chen, S.; Liu, T.; Lai, J. Y. L.; Zou, Y.; Ade, H.; Yan, H. Efficient All-Polymer Solar Cells based on a New Polymer Acceptor Achieving 10.3% Power Conversion Efficiency. *ACS Energy Lett.* **2019**, *4*, 417-422.

[41] Tran, D. K.; Kolhe, N. B.; Hwang, Y. J.; Kuzuhara, D.; Koganezawa, T.; Jenekhe, S. A. Effects of a Fluorinated Donor Polymer on the Morphology, Photophysics, and Performance of All-Polymer Solar Cells Based on Naphthalene Diimide-Arylene Copolymer Acceptors. *ACS Appl. Mater. Interfaces* **2020**, *12*, 16490-16502.

[42] Wang, W.; Wu, Q.; Sun, R.; Guo, J.; Wu, Y.; Shi, M.; Yang, W.; Li, H.; Min, J. Controlling Molecular Mass of Low-Band-Gap Polymer Acceptors for High-Performance All-Polymer Solar Cells. *Joule* **2020**, *4*, 1070-1086.

[43] Fan, Q.; Su, W.; Chen, S.; Kim, W.; Chen, X.; Lee, B.; Liu, T.; Méndez-Romero, U. A.; Ma, R.; Yang, T.; Zhuang, W.; Li, Y.; Li, Y.; Kim, T.-S.; Hou, L.; Yang, C.; Yan, H.; Yu, D.; Wang, E. Mechanically Robust All-Polymer Solar Cells from Narrow Band Gap Acceptors with Hetero-Bridging Atoms. *Joule* **2020**, *4*, 658-672.

[44] Feng, K.; Huang, J.; Zhang, X.; Wu, Z.; Shi, S.; Thomsen, L.; Tian, Y.; Woo, H. Y.; McNeill, C. R.; Guo, X. High-Performance All-Polymer Solar Cells Enabled by n-Type Polymers with an Ultranarrow Bandgap Down to 1.28 eV. *Adv. Mater.* **2020**, 2001476.

[45] Lee, J. W.; Sung, M. J.; Kim, D.; Lee, S.; You, H.; Kim, F. S.; Kim, Y. H.; Kim, B. J.; Kwon, S. K. Naphthalene Diimide-Based Terpolymers with Controlled Crystalline Properties for Producing High Electron Mobility and Optimal Blend Morphology in All-Polymer Solar Cells. *Chem. Mater.* **2020**, *32*, 2572-2582.

[46] Xie, B.; Zhang, K.; Hu, Z.; Fang, H.; Lin, B.; Yin, Q.; He, B.; Dong, S.; Ying, L.; Ma, W.; Huang, F.; Yan, H.; Cao, Y. Polymer Pre-Aggregation Enables Optimal Morphology and High Performance in All-Polymer Solar Cells. *Solar RRL* **2020**, *4*, 1900385.

[47] Fan, Q.; Ma, R.; Liu, T.; Su, W.; Peng, W.; Zhang, M.; Wang, Z.; Wen, X.; Cong, Z.; Luo, Z.; Hou, L.; Liu, F.; Zhu, W.; Yu, D.; Yan, H.; Wang, E. 10.13% Efficiency All-Polymer Solar Cells Enabled by Improving the Optical Absorption of Polymer Acceptors. *Solar RRL* **2020**, *4*, 2000142.

[48] Du, J.; Hu, K.; Meng, L.; Angunawela, I.; Zhang, J.; Qin, S.; Liebman-Pelaez, A.; Zhu, C.; Zhang, Z.; Ade, H.; Li, Y. High-Performance All-Polymer Solar Cells: Synthesis of Polymer Acceptor by a Random Ternary Copolymerization Strategy. *Angew. Chem. Int. Ed. Engl.* **2020**, *59*, 1-6.

[49] Yao, H.; Ma, L.-K.; Yu, H.; Yu, J.; Chow, P. C. Y.; Xue, W.; Zou, X.; Chen, Y.; Liang, J.; Arunagiri, L.; Gao, F.; Sun, H.; Zhang, G.; Ma, W.; Yan, H. All-Polymer Solar Cells with over 12% Efficiency and a Small Voltage Loss Enabled by a Polymer Acceptor Based on an Extended Fused Ring Core. *Adv. Energy Mater.* **2020**, 2001408.

[50] Jia, T.; Zhang, J.; Zhong, W.; Liang, Y.; Zhang, K.; Dong, S.; Ying, L.; Liu, F.; Wang, X.; Huang, F.; Cao, Y. 14.4% efficiency all-polymer solar cell with broad absorption and low energy loss enabled by a novel polymer acceptor. *Nano Energy* **2020**, *72*, 104718.

[51] Zhang, Z.-G.; Yang, Y.; Yao, J.; Xue, L.; Chen, S.; Li, X.; Morrison, W.; Yang, C.; Li, Y. Constructing a Strongly Absorbing Low-Bandgap Polymer Acceptor for High-Performance All-Polymer Solar Cells. *Angew. Chem. Int. Ed.* **2017**, *56*, 13503-13507.

[52] Zhang, Z.-G.; Li, Y. Polymerized Small-Molecule Acceptors for High-Performance All-Polymer Solar Cells. *Angew. Chem. Int. Ed.* **2021**, *60*, 4422-4433.

[53] Wang, Y.; Lee, J.; Hou, X.; Labanti, C.; Yan, J.; Mazzolini, E.; Parhar, A.; Nelson, J.; Kim, J. S.; Li, Z. Recent Progress and Challenges toward Highly Stable Nonfullerene Acceptor‐Based Organic Solar Cells. *Adv. Energy Mater.* **2020**, *11*, 2003002.

[54] Li, C.; Zhou, J.; Song, J.; Xu, J.; Zhang, H.; Zhang, X.; Guo, J.; Zhu, L.; Wei, D.; Han, G.; Min, J.; Zhang, Y.; Xie, Z.; Yi, Y.; Yan, H.; Gao, F.; Liu, F.; Sun, Y. Non-fullerene acceptors with branched side chains and improved molecular packing to exceed 18% efficiency in organic solar cells. *Nature Energy* **2021**.

[55] Holliday, S.; Ashraf, R. S.; Wadsworth, A.; Baran, D.; Yousaf, S. A.; Nielsen, C. B.; Tan, C. H.; Dimitrov, S. D.; Shang, Z.; Gasparini, N.; Alamoudi, M.; Laquai, F.; Brabec, C. J.; Salleo, A.; Durrant, J. R.; McCulloch, I. High-efficiency and air-stable P3HT-based polymer solar cells with a new non-fullerene acceptor. *Nat. Commun.* **2016**, *7*, 11585.

[56] Baran, D.; Ashraf, R. S.; Hanifi, D. A.; Abdelsamie, M.; Gasparini, N.; Rohr, J. A.; Holliday, S.; Wadsworth, A.; Lockett, S.; Neophytou, M.; Emmott, C. J. M.; Nelson, J.; Brabec, C. J.; Amassian, A.; Salleo, A.; Kirchartz, T.; Durrant, J. R.; McCulloch, I. Reducing the efficiency-stability-cost gap of organic photovoltaics with highly efficient and stable small molecule acceptor ternary solar cells. *Nat. Mater.* **2016**, *advance online publication*.

[57] Li, S.; Li, C.-Z.; Shi, M.; Chen, H. New Phase for Organic Solar Cell Research: Emergence of Y-Series Electron Acceptors and Their Perspectives. *ACS Energy Lett.* **2020**, *5*, 1554-1567.

[58] Fu, H.; Wang, Z.; Sun, Y. Polymer Donors for High‐Performance Non‐Fullerene Organic Solar Cells. *Angew. Chem. Int. Ed.* **2019**, *58*, 4442-4453.

[59] Qian, D. P.; Ye, L.; Zhang, M. J.; Liang, Y. R.; Li, L. J.; Huang, Y.; Guo, X.; Zhang, S. Q.; Tan, Z. A.; Hou, J. H. Design, Application, and Morphology Study of a New Photovoltaic Polymer with Strong Aggregation in Solution State. *Macromolecules* **2012**, *45*, 9611-9617.

[60] Zhao, W.; Qian, D.; Zhang, S.; Li, S.; Inganäs, O.; Gao, F.; Hou, J. Fullerene-Free Polymer Solar Cells with over 11% Efficiency and Excellent Thermal Stability. *Adv. Mater.* **2016**, *28*, 4734-4739.

[61] Zhang, M.; Guo, X.; Ma, W.; Ade, H.; Hou, J. A large‐bandgap conjugated polymer for versatile photovoltaic applications with high performance. *Adv. Mater.* **2015**, *27*, 4655-4660.

[62] Zhang, S.; Qin, Y.; Zhu, J.; Hou, J. Over 14% Efficiency in Polymer Solar Cells Enabled by a Chlorinated Polymer Donor. *Adv. Mater.* **2018**, *30*, e1800868.

[63] Fan, Q.; Zhu, Q.; Xu, Z.; Su, W.; Chen, J.; Wu, J.; Guo, X.; Ma, W.; Zhang, M.; Li, Y. Chlorine substituted 2D-conjugated polymer for high-performance polymer solar cells with 13.1% efficiency via toluene processing. *Nano Energy* **2018**, *48*, 413-420.

[64] Burlingame, Q.; Ball, M.; Loo, Y.-L. It's time to focus on organic solar cell stability. *Nature Energy* **2020**, *5*, 947-949.

[65] Lu, L.; Zheng, T.; Wu, Q.; Schneider, A. M.; Zhao, D.; Yu, L. Recent Advances in Bulk Heterojunction Polymer Solar Cells. *Chem. Rev.* **2015**, *115*, 12666-12731.

[66] Wadsworth, A.; Moser, M.; Marks, A.; Little, M. S.; Gasparini, N.; Brabec, C. J.; Baran, D.; McCulloch, I. Critical review of the molecular design progress in non-fullerene electron acceptors towards commercially viable organic solar cells. *Chem. Soc. Rev.* **2019**, *48*, 1596-1625.

[67] Yan, C.; Barlow, S.; Wang, Z.; Yan, H.; Jen, A. K. Y.; Marder, S. R.; Zhan, X. Non-fullerene acceptors for organic solar cells. *Nature Reviews Materials* **2018**, *3*, 18003.

[68] Zhang, H.; Yao, H.; Hou, J.; Zhu, J.; Zhang, J.; Li, W.; Yu, R.; Gao, B.; Zhang, S.; Hou, J. Over 14% Efficiency in Organic Solar Cells Enabled by Chlorinated Nonfullerene Small-Molecule Acceptors. *Adv. Mater.* **2018**, *30*, e1800613.

[69] Yuan, J.; Zhang, Y. Q.; Zhou, L. Y.; Zhang, G. C.; Yip, H. L.; Lau, T. K.; Lu, X. H.; Zhu, C.; Peng, H. J.; Johnson, P. A.; Leclerc, M.; Cao, Y.; Ulanski, J.; Li, Y. F.; Zou, Y. P. Single-Junction Organic Solar Cell with over 15% Efficiency Using Fused-Ring Acceptor with Electron-Deficient Core. *Joule* **2019**, *3*, 1140-1151.

[70] Liu, S.; Yuan, J.; Deng, W. Y.; Luo, M.; Xie, Y.; Liang, Q. B.; Zou, Y. P.; He, Z. C.; Wu, H. B.; Cao, Y. High-efficiency organic solar cells with low non-radiative recombination loss and low energetic disorder. *Nat. Photonics* **2020**, *14*, 300-+.

[71] Cui, Y.; Yao, H.; Zhang, J.; Zhang, T.; Wang, Y.; Hong, L.; Xian, K.; Xu, B.; Zhang, S.; Peng, J.; Wei, Z.; Gao, F.; Hou, J. Over 16% efficiency organic photovoltaic cells enabled by a chlorinated acceptor with increased open-circuit voltages. *Nat. Commun.* **2019**, *10*, 2515.

[72] Zhou, Z.; Liu, W.; Zhou, G.; Zhang, M.; Qian, D.; Zhang, J.; Chen, S.; Xu, S.; Yang, C.; Gao, F.; Zhu, H.; Liu, F.; Zhu, X. Subtle Molecular Tailoring Induces Significant Morphology

Optimization Enabling over 16% Efficiency Organic Solar Cells with Efficient Charge Generation. *Adv. Mater.* **2019**, *n/a*, 1906324.

[73] Cui, Y.; Yao, H.; Hong, L.; Zhang, T.; Xu, Y.; Xian, K.; Gao, B.; Qin, J.; Zhang, J.; Wei, Z.; Hou, J. Achieving Over 15% Efficiency in Organic Photovoltaic Cells via Copolymer Design. *Adv. Mater.* **2019**, *31*, 1808356.

[74] Sun, H.; Liu, T.; Yu, J.; Lau, T.-K.; Zhang, G.; Zhang, Y.; Su, M.; Tang, Y.; Ma, R.; Liu, B.; Liang, J.; Feng, K.; Lu, X.; Guo, X.; Gao, F.; Yan, H. A monothiophene unit incorporating both fluoro and ester substitution enabling high-performance donor polymers for non-fullerene solar cells with 16.4% efficiency. *Energy Environ. Sci.* **2019**, *12*, 3328-3337.

[75] Cao, F.-Y.; Tseng, C.-C.; Lin, F.-Y.; Chen, Y.; Yan, H.; Cheng, Y.-J. Selenophene-Incorporated Quaterchalcogenophene-Based Donor–Acceptor Copolymers To Achieve Efficient Solar Cells with Jsc Exceeding 20 mA/cm2. *Chem. Mater.* **2017**, *29*, 10045-10052.

[76] Xu, Z.; Fan, Q. P.; Meng, X. Y.; Guo, X.; Su, W. Y.; Ma, W.; Zhang, M. J.; Li, Y. F. Selenium-Containing Medium Bandgap Copolymer for Bulk Heterojunction Polymer Solar Cells with High Efficiency of 9.8%. *Chem. Mater.* **2017**, *29*, 4811-4818.

[77] Dou, L.; Chang, W. H.; Gao, J.; Chen, C. C.; You, J.; Yang, Y. A selenium-substituted low-bandgap polymer with versatile photovoltaic applications. *Adv. Mater.* **2013**, *25*, 825-31.

[78] Chang, W. H.; Meng, L.; Dou, L. T.; You, J. B.; Chen, C. C.; Yang, Y.; Young, E. P.; Li, G.; Yang, Y. A Selenophene Containing Benzodithiophene-alt-thienothiophene Polymer for Additive-Free High Performance Solar Cell. *Macromolecules* **2015**, *48*, 562-568.

[79] Courtright, B. A.; Jenekhe, S. A. Polyethylenimine Interfacial Layers in Inverted Organic Photovoltaic Devices: Effects of Ethoxylation and Molecular Weight on Efficiency and Temporal Stability. *ACS Appl. Mater. Interfaces* **2015**, *7*, 26167-26175.

[80] Malliaras, G. G.; Salem, J. R.; Brock, P. J.; Scott, C. Electrical characteristics and efficiency of single-layer organic light-emitting diodes. *Phys. Rev. B* **1998**, *58*, R13411-R13414.

[81] Bathula, C.; Khadtare, S.; Buruga, K.; Kadam, A.; Shrestha, N. K.; Noh, Y. Y. Selenophene based benzodithiophene polymers as potential candidates for optoelectronic applications. *Dyes Pigm.* **2018**, *149*, 639-643.

[82] Cui, C. H.; Fan, H. J.; Guo, X.; Zhang, M. J.; He, Y. J.; Zhan, X. W.; Li, Y. F. Synthesis and photovoltaic properties of D-A copolymers of benzodithiophene and naphtho[2,3-c]thiophene-4,9-dione. *Polym. Chem.* **2012**, *3*, 99-104.

[83] Huang, X. X.; Weng, K. K.; Huo, L. J.; Fan, B. B.; Yang, C. H.; Sun, X. B.; Sun, Y. M. Effects of a heteroatomic benzothienothiophenedione acceptor on the properties of a series of wide-bandgap photovoltaic polymers. *J. Mater. Chem. C* **2016**, *4*, 9052-9059.

[84] Cordero, B.; Gómez, V.; Platero-Prats, A. E.; Revés, M.; Echeverría, J.; Cremades, E.; Barragán, F.; Alvarez, S. Covalent radii revisited. *Dalton Transactions* **2008**, 2832-2838.

[85] Mantina, M.; Chamberlin, A. C.; Valero, R.; Cramer, C. J.; Truhlar, D. G. Consistent van der Waals Radii for the Whole Main Group. *J. Phys. Chem. A* **2009**, *113*, 5806-5812.

[86] Vogel, L.; Wonner, P.; Huber, S. M. Chalcogen Bonding: An Overview. *Angew. Chem. Int. Ed.* **2019**, *58*, 1880-1891.

[87] Pascoe, D. J.; Ling, K. B.; Cockroft, S. L. The Origin of Chalcogen-Bonding Interactions. *J. Am. Chem. Soc.* **2017**, *139*, 15160-15167.

[88] Huang, H.; Yang, L.; Facchetti, A.; Marks, T. J. Organic and Polymeric Semiconductors Enhanced by Noncovalent Conformational Locks. *Chem. Rev.* **2017**, *117*, 10291-10318.

[89] Zhu, L.; Zhang, M.; Zhou, G.; Hao, T.; Xu, J.; Wang, J.; Qiu, C.; Prine, N.; Ali, J.; Feng, W.; Gu, X.; Ma, Z.; Tang, Z.; Zhu, H.; Ying, L.; Zhang, Y.; Liu, F. Efficient Organic Solar Cell with 16.88% Efficiency Enabled by Refined Acceptor Crystallization and Morphology with Improved Charge Transfer and Transport Properties. *Adv. Energy Mater.* **2020**, *10*, 1904234.

[90] Bruker (2007) APEX2 (Version 2.1-4), S. v. A., SADABS (version 2007/4), BrukerAXS Inc, Madison, Wisconsin, USA.

[91] Sheldrick, G. Crystal structure refinement with SHELXL. *Acta Crystallographica Section C* **2015**, *71*, 3-8.

[92] Sheldrick, G. M. SHELXL-97. *Program for crystal-structure refinement* **1997**.

[93] Mackay, S.; Edwards, C.; Henderson, A.; Gilmore, C.; Stewart, N.; Shankland, K.; Donald, A. maXus 1.1. *A computer program for the solution and refinement of crystal structures from X-ray diffraction data, University of Glasgow, Scotland, Nonius, The Netherlands, and MacScience, Japan* **1997**.

[94] Waasmaier, D.; Kirfel, A. New analytical scattering-factor functions for free atoms and ions. *Acta Crystallogr. Sect. A: Found. Crystallogr.* **1995**, *51*, 416-431.

[95] Kim, W.; Choi, J.; Kim, J.-H.; Kim, T.; Lee, C.; Lee, S.; Kim, M.; Kim, B. J.; Kim, T.-S. Comparative Study of the Mechanical Properties of All-Polymer and Fullerene–Polymer Solar Cells: The Importance of Polymer Acceptors for High Fracture Resistance. *Chem. Mater.* **2018**, *30*, 2102-2111.

[96] Kim, T.; Kim, J. H.; Kang, T. E.; Lee, C.; Kang, H.; Shin, M.; Wang, C.; Ma, B.; Jeong, U.; Kim, T. S.; Kim, B. J. Flexible, highly efficient all-polymer solar cells. *Nat. Commun.* **2015**, *6*, 8547.

[97] Gao, L.; Zhang, Z. G.; Xue, L.; Min, J.; Zhang, J.; Wei, Z.; Li, Y. All-Polymer Solar Cells Based on Absorption-Complementary Polymer Donor and Acceptor with High Power Conversion Efficiency of 8.27%. *Adv. Mater.* **2016**, *28*, 1884-1890.

[98] Kolhe, N. B.; Tran, D. K.; Lee, H.; Kuzuhara, D.; Yoshimoto, N.; Koganezawa, T.; Jenekhe, S. A. New Random Copolymer Acceptors Enable Additive-Free Processing of 10.1%

Efficient All-Polymer Solar Cells with Near-Unity Internal Quantum Efficiency. *ACS Energy Lett.* **2019**, *4*, 1162-1170.

[99] Jenekhe, S. A.; Lu, L.; Alam, M. M. New Conjugated Polymers with Donor−Acceptor Architectures: Synthesis and Photophysics of Carbazole−Quinoline and Phenothiazine−Quinoline Copolymers and Oligomers Exhibiting Large Intramolecular Charge Transfer. *Macromolecules* **2001**, *34*, 7315-7324.

[100] Zhu, Y.; Champion, R. D.; Jenekhe, S. A. Conjugated Donor−Acceptor Copolymer Semiconductors with Large Intramolecular Charge Transfer: Synthesis, Optical Properties, Electrochemistry, and Field Effect Carrier Mobility of Thienopyrazine-Based Copolymers. *Macromolecules* **2006**, *39*, 8712-8719.

[101] Wu, J.-S.; Cheng, S.-W.; Cheng, Y.-J.; Hsu, C.-S. Donor–acceptor conjugated polymers based on multifused ladder-type arenes for organic solar cells. *Chem. Soc. Rev.* **2015**, *44*, 1113-1154.

[102] Cheng, Y. J.; Yang, S. H.; Hsu, C. S. Synthesis of conjugated polymers for organic solar cell applications. *Chem. Rev.* **2009**, *109*, 5868-5923.

[103] Guo, X.; Kim, F. S.; Seger, M. J.; Jenekhe, S. A.; Watson, M. D. Naphthalene Diimide-Based Polymer Semiconductors: Synthesis, Structure–Property Correlations, and n-Channel and Ambipolar Field-Effect Transistors. *Chem. Mater.* **2012**, *24*, 1434-1442.

[104] Kim, F. S.; Guo, X.; Watson, M. D.; Jenekhe, S. A. High-mobility ambipolar transistors and high-gain inverters from a donor-acceptor copolymer semiconductor. *Adv. Mater.* **2010**, *22*, 478-482.

[105] Sun, H.; Guo, X.; Facchetti, A. High-Performance n-Type Polymer Semiconductors: Applications, Recent Development, and Challenges. *Chem* **2020**, *6*, 1310-1326.

[106] Sun, H.; Wang, L.; Wang, Y.; Guo, X. Imide-Functionalized Polymer Semiconductors. *Chem. Eur. J.* **2019**, *25*, 87-105.

[107] Hwang, Y. J.; Ren, G. Q.; Murari, N. M.; Jenekhe, S. A. n-Type Naphthalene Diimide-Biselenophene Copolymer for All-Polymer Bulk Heterojunction Solar Cells. *Macromolecules* **2012**, *45*, 9056-9062.

[108] Yan, H.; Chen, Z.; Zheng, Y.; Newman, C.; Quinn, J. R.; Dötz, F.; Kastler, M.; Facchetti, A. A high-mobility electron-transporting polymer for printed transistors. *Nature* **2009**, *457*, 679-686.

[109] Tremel, K.; Fischer, F. S. U.; Kayunkid, N.; Pietro, R. D.; Tkachov, R.; Kiriy, A.; Neher, D.; Ludwigs, S.; Brinkmann, M. Charge Transport Anisotropy in Highly Oriented Thin Films of the Acceptor Polymer P(NDI2OD-T2). *Adv. Energy Mater.* **2014**, *4*, 1301659.

[110] Fan, B. B.; Ying, L.; Wang, Z. F.; He, B. T.; Jiang, X. F.; Huang, F.; Cao, Y. Optimisation of processing solvent and molecular weight for the production of green-solvent-

processed all-polymer solar cells with a power conversion efficiency over 9%. *Energy Environ. Sci.* **2017**, *10*, 1243-1251.

[111] Choi, J.; Kim, W.; Kim, S.; Kim, T.-S.; Kim, B. J. Influence of Acceptor Type and Polymer Molecular Weight on the Mechanical Properties of Polymer Solar Cells. *Chem. Mater.* **2019**, *31*, 9057-9069.

[112] Zhou, N.; Dudnik, A. S.; Li, T. I. N. G.; Manley, E. F.; Aldrich, T. J.; Guo, P.; Liao, H.-C.; Chen, Z.; Chen, L. X.; Chang, R. P. H.; Facchetti, A.; Olvera de la Cruz, M.; Marks, T. J. All-Polymer Solar Cell Performance Optimized via Systematic Molecular Weight Tuning of Both Donor and Acceptor Polymers. *J. Am. Chem. Soc.* **2016**, *138*, 1240-1251.

[113] Hwang, Y. J.; Murari, N. M.; Jenekhe, S. A. New n-type polymer semiconductors based on naphthalene diimide and selenophene derivatives for organic field-effect transistors. *Polym. Chem.* **2013**, *4*, 3187-3195.

[114] Kim, Y.; Cho, H. H.; Kim, T.; Liao, K.; Kim, B. J. Terpolymer approach for controlling the crystalline behavior of naphthalene diimide-based polymer acceptors and enhancing the performance of all-polymer solar cells. *Polym. J.* **2016**, *48*, 517-524.

[115] Ren, G. Q.; Schlenker, C. W.; Ahmed, E.; Subramaniyan, S.; Olthof, S.; Kahn, A.; Ginger, D. S.; Jenekhe, S. A. Photoinduced Hole Transfer Becomes Suppressed with Diminished Driving Force in Polymer-Fullerene Solar Cells While Electron Transfer Remains Active. *Adv. Funct. Mater.* **2013**, *23*, 1238-1249.

[116] Liu, X.; Zhang, C.; Duan, C.; Li, M.; Hu, Z.; Wang, J.; Liu, F.; Li, N.; Brabec, C. J.; Janssen, R. A. J.; Bazan, G. C.; Huang, F.; Cao, Y. Morphology Optimization via Side Chain Engineering Enables All-Polymer Solar Cells with Excellent Fill Factor and Stability. *J. Am. Chem. Soc.* **2018**, *140*, 8934-8943.

[117] Li, Z.; Ying, L.; Xie, R.; Zhu, P.; Li, N.; Zhong, W.; Huang, F.; Cao, Y. Designing ternary blend all-polymer solar cells with an efficiency of over 10% and a fill factor of 78%. *Nano Energy* **2018**, *51*, 434-441.

[118] Fan, B.; Ying, L.; Zhu, P.; Pan, F.; Liu, F.; Chen, J.; Huang, F.; Cao, Y. All-Polymer Solar Cells Based on a Conjugated Polymer Containing Siloxane-Functionalized Side Chains with Efficiency over 10%. *Adv. Mater.* **2017**, *29*, 1703906.

[119] Li, Z.; Xu, X.; Zhang, W.; Meng, X.; Genene, Z.; Ma, W.; Mammo, W.; Yartsev, A.; Andersson, M. R.; Janssen, R. A. J.; Wang, E. 9.0% power conversion efficiency from ternary all-polymer solar cells. *Energy Environ. Sci.* **2017**, *10*, 2212-2221.

[120] Fan, B.; Zhu, P.; Xin, J.; Li, N.; Ying, L.; Zhong, W.; Li, Z.; Ma, W.; Huang, F.; Cao, Y. High-Performance Thick-Film All-Polymer Solar Cells Created Via Ternary Blending of a Novel Wide-Bandgap Electron-Donating Copolymer. *Adv. Energy Mater.* **2018**, *8*, 1703085.

[121] Li, Z.; Xu, X.; Zhang, W.; Meng, X.; Ma, W.; Yartsev, A.; Inganas, O.; Andersson, M. R.; Janssen, R. A.; Wang, E. High Performance All-Polymer Solar Cells by Synergistic Effects of Fine-Tuned Crystallinity and Solvent Annealing. *J. Am. Chem. Soc.* **2016**, *138*, 10935-10944.

[122] Lee, C.; Giridhar, T.; Choi, J.; Kim, S.; Kim, Y.; Kim, T.; Lee, W.; Cho, H. H.; Wang, C.; Ade, H.; Kim, B. J. Importance of 2D Conjugated Side Chains of Benzodithiophene-Based Polymers in Controlling Polymer Packing, Interfacial Ordering, and Composition Variations of All-Polymer Solar Cells. *Chem. Mater.* **2017**, *29*, 9407-9415.

[123] Cho, H. H.; Han, G.; Younts, R.; Lee, W.; Gautam, B. R.; Lee, S.; Lee, C.; Kim, T.; Kim, F. S.; Gundogdu, K.; Kim, B. J. Impact of highly crystalline, isoindigo-based small-molecular additives for enhancing the performance of all-polymer solar cells. *J. Mater. Chem. A* **2017**, *5*, 21291-21299.

[124] Lee, C.; Kang, H.; Lee, W.; Kim, T.; Kim, K. H.; Woo, H. Y.; Wang, C.; Kim, B. J. High-performance all-polymer solar cells via side-chain engineering of the polymer acceptor: the importance of the polymer packing structure and the nanoscale blend morphology. *Adv. Mater.* **2015**, *27*, 2466-2471.

[125] Kim, A.; Park, C. G.; Park, S. H.; Kim, H. J.; Choi, S.; Kim, Y. U.; Jeong, C. H.; Chae, W. S.; Cho, M. J.; Choi, D. H. Highly efficient and highly stable terpolymer-based all-polymer solar cells with broad complementary absorption and robust morphology. *J. Mater. Chem. A* **2018**, *6*, 10095-10103.

[126] Shi, S.; Yuan, J.; Ding, G.; Ford, M.; Lu, K.; Shi, G.; Sun, J.; Ling, X.; Li, Y.; Ma, W. Improved All‐Polymer Solar Cell Performance by Using Matched Polymer Acceptor. *Adv. Funct. Mater.* **2016**, *26*, 5669-5678.

[127] Oh, J.; Kranthiraja, K.; Lee, C.; Gunasekar, K.; Kim, S.; Ma, B.; Kim, B. J.; Jin, S. H. Side-Chain Fluorination: An Effective Approach to Achieving High-Performance All-Polymer Solar Cells with Efficiency Exceeding 7. *Adv. Mater.* **2016**, *28*, 10016-10023.

[128] Earmme, T.; Hwang, Y. J.; Subramaniyan, S.; Jenekhe, S. A. All-polymer bulk heterojuction solar cells with 4.8% efficiency achieved by solution processing from a co-solvent. *Adv. Mater.* **2014**, *26*, 6080-6085.

[129] Huo, L.; Liu, T.; Sun, X.; Cai, Y.; Heeger, A. J.; Sun, Y. Single-Junction Organic Solar Cells Based on a Novel Wide-Bandgap Polymer with Efficiency of 9.7%. *Adv. Mater.* **2015**, *27*, 2938-2944.

[130] Li, Z.; Lin, J. D. A.; Phan, H.; Sharenko, A.; Proctor, C. M.; Zalar, P.; Chen, Z.; Facchetti, A.; Nguyen, T.-Q. Competitive Absorption and Inefficient Exciton Harvesting: Lessons Learned from Bulk Heterojunction Organic Photovoltaics Utilizing the Polymer Acceptor P(NDI2OD-T2). *Adv. Funct. Mater.* **2014**, *24*, 6989-6998.

[131] Cowan, S. R.; Roy, A.; Heeger, A. J. Recombination in polymer-fullerene bulk heterojunction solar cells. *Phys. Rev. B* **2010**, *82*, 245207.

[132] Wetzelaer, G. A. H.; Kuik, M.; Lenes, M.; Blom, P. W. M. Origin of the dark-current ideality factor in polymer:fullerene bulk heterojunction solar cells. *Appl. Phys. Lett.* **2011**, *99*, 153506.

[133] Kirchartz, T.; Deledalle, F.; Tuladhar, P. S.; Durrant, J. R.; Nelson, J. On the Differences between Dark and Light Ideality Factor in Polymer:Fullerene Solar Cells. *J. Phys. Chem. Lett.* **2013**, *4*, 2371-2376.

[134] Ye, L.; Jiao, X.; Zhou, M.; Zhang, S.; Yao, H.; Zhao, W.; Xia, A.; Ade, H.; Hou, J. Manipulating Aggregation and Molecular Orientation in All-Polymer Photovoltaic Cells. *Adv. Mater.* **2015**, *27*, 6046-6054.

[135] Müller-Buschbaum, P. The Active Layer Morphology of Organic Solar Cells Probed with Grazing Incidence Scattering Techniques. *Adv. Mater.* **2014**, *26*, 7692-7709.

[136] Smilgies, D. M. Scherrer grain-size analysis adapted to grazing-incidence scattering with area detectors. *J. Appl. Crystallogr.* **2009**, *42*, 1030-1034.

[137] Chen, W.; Zhang, Q. Recent progress in non-fullerene small molecule acceptors in organic solar cells (OSCs). *J. Mater. Chem. C* **2017**, *5*, 1275-1302.

[138] He, D.; Zhao, F. W.; Jiang, L.; Wang, C. R. A-D-A small molecule acceptors with ladder-type arenes for organic solar cells. *J. Mater. Chem. A* **2018**, *6*, 8839-8854.

[139] Dey, S. Recent Progress in Molecular Design of Fused Ring Electron Acceptors for Organic Solar Cells. *Small* **2019**, *15*, e1900134.

[140] Yao, C.; Liu, B.; Zhu, Y. N.; Hong, L.; Miao, J. S.; Hou, J. H.; He, F.; Meng, H. Highly fluorescent anthracene derivative as a non-fullerene acceptor in OSCs with small non-radiative energy loss of 0.22 eV and high PCEs of over 13%. *J. Mater. Chem. A* **2019**, *7*, 10212-10216.

[141] Fei, Z.; Eisner, F. D.; Jiao, X.; Azzouzi, M.; Rohr, J. A.; Han, Y.; Shahid, M.; Chesman, A. S. R.; Easton, C. D.; McNeill, C. R.; Anthopoulos, T. D.; Nelson, J.; Heeney, M. An Alkylated Indacenodithieno[3,2-b]thiophene-Based Nonfullerene Acceptor with High Crystallinity Exhibiting Single Junction Solar Cell Efficiencies Greater than 13% with Low Voltage Losses. *Adv. Mater.* **2018**, *30*, 1705209-n/a.

[142] Zhao, W.; Li, S.; Yao, H.; Zhang, S.; Zhang, Y.; Yang, B.; Hou, J. Molecular Optimization Enables over 13% Efficiency in Organic Solar Cells. *J. Am. Chem. Soc.* **2017**, *139*, 7148-7151.

[143] Qin, J. Q.; Zhang, L. X.; Xiao, Z.; Chen, S. S.; Sun, K.; Zang, Z. G.; Yi, C. Y.; Yuan, Y. B.; Jin, Z. W.; Hao, F.; Cheng, Y. H.; Bao, Q. Y.; Ding, L. M. Over 16% efficiency from thick-film organic solar cells. *Science Bulletin* **2020**, *65*, 1979-1982.

[144] Meng, L.; Zhang, Y.; Wan, X.; Li, C.; Zhang, X.; Wang, Y.; Ke, X.; Xiao, Z.; Ding, L.; Xia, R.; Yip, H. L.; Cao, Y.; Chen, Y. Organic and solution-processed tandem solar cells with 17.3% efficiency. *Science* **2018**, *361*, 1094-1098.

[145] Hu, L.; Liu, Y.; Mao, L.; Xiong, S. X.; Sun, L. L.; Zhao, N.; Qin, F.; Jiang, Y. Y.; Zhou, Y. H. Chemical reaction between an ITIC electron acceptor and an amine-containing interfacial layer in non-fullerene solar cells. *J. Mater. Chem. A* **2018**, *6*, 2273-2278.

[146] Aldrich, T. J.; Matta, M.; Zhu, W.; Swick, S. M.; Stern, C. L.; Schatz, G. C.; Facchetti, A.; Melkonyan, F. S.; Marks, T. J. Fluorination Effects on Indacenodithienothiophene Acceptor Packing and Electronic Structure, End-Group Redistribution, and Solar Cell Photovoltaic Response. *J. Am. Chem. Soc.* **2019**, *141*, 3274-3287.

[147] Wang, Y. W.; Lan, W. X.; Li, N.; Lan, Z. J.; Li, Z.; Jia, J. N.; Zhu, F. R. Stability of Nonfullerene Organic Solar Cells: from Built-in Potential and Interfacial Passivation Perspectives. *Adv. Energy Mater.* **2019**, *9*, 1900157.

[148] Luke, J.; Speller, E. M.; Wadsworth, A.; Wyatt, M. F.; Dimitrov, S.; Lee, H. K. H.; Li, Z.; Tsoi, W. C.; McCulloch, I.; Bagnis, D.; Durrant, J. R.; Kim, J. S. Twist and Degrade—Impact of Molecular Structure on the Photostability of Nonfullerene Acceptors and Their Photovoltaic Blends. *Adv. Energy Mater.* **2019**, *9*, 1803755.

[149] Doumon, N. Y.; Houard, F. V.; Dong, J. J.; Yao, H. F.; Portale, G.; Hou, J. H.; Koster, L. J. A. Energy level modulation of ITIC derivatives: Effects on the photodegradation of conventional and inverted organic solar cells. *Org. Electron.* **2019**, *69*, 255-262.

[150] Du, X. Y.; Heumueller, T.; Gruber, W.; Classen, A.; Unruh, T.; Li, N.; Brabec, C. J. Efficient Polymer Solar Cells Based on Non-fullerene Acceptors with Potential Device Lifetime Approaching 10 Years. *Joule* **2019**, *3*, 215-226.

[151] Guo, J.; Wu, Y.; Sun, R.; Wang, W.; Guo, J.; Wu, Q.; Tang, X. F.; Sun, C. K.; Luo, Z. H.; Chang, K.; Zhang, Z. H.; Yuan, J.; Li, T. F.; Tang, W. H.; Zhou, E. J.; Xiao, Z.; Ding, L. M.; Zou, Y. P.; Zhan, X. W.; Yang, C. L.; Li, Z.; Brabec, C. J.; Li, Y. F.; Min, J. Suppressing photo-oxidation of non-fullerene acceptors and their blends in organic solar cells by exploring material design and employing friendly stabilizers. *J. Mater. Chem. A* **2019**, *7*, 25088-25101.

[152] Park, S.; Son, H. J. Intrinsic photo-degradation and mechanism of polymer solar cells: the crucial role of non-fullerene acceptors. *J. Mater. Chem. A* **2019**, *7*, 25830-25837.

[153] Speller, E. M.; Clarke, A. J.; Aristidou, N.; Wyatt, M. F.; Francas, L.; Fish, G.; Cha, H.; Lee, H. K. H.; Luke, J.; Wadsworth, A.; Evans, A. D.; McCulloch, I.; Kim, J. S.; Haque, S. A.; Durrant, J. R.; Dimitrov, S. D.; Tsoi, W. C.; Li, Z. Toward Improved Environmental Stability of Polymer:Fullerene and Polymer:Nonfullerene Organic Solar Cells: A Common Energetic Origin of Light- and Oxygen-Induced Degradation. *ACS Energy Lett* **2019**, *4*, 846-852.

[154] Limbu, S.; Pont, S.; Doust, A. B.; Kwon, S.; Fuller, P.; Tan, E.; Durrant, J. R.; Kim, J. S. Impact of Initial Bulk-Heterojunction Morphology on Operational Stability of Polymer:Fullerene Photovoltaic Cells. *Advanced Materials Interfaces* **2019**, *6*, 1801763.

[155] Du, X.; Heumueller, T.; Gruber, W.; Almora, O.; Classen, A.; Qu, J.; He, F.; Unruh, T.; Li, N.; Brabec, C. J. Unraveling the Microstructure-Related Device Stability for Polymer Solar Cells Based on Nonfullerene Small-Molecular Acceptors. *Adv. Mater.* **2020**, *32*, e1908305.

[156] Zhang, Z. H.; Yu, J. S.; Yin, X. X.; Hu, Z. H.; Jiang, Y. F.; Sun, J.; Zhou, J.; Zhang, F. J.; Russell, T. P.; Liu, F.; Tang, W. H. Conformation Locking on Fused-Ring Electron Acceptor for High-Performance Nonfullerene Organic Solar Cells. *Adv. Funct. Mater.* **2018**, *28*, 1705095.

[157] Liu, Y.; Zhang, Z.; Feng, S.; Li, M.; Wu, L.; Hou, R.; Xu, X.; Chen, X.; Bo, Z. Exploiting Noncovalently Conformational Locking as a Design Strategy for High Performance Fused-Ring Electron Acceptor Used in Polymer Solar Cells. *J. Am. Chem. Soc.* **2017**, *139*, 3356-3359.

[158] Feng, S.; Li, M.; Tang, N.; Wang, X.; Huang, H.; Ran, G.; Liu, Y.; Xie, Z.; Zhang, W.; Bo, Z. Regulating the Packing of Non-Fullerene Acceptors via Multiple Noncovalent Interactions for Enhancing the Performance of Organic Solar Cells. *ACS Appl. Mater. Interfaces* **2020**, *12*, 4638-4648.

[159] Cai, Z.; Awais, M. A.; Zhang, N.; Yu, L. Exploration of Syntheses and Functions of Higher Ladder-type π-Conjugated Heteroacenes. *Chem* **2018**, *4*, 2538-2570.

[160] Wang, Y.; Guo, H.; Ling, S.; Arrechea-Marcos, I.; Wang, Y.; Lopez Navarrete, J. T.; Ortiz, R. P.; Guo, X. Ladder-type Heteroarenes: Up to 15 Rings with Five Imide Groups. *Angew. Chem. Int. Ed. Engl.* **2017**, *56*, 9924-9929.

[161] Miao, Q. Ten years of N-heteropentacenes as semiconductors for organic thin-film transistors. *Adv. Mater.* **2014**, *26*, 5541-9.

[162] Lee, J.; Kalin, A. J.; Yuan, T.; Al-Hashimi, M.; Fang, L. Fully conjugated ladder polymers. *Chem Sci* **2017**, *8*, 2503-2521.

[163] Cai, Z.; Zhao, D.; Sharapov, V.; Awais, M. A.; Zhang, N.; Chen, W.; Yu, L. Enhancement in Open-Circuit Voltage in Organic Solar Cells by Using Ladder-Type Nonfullerene Acceptors. *ACS Appl. Mater. Interfaces* **2018**, *10*, 13528-13533.

[164] Li, S. X.; Liu, W. Q.; Li, C. Z.; Lau, T. K.; Lu, X. H.; Shi, M. M.; Chen, H. Z. A non-fullerene acceptor with a fully fused backbone for efficient polymer solar cells with a high open-circuit voltage. *J. Mater. Chem. A* **2016**, *4*, 14983-14987.

[165] Dai, G.; Chang, J.; Shi, X.; Zhang, W.; Zheng, B.; Huang, K.-W.; Chi, C. Thienoacene-Fused Pentalenes: Syntheses, Structures, Physical Properties and Applications for Organic Field-Effect Transistors. *Chem. Eur. J.* **2015**, *21*, 2019-2028.

[166] Gronowitz, S.; Westerlund, C.; Hörnfeldt, A. B. The Synthetic Utility of Heteroaromatic Azido Compounds. I. Preparation and Reduction of Some 3-Azido-2-substituted Furans, Thiophenes, and Selenophenes. *Acta Chem. Scand., Ser. B* **1975**, *29*, 224.

[167] Airey, J.; Barrague, M.; Edwards, M. L.; Ferro, M.; Friedrich, D.; Gillespy, T. A.; Jurcak, J.; Musick, K.; Weintraub, P. M. A Convenient Preparation of Thieno[3,2-c]pyrazole. *Synthesis-Stuttgart* **2014**, *46*, 96-100.

[168] Degl'innocenti, A.; Funicello, M.; Scafato, P.; Spagnolo, P. Reaction of Ortho-Azidohetarenecarbaldehydes with Bis(Trimethylsilyl)Sulfide - a Novel Route to Fused Isothiazoles. *Chem. Lett.* **1994**, *23*, 1873-1876.

[169] Bjork, M.; Grivas, S. Synthesis of novel 2-aminoimidazo[4,5-b]pyridines, including the thieno analogue of the cooked-food mutagen IFP. *J. Heterocycl. Chem.* **2006**, *43*, 101-109.

[170] Ahmed, E.; Earmme, T.; Ren, G. Q.; Jenekhe, S. A. Novel n-Type Conjugated Ladder Heteroarenes: Synthesis, Self-Assembly of Nanowires, Electron Transport, and Electroluminescence of Bisindenoanthrazolines. *Chem. Mater.* **2010**, *22*, 5786-5796.

[171] Li, H. Y.; Earmme, T.; Subramaniyan, S.; Jenekhe, S. A. Bis(Naphthalene Imide)diphenylanthrazolines: A New Class of Electron Acceptors for Efficient Nonfullerene Organic Solar Cells and Applicable to Multiple Donor Polymers. *Adv. Energy Mater.* **2015**, *5*, 1402041.

[172] Comyn, J. Contact Angles and Adhesive Bonding. *Int. J. Adhes. Adhes.* **1992**, *12*, 145-149.

[173] Huang, H.; Guo, Q.; Feng, S.; Zhang, C. e.; Bi, Z.; Xue, W.; Yang, J.; Song, J.; Li, C.; Xu, X.; Tang, Z.; Ma, W.; Bo, Z. Noncovalently fused-ring electron acceptors with near-infrared absorption for high-performance organic solar cells. *Nat. Commun.* **2019**, *10*, 3038.

[174] Babel, A.; Jenekhe, S. A. Morphology and Field-Effect Mobility of Charge Carriers in Binary Blends of Poly(3-hexylthiophene) with Poly[2-methoxy-5-(2-ethylhexoxy)-1,4-phenylenevinylene] and Polystyrene. *Macromolecules* **2004**, *37*, 9835-9840.

[175] Jeffrey, G. A., *An Introduction to Hydrogen Bonding*. Oxford University Press: 1997.

[176] Mathews, I.; Kantareddy, S. N.; Buonassisi, T.; Peters, I. M. Technology and Market Perspective for Indoor Photovoltaic Cells. *Joule* **2019**, *3*, 1415-1426.

VITA

Xiaomei Ding was born and raised in Hai'an, Jiangsu, China in 1991. She began her journey from the elementary school and middle school in her village. These schools were funded by Dr. Ke-Chuan Ke, an accomplished scientist and medical doctor from Hai'an, who had been studying and working in America since 1940s. From 2006 to 2009, she attended Hai'an Senior School of Jiangsu Province and was a member of the Top Class. After high school, she studied at School of Chemistry and Chemical Engineering in Nanjing University and earned Bachelor of Science in Chemistry in 2013. She then moved to Seattle, Washington and continued to pursue PhD in Chemistry at University of Washington. She conducted graduate research in organic semiconductors and organic optoelectronic devices under supervision of Professor Samson A. Jenekhe.

The following is the list of the author's publications:

1. **Ding, X.**; Tran, D. K.; West, S. M.; Nguyen, M; Kuzuhara, D.; Koganezawa, T.; Kaminsky, W., Jenekhe, S. A. Ladder Molecule Acceptors for High-Performance Organic Solar Cells: Design, Synthesis, Enhanced Intrinsic Stability and Photovoltaic Properties. *in preparation*.

2. **Ding, X.**; Tran, D. K.; West, S. M.; Kuzuhara, D.; Koganezawa, T.; Kaminsky, W.; Jenekhe, S. A. Effects of Side Chains and Halogenations on Ladder Molecule Acceptors. *in preparation*.

3. **Ding, X.**; Tran, D. K.; Kaminsky, W.; Kuzuhara, D.; Koganezawa, T.; Jenekhe, S. A. Synthesis and Characterization of Selenophene-Containing P-Type Semiconducting Polymers for Organic Solar Cells . *in preparation*.

4. **Ding, X.**; Tran, D. K.; Kuzuhara, D.; Koganezawa, T.; Jenekhe, S. A. Comparative Study of Selenophene- and Thiophene-Containing n-Type Semiconducting Polymers for High Performance All-Polymer Solar Cells. *ACS Appl. Polym. Mater.* **2020**, *3*, 49-59.

5. Tran, D. K.; Robitaille, A.; Hai, I. J.; **Ding, X.**; Kuzuhara, D.; Koganezawa, T.; Chiu, Y.-C.; Leclerc, M.; Jenekhe, S. A. Elucidating the impact of molecular weight on morphology, charge transport, photophysics and performance of all-polymer solar cells. *J. Mater. Chem. A* **2020**, *8*, 21070-21083.

6. Kolhe, N. B.; West, S. M.; Tran, D. K.; **Ding, X.**; Kuzuhara, D.; Yoshimoto, N.; Koganezawa, T.; Jenekhe, S. A. Designing High Performance Nonfullerene Electron Acceptors with Rylene Imides for Efficient Organic Photovoltaics. *Chem. Mater.* **2020**, *32*, 195-204.

7. Liu, Z.; Zhai, D.; Pan, L.; Qiu, H.; Li, W.; **Ding, X.**; Shi, Y., Template Synthesis of Freestanding Nanostructural Membrane of Polyaniline. *Chem. Lett.* **2011,** *40* (6), 644-645.